ADDIS ABABA UNIVERSITY

SCHOOL OF GRADUATE STUDIES

Chemically Modified Electrodes for the Electrochemical Determination of Selected Pesticides and Pharmaceuticals

Molla Tefera Negash

June 2016

Chemically Modified Electrodes for the Electrochemical Determination of Selected Pesticides and Pharmaceuticals

Molla Tefera Negash

A Thesis Submitted to the Department of Chemistry in Partial Fulfillment of the Requirements for the Degree of Doctor of Philosophy in Chemistry, Addis Ababa University

Supervisors: Merid Tessema (PhD)

Shimelis Admassie (PhD)

June 2016

Abstract

In this study, electrochemical sensors were developed for the determination of pesticides and pharmaceutical drugs based on poly(4-amino-3-hydroxynaphthalene sulfonic acid) (poly(AHNSA)), multi-walled carbon nanotubes (MWCNTs), mercury film (MF) and composites of cobalt nanoparticles-polypyrrole (CoNPs/PPy), graphene oxide-polypyrrole (GO/PPy) and multi-walled carbon nanotubes-poly(4-amino-3-hydroxynaphthalene sulfonic acid) (MWCNTs/poly(AHNSA)) modified glassy carbon electrode (GCE).

CoNPs/PPy/GCE composite electrode was fabricated by electropolymerization of pyrrole in $LiClO_4$ solution onto the GCE using cyclic voltammetry followed by drop coating CoNPs on the surface of PPy/GCE. The morphological structure and surface analysis of the electrodes were characterized using scanning electron microscopy, transmission electron microscopy, energy dispersive spectroscopy (EDS), Ultra violet-Visible spectroscopy (UV–Vis), Fourier Transform Infrared Spectroscopy (FT-IR), electrochemical impedance spectroscopy (EIS) and cyclic voltammetry (CV). The characterization results demonstrated that PPy chains interacted with CoNPs in the composite through donor-acceptor bonds. The sensor exhibited a high electroactive surface area and a low electron transfer resistance towards phoxim. Under the optimal conditions, the sensor showed linear relationship between the peak current and the concentration of phoxim in the range of 0.025 μM–12 μM with the detection limit of 0.0045 μM. Besides, the sensor exhibited excellent reproducibility, good stability and selectivity towards possible interfering substances. The sensor was also successfully applied for the determination of phoxim in water samples.

Graphene oxide-polypyrrole modified glassy carbon electrode (GO/PPy/GCE) composite was prepared by electrochemical polymerization of a mixture containing 30 μL of GO suspension and 10 μL of 0.25 M pyrrole in 0.1 M $LiClO_4$ using cyclic voltammetry. SEM, FT-IR, UV-Vis and Raman spectroscopy were used to study the morphology and composition of GO/PPy/GCE. The results showed that GO layers have been successfully incorporated into the PPy film. The electrochemical behavior of the sensor was also characterized using EIS and CV. The voltammetric response showed a higher current response and a lower reduction potential at

GO/PPy/GCE for phenothrin reduction. The potential shift and current enhancement at the surface of GO/PPy/GCE demonstrated that the sensor exhibited favorable electron transfer kinetics and electrocatalytic activity towards the reduction of phenothrin. The sensor showed a linear response for phenothrin between 0.025 μM to 20 μM and a detection limit of 0.0138 μM. The applicability of the proposed method was carried for the determination of phenothrin in fruit juice samples.

Fenitrothion was determined electrochemically on the surface of multiwall carbon nanotubes modified glassy carbon electrode (MWCNTs/GCE). The modified electrode showed three times higher surface active area as compared with glassy carbon electrode. The experimental parameters (amount of MWCNTs, pH of the fenitrothion solution and adsorption parameters) were optimized. The reduction current showed a linear relationship with the concentration of fenitrothion in a range of 0.01 μM to 5.0 μM, with a detection limit of 0.0064 μM. The practical applicability of method was demonstrated in the assessment of fenitrothion in soil and teff samples and good recoveries varied from 86.7% to 93.3% were obtained.

The electrochemical behavior of endosulfan was investigated at the surface of glassy carbon electrode modified with mercury film (MF/GCE). The electrode showed a linear response to endosulfan in the concentration range of 0.01-5.0 μM, with a detection limit of 0.0059 μM. The modified electrode also exhibited good stability and reproducibility. The sensor was successfully applied for the determination of endosulfan in onion and tomato samples.

A poly(4-amino-3-hydroxynaphthalene sulfonic acid) modified glassy carbon electrode was employed for the simultaneous determination of caffeine and paracetamol using square-wave voltammetry. Poly(AHNSA)/GCE were electrochemically deposited on a glassy carbon electrode by scanning the potential in the potential range of -0.8 V to 2.0 V at a scan rate of 0.1 V s^{-1} for fifteen cycles in 0.1 M HNO_3 solution. The performance of the sensor was investigated using CV and SWV and it showed a linear response for both caffeine and paracetamol in the concentrations range of 10–125 μM. The detection limits were 0.79 μM and 0.45 μM for caffeine and paracetamol, respectively. The effects of some interfering substances in the determination of caffeine and paracetamol were also studied and their interferences were found

to be negligible which proved the selectivity of the modified electrode. The method was successfully applied for the quantitative determination of caffeine and paracetamol in Coca-Cola, Pepsi-Cola and tea samples.

Finally, a sensitive voltammetric method was developed based on glassy carbon electrode modified with a combination functionalized MWCNTs and poly(AHNSA) for the determination of uric acid (UA). The sensor was prepared by drop coating MWCNTs solution on the surface of poly(AHNSA)/GCE. A significant enhancement in the oxidation peak current of UA was observed at MWCNTs/poly(AHNSA)/GCE compared with bare GCE, poly(AHNSA)/GCE and MWCNTs/GCE. The electrode demonstrated a wide linear response in the range from 1.0–100 μM, with a low detection limit of 0.046 μM and was successfully employed for quantification of UA in urine samples.

Acknowledgments

The experimental part of this work would not have been accomplished without the assistance of many people and institutions. First and for most, I would like to express my deep and sincere gratitude to my advisors, Dr. Merid Tessema and Dr. Shimelis Admassie for their continuous encouragement, advice, valuable discussion and arranging facilities without hesitation and their warm assistance and support throughout my research study. They shared their own huge life experiences and gave me energy and stimuli to finish my research. Besides, I also thank their critical comments on the courses, seminars, manuscript and thesis work.

I am very pleased and appreciate Dr. Solomon Mehertie for taking time to support laboratory works, engaging scientific discussions and reviewing manuscripts. I also would like to extend my acknowledgement to Dr. Negussie Negash for providing me many materials and share so many hours of encouraging and invaluable advice with out in reservation and insight throughout my studies. Besides, I also appreciate his critical comments and constructive criticism given to me.

I would like to extend my appreciation to Prof. Priscilla Baker who hosting and supervising me as an exchange student and providing all the chemicals, apparatus and instrumentation required for my research for six months in Department of Chemistry and Sensor Lab, University of the Western Cape, South Africa. In addition, she has made a lot of effort in processing to extend my visa process in order to accomplish the remaining work according the plan.

I am thankful to Sensor lab staff members especially Professor Emmanuel Iwuoha and Dr. Tesfaye Waryo who made the materials for my work easily accessed and helped me in familiarizing the instruments and the environment in general.

I also would like to extend my acknowledgement to the Physics Department at University of the Western Cape for their assistance with HRTEM and (HR)SEM experiments. I am grateful to my friends Dr. Melisew, Dr. Tewodros and Mr. Fikreyohannes with his wife Firehiwot who provided pleasant atmosphere and good time in order to feel I am at home.

I would like to acknowledge all the academic and technical staff members of the Department of Chemistry, Addis Ababa University for their support over the years. My special thanks to Prof. Wondimagegne Mamo for his generous permission to do some extraction experiments for sample analysis in his research laboratory and encouraging every time we have met.

I would like to express my thanks to the Department of Chemistry, Addis Ababa University, for providing me this scholarship, for the financial support and giving me access to laboratory facilities for this study. I would like to thank Dr. Ahmed Mustefa, Head Department of Chemistry for his special treatment and facilitating my travel to South Africa.

My Special thanks also go to my colleagues Dr. Alemnew and Dr. Meareg who were members of our electroanalytical group for their continuous guiding and motivation being here with me. I would like to show my gratitude to PhD students of analytical chemistry and physical streams particularly, Birhanu Mekassa, Dessie Tebebe and Tesfaye H/Mariam for their friendship, ideas and continuous support in carrying out this study.

I would also like to acknowledge the University of Gondar, for sponsoring me to do my PhD together with different supports for completing the work.

Finally, I would like to thank my sons Beaman and Yonatan and wife Tigist Alemnew for their understanding, tolerance and exciting support during my long stay far from home. I am also very pleased and appreciate my parents for their prayers, supports and love.

Contents

Abstract i

Acknowledgments iv

List of Figures xii

List of Schemes xviii

List of Tables xix

List of Abbreviation xxi

1. INTRODUCTION 1

1.1. Electrochemical sensors 1

1.2. Conducting polymers and carbon nanotubes 2

1.2.1. Conducting polymers 2

1.2.2. Polypyrrole (PPy) 6

1.2.3. Synthesis of polypyrrole 6

1.3. Carbon nanotubes 8

1.3.1. Synthesis of carbon nanotubes 9

1.3.2. Properties of carbon nanotubes 10

1.4. Modified electrodes 13

1.4.1. Polymer modified electrodes 16

1.4.2. Carbon nanotubes modified electrodes 19

1.4.3. Mercury film modified electrodes 20

2. ELECTROANALYTICAL TECHNIQUES 21

2.1. Electrochemical cells 21

2.2. Electrode processes 25

2.3. Cyclic voltammetry 26

2.4. Square wave voltammetry 29

2.5. Electrochemical impedance spectroscopy (EIS) 31
3. SURFACE CHARACTERIZATION 38
3.1. Scanning electron microscope (SEM) 38
3.2. High resolution transmission electron microscope (HRTEM) 41
3.3. Fourier transform infrared spectroscopy (FTIR) 42
3.4. Raman spectroscopy 43
3.5. Ultraviolet-Visible spectroscopy (UV-Vis) 44
4. OBJECTIVES OF THE STUDY 45
4.1. General objective 45
4.2. Specific objectives 45
5. MATERIALS AND METHODS 46
5.1. Chemicals and reagents 46
5.2. Apparatus and instrumentations 47
5.3. Preparation of modified electrodes 48
5.3.1. CoNPs/PPy/GCE 48
5.3.2. GO/PPy/GCE 49
5.3.3. MWCNTs/GCE 50
5.3.4. MF/GCE 50
5.3.5. Poly(AHNSA)/GCE 50
5.3.6. MWCNTs/poly(AHNSA)/GCE 51
5.4. Preparation of samples 51
5.4.1. Water samples 51
5.4.2. Fruit juice samples 51
5.4.3. Soil and teff samples 51
5.4.4. Onion and tomato samples 52

5.4.5. Coca-cola, pepsi-cola and tea samples 53
5.4.6. Urine samples 53
6. RESULTS AND DISCUSSION 54
6.1. Synthesis, characterization and electrochemical application of cobalt nanoparticles-polypyrrole modified glassy carbon electrode for the determination of phoxim 54
6.1.1. Background 54
6.1.2. Electropolymerization and characterization of electrode materials 55
6.1.3. Surface Characterization 56
6.1.4. Electrochemical characterization 62
6.1.5. Electrochemical behavior of phoxim 64
6.1.6. Effect of pH 67
6.1.7. Effect of scan rate 68
6.1.8. Effects of accumulation potential and time 69
6.1.9. Calibration curve 70
6.1.10. Repeatability, reproducibility and stability 72
6.1.11. Interference study 72
6.1.12. Application 73
6.2. Electrochemical determination of phenothrin in fruit juices at graphene oxide-polypyrrole modified glassy carbon electrode 75
6.2.1. Background 75
6.2.2. Prepartion of GO/PPy/GCE 76
6.2.3. Surface characterization 78
6.2.4. Electrochemical behaviors of phenothrin 83
6.2.5. Effects of scan rate and pH 85
6.2.6. Effects of accumulation potential and time 88

6.2.7. Calibration curve 89
6.2.8. Repeatability, reproducibility and stability 90
6.2.9. Interference study 91
6.2.10. Application 91
6.3. Determination fenitrothion at multiwalled carbon nanotubes modified glassy carbon electrode 93
6.3.1. Background 93
6.3.2. Electrochemical characterization of MWCNTs/GCE 94
6.3.3. Electrochemical behavior of fenitrothion 95
6.3.4. Effect of varying the amount of MWCNTs on fenitrothion determination 96
6.3.5. Effect of pH 96
6.3.6. Effect of scan rate 97
6.3.7. Effects of accumulation potential and time 98
6.3.8. Effect of square wave parameters 99
6.3.9. Calibration curve 100
6.3.10. Repeatability, reproducibilty and stability 101
6.3.11. Interference study 102
6.3.12. Application 103
6.4. Voltammetric determination of endosulfan in vegetable samples using mercury film modified glassy carbon electrode 104
6.4.1. Background 104
6.4.2. Electrochemical behavior of endosulfan at MF/GCE 105
6.4.3. Effect of pH 106
6.4.4. Effect of scan rate 108
6.4.5. Effects of accumulation potential and time 109

6.4.6. Calibration curve 110
6.4.7. Repeatability, reproducibility and stability 112
6.4.8. Interference study 112
6.4.9. Application 113
6.5. Simultaneous determination of caffeine and paracetamol by square wave voltammetry at poly(4-amino-3-hydroxynaphthalene sulfonic acid) modified glassy carbon electrode 115
6.5.1. Background 115
6.5.2. Electrochemical properties of poly(AHNSA)/GCE 116
6.5.3. Electrochemical behavior of caffeine and paracetamol 117
6.5.4. Electrochemical behavior of caffeine and paracetamol mixture 119
6.5.5. Effect of pH 120
6.5.6. Effect of scan rate 125
6.5.7. Optimization of square wave voltammetric parameters 126
6.5.8. Determination of caffeine and paracetamol 126
6.5.9. Repeatability and stability of the modified electrode 130
6.5.10. Interference study 131
6.5.11. Application 132
6.6. An electrochemical sensor based on multiwalled carbon nanotubes coated poly(AHNSA) modified electrode for the determination of uric acid 135
6.6.1. Background 135
6.6.2. Electrochemical behavior of uric acid 137
6.6.3. Effect of pH 138
6.6.4. Effect of scan rate 140
6.6.5. Accumulation potential and time 141
6.6.6. Calibration curve 142

6.6.7. Repeatbility and stability 144
6.6.8. Interference study 145
6.6.9. Applications 145
7. CONCLUSIONS 147
8. REFERENCES 149

List of Figures

Figure 1.1. Structure of polyacetylene 4

Figure 1.2. Doping mechanism of polyacetylene 5

Figure 1.3. Chemical polymerization of polypyrrole.....7

Figure 1.4. Electrochemical polymerisation of polypyrrole.....8

Figure 1.5. Structures of SWCNTs (A) and MWCNTs (B).....9

Figure 1.6. Covalent functionalized carbon nanotube 12

Figure 1.7. Electrocatalytic reaction on chemically modified electrode (Med- modifier and A-analyte).....14

Figure 2.1. An electrochemical cell with three electrode system 24

Figure 2.2. Potential–time excitation waveform (A) and cyclic voltammogram (B) 28

Figure 2.3. Square wave voltammetry potential waveform (A) and response for a forward current (if), a reverse current (i_r) and net current (i_{net}) (B) 30

Figure 2.4. The impedance plotted as a planar vector using rectangular and polar coordinates...33

Figure 2.5. Nyquist plot (A) and Bode plot (B).....34

Figure 2.6. Randles equivalent circuit.....36

Figure 3.1. Working ranges of various electron microscopy techniques and optical microscopy 38

Figure 3.2. Generation of X-rays 40

Figure 6.1. Cyclic voltammograms of (A) electropolymerization of 0.25 M pyrrole in 0.10 M $LiClO_4$ and (B) a monomer free 0.10 M $LiClO_4$ on GCE (a) and PPy/GCE (b). 56

Figure 6.2. FTIR spectra of PPy and CoNPs/PPy.....57

Figure 6.3. UV-Vis spectra of CoNPs, PPy and CoNPs/PPy.....58

Figure 6.4. HRSEM images of PPy (A) CoNPs (B) and CoNPs/PPy (C) 60

Figure 6.5. HRTEM images of PPy (A) CoNPs (B) and CoNPs/PPy (C) 61

Figure 6.6. Size distribution of CoNPs (A) and CoNPs/PPy (B) 61

Figure 6.7. EDS images of PPy (A) CoNPs (B) and CoNPs/PPy (C) 62

Figure 6.8. Cyclic voltammograms of 5 μM phoxim in 0.1 M PBS (pH 7) at GCE (a), PPy/GCE (b), CoNPs/GCE (c) and CoNPs/PPy/GCE (d).....64

Figure 6.9. Nyquist plot of 20 μM phoxim in ethanol for the GCE (a), PPy/ GCE (b), CoNPs/GCE (c) and CoNPs/PPy/GCE (d) 66

Figure 6.10. (A) Nyquist plots of CoNPs/PPy/GCE for various concentrations of phoxim in PBS pH 7 solution: 1.0 μM (a), 2 μM (b), 5 μM (c) and 10 μM (d) phoxim at CoNPs/PPy/GCE and (B) plot of $1/R_{ct}$ *vs* concentration of phoxim. 67

Figure 6.11. Effect of pH of PBS on the peak current for 5 μM phoxim at CoNPs/PPy/GCE (A) and plot of peak potential *vs* pH (B).....68

Figure 6.12. Cyclic voltammograms for 5.0 μM phoxim in 0.1 M PBS pH 6.0 at the CoNPs/PPy/GCE at various scan rates (A) and plot of the peak current *vs* scan rates (B).....69

Figure 6.13. Effects of accumulation potential (A) and accumulation time (B) on the peak current of 2.5 μM phoxim in PBS solution (pH 6) at the surface of CoNPs/PPy/GCE.....70

Figure 6.14. Square wave voltammograms for various concentrations of phoxim in PBS pH 6.0 at CoNPs/PPy/GCE electrode: (a) 0.025, (b) 0.05, (c) 0.5, (d) 1.5, (e) 3.5, (f) 5.0, (g) 7.5, (h) 10 and (i) 12 μM. Inset: The calibration plot of peak current with concentrations of phoxim at CoNPs/PPy/GCE. 71

Figure 6.15. Square wave voltammograms of CoNPs/PPy/GCE for water samples spiked with different concentrations of standard phoxim (a = 0 μM, b = 0.75 μM, c = 2 μM, d = 4 μM and e = 6 μM) 74

Figure 6.16. Structure of phenothrin.....76

Figure 6.17. Cyclic voltammograms of electropolymerization of a solution of 0.25 M pyrrole in 0.10 M $LiClO_4$ and GO.....77

Figure 6.18. SEM images of the GO (A) and GO/PPy (B).....80

Figure 6.19. FTIR spectra of GO, PPy and GO/PPy.....81

Figure 6.20. UV–Vis spectra of GO, PPy and GO/PPy.....81

Figure 6.21. Raman spectra of GO, PPy and GO/PPy.....82

Figure 6.22. Nyquist plots of 0.1 mM phenothrin at GCE (a), PPy/GCE (b), GO/GCE (c) and GO/PPy/ GCE (d).....83

Figure 6.23. Cyclic voltammograms of 10 μM phenothrin in PBS (pH 7.0) at GCE (a), GO/GCE (b), PPy/GCE (c) and GO/PPy/GCE (d) at 0.1 V s^{-1}.....84

Figure 6.24. Cyclic voltammograms of 10 μM phenothrin in PBS of pH 7.0 at GO/PPy/GCE for various scan rates: (a) 0.05, (b) 0.06, (c) 0.07, (d) 0.08, (e) 0.09, (f) 0.1, (g) 0.11 and (h) 0.12 V s^{-1} (A) and plot of current *vs* scan rate (B).....86

Figure 6.25. Plot of peak potential *vs* logarithm of scan rate for 10 μM phenothrin in PBS of pH 7.0 at GO/PPy/GCE.....87

Figure 6.26. Plot of peak current and peak potential for 10 μM phenothrin at GO/PPy/GCE in PBS of varying pH.....88

Figure 6.27. Effects of accumulation potential (A) and accumulation time (B) on the peak current of 10 μM phenothrin in PBS (pH 6.5).....89

Figure 6.28. Square wave voltammograms of various concentrations of phenothrin (0.025, 0.05, 1.0, 2.5, 5.0, 7.5, 10, 15 and 20 μM in PBS pH 6.5) at GO/PPy/GCE (A) and the calibration plot of phenothrin at GO/PPy/GCE (B).....90

Figure 6.29. Structure of fenitrothion.....93

Figure 6.30. Cyclic voltammograms of 40 μM fenitrothion solution at GCE (a), 0.1 M PBS (pH 7.0) at MWCNTs/GCE (b) and 40 μM fenitrothion solution at MWCNTs/GCE(c). Scan rate: 0.1 V s^{-1}.....95

Figure 6.31. Effect of amount MWCNTs on the reduction peak current of 40 μM fenitrothion in 0.1 M PBS pH 7.0 at 0.1 V s^{-1}.....96

Figure 6.32. Cyclic voltammograms for 40 μM fenitrothion in 0.1 M PBS at various pH (A) and plots of peak current and peak potential *vs* pH for 40 μM fenitrothion at MWCNTs/GCE (B) 97

Figure 6.33. Cyclic voltammograms (A) for 40 μM fenitrothion in 0.1 M PBS (pH 6.0) at MWCNTs/GCE at various scan rates (0.04, 0.06, 0.08, 0.1, 0.12, 0.14, 0.16, 0.18, 0.2 and 0.225 V s^{-1}) and plot of reduction peak current *vs* scan rate (B) 98

Figure 6.34. Effects of accumulation potential (A) and accumulation time (B) on the peak current for 40 μM fenitrothion in 0.1 M PBS of pH 6.0 at MWCNTs/GCE 99

Figure 6.35. Square wave voltammograms of fenitrothion (a) 0.01 μM, (b) 0.2 μM, (c) 0.5 μM, (d) 0.75 μM, (e) 1.0 μM, (f) 1.25 μM, (g) 1.5 μM, (h) 2.0 μM, (i) 2.5 μM, (j) 3.0 μM, (k) 3.5 μM, (l) 4.0 μM and (m) 5.0 μM (A) and calibration plot of peak current *vs* concentrations of fenitrothion at MWCNTs/GCE (B) 100

Figure 6.36. Cyclic voltammograms of 50 μM endosulfan at GCE (a) and MF/GCE (b) in BRB pH 7.0 at scan rate of 0.1 V s^{-1} 106

Figure 6.37. Cyclic voltammograms of 50 μM endosulfan at MF/GCE in various pH values of BRB (A) and plots of the peak current and potential *vs* pH of BRB (B)..... 107

Figure 6.38. Cyclic voltammograms of 50 μM endosulfan in BRB solution (pH 5) at MF/GCE with increasing scan rates (0.05-0.3 V s^{-1}) (A) and plot of peak current *vs* scan rate (B) 108

Figure 6.39. Plot of peak potential *vs* logarithm of scan rate for 50 μM endosulfan in BRB (pH 5) at MF/GCE 109

Figure 6.40. Effect of accumulation time (A) and accumulation potential (B) on the peak currents of endosulfan in BRB pH 5.0 110

Figure 6.41. Square wave voltammograms of various concentration of endosulfan (from a to h): 0.05, 0.5, 1.0, 2.5, 3.5, 5.0, 7.0 and 10 μM in BRB pH 5 (A) and plot of the peak current *vs* concentration of endosulfan (B) 111

Figure 6.42. Square wave voltammograms of onion (A) and tomato (B) samples without (a) and spiked with 1.0 μM (b), 1.5 μM (c) and 2.5 μM (d) standard endosulfan in BRB pH 5.0 at MF/GCE 114

Figure 6.43. Cyclic voltammetric electropolymerization of $2x10^{-3}$ M AHNSA in 0.1 M HNO_3 at GCE. Inset: Cyclic voltammetry of poly(AHNSA)/GCE in a 0.1 M HNO_3 at 0.1 V s^{-1}.....117

Figure 6.44. Cyclic voltammograms of poly(AHNSA/GCE without caffeine (a), 1.0 mM caffeine at GCE (b) and poly(AHNSA)/GCE (c) in 0.1 M ABS (pH 5.0), at scan rate of 0.1 V s^{-1} 118

Figure 6.45. Cyclic voltammograms of 0.1 M ABS (pH 5.0) at poly(AHNSA)/GCE (a), 0.1 mM paracetamol in ABS (pH 5.0) at GCE (b) and at poly(AHNSA)/GCE (c), at a scan rate of 0.1 V s^{-1} 119

Figure 6.46. Cyclic voltammograms of 0.1 M ABS (pH 5.0) at poly(AHNSA)/GCE (a) 1.0 mM caffeine and 0.1 mM paracetamol at GCE (b) and (c) at poly(AHNSA)/GCE at a scan rate of 0.1 V s^{-1} 120

Figure 6.47. Cyclic voltammograms of 1.0 mM caffeine in ABS of various pH value at poly(AHNSA)/GCE. Inset: plot of peak currents *vs* pH at a scan rate of 0.1 V s^{-1}. 122

Figure 6.48. Plot of peak potential values for 1.0 mM caffeine as a function of pH at poly(AHNSA)/GCE.....122

Figure 6.49. Cyclic voltammograms for 0.1 mM paracetamol in ABS of various pH value at poly(AHNSA)/GCE. Inset: plot of peak currents *vs* pH at a scan rate of 0.1 V s^{-1}. 123

Figure 6.50. Plot of peak potentials for 0.1 mM paracetamol as a function of pH at poly(AHNSA)/GCE.....124

Figure 6.51. Cyclic voltammograms of 1.0 mM caffeine and 0.1 mM paracetamol in ABS pH 4.5 at the poly(AHNSA)/GCE at various scan rates (0.075, 0.10, 0.125, 0.150, 0.175, 0.20, 0.225, 0.250 and 0.275 V s^{-1}) (A) and plot of peak current *vs* scan rate of caffeine and paracetamol (B) 125

Figure 6.52. Square wave voltammograms of 5, 8, 10, 20, 30, 40, 60, 80, 100 and 125 μM of caffeine and 2 μM paracetamol at poly(AHNSA)/GCE. Inset: plot of the peak current of caffeine *vs* concentration.....127

Figure 6.53. Square wave voltammograms of 3, 6, 8, 10, 15, 20, 30, 40, 50 and 60 μM of paracetamol and 10 μM caffeine in ABS (pH 4.5) at poly(AHNSA)/GCE. Inset: plot of current responses *vs* paracetamol concentration. 129

Figure 6.54. Square wave voltammograms for different concentrations (a = 10, b = 20, c = 30, d = 40, e = 60, f = 80, g = 100 and h = 125 μM) of caffeine and paracetamol at poly(AHNSA)/GCE. Inset: plot of current *vs* the concentration of caffeine and paracetamol. 130

Figure 6.55. Cyclic voltammograms for 1.0 mM UA in 0.1 M PBS (pH 7) at GCE (a), Poly(AHNSA)/GCE (b), MWCNTs/GCE (c) and MWCNTs/Poly(AHNSA)/GCE (d) at scan rate of 0.1 V s^{-1} 138

Figure 6.56. Cyclic voltammograms for 1.0 mM UA in 0.1 M PBS of various pH (pH 5.0-8.5) at MWCNTs/poly(AHNSA)/GCE at scan rate of 0.1 V s^{-1}.....139

Figure 6.57. Effects of pH on the anodic peak potential for 1.0 mM UA in PBS at scan rate of 0.1 V s^{-1}.....139

Figure 6.58. Cyclic voltammograms for 1.0 mM UA in PBS (pH 7.0) at various scan rates (0.05–0.25 V s^{-1}). Inset: plot of peak currents *vs* scan rates 141

Figure 6.59. Effect of accumulation potential (A) and accumulation time (B) on the peak current for 0.1 mM UA.....142

Figure 6.60. Square wave voltammograms responses for various concentrations of UA in PBS pH 7.0 (from a to h): 1.0, 5.0, 10, 20, 40, 60, 80 and 100 μM at MWCNTs/poly(AHNSA)/GCE. Inset: plot of peak current *vs* the concentration of UA 143

Figure 6.61. Square wave voltammograms of 5 mL urine sample diluted with 0.1 M PBS (pH 7.0) (dash line) and after addition of 50 μM UA to the urine sample (solid line) ...146

List of Schemes

Scheme 1. Synthesis route of functionalized MWNT-benzimidazole 12

Scheme 2. Proposed electropolymerization route of poly(AHNSA) 19

Scheme 3. Proposed active-site structure of CoNPs/PPy. 58

Scheme 4. Illustration of the preparation of CoNPs/PPy/GCE sensor 63

Scheme 5. Mechanism of phoxim reduction. 68

Scheme 6. Route for fabrication of GO/PPy/GCE 78

Scheme 7. Mechanism of phenothrin reduction 86

Scheme 8. Mechanism of endosulfan reduction in acidic solution (A) and basic solution (B) ... 107

Scheme 9. Oxidation reaction of caffeine 124

Scheme 10. Oxidation-reduction reaction of paracetamol 124

Scheme 11. Mechanism of UA oxidation 140

List of Tables

Table 6.1. Surface area of the modified electrodes.....63

Table 6.2. Comparison of different electrochemical sensors reported for the determination of phoxim 71

Table 6.3. Influence of potential interferences on the voltammetric response of CoNPs/PPy/GCE to 10 μM phoxim.....73

Table 6.4. Recovery of phoxim in river water sample.....74

Table 6.5. Influence of interfering substances on the voltammetric response for 10 μM phenothrin in PBS pH 6.5.....91

Table 6.6. Recovery study of phenothrin in juice samples (n= 3).....92

Table 6.7. Comparison of analytical parameters for the reduction of fenitrothion at MWCNTs/GCE and other electrodes.....101

Table 6.8. Effect of interferents on detection of fenitrothion at MWCNTs/GCE 102

Table 6.9. Recovery study of fenitrothion in soil and teff samples (n = 3) at the MWCNTs/GCE 103

Table 6.10. Comparison of analytical performance for the reduction of endosulfan using different electrochemical sensors 111

Table 6.11. Influence of potential interfering species on the current response of endosulfan 113

Table 6.12. Recovery study of endosulfan in onion and tomato samples (n=3) 114

Table 6.13. Effect of interfrences in the analysis of 40 μM caffeine and 40 μM paracetamol under optimized conditions.....131

Table 6.14. Recovery test for caffeine and paracetamol in coca-cola, pepsi-cola and tea samples (n=3). 133

Table 6.15. Comparison of the analytical performance of poly(AHNSA)/GCE for caffeine and paracetamol determination with previously reported work. 134

Table 6.16. Comparison of the electrode with previously reported electrodes for the determination of UA. 144

Table 6.17. Effects of interferences on the response of UA. 145

Table 6.18. Recovery study of UA in urine sample (n = 3) 146

List of Abbreviation

ABS	Acetate buffer solution
AgNps	Silver nanoparticles
AHNSA	4-amino-3-hydroxynaphthalene sulfonic acid
AuNps	Gold nanoparticles
BE	Backscattered electrons
BRB	Britton–Robinson buffer
CCD	Chemical vapor deposition
CNTs	Carbon nanotubes
CoNPs	Cobalt nanoparticels
CPs	Conductive polymers
CV	Cyclic voltammetry
CVD	Chemical vapor deposition
DC	Direct current
DMF	Dimethyl formamide
DPV	Differential pulse voltammetry
DTGS	Deuterium tryglycine sulfate
EDS	Energy dispersive spectroscopy
EIS	Electrochemical impedance spectroscopy
ET	Everhart-Thornley (ET)
FTIR	Fourier transform infrared spectroscopy
GCE	Glassy carbon electrode
GO	Graphene oxide
HRSEM	High resolution scanning electron microscope

HRTEM	High resolution transmission electron microscope
ICPs	Intrinsically conductive polymers
LBL	Layer-by-layer
LSV	Linear sweep voltammetry
MF	Mercury Film
MnNPs	Manganese nanoparticles
MWCNTs	Multiwall carbon nanotubes
NADH	Nicotinamide adenine dinucleotide
PANI	Polyaniline
PBS	Phosphate buffer solution
PPy	Polypyrrole
PtNPs	Platinum Nanoparticles
RSD	Relative standard deviations
SE	Secondary electrons
SEM	Scanning electron microscope
SWCNTs	Single wall carbon nanotubes
SWV	Square wave voltammetry
UA	Uric acid
UV-Vis	Ultraviolet-Visible spectroscopy
WDS	Wavelength dispersive spectrometer

1. INTRODUCTION

Electrochemistry is an interfacial science which is concerned with the interactions between chemical species and interfaces. The interface provides a suitable site for the reaction and a source or sinks for electrons [1]. The reactions in electrochemical processes involve a transfer of electrons from the electrode to the reduced species in solution and the transfer of an ion from the solution to the electrode surface [2]. The electrochemical process can be described by measuring some electrical properties which directly or indirectly related to the concentration of some particular chemical species. Electrical properties such as potential, current, resistance or conductance, or combinations of these are commonly measured. The distinction between various electroanalytical techniques reflects the type of electrical signal used for quantification. Compared with other analytical methods, electrochemical methods have the advantage of low cost, high sensitivity, easy operation, potential for miniaturization and automation, construction of simple portable devices for fast screening purposes and in-field/on-site monitoring [3, 4].

1.1. Electrochemical sensors

A sensor is a device which measures a physical quantity and converts the measurement into signals to be recorded elsewhere for further interpretation [5, 6]. Sensors can be classified as physical and chemical sensors. A physical sensor is sensitive to physical responses such as pressure, temperature, etc., while a chemical sensor provides continuous response which relates to the quantity of a specific chemical species. A chemical sensor consists of a receptor element, which responds in a selective way, and a transducer, which converts the chemical information into an analytical signal. A good sensor has good specificity and sensitivity, insensitivity to any other property likely to be encountered in its application, and does not influence the measured quantity [7, 8].

Based on the types of transducer used, chemical sensors can be classified as electrochemical, electrical, optical, piezoelectrical or thermal. The current interest in analytical field is the use of new materials with chemical (molecular) recognition properties to carry out direct measurements without the necessity for a previous separation step [9]. Compared with other types of sensors,

electrochemical sensors are most rapidly growing because of their remarkable sensitivity, experimental simplicity and low cost [7]. Electrochemical sensors are important subclasses of chemical sensors in which the electrode is used as the transduction element, and is highly qualified for meeting the size, cost, and power requirements of on-site environmental monitoring [10]. Species can be determined quantitatively and qualitatively in solution. Electrochemical sensors can operate in potentiometric, sweep or pulse voltammetric techniques [6, 11, 12]. They are characterized by high sensitivity, good selectivity, wide linear range, minimal space and power requirements, and low-cost instrumentation. Electrochemical devices have been used in a wide range of applications for several decades for drugs, water contaminants [13], explosives [14], carcinogen monitoring (e.g. N-nitroso compounds or aromatic amines), development of (bio)sensors for the determination and control of pesticides [15, 16], energy conversion and storage [10, 17, 18].

1.2. Conducting polymers and carbon nanotubes

1.2.1. Conducting polymers

Following the discovery of the simplest and the first conducting polymer-polyacetylene, many studies were conducted and these studies led to a Nobel Prize for Heeger (USA), MacDiarmid (USA, New Zealand) and Shirakawa (Japan) in 2000. Since then, different types of conducting polymers such as poly(pyrrole), poly(aniline), poly(thiophene) and poly(3,4-ethylenedioxythiophene) have been prepared with a wide range of conductivities. Chemists, physicists and engineers were engaged in the development, improvement and applications of intrinsically conducting polymers [19, 20].

Polymers can be natural or synthetic and are long-chain molecules (macromolecules) consisting of small building blocks or repeating units (monomers) connected to each other through covalent bonds. Initially, polymers were considered as plastic materials with insulating properties and are among the most used materials in the modern world. However, it has been discovered that some polymers have showed conducting properties. Conducting polymers show combination of characteristics of metallic and semiconductor, not exhibited by any other known material. These

special properties are due to the presence of conjugated double bonds along the backbone of the polymer, which enable the overlapping of π-orbital along the molecule (Figure 1.1). The π-electrons in the conjugated systems are loosely bound and delocalized over the whole system and are shared by many atoms. As a result, they can move around the whole system [21, 22].

A tremendous amount of research has been carried out in the field of conducting polymers since 1977 when the conjugated polymer polyacetylene was discovered to conduct electricity through halogen doping [23]. Intrinsic conducting polymers or electroactive conjugated polymers exhibit interesting electrical and optical properties, which were found only in organic systems. The transfers of electrons occur by the movement of electrons through overlapping and unoccupied electronic energy states. However, due to being molecular in nature and lacking long-range order, conductive polymers are markedly different from all the familiar inorganic semiconductors such as Si and Ge [24].

Based on the energy gap (band gap) between the conduction and valence band, materials can be classified as either conductor, insulator, or semiconductor. The energy difference between these two bands determines the resistance of the material to the passage of electrical current. The gap between the valence and conduction bands is large in insulating materials. Hence, it is difficult to promote electrons from the valance band to the conduction band which limits the flow of current through the material. Semiconductors have distinct valence and conduction bands, but the energy gap is not as large as insulators. However, in conductors, the conductance and valence band overlap. Conducting polymers, which combine the electronic characteristic of metals and inorganic semiconductors, possess the attractive advantage of having easy control of synthesis over the properties of the polymeric exposed surface such as structure, morphology and thickness [25, 26].

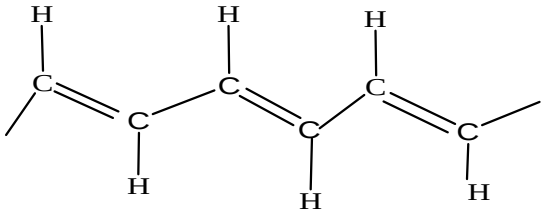

Figure 1.1. Structure of polyacetylene

The properties of intrinsically conducting polymers (ICPs) depend strongly on doping level, ion size of the dopant, protonation level and water content [24]. For instance, the conductivity of polyaniline is reduced as the pH is increased, leading to a decrease in proton doping. However, the conductivity of intrinsically conducting polymers such as polythiophene or polypyrrole demonstrates very little pH dependence. The effect of counter ion incorporated into the polymer as a dopant during polymer synthesis or testing on the pH stability of the intrinsically conducting polymers can also be important. Therefore, it is important to test the pH stability of intrinsically conductive polymers during incorporation of counter ion into the polymer as a dopant during polymer synthesis [25]. PANI for instance, shows high conductivity upon doping with simple Bronsted acids. PPy films doped with p-toluene sulphonate give good mechanical properties and chemical durability against oxidation. On doping, pristine (neutral) conductive polymer changes in to highly conductive polymers. The electronic conductivity originates from partial oxidation of conjugated π-bonds and these positive charges are equilibrated by inorganic anions, which can diffuse through the polymer net work. Charging and discharging of the film is accompanied by insertion and expulsion of anions of the supporting electrolyte. Alternatively, the conductive polymers can be partly reduced with cations as counter ions. Introduction of subtly different dopant groups into ICPs including variations in doping level results in different conductivities of the material. These dopants can be incorporated in to the polymer through chemically, electrochemically, or optically [27, 28].

The doping process in CPs is slightly different from those in inorganic crystal (semiconductors). In semiconductors, doping is introduced by replacing atoms in the crystalline by acceptor or donor atoms. In oxidation doping (p-doping), an electron is taken from the valence band of the polymer (Figure 1.2A) and thus forming radical cations, *i.e.* polarons (Figure 1.2B). Here, the

chemical bonds are deformed and the unpaired electrons inside the gap become closer to the top of the valence band. The cation-radical in the polymer backbone is delocalized within several repeating units. The location of the electronic level of unpaired electrons in the gap, correlated with appearance of positive charge and the related transformation of the chemical bonds around this level, is equivalent to the formation of a positively charged polaron. With further oxidation, more electrons are withdrawn from the valence band; the polarons interact with each other and merging the localized polaronic levels into a continuous polaronic band. At high levels of doping, polaronic charge carriers may recombine their spins forming spinless, double charged bipolaronic charge carriers and these expand their own bands in the gap at the expense of the polaronic and valence bands (Figure 1.2C). Reduction doping (n-doping) causes the appearance of negatively charged polarons in the gap near the bottom of the conduction band, similar to the formation of positively charged polarons considered above. The formation of the electronic band structure with doping level suggests the appearance of a metal-like conductivity.

The motion of delocalized electrons occurs through conjugated systems; however, the electron hopping mechanism is likely to be operative, especially between chains (interchain conduction) and defects. Electrochemical transformation usually leads to a reorganization of the bonds of the polymers prepared by oxidative or less frequently reductive polymerization of benzoid or nonbenzoid (mostly amines) and heterocyclic compounds [25].

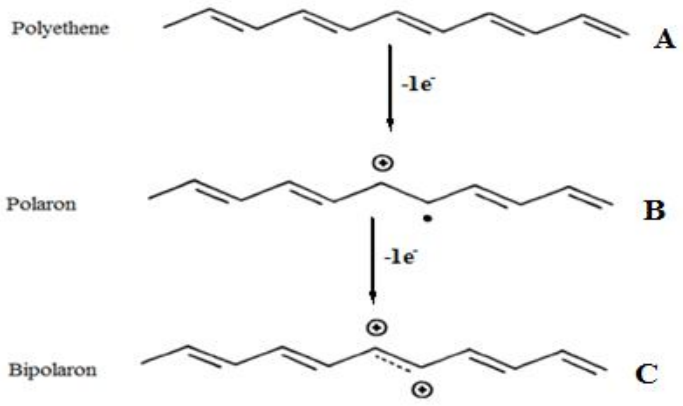

Figure 1.2. Doping mechanism of polyacetylene

1.2.2. Polypyrrole (PPy)

Polypyrrole is a conducting polymer which has an attractive characteristics due to its high electrical conductivity (10^1–10^3 S cm^{-1}), its ease and high flexibility in preparation, good mechanical properties, high environmental and thermal stabilities. As a consequence, PPy is a promising material for commercial applications compared with many other conducting polymers [29, 30]. The electrical conductivity of PPy is the result of two important factors, the number and mobility of charge carriers. The positive charges created on the polymer backbone are the charge carriers for the electrical conduction. Like other conducting polymers, the electrical conductivity of PPy also depends on the electropolymerization conditions such as temperature, the type and concentration of dopant anion [31-33].

1.2.3. Synthesis of polypyrrole

Polypyrrole is most commonly synthesized through chemical and electrochemical polymerizations. Chemical polymerizataion is a simple, fast and controllable process which proceeds in the presence of the monomer (pyrrole) and oxidants such as $K_2S_2O_8$, $FeCl_3$, $(NH_4)_2S_2O_8$ and $CuCl_2$ with appropriate electrolyte. Iron(III) chloride and water have been found to be the best chemical oxidant and solvent for chemical polymerisation with respect to desirable conductivity characteristics, respectively. Figure 1.3 shows the overall polymerisation of polypyrrole with ferric chloride oxidant. The monomer and the oxidant form intermediate species with time such as dimers, trimers, oligomers and finally polymer chain of linked monomer with an alternate single and double bonds [34].

The oxidizing agent Fe^{3+} ions are reduced to Fe^{2+}, imparting +1 charge and donating their excess Cl^- ion as dopant ion to the polymer. The electrical neutrality of the polymer can be maintained by incorporation of anions from the reaction solution such as chloride ion from $FeCl_3$. Here, the properties of the polymer are strongly influenced by the type of the solvent, reaction temperature, time, nature and concentration of the oxidizing agent. Polypyrrole containing substituents like long-chain alkyl and sulphonic groups are more soluble in common organic solvents. However, in such polymers the π-conjugation along the polymer chain decreases and brings a significant

decrease in the electrical conductivity of the polymer. Furthermore, it is tedious and leads to low efficiency and high cost [30, 35, 36].

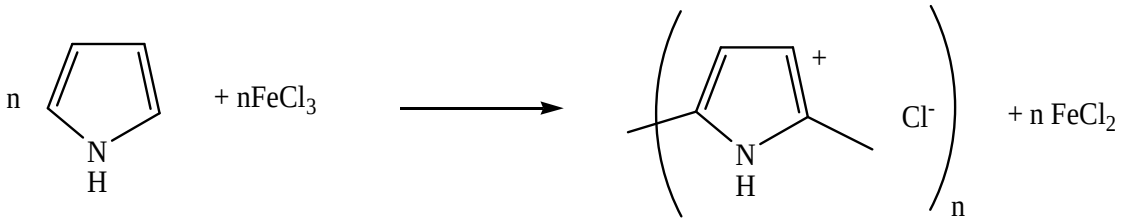

Figure 1.3. Chemical polymerization of polypyrrole

Electrochemical polymerization produces thin films with a thickness of a few micrometers on an electrode surface with better conductivity and long-term stability. It is carried out by electropolymerizing a solution containing the monomer and an anionic dopant at the surface of an electrode anodically. The monomer is oxidised to a radical cation and reacts with another monomer to form a dimer, oligomeric and then the polymer products. The overall electropolymerization of polypyrrole can be simply shown as in Figure 1.4. The extended conjugation in the polymer results in a lowering of the oxidation potential compared to the monomer. Like chemical polymerization, the quality and quantity of the resulting polymer films in electrochemical polymerization are affected by various factors, such as the nature and concentration of the monomer, counter ion, solvent, the electrode type, applied potential, temperature and pH of the solution. Since the oxidation potential of pyrrole is relatively low, its electrochemical polymerization can be carried in aqueous electrolytes. In this method, dopants are not only critical to establish the electrical neutrality of the polymer film, but also determine the morphology and the conductivity of the polypyrrole. The conductivity can be enhanced significantly by using aromatic sulfonate dopants [31, 33, 37, 38]. In general, electrochemical polymerization produces a very thin and uniform polymer films on the surface of an electrode with high degree of geometrical conformity and controllable thickness using a potentiodynamic cycling at specific scan cycles [39].

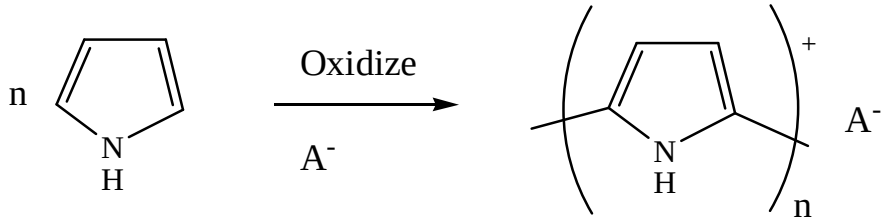

Figure 1.4. Electrochemical polymerisation of polypyrrole

1.3. Carbon nanotubes

The development of advanced researches in the areas of nanoscience and nanotechnology is making the possible creation of new materials based on carbon structures with unique properties and potential applications of various nanostructures [40, 41]. Since the discovery of carbon nanotubes (CNTs) by Iijima in 1991, they have generated interest by researchers in various fields of study. CNTs are the allotropes of carbon which consist of carbon atoms with sp^2 hybridization arranged in graphene sheets rolled up in a tube [42, 43]. Based on the rolling layers of graphene sheets, CNTs are classified into single-walled carbon nanotube (SWCNTs) and multi-walled carbon nanotubes (MWCNTs). SWCNTs are cylinders like in which a single graphene sheet rolled-up with diameters usually between 1 nm and 2 nm and lengths up to several micrometers or more [44, 45]. Multi-walled carbon nanotubes (MWCNTs) are composed of several tens of concentric cylinders of graphene sheets with a layer spacing of 0.3–0.4 nm, with diameters from 10 to 200 nm and lengths up to hundreds of microns (Figure 1.5) [46-48]. These electrical hybrid tubes make MWCNTs metallic conductors, which in some respect allowing them more suitable for electrochemical applications [43].

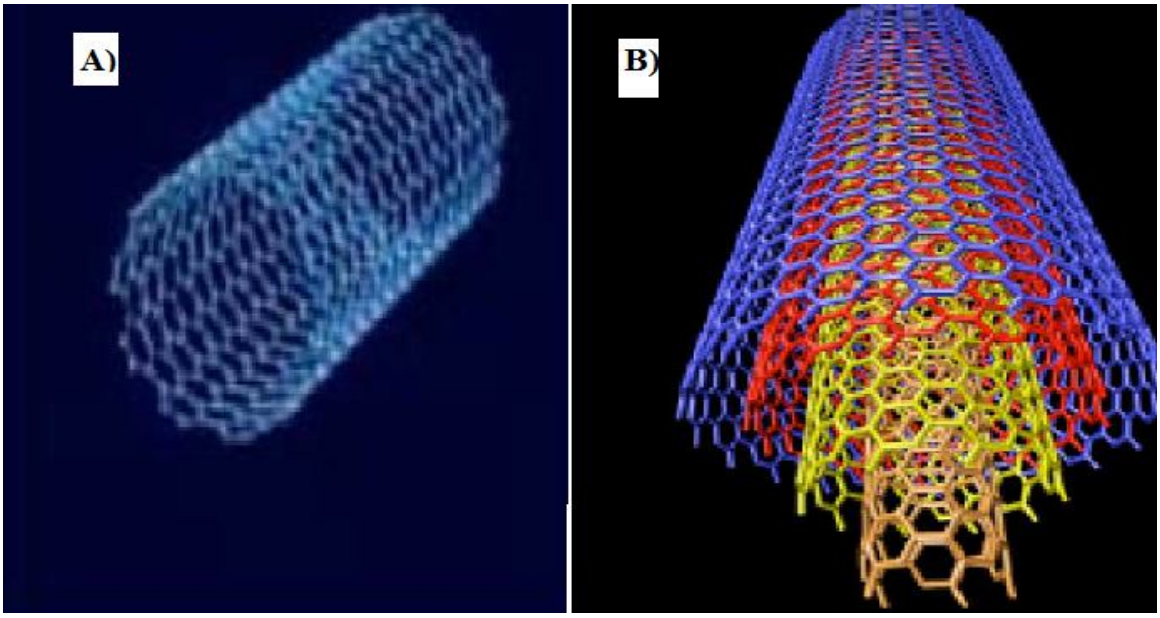

Figure 1.5. Structures of SWCNTs (A) and MWCNTs (B)

1.3.1. Synthesis of carbon nanotubes

Carbon nanotubes (CNTs) have attracted a lot of interest in recent years due their unique properties, such as good chemical stability, high surface area, excellent mechanical strength, and extraordinary electrical conductivity. However, these properties of the CNTs are strongly influenced by methods of synthesis. The synthesis of CNTs can be accomplished in a wide variety of methods that involve the catalytic decomposition of carbon containing gas or solid. The temperature, pressure and the types of metal catalyst, carrier gas and the carbon sources influences the properties of the synthesized CNTs. Arc discharge, laser ablation and chemical vapor deposition (CVD) are the most common synthesis techniques [48, 49].

The arc-discharge method is the most common method of producing CNTs. It consists of two graphite rods placed end to end, separated by approximately 1 mm, in an enclosure usually filled with an inert gas (helium, argon) at low pressure (50-700 mbar). By applying a DC voltage between two graphite rods, the evaporated anode generates MWCNTs as a major product and fullerenes in the form of soot. On using methane as a carbon sources, MWCNTs can also be

synthesized at large scale. SWCNTs also synthesized when a metal catalyst like Fe or Co is used as anode in place of graphite. The limitation of the arc discharge method is the removal of impurities such as non-carbon nanotube and metal catalyst is very expensive than the production of CNTs [46].

In laser ablation, a laser beam of CO_2 is introduced onto the carbon composite doped with catalytic metals located in the center of a quartz tube furnace. The target is vaporized in a high-temperature argon atmosphere and SWCNTs are formed; and the produced SWCNTs are conveyed by the gas to a special collector. This method is widely used for the production of SWCNTs. Temperatures of the furnace, type of catalyst and flow rate affect the quality of SWCNTs. Compared with the arc discharge mthod, laser ablation has several advantages, such as the high quality diameter and controlled the growth of SWCNTs [50].

The chemical vapor deposition method involves the decomposition of various hydrocarbons such as methane, ethane, ethylene, acetylene and ethanol as the source of carbon under an inert atmosphere with iron/graphite, cobalt/graphite, or iron/silica as catalyst with plasma irradiation. The composition, morphology and property of catalysts are crucial in determining the yield and quality of the nanotubes. By controlling the growth conditions, SWCNTs can be synthesized. It has been shown that the size of the catalyst and the proportion between the carbon source and the catalyst determines the diameter and the thickness of the CNTs, respectively. In comparison with the other techniques, CVD is very economic and easily scaled-up to batch-scale production [51, 52].

1.3.2. Properties of carbon nanotubes

CNTs have excellent mechanical strength. This is because the carbon-carbon covalent bonds in CNTs are strong and the arrangement of these bonds oriented along the axis of the nanotubes produces a very strong material with an extremely high strength-to-weight ratio [49]. The circular curvature of CNTs causes quantum confinement and σ–π rehybridization. In such cases, three σ bonds are slightly out of plane and for compensation the π-orbitals are more delocalized outside the tube. The distortion of electron cloud induced by the curvature yields a rich π-

electron conjugation outside the tube, so that rich CNTs become more electrochemically active and electrically and thermally more conductive. In addition to the σ–π rehybridization, the high surface area and the presence of potential topological defects induce local perturbations in the electronic structure and changes the chemical, electrochemical and biochemical reactivity. Thus, compared with analogue graphite, molecular adsorption and charge transfer in CNTs can be more facilitated [53].

However, due to the strong π-π interactions between the aromatic rings, CNTs tend to aggregate in aqueous solutions, making difficult their dispersion and further use for the development of electro(bio)chemical sensors. Therefore, attempts have also been made to prepare hydrophilic surface CNTs to overcome the dispersion problem in polar, non-polar and aqueous media. Functionalization of CNTs is an effective way to enhance the physical properties and improve the solubility. Depending on the interactions between the CNTs and active materials, functionalization can be covalent and non-covalent functionalization [54, 55].

Non-covalent functionalization is the wrapping of polymer around the CNTs to form supermolecular complexes of CNTs through the Van der Waals interactions and π-π stacking. Surfactants have been employed for non-covalent functionaliztion of CNTs. Surfactants are adsorbed on the CNTs surface by physical adsorption and overcome the Van der Waals attraction by electrostatic repulsive forces. Thus, the surface tension of CNTs is lowered and effectively prevents the formation of aggregates. Furthermore, non-covalent functionalization can be carried out by inserting guest atoms or molecules into the inner cavity, the ends or on the sidewalls of CNTs through capillary effect. This method of functionalization is particularly interesting because it does not perturb the conjugated system of the CNTs sidewalls and thus it maintains the unique electronic, structural and optical properties of the material.

In covalent functionalization, CNTs are functionalized irreversibly with strong acids such as HNO_3, H_2SO_4 or a mixture of these or with strong oxidants such as $KMnO_4$ and ozone. Through oxidative treatments, the original CNTs with closed tips were transformed into shorter, open-ended nanotubes with oxygenated functional groups such as carboxylic acid, ketone, alcohol and ester groups (Figure 1.6). These functional groups have rich chemistry and the CNTs can be used

as precursors for further chemical reactions, such as esterification. For instance, MWCNTs-benzimidazole can be synthesized between functionalized MWCNTs and 1,2-phenylenediamine (Scheme 1) [56-58].

Inaddition, the sides of CNTs can also undergo reactions with molecules of high chemical reactivity like fluorine. The carbon atoms at the defect sites change from sp^2 to sp^3 hybridization, leading to a disruption of the electronic structure of CNTs. The weak C-F bonds in functionalized CNTs provide substitution sites for additional functionalization with amino, alkyl and hydroxyl groups. Covalent modification of the nanotube sidewalls totally changes the electronic properties of the CNTs, as a result the application of functionalized CNTs for sensing molecules becomes a big challenge [59].

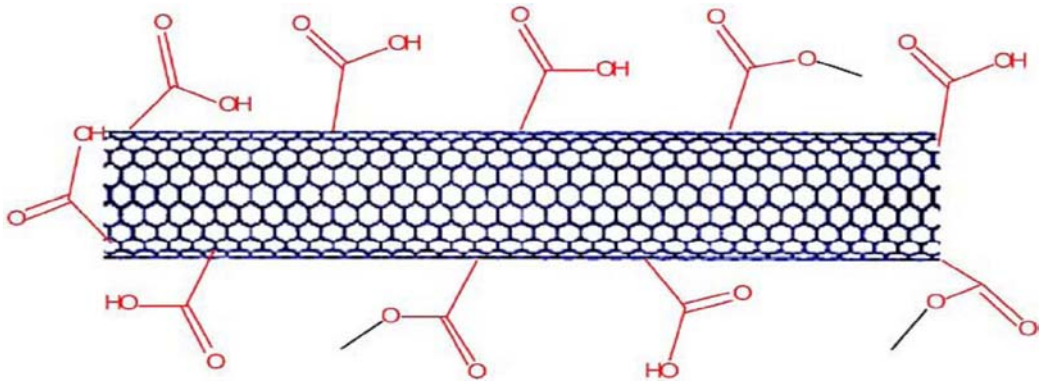

Figure 1.6. Covalent functionalized carbon nanotube

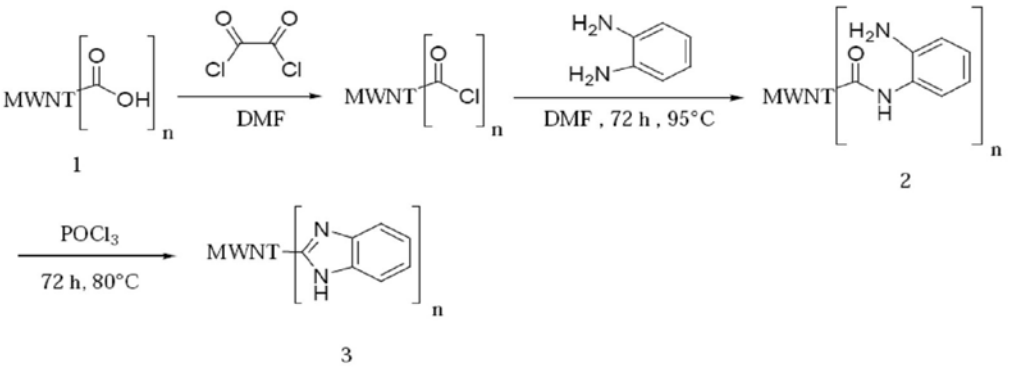

Scheme 1. Synthesis route of functionalized MWCNTs-benzimidazole

1.4. Modified electrodes

The concept of modified electrodes is certainly one of the exciting developments of the last three decades due to their wide range of applications, such as in electrocatalysis, corrosion protection, energy storage and electrochromic display [60]. In electroanalysis, the electrode itself can act as a reactant to pump (reduction) or withdraw (oxidation) electron in the reaction. Many compounds that are important biologically and environmentally show no response within a potential window at solid electrodes or for direct electrochemical detections usually require high potential. This can produce large background current, resulting in inferior detection limits. Also, passivation and deactivation of the electrode surface due to the adsorption of macromolecules or of reaction products, greatly affect the stability of the electrode response and reproducibility. Furthermore, coexisting components, which may be present in concentrations much larger than the analytes, may severely interfere within the determination of trace analytes. As a result, complicated sample pretreatments are often employed to eliminate or separate interfering components [61, 62]. These behaviors often can be controlled by manipulating the chemical nature of the electrode surface. In this case, the electrode surface needs to be modified with an additional layer capable of interacting specifically with sample components. Depending on the nature of interactions provided by additional layer, the response toward the target species is enhanced and/or the response of interfering species is attenuated. In either case an increase in the selectivity ratio analyte/interferent is observed [63]. The underlying motivations of electrode surface modifications stem is the desire for improving electrocatalysis and freedom from surface fouling effects. Alternatively, electrodes can be modified to prevent undesirable reactions from competing kinetically with the desired electrode process [60, 64]. Conventional electrode materials such as metallic electrodes (Pt, Ag or Au) or carbon materials such as glassy carbon may serve as a substrate for modification. Metallic electrodes such as Au, Ag and Pt can be used as a base for modification because their surfaces provide reproducible results and clean surfaces can be produced and maintained in the laboratory environment. Carbon electrodes are commonly employed as a substrate for covalent attaching schemes. This is due to the presence of sp^2 hybridized carbon atoms and oxygen-containing functional groups (i.e., carboxylic acids, alcohols and ketones) resulting on pretreatment [25, 65].

The surface properties and reactivities of the electrodes can be controlled through surface modification, since the immobilization transfers the physicochemical properties of the modifier to the electrode surface. This process could impart a high degree of selectivity or sensitivity to the electrochemical transducers [66]. The modifier may act as a fast electron transfer mediator between the electrode and analyte species which is oxidized or reduced slowly or not at all at the bare electrode (Figure 1.7).

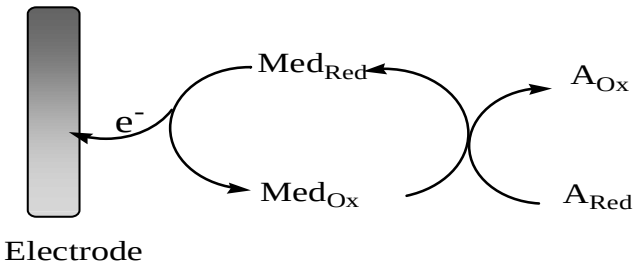

Figure 1.7. Electrocatalytic reaction on chemically modified electrode (Med- mediator and A-analyte)

The overall process at the electrode surface can be described as:

$$M_{Ox} + A_{red} \rightarrow M_{Red} + A_{ox}$$

$$M_{Red} - ne \rightarrow M_{Ox}$$

The transfer of electrons takes place between the electrode and mediator and not directly between the electrode and the analyte. In essence, then, the mediator can be considered to function simply as an electron shuttle between the electrode and the analyte. The net results of this electron shuttling are a lowering of the overvoltage to the formal potential of the mediator and increase in current density.

There are various methods of modifying the surface of an electrode: physisorption, chemisorption, covalent attachment and electropolymerization.

Physisorption is a physical method of modifying an electrode by coating with organic or organometallic complexes in non-aqueous solution followed by droplet evaporation. For examples, phenothiazine derivatives modified graphite electrode are prepared by coating in DMF solution for oxidation of NADH and a solution of MWCNTs in acetone was drop coated on the surface of GCE for the electrochemical oxidation of dopamine and ascorbic acid.

Chemisorption involves the spontaneous adsorption of molecules like thiols on the surface of metal electrodes through metal-sulfur interaction to form monolayers. The common electrode which is employed in such modification technique is gold electrode. Silver, copper, platinum, and mercury can also be utilized as electrode. The modification of gold electrode is shown below:

$$RSH + Au \leftrightarrow RS - Au + e^{-} + H^{+}$$

This method is limited in forming multimolecular layer and layers, because they are slowly leached into the contacting solution phase during electrochemical or other investigations on the chemisorbed layer. However, mixed monolayers can be made by the simultaneous deposition of multiple precursors from the same solution [20, 67-69].

In covalent attachment the modifiers are covalently attached on the surface of the electrode in order to form several monomolecular layers. Due to the tendency of bearing different functionalities such as carboxylic acids, alcohols and ketones, carbon electrodes are appropriate substrate for covalent modifications. For instance, amino-group containing compounds are easily accessible for such modification [25].

The extended nature of the π-electron system in the conjugated polymer allows to exercise various modification techniques. These are: dip-coating, spin-coating, drop-coating, layer-by-layer (LBL) self-assembly technique and electrochemical deposition. The deposition method of CPs strongly affects the electrical properties of the final product.

Dip-coating of a substrate (electrode) can occur either by dipping the substrate in to a solution of the polymer or immersing the substrate into the monomer and oxidant solutions. The adsorbed monomer will be polymerized on the surface of the substrate. In spin-coating the polymer film

can be prepared by spreading soluble conducting polymers on a rotating electrode followed by solvent evaporation. The thickness of the film can be controlled by the concentration of the solution and rotation rate of the substrate. The other method is drop-coating, in which a solution of the polymer is droped onto the surface of the electrode and allowing the solvent to evaporate. It can also occur by dropping the monomer and oxidant solutions and letting them to react on a substrate. Layer-by-layer (LBL) self-assembly technique is another method of forming a polymer film throguh alternatively immersing a substrate into a polymeric anion solution and a polymeric cation solution. Here, the film consists of two electrolytes and the thickness of the LBL film depends on the number of repeating times. Finally, the most convenient and attractive method to deposit a conducting polymer film is electropolymerization. It involves electrochemical polymerization of a monomer solution on the surface of a substrate. This method has several advantages over the other methods such as being free of residual oxidant, ease to control the reaction conditions and film thickness through changing the current, potential, the scan rate or the number of voltammetric cycles. In addition, due to the polymerization of the monomer directly on the surface of the substrate film, it minimizes the use of a large number of volatile organic solvents. Because of these excellent features, the electropolymerization method has a promising future in constructing simple, highly stable, rapid and selective sensors. The choice of the modifier must account for the reactivity of the target surface site [70, 71].

1.4.1. Polymer modified electrodes

Due to moderately high conductivity, low cost, relatively high stability and facile production by electrodeposition, the conducting polymers: polypyrrole (PPy) and polyaniline (PANI) were frequently used for electrode modification [72]. These conjugated polymers used in sensor devices exhibit enhanced in electrocatalytic activity towards the oxidation or reduction of several chemical and biochemical compounds where some of the functional groups in polymers act as catalysts [73].

Polypyrrole is the most common conducting polymer which has been successfully used as an electrode material for electrochemical sensors and energy storage devices because of its high conductivity and fast redox electroactivity. However, its stability has been limited due to

continuous swelling/shrinkage of the interlaced polymer chains during charge/discharge processes. Besides, PPy usually shows a poor insolubility in common solvents and infusibility limits its commercial application. In recent years, there has been an enormous interest in the fabrication of composites with unique and tailored properties for various applications because they have better performance when compared with that of the individual components [74, 75].

Nanocomposites of metal-polymers or metal oxide-polymer composites are important classes of materials in the area of nanotechnology [76]. Owing to small dimensional size, good conductivity and excellent catalytic activity of nanomaterials, composites of conducting polymers with metal nanoparticles can accelerate electron transfer rate, enhance conductivity of electrodes and have good biocompatibility in electronics, sensors and catalysis applications [77, 78]. While, the porous structure of conducting polymer allows the dispersion of the metal nanoparticles into the polymer matrix in order to stabilize the formation of metal nanoparticles and to prevent their agglomeration process. Based on the unique advantages of nanosize materials, a considerable amount of research has been carried out in developing methods for the production of nanoparticles and nanocomposites of electroactive polymers with noble metals or metal oxides [79–81]. On this basis, electrochemical sensors based on metal nanoparticles–polypyrrole composites such as AgNPs/PPy [82], CuNPs/PPy/GCE [83], PtNPs/PPy [84], AuNPs/PPy [85-88] and MnNPs/PPy [89] have already been developed.

Graphene oxide (GO) is a new carbon-based nanoscale material that provides an alternative path to graphene. Graphene oxide is a single-layer of graphite oxide, which is an oxidation by-product of graphite with its base made of oxygen-containing groups. Recently, GO has recived a great interest due to its low cost, easy access, and widespread ability to be converted in to graphene. Depending on the amount of oxidant and oxidation time, GO contains multiple defects. The amounts of oxidizing agent as well as the method of synthesis also determine the ability for graphene oxide to conduct [90]. Furthermore, oxygen-containing groups also enable GO to exhibit excellent hydrophilic properties which further allows its interaction with nanomaterials and polymers to form composites [91, 92]. The high surface-to-volume ratio of GO, in conjunction with its high dispersibility in both water and organic solvents as well as its wide range of reactive surface-bound functional groups, GO-based materials have been used to design

and prepare GO-based electrodes for a wide range of applications in electrochemical sensors and electroanalysis [93, 94]. Recently, GO-PPy composites have also become appealing sensor materials because of their combined effects, and better electrochemical performance than PPy alone [95]. The composites of GO-PPy have been fabricated as a promising material for supercapacitors [96-98], solar cell [99] and glucose biosensor [100].

Polyaniline (PANI) is one of the highly pursued conducting polymers in recent times owing to its excellent electrical and optical properties, better air and water stability and easy and cheap synthesis route. Due to these properties, polyaniline have been utilized for a variety of applications such as electrocatalysis, batteries, protection against corrosion and separation membranes. However, the utility of PANI limited in acidic media (pH <3) and the neutral polymer is also insoluble in common solvents. In order to use PANI in neutral pH ranges in aqueous media and to improve the solubility, it should be doped with some organic dopants (anionic species) such as benzenesulfonic acid, polystyrene sulfonate (PSS) or through electro-copolymerization techniques of self-doped polymers by introducing sulfonic acid groups into the polymer backbone. These negatively charged groups act as intramolecular dopant anions that are able to compensate positive charges at protonated nitrogen atoms of the polymer backbone, thus replacing auxiliary dopant anions [20, 23, 101].

Literature reviews show that polymers of 1-aminonaphthalene and its derivatives have been successfully utilized for corrosion protection, sensors or electrochromic devices. In particular, poly(4-amino-3-hydroxynaphthalene-sulfonic acid) a polymer of a monomer 4-amino-3-hydroxynaphthalene-sulfonic acid (AHNSA) has been used as a sensor for the detection of drugs [102-105] and pesticides [106]. Marjanovic *et al*. have reported the oxidative polymerization of AHNSA with ammonium peroxydisulfate as an oxidant. The result has shown that (Scheme 2) polymerization of AHNSA proceeds through the oxidation of the $–NH_2$ group [107].

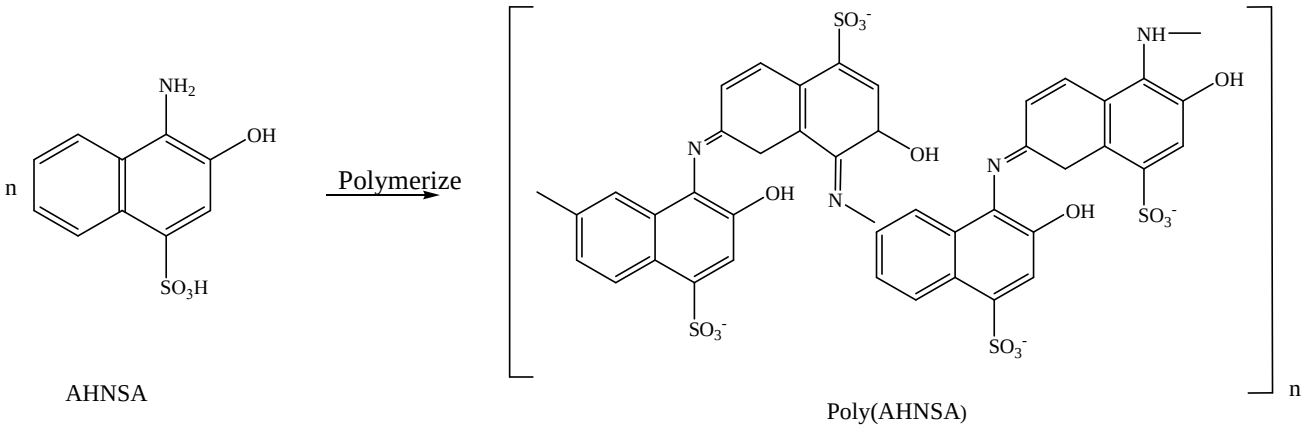

AHNSA

Poly(AHNSA)

Scheme 2. Proposed electropolymerization route of poly(AHNSA)

1.4.2. Carbon nanotubes modified electrodes

CNTs-modified electrodes have shown excellent electroanalytical properties, such as wide potential window, low background current, low detection limits, high sensitivities, reduction of over potentials and resistance to surface fouling. CNTs modified electrodes have been successfully utilized in the sensitive detection of various drugs [108-113] and pesticides [114, 115]. Most of these electrochemical sensors were based on the modification of the working electrodes with CNTs only. However, recently CNTs-conductive polymers composite film modified electrodes have received increasing attention in analytical studies. In the composites, the solubilities of CNTs in organic solvents were significantly enhanced and the polymer matrices exhibit high compatibility in the presence of CNTs. As a consequence, the composites of CPs and CNTs have improved properties such as sensitivity and stability [116, 117]. These advantageous have made researchers to design and prepare sensors based on CNTs-CPs composites [118]. There are several methods to prepare polymer-CNTs composites, such as polymerization followed by coating, in situ polymerization, mini-emulsion polymerization, electrochemical, electrospinning, and other methods [119]. The coating of CNTs solution or suspension on the polymer modified electrode surface is a simple method [108]. MWCNTs/poly(melatonin) [116], MWCNTs/PEDOT [120], Poly(3-methyl thiophene)/MWCNTs [121, 122], polyaniline/SWCNTs [123], MWCNTs/polypyrrole composite

electrodes [124] are among the the composites of CNTs-CPs which have been utilized as sensor materials.

1.4.3. Mercury film modified electrodes

Narrow negative potential range of glassy carbon electrode, which reaches to around -1.0 V without significant hydrogen evolution in common aqueous media, limits the use of glassy carbon electrode for monitoring reducible species at more negative reduction potential [125]. Although, the use of mercury electrode for electrochemical analysis has been recently restricted due to environmental unfriendly, they are nearly ideal electrodes for the study of the electrochemical reduction of substances at very high negative reduction potential with negligible interference of dissolved oxygen. Its working potential extends from +0.4 V to -2.5 V [126–128]. Since the amount of mercury required for film formation is much smaller than required for other mercury electrodes, the contamination caused by the use of mercury film as an electrode is insignificant. Besides, the mercury film has a tremendous resolving power of closely spaced peaks [129–131].

2. ELECTROANALYTICAL TECHNIQUES

Electroanalytical techniques have undergone many important developments in recent decades. They are routinely used for measurements in the laboratory, mostly for fundamental research in almost every chemical and biochemical research areas. They are not only used to study the nature of oxidation and reduction processes to unravel reaction mechanisms, but also used in studying the kinetics and thermodynamics of electron and ion transfer processes. Besides, it is apparent that electroanalytical techniques at varying levels of sensitivity are required to solve analytical problems. As a result, electroanalytical methods are widely used in specific studies and monitoring of industrial materials, biological samples and the environment. The choice of electroanalytical methods for analytical purpose depends upon the specific analyte, nature of the sample matrix, the parameter to be determined and the sensitivity and selectivity requirements. The techniques are characterized by instrumental simplicity, moderate cost and portability. Most electroanalytical techniques, such as cyclic voltammetry (CV), differential pulse voltammetry (DPV), square wave voltammetry (SWV) and stripping voltammetry are based on the concept of continuously changing the applied potentials at the electrode-solution interface and the resulting current is measured.

In this study, the electrochemical behavior of sensors and analytes are studied using the electroanalytical methods: cyclic voltammetry, square wave voltammetry and electrochemical impedance spectroscopy [3, 4, 10, 132, 133].

2.1. Electrochemical cells

The modern electroanalytical system for voltammetric measurements is usually composed of three components: a potentiostat, a personal computer and an electrochemical cell (Figure 2.1). Depending on the application, various cell designs and experimental assemblies are employed. The potentiostat consists of various components including electrometer circuits, various converters and amplifiers, as well as microprocessors with internal memory. In order to perform electrochemical experiments quickly and to increase the sensitivity by discriminating capacitative currents, modern potentiostat in a digital system containing “staircase’’ modulated

potential with ‘‘steps’’ can be utilized. The most frequent waveforms in modern potentiostats are linear or cyclic scan, differential pulse, and square wave. The choice of a particular instrument will be determined by the information (qualitative or quantitative) needed and the size of the electrodes. Depending on the type of techniques, the electrochemical cell can encompass a number of electrodes. For instance, potentiometry measurement requires two electrodes, while voltammetry three electrodes. Electroanalytical measurements with three electrodes systems are preferred over those involving two electrodes due to the reduction in uncompensated resistance. An electrochemical cell is considered to be a sample holder which consists of a solution of the analyte of interest, supporting electrolyte and the electrodes. The three electrodes are:-working electrode, reference electrode and auxiliary or counter electrode.

Working electrode (WE): It is an electronic conductor at which the reaction or transfer of electrons takes place. Solid or mercury-based electrodes are used as working electrodes in voltammetric techniques. In general, solid electrode materials have the advantage of being more mechanically stable, and they provide a larger anodic range than mercury-based electrodes. The mercury electrode has high hydrogen overpotential and can be a choice for analytes reduced at higher cathodic potential [25].

The most common solid working electrodes can be inert materials such as Au, Ag, Pt, glassy carbon (GC), etc. However, for corrosion purposes, the working electrode would be the one which corrodes easily. The size and shape of the working electrode also varies and it depends on the application. The choice of a working electrode for electrochemical analysis depends on the redox behavior of the target analyte, potential window, electrical conductivity, surface reproducibility, mechanical properties, cost availability and toxicity and the background current over the potential region for the measurement. Besides, the solubility and adsorption properties of the reaction products on the surface of the electrode and the reaction mechanism also determine the electrode type. For example, lead ions are reduced in to lead atoms at mercury electrode and the reduction is fast and reversible, while on a platinium electrode the electrochemical process is complicated by nucleation and growth of lead micro-crystals [27].

In the presence of electroactive species in the electrochemical cell, the applied potential will produce a change in the concentration of the monitored electroactive species at the electrode surface by electrochemically reducing or oxidizing them. Changing the concentration of any electroactive participant at the working electrode surface will cause mass transport toward the electrode, and current will flow through the electrodes directly proportional to the analyte concentration. This simple dependence between the measured current and analyte concentration makes voltammetric techniques to be routinely used for the quantitative determination of a variety of inorganic and organic compounds [25, 132].

Counter Electrode (CE): It is an electrode at which a counter reaction to that of the working electrode takes place. Pt wire, graphite, or thin pieces of gold are among the most frequently used as counter electrodes in voltammetric techniques. The purpose of the counter electrode is to preserve electroneutrality in the system, which is usually electrolysis of the supporting electrolyte or solvent and in order current flows without the need for using a large overpotential. Therefore, the area of counter electrode must be larger than the area of the working electrode in order to ensure the area of the electrode will not be a limiting factor in the kinetics of the electrochemical process under investigation [134].

Reference Electrode (RE): Refrence electrode keeps the potential of an electrode constant regardless of the properties of the solution. The main criteria for an electrode to be classified as a reference electrode are the tendency to provide a reversible half-reaction based on Nernstian behavior with a constant potential over time, and to be easy to assemble and maintain. Calomel electrode (Hg_2Cl_2(s)/Hg), and silver/silver chloride electrode (Ag/AgCl) are the most common reference electrodes. They are constructed using an aqueous solution of saturated potassium chloride (KCl) and their potentials are determined by the concentration of chloride ion. These electrodes are commercially available in a variety of sizes and shapes. The effective separation of the reference electrode, on the other hand, can be decisive for the quality and accuracy of electrochemical measurements; in particular, for reference electrodes which contain ions that can influence certain reactions at the working electrode. The high stability of the reference electrode potential is usually reached by employing a redox system with constant (buffered or saturated) concentrations of each participants of the redox reaction. These reference electrodes are normally

contacted to the electrolyte through a porous frit that serves as a salt bridge. Moreover, the current flow through the RE is kept close to zero, which is achieved by using the CE to close the current circuit in the cell together with very high input impedance on the electrometer.

The reference and counter electrodes should be located on the downstream side of the working electrode, so that reaction products at the counter electrode or leakage from the reference electrode do not interfere with the working electrode [132-134].

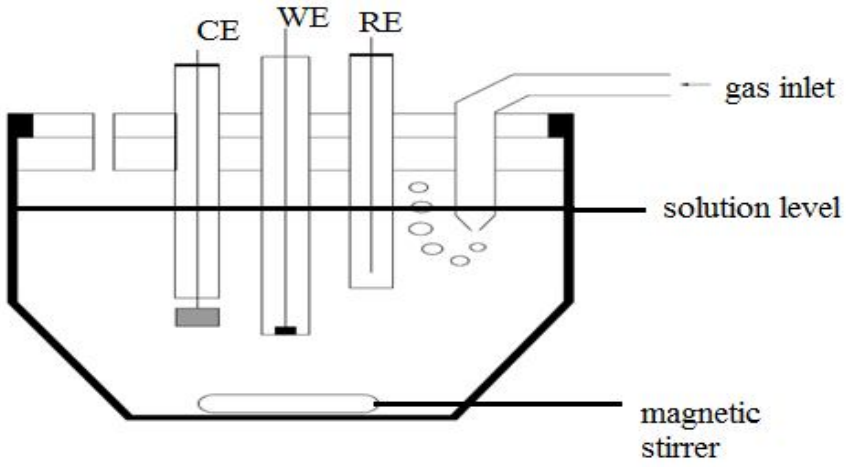

Figure 2.1. An electrochemical cell with three electrode system

Supporting electrolytes: Supporting electrolytes are inert soluble substances added to the solution to avoid electrochemical reaction at the counter electrode during the course of electrochemical measurements. Since, the concentration of the supporting electrolyte is always much larger than (0.1 M–1.0 M) that of the redox species unless ultramicroelectrodes are employed, it carries most of the ionic current and decrease the resistance of the solution by increasing the solution conductivity. Besides, it maintains a constant ionic strength and eliminates electromigration effects. The supporting electrolyte should be prepared from highly purified reagents, and should not be easily oxidized or reduced. Supporting electrolyte may be an inorganic salt, a mineral acid, a buffer or a chelating reagent [135].

2.2. Electrode processes

Electrochemical reactions involve the transport of electroactive species to or from the electrode and the transfer of electrons across the interface. The net rate of the reaction and the measured current may be limited by either mass transport of the reactant or the rate of electron transfer. There are three ways in which material may be transported to the electrode surface: diffusion, migration and convection.

Diffusion is the spontaneous movement of electroactive species under the influence of concentration gradient, from regions of high concentration to regions of lower ones, aimed at minimizing concentration differences. Concentration gradients between the vicinity of the electrode and the bulk solution arise as the analyte is consumed and the product is formed at the electrode. The rate of diffusion is related to the concentration gradient rather than the concentration of the analyte in the solution.

Convection is the transport of the electroactive species to the electrode as a result of an imbalance forces on the solution. The driving force for convection is due to stirring the solution, rotating and vibrating the electrodes, or even simply expanding its volume (which is a movement of its surface against the solution) like dropping mercury electrode.

Migration is the movement of charged particles under the influence of an electric field generated by the electrode toward every ion having opposite charge. In addition, it is also due to the contemporary repulsion force of every ion having the same charge as the electrode.

Among the three mass transport modes, only diffusion can be related to the concentration of the electroactive compound. Such phenomenon can be greatly simplified by suppressing the electromigration through the addition of high concentration of the supporting electrolyte (compared to the concentration of the electroactive ions). The effects of convection can be eliminated by preventing stirring and vibrations in the electrochemical cell. When the rate of the reaction is limited by mass transport (or diffusion), the electrode process is diffusion limited. On

the other hand, if the heterogeneous electron transfer is a sluggish step in the process, the reaction a surface-limited process [27, 68, 136].

2.3. Cyclic voltammetry

Cyclic voltammetry involves the measurement of current based on various applied potential at the working electrode in both directions at a given scan rate and it is one of the most exploited techniques in electrochemical studies. It is widely used for identification of electroactive species, provides electrochemical information on the reaction rates, the number of electroactive species in a solution if each reacts at different applied potentials. Cyclic voltammetry (CV) can be used in single cycle or multicycle modes. Because of the capacitative current flowing at the electrode/electrolyte interface, CV is rarely used for quantification. The potential applied to the working electrode serves as a driving force for the reaction. It is a controlled parameter that causes the chemical species present in solution to be electrolyzed (reduced or oxidized) at the electrode surface. The magnitude of the measured current is an indicator of the amount of substances being oxidized or reduced and the corresponding peak potential is the characteristic for the redox process but also influenced by the electrode material. The values of peak potentials and peak currents provide the basis for classifying redox systems as reversible, irreversible or quasi-reversible systems.

A reversible process is a process in which both the reactive species exchange electrons rapidly with the working electrode. The initial potential, E1, is the potential applied to the working electrode and final potential, E2, is the potential where the sweep is reversed to its initial value. As the applied potential is increased from E1, the current will also increase and reaches a maximum at $E_{p,f}$. Then after, the current decreases utill it reaches the switching potential, E2. After reaching the potential E2, the sweep is reversed to E1, the concentration of the analyte near the electrode surface diminished, and thus the current decreased. This constitutes one cycle of the cyclic voltammogram (Figure 2.2). The shape of the cyclic voltammogram gives information about the type of the electrode reaction, the number of electrons involved in the elementary step of the electrochemical transformation, as well as about additional phenomena coupled to the

electrochemical reaction of interest, like those for coupled chemical reactions or adsorption [4, 13, 25, 132, 137, 138].

The main instrumental parameter in cyclic voltammetry is the scan rate (v = dE/dt), it controls the time scale of the voltammetric experiment. The electrode potential at the working electrode is changed with time and the current response depends on the scan rate. By varying the scan rate, we can also investigate the kinetics of the reactions and/or the mass transfer process.

The electrode potential is related with the scan rate:

$$E(t) = Ei \pm vt \quad (1)$$

After reaching the final value usually set at electrode potential values, the electrode potential is scanned back to the initial value:

$$E(t) = Ef \pm vt \quad (2)$$

Several species that react at different applied potentials can be determined almost simultaneously in the same experiment without the need for prior separation [132, 139]. The maximum current is called the peak current and the potential at maximum peak current is called the peak potential.

For an electrochemically reversible reaction, the peak current (at 25°C) is given by the Randles–Sevcik equation and it is proportional to the square root of the scan rate.

$$i_p = (2{\cdot}69\times10^5)n^{3/2}ACD^{1/2}v^{1/2}, \quad (3)$$

where, i_p refers to the peak current, A is the surface area of the electrode (in cm^2), v is the scan rate (in V s^{-1}) and C is the concentration (in mol cm^{-3}), n is the number of electrons, D is the diffusion coefficient (in cm^2 s^{-1}). Accordingly, the current is directly proportional to the concentration of analyte and increases with the square root of the scan rate. Such dependence on the scan rate is indicative of electrode reactions controlled by mass transport (semi-infinite linear diffusion). The reverse-to-forward peak current ratio, $i_p,r/i_p,f$, is unity for a simple reversible couple.

The position of the peaks on the potential axis (E_p) is related to the formal potential of the redox couple. The formal potential for a reversible couple is centered between E_{pa} and E_{pc}:

$$E^{o'} = \frac{E_{pa} + E_{pc}}{2} \qquad (4)$$

For multi-electron transfer processes, the cyclic voltammogram consists of several distinct peaks, if the $E^{o'}$ values for the individual steps are successively higher and are well separated.

Besides, the separation between the peak potentials is given by:

$$\Delta Ep = E_{pa} - E_{pc} = \frac{0.059}{n} V \qquad (5)$$

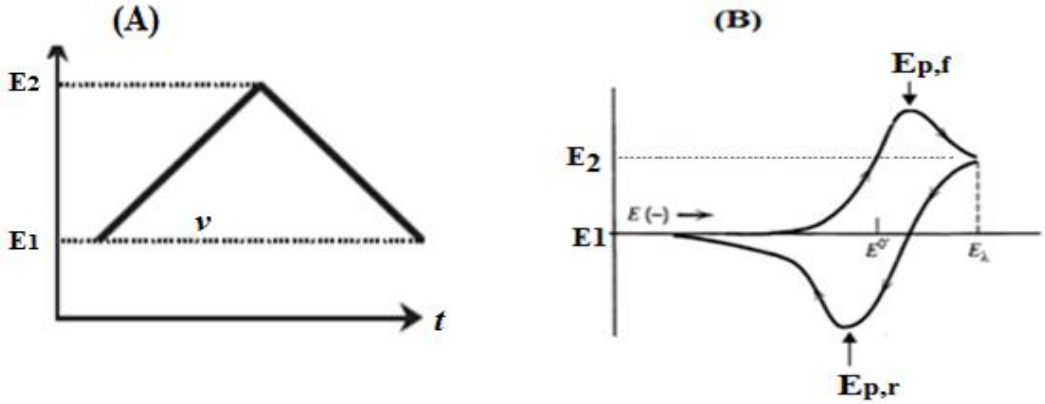

Figure 2.2. Potential–time excitation waveform (A) and cyclic voltammogram (B)

For irreversible processes (those with sluggish electron exchange), the individual peaks are reduced in size and widely separated. Totally irreversible systems are characterized by a shift of the peak potential with the scan rate:

$$E_p = E^o - \left(\frac{RT}{\alpha nF}\right)\left[0.78 - \ln\left(\frac{k}{(D)^{1/2}}\right) + \ln\left(\frac{\alpha nFv}{RT}\right)^{1/2}\right] \qquad (6)$$

where α is the transfer coefficient, k is standard rate constant and n is the number of electrons involved in the charge-transfer step.

The peak potential occurs at a potential higher than E°, with the overpotential related to $k°$ and α. The peak current is also proportional to the bulk concentration and square root of scan rate. The

magnitude of peak current will be lower in height (depending on the value of α) as compared with the current obtained in a reversible system [68] and is given as:

$$i_p = (2.99x10^5)n(\alpha n)^{1/2}ACD^{1/2}v^{1/2} \quad (7)$$

For an adsorbed species which reduced irreversibly [136], the peak current and potential are related with the scan rate with the equation:

$$i_p = \frac{\alpha F^2 A v \Gamma_o^*}{2.718\,RT} \quad (8)$$

$$E_p = E^{o'} + \frac{RT}{\alpha F}\ln\left(\frac{RT}{\alpha F}\frac{k^o}{v}\right) \quad (9)$$

Where Γ_0^* surface coverage and other symbols have their usual meanings.

2.4. Square wave voltammetry

Square wave voltammetry is a powerful electrochemical technique that can be applied in both electrokinetic and analytic measurements [3]. The excitation signal in SWV consists of a symmetrical square wave pulse of amplitude, E_{sw} superimposed on staircase wave form (Figure 2.3A). At each step of the staircase ramp, two equal in height and oppositely directed potential pulses are imposed. SWV data can be characterized in terms of amplitude (E_{sw}), pulse width (t_p), step potential (ΔE_s) and frequency (f) [27, 40, 136].

The current is sampled twice during each square wave cycle, once at the end of the forward pulse and once at the end of the reverse pulse. The reverse pulse causes the reverse reaction of the product of the forward pulse. The net current is obtained on subtracting the forward and backward currents of a single potential pulse and its value is larger than either of the forward or the reverse current value. This is due to the fact that the reverse current has a negative sign and the difference of the two currents in SWV becomes their sum. The currents are plotted as a function of the corresponding potential of the staircase waveform (Figure 2.3B).

In each of the forward and reverse cycles, the charging current decreases exponentially with time, while the faradaic current is inversely proportional to the square root of time. At the end of

each cycle, the charging current is smaller than the faradaic current. Since the charging current depends on the difference between the electrode potential and potential of zero charge, it is partly eliminated by the subtraction of currents measured at the end of two successive half-cycles [27, 68, 136, 140, 141].

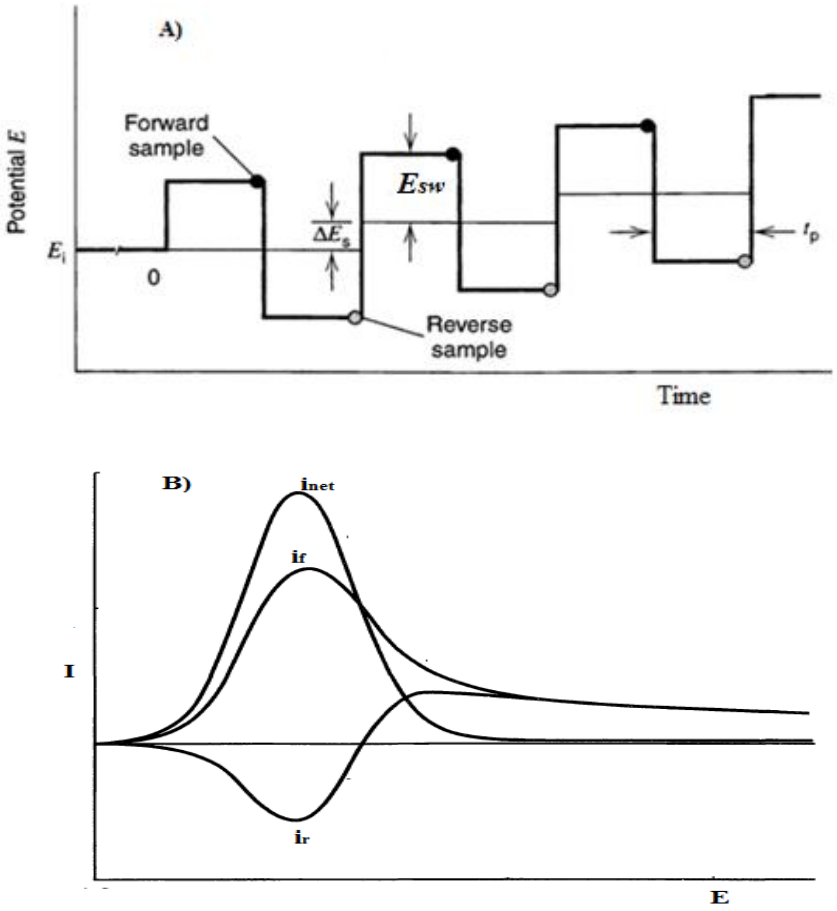

Figure 2.3. Square wave voltammetry potential waveform (A) and response for a forward current (if), a reverse current (i_r) and net current (i_{net}) (B)

SWV has several advantages for electroanalysis. First, the use of SWV reduces the effects of charging current and as a result the scan rate can be increased drastically. The second advantage of SWV is in the negative potential region, oxygen may not require excluding from the analyte solution; unless it directly interferes with the electrode reaction under study. This is due to, in the limiting current region for oxygen reduction, the forward and reverse currents are equal which

leading to a zero net current. In addition, during a scan from negative potentials in the positive direction, a fast effective scan rate means that no electroactive oxygen species have the time to diffuse to the electrode surface from the bulk solution. As a result, the experimental time is less and the procedures are simplified because prior bubbling of nitrogen or argon in the solution is avoided. The other advantage of SWV, the height of the peak is usually quite easy to read and thus increases the accuracy and sensitivity. In general, for reversible and irreversible SWV currents are 4 and 3.3 times higher, respectively, than the analogous differential pulse response [4, 68].

2.5. Electrochemical impedance spectroscopy (EIS)

In a direct circuit (DC), a resistor is the only element which resists the flow of electric currents (electrons). This ideal resistor obeys Ohm's Law at all current and voltage levels and its value is independent of frequency.

In an alternating circuit (AC), impedance is a measure of the ability of a circuit to resist the flow of electrical current. Unlike resistance, it is not limited by the Ohm's Law. Impedance is a combination of resistors, capacitors, or inductors. EIS uses small amplitude perturbing sinusoidal voltage signal to an electrochemical cell and the resulting current response is measured [142, 143]. This small imposed perturbation can be an applied potential or applied current. It sensing events at the surface of an electrode and is widely used in different fields studies [144]. It has many advantages over the other electrochemical techniques. Since it applies a small amplitude AC signal, it is a non-destructive method for evaluating a wide range of materials, including coatings, anodized films and corrosion inhibitors [145]. It can also be provide detail information of systems under examination; parameters such as corrosion rate, electrochemical mechanisms and reaction kinetics, detection of localized corrosion, can all be determined from these data [146, 147]. The response to the applied perturbation (potential or current) which is generally sinusoidal, can differ in phase and amplitude from the applied signal. Moreover, measurement of the phase difference and the amplitude (i.e. the impedance) permits analysis of the electrode process in relation to contributions from diffusion, kinetics, double layer, coupled homogeneous

reactions, etc. [148]. If a sinusoidal potential excitation is applied to the electrode/solution interface, the potential and current can be expressed as:

$$E(t) = E_o \sin(\omega t) \quad (10a)$$

$$I(t) = I_o \sin(\omega t + \theta) \quad (10b)$$

Where E_o and I_o are constants, ω is radial frequency in rad/s and θ is the phase shift angle between E(t) and I(t).

An analogous to Ohm's Law, based on eqn. (10a) and (10b) the impedance of the system can be calculated as:

$$Z = \frac{E(t)}{I(t)} = \frac{E_o \sin(\omega t)}{I_o \sin(\omega t + \theta)} \quad (11)$$

The impedance (Z) can be described based on the real-axis (Z') and imaginary-axis (Z'') components as given in Figure 2.4.

$$Z(\omega) = Z' + jZ'' \quad (12)$$

The impedance and phase angle are related to the real and imaginary axises according to equations 13 and 14:

$$|Z| = \left[(Z')^2 + (Z'')^2\right]^{\frac{1}{2}} \quad (13)$$

$$\theta = \tan^{-1}(Z''/Z') \quad (14)$$

The impedance is also related to the resistance (*R*), reactance (Xc) and capacitance (*C*) by equation (15):

$$Z = R - jX_C = R - \frac{j}{\omega C} \quad (15)$$

where j is an imaginary number with a value of $\sqrt{-1}$, $\omega = 2\pi f$, f is the frequency measured in Hertz (Hz).

In a DC, a resistor that does not have any capacitance and impedance becomes frequency independent [25, 149], i.e, Z = Z' = R.

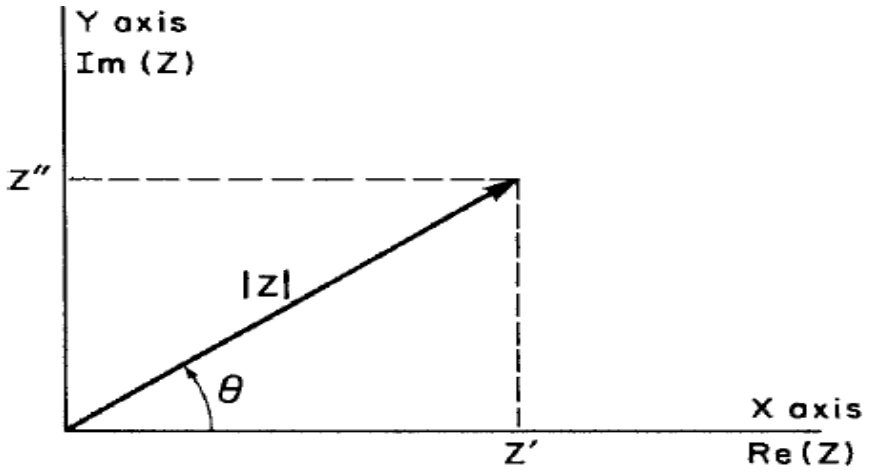

Figure 2.4. The impedance plotted as a planar vector using rectangular and polar coordinates

The results in impedance measurement can be expressed commonly using Nyquist plot and Bode plot. Nyquist plot contains the real part of impedance in the X-axis and imaginary part of the impedance in the y-axis for different values of frequency (Figure 2.5A). The plot includes a semicircle portion at higher frequencies corresponding to electron transfer limited process and a linear part at a lower frequency range representing diffusion limited process [150, 151]. However, Nyquist plot is limited in determining the frequency by simply looking at the plot. When an electrode process involves several steps, sometimes a succession of semicircles side by side are obtained, corresponding to RC parallel combinations in series and with different RC time constants, from which it is possible to deduce the corresponding parameters [148].

Bode plot is a plot of impedance against the logarithm of frequency or phase angle against the logarithm of frequency (Figure 2.5B). The Bode plot directly displays the frequency dependence of impedance.

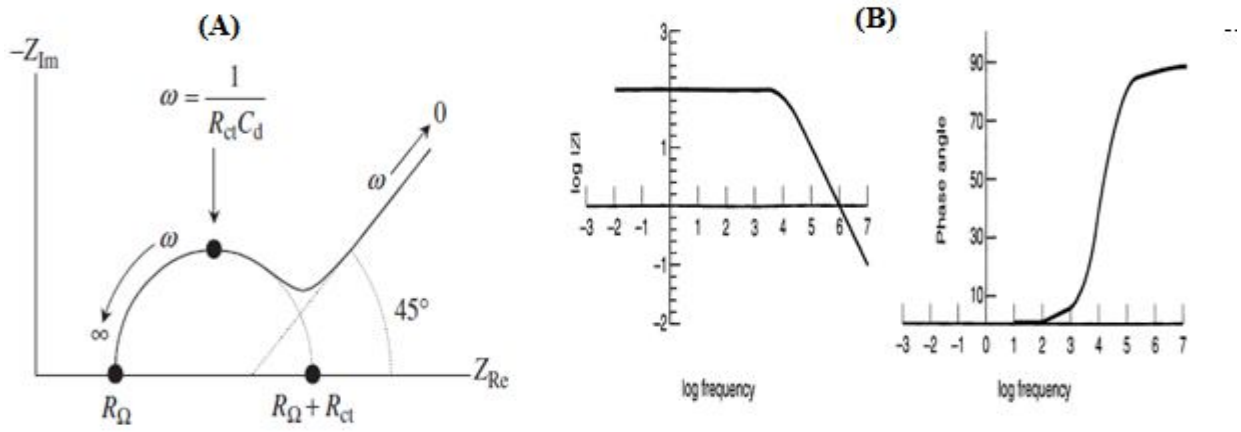

Figure 2.5. Nyquist plot (A) and Bode plot (B)

Solution resistance, (R_Ω) is the resistance developed between the working electrode and the reference electrode due to electrolyte. It is determined by the type of ions, ionic concentration, temperature, solution conductivity and the geometry of the cell, namely the distance between the electrodes and the cross-sectional area of the solution linking the electrodes. Mathematically, it can be expressed as:

$$R = \frac{\rho l}{A} \qquad (16)$$

where ρ is the resistivity of the solution, l is the length and A is the area of the cell. Its measurement is taken at the high frequency intercept close to the origin of the Nyquist plot [25].

Charge transfer resistance, R_{ct} is the resistance associated with the charge transfer mechanisms for electrode reactions. It controls the electron transfer kinetics of a substance at the electrode interface. The semicircle portion at higher frequencies in the Nyquist plot corresponds to the charge transfer resistance (R_{ct}) at the electrode surface [150, 151]. Its value depends on the kind of the reaction, temperature, concentration of the reactants and the potential.

The charge transfer resistance can be expressed in terms of exchange current, I_o under equilibrium using the formula

$$R_{ct} = \frac{RT}{nFi_o} \quad (17)$$

The current density depends on the concentration of the analyte as shown below

$$i_o = nFAk^oC \quad (18)$$

Where R is the gas constant, k is charge transfer rate constant, T is the temperature (K), A is the electrode area (cm^2), C corresponds to the bulk concentration of the redox species (mol cm^{-3}), and n is the number of transferred electrons per molecule of the redox species.

After substituting the values in eqn. 18 into eqn. 17, charge transfer resistance, R_{ct} and concentration of the redox species can be related by the following equation:

$$R_{ct} = \frac{RT}{n^2F^2Ak^oC} \quad (19)$$

where, k is the potential dependent charge transfer rate constant, A is surface area of the electrode, C is the concentration of the analyte, F is the Faradays constant, T is the temperature and R is the gas constant [136, 142, 143, 144, 152, 153].

Double layer capacitance, C_d develops at the interface between an electrode and its surrounding electrolyte as a result of ions from the solution "sticking on" the electrode surface in order to adjust the ionic atmosphere until the charge balance between the electrode surface and the solution is maintained. The charged electrode is separated from the charged ions. Charges separated by an insulator form a capacitor. The value of the double layer capacitance depends on the electrode area, temperature, nature and ionic strength of the electrolyte and impurity adsorption [25].

Warburg impedance, Z_W is a resistance resulting from the diffusion of ions from the bulk solution to the electrode surface. Z_w is a complex number with real and imaginary parts depending on the perturbation frequency:

$$Z_w = \sigma\omega^{\frac{-1}{2}} - j\sigma\omega^{\frac{-1}{2}} \quad (20)$$

σ is the Warburg coefficient defined as:

$$\sigma = \frac{RT}{n^2 F^2 A\sqrt{2}}\left(\frac{1}{C_O^{*}\sqrt{D_O}} + \frac{1}{C_R^{*}\sqrt{D_R}}\right) \qquad (21)$$

In which, D_O is the diffusion coefficient of the oxidant, D_R is the diffusion coefficient of the reductant, A is the surface area of the electrode, n is the number of electrons involved, C_O* is the concentration of the oxidant, C_R* is concentration of the reductant, F is the Faradays constant, T is the temperature and R is the gas constant.

The value of Warburg impedance is small at higher frequencies since diffusing reactants do not move very far, but at low frequencies, the reactants have to diffuse farther and the Warburg impedance increases. The mass transfer impedance depends on the mode of mass transport within the cell.

The R_Ω, R_{ct}, C_d and Z_W can be represented simultaneously using Randles circuit. It is assumed that the charge transfer resistance and the Warburg impedance are both parallel to the interfacial capacity (Figure 2.6).

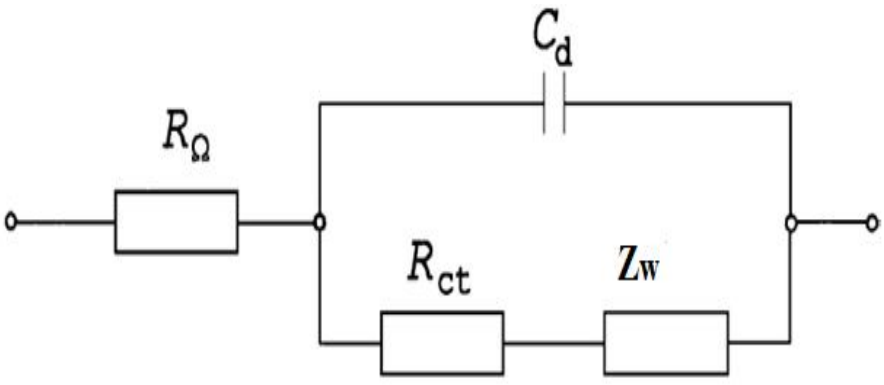

Figure 2.6. Randles equivalent circuit

At low frequency ($\omega \rightarrow 0$), the reaction is controlled solely by diffusion, while at high frequency ($\omega \rightarrow \infty$) the reaction is purely kinetic and $R_{ct} \gg Z_w$.

$$Z(\omega \rightarrow 0) = R_\Omega + R_{ct} \qquad (22)$$

$$Z(\omega \to \infty) = R_{\Omega} \quad (23)$$

$$Z' = R_{\Omega} + R_{ct} + \sigma \omega^{-1/2} \quad (24)$$

$$Z'' = -\sigma \omega^{-1/2} - 2\sigma^2 C_d \quad (25)$$

For very high frequency, Z" ($= -\frac{1}{\omega C_d}$) is very small, but rises as the frequency diminishes [25, 148].

3. SURFACE CHARACTERIZATION

Eventhough, electrochemical methods are powerful and sensitive in providing information about the kinetics of electron transfer and film porosity, they are limited in providing information about surface structure or elemental composition. Therefore, it needs other techniques in order characterize completely the surface of electrodes [136].

Electron microscopes are scientific instruments that use a beam of highly energetic electrons to examine materials on a very fine scale. They provide information on topography, morphology, composition (the elements and compounds that the object is composed of and the relative amounts of them) and crystallographic information (how the atoms are arranged in the object). Microscopic techniques which use electrons as energy source are preferable over light using microscopes because they image substances at a very high depth with high resolution by using electromagnetic radiation of shorter wavelengths (Figure 3.1).

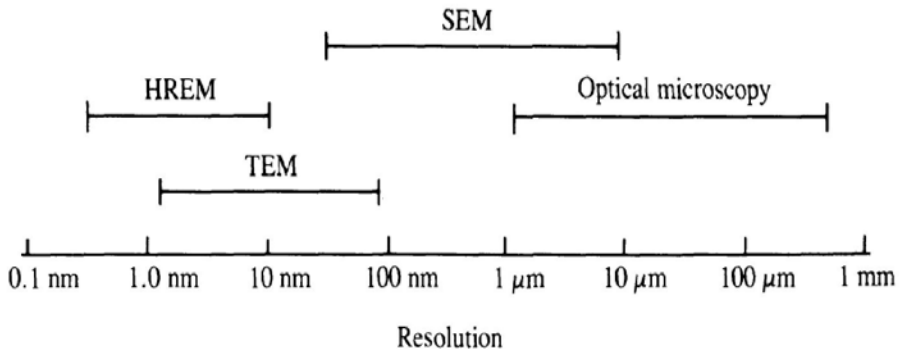

Figure 3.1. Working ranges of various electron microscopy techniques and optical microscopy

3.1. Scanning electron microscope (SEM)

SEM is a powerful microscopic method that uses beams of electrons rather than light to form an image of objects. It helps to characterize physical properties such as morphology, shape, size or size distribution of materials at the microscale and nanoscale [154]. In SEM, a set of coils moves the electron beam across a sample in a two dimensional grid. When a high energy beam of

electrons originating in the electron beam hits the specimen, the electrons penetrate a distance directly proportional to the energy of the beam and inversely proportional to the specimen density. As the primary electrons interact with specimen atoms, the energy is dissipated within an interaction volume. From 20 to 30% of the primary electrons collide with specimen atoms, rebound elastically with little energy loss, and are scattered out of the specimen. The reemerging beams of electrons are known as backscattered electrons (BE). When the primary electron beam hits the specimen, atoms may be ionized by the forced emission of electrons which is referred to as secondary electrons [155]. These secondary electrons are attracted to and detected by a positively charged detector and SEM is then translated into signals which are amplified and analysed before being translated into understandable images. The signals are derived from electron-sample interaction and reveal information about the sample including external morphology (texture), chemical composition, crystalline structure and orientation of materials making up the sample. The preparation of sample for SEM analysis is relatively easy as most SEM measurements only require the sample to be conductive and the thickness is monitored using the principle of the quartz crystal microbalance; when a sputtered material is deposited on an oscillating quartz crystal its frequency is decreased in relation to the mass of the material deposited.

The SEM is usually equipped with an X-ray analyzer and an X-ray dispersion spectrometry (EDS), also referred to as EDX (for energy dispersive analysis of X-rays), which yields information about the elemental composition of the material being analyzed. The secondary electrons are emitted from an atom and they create “holes” in the electronic configuration. These holes will be filled through electrons jump from higher shells through the release of excess energy as characteristic X-rays, so called because the properties of the X-ray (energy and wavelength) are characteristic of the element from which it was derived (Figure 3.2). The X-rays being emitted by atom in sample are analyzed.

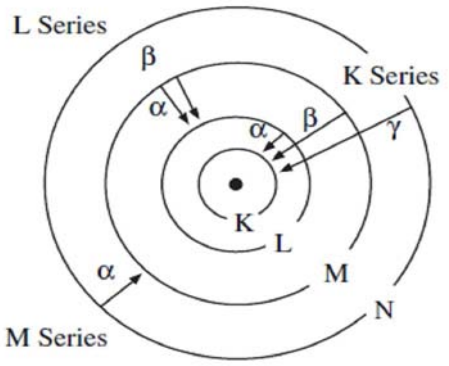

Figure 3.2. Generation of X-rays

SEM is equipped with a detector for imaging, secondary and backscattered electrons, and X-rays for compositional analysis. The most commonly used detector for secondary electrons (SEs) is the Everhart-Thornley (ET) detector. This detector consists of a collector, scintillator, light pipe, and photomultiplier. SEs are attracted to the collector of the ET detector by its small positive charge. A scintillator element is provided with a large positive charge that accelerates the electrons toward the ET. The electrons emit light when they crash into the scintillator, and this light is carried by the light pipe out of the specimen chamber to an external photomultiplier tube where the light energy is converted to an electric current.

However, BE can be detected using scintillator and solid state detectors. A scintillator type BE detector is similar to the ET detector but larger in size and positioned so that more BEs strike it. A solid state type BE detector consists of a semiconductor "diode." When struck by aBE, the semiconductor produces an electron-hole pair, the components of which migrate in opposite directions under the influence of a small applied field. These moving charges produce an electrical current.

An EDS unit is a very sophisticated device that accurately measures very miniscule amount of ionization current produced when an X-ray is absorbed in a silicon sensing element (silicon diode). Two types of X-ray spectrometers can be employed: EDS detector and wavelength dispersive spectrometer (WDS). In EDS a multichannel analyser gives the photon energy

spectrum, while WDS is based on measuring the wavelength, and the wavelengths corresponding to the ejected photons to be determined. In both cases, peaks can be assigned to particular elements with the corresponding percentage present in the sample. The peaks that overlap in EDS are observed as discrete peaks in WDS [148, 155].

3.2. High resolution transmission electron microscope (HRTEM)

HRTEM is a powerful technique which is widely used for analyzing crystal structures and lattice imperfections in various kinds of advanced materials on an atomic scale. HRTEM images depend on some optical factors in the imaging process by the electron lens and on the scattering process of the electrons incident on the crystal specimen. HRTEM image shows the position of atoms relative to others. HRTEM resolution is an important quality to measure for imaging systems, which helps to produce images showing distinct separation of discrete objects (atoms or columns of atoms) and the determination of their relative positions. Higher resolution allows the identification of closer objects; improves the detection of weaker signals and making possible imaging of lighter atoms in the presence of heavier ones [156]. In an HRTEM, beams of electrons are emitted in the electron gun by thermionic or field emission. A multistage condenser lens system permits variation of the illumination aperture and the area of illumination. The intensity behind the specimen is imaged with a lens system onto a fluorescent screen. The image is recorded digitally using a CCD camera [157]. In contrast to SEM, HRTEM can be used to probe surfaces and subsurface regions because the electrons used for imaging transmit the samples. This is particularly of interest in cases where buried interfaces need to be studied with near atomic resolution [158]. In high resolution transmission electron microscopy, lens aberrations play a key role in the imaging and the interpretation of object structures on an atomic scale. Aberrations are beneficial and detrimental to high resolution imaging at the same time: On the one hand, they introduce unwanted blurring in any imaging plane, hence obscuring the finest object details. On the other hand, they are urgently needed to produce the desired phase contrast of the very thin objects required for high-resolution structure investigations [159].

3.3. Fourier transform infrared spectroscopy (FTIR)

Different spectroscopic techniques operate over limited frequency ranges within the electromagnetic spectrum, depending on the processes that are involved and on the magnitudes of the energy changes associated with these processes. FTIR is a rapid, nondestructive and time saving method that can detect the interaction between an infrared radiation and a sample that can be solid, liquid or gaseous. FTIR radiation encompasses a long range of wavelengths, which consists of other subregions: near, middle and far infrared regions. However, most infrared spectroscopic measurement are performed in the mid- infrared region, which covers the spectral region between 400 cm^{-1} and 4000 cm^{-1}. It measures the frequencies at which the sample absorbs and also the intensities of these absorptions. Since, functional groups are responsible for the absorption of radiation at different frequencies; it is possible to identify the composition of a sample [160].

Chemical bonds vibrate at a characteristic frequency representative of their structure, bond angle and length. The frequencies absorbed by the sample are helpful for the identification of the composition due to the fact that functional groups are responsible for the absorption of radiation at different frequencies. Individual absorption peaks can then be identified and assigned to individual chemical bonds which help for identification of individual compounds in complex systems qualitatively or quantitatively. FTIR spectroscopic imaging has significant advantages compared to many other imaging methods for the characterization of molecules because it relies on the characteristic absorbance of corresponding molecular vibrations in the sample. Therefore, FTIR imaging does not require the use of added dyes or labelling methods for visualisation of different chemical components in the sample [161-163].

FTIR spectrometer use Nernst glower (a fused mixture of zirconium, yttrium, and thorium oxides molded), nichrome wire (a film of black oxide formed on the coil) and a Globar rod (made of silicon carbide) as radiation sources. Commonly used detectors are pyroelectric devices incorporating deuterium tryglycine sulfate (DTGS) in a temperature resistant alkali halide window. A Michelson interferometer, which consists of two perpendicularly plane mirrors, one of which can travel in a direction perpendicular to the plane is the most common interferometer

used in FTIR spectrometry. The radition from the source is passed through an interferometer to the sample before reaching the detector. Upon amplification of the signal, in which high frequency contributions have been eliminated by a filter, the data are converted to digital form by an analog-to-digital converter and are transferred to the computer for Fourier-transformation [164].

3.4. Raman spectroscopy

Raman spectroscopy is the most powerful technique in order to get information on the vibrational and electronic structures of substances. The Raman effect arises when a beam of intense monochromatic radiation passes through a sample that contains molecules that can undergo a change in molecular polarizability as they vibrate. It uses a single frequency of radiation to irradiate the sample and it is this radiation scattered from the molecule which is detected. A very small fraction of the incoming radiation undergoes inelastic scattering, in which the scattered wave compared with the incoming wave results in a different frequency. The basic principle in Raman spectroscopy is when a light interacts with the molecule and the cloud of electrons round the nuclei distorts to form a short-lived state called a 'virtual state'. This state is not stable and the photon is quickly re-radiated to the vibrational state. The energy changes that can be detected in vibrational spectroscopy are those required to cause nuclear motion. If the scattering process is from the ground vibrational state to a higher energy excited on absorption of energy by the molecule, it is a Stokes scattering. However, scattering from molecules which are present in the excited vibrational state due to thermal energy, to the ground state, is called anti-Stokes scattering. The difference between the incident radiation and the Raman scattered radiation produces the vibrational spectrum of interest. Raman scattering (both Stokes and anti-Stokes) are relatively inefficient processes, so that a very intense excitation sources are required.

This incident radiation does not raise the molecule to any particular quantized level, it only polarizes the molecule and is considered to be in virtual or quasi-excited state. The shift in frequency of the scattered Raman radiation is proportional to one of the vibrational energy levels involved in the transition.

The Raman spectrometer consists of laser excitation unit and a spectrometer unit using gratings with 1200 grooves mm^{-1}. The laser sources can be He-Ne or Ar-Kr laser and multialkali-metal cathode and the gallium arsenide photocathode as detectors, which depend on the laser line used. Raman spectroscopy can be performed on a liquid, solution, transparent or translucent solid, powder, pellet, or gas samples. Water is an excellent solvent for Raman work because of its low scattering [148, 165].

3.5. Ultraviolet-Visible spectroscopy (UV-Vis)

Ultraviolet-visible spectroscopy (UV-Vis) is an analytical technique which involves the absorption of light by molecules in ultraviolet-visible region. The absorption in the visible range directly corresponds to the color of the chemicals involved. UV-Vis can be used to identify some chemical species and to determine the concentration of the solution based on the absorbance. This is because the wavelength at which a molecule absorbs light is a function of its electronic structure and the amount of UV-Vis light that is absorbed by a sample is related with the number (amount) of molecules. The amount light absorbed by a sample is proportional to the concentration of the absorbing species in accordance with the Beer-Lambert's law:

$$A = \varepsilon bc \qquad (26)$$

where, A is the absorbance, ε is the molar absorbtivity, b is the path length and c is the concentration of the absorbing species [166-168].

4. OBJECTIVES OF THE STUDY

4.1. General objective

The general objective of this research was to develop electrochemical sensors based on chemically modified electrodes for sensitive and selective determination of pesticides (endosulfan, fenitrothion, phoxim and phenothrin) and pharmaceuticals (caffeine, paracetamol and uric acid) in environmental samples.

4.2. Specific objectives

The specific objectives of the study include:

- To synthesize cobalt nanoparticles and cobalt nanoparticles-polypyrrole composite
- To develop an electrochemical sensor based on cobalt nanoparticles-polypyrrole composite
- To characterize CoNPs/PPy films using HRTEM, HRSEM, FTIR, UV-Vis, CV and EIS
- To develop a graphene oxide-polypyrrole (GO/PPy) electrochemical sensor
- To characterize the GO/PPy film using SEM, FTIR, UV-Vis, Raman spectroscopy, CV and EIS
- To prepare electrochemical sensors: poly(AHNSA), MWCNTs, MWCNTs/poly(AHNSA) and mercury film
- To investigate the electrochemical behavior of pesticides and pharmaceuticals
- To establish optimum conditions for the determination of pesticides and pharmaceuticals
- To investigate the effect of interfering substances in the electrochemical determination of pesticides and pharmaceuticals
- To apply the sensors for the determination of pesticides and pharmaceuticals environmental samples

5. MATERIALS AND METHODS

5.1. Chemicals and reagents

In this study, all chemicals and reagents used are of analytical grades and were used without any further purification. Endosulfan, fenitrothion, methanol, multiwalled carbon nanotubes (density ~2.1 g/mL at 25 C, diameter: 7.5–15 nm, length: 0.5–10 μm, purity > 99%), phenothrin, phoxim, caffeine, paracetamol, uric acid, 4-amino-3-hydroxynaphthalene sulfonic acid (AHNSA), acetic acid and sodium acetate, cobalt chloride hexahydrate, pyrrole, sodium borohydride, graphite powder, sulfuric acid, sodium nitrate, potassium permanganate, sodium hydroxide, hydrogen peroxide, dimethyl formamide, lithium perchlorate, ethanol, potassium ferrocynide, potassium chloride, dipotassium hydrogen phosphate, potassium dihydrogen phosphate and substances used for interference experiments were all purchased from Sigma-Aldrich.

The stock solutions of endosulfan and fenitrothion were prepared by dissolving with acetonitrile/water (1:1, v/v) and methanol, respectively and stored at 4 ^{o}C until use. Mercury solutions were prepared by dissolving mercury(II) nitrate monohydrate in double distilled water. Phosphate buffer solutions were prepared using 0.1 M dipotassium hydrogen phosphate and 0.1 M potassium dihydrogen phosphate. Britton-Robinson buffer (BRB) solutions were prepared by mixing 0.04 M boric acid, 0.04 M phosphoric acid and 0.04 M acetic acid, and the pH of the solutions were adjusted with 0.2 M NaOH. Acetate buffer solution also prepared with 0.1 M acetic acid and 0.1 M sodium acetate. All chemicals were analytical reagent grade and all the aqueous solutions were prepared with double distilled water. The working solutions of endosulfan and fenitrothion were prepared by diluting the stock solutions with Britton-Robinson and phosphate buffer solutions, respectively.

The standard solutions of phoxim and phenothrin were dissolved in ethanol and stored in a refrigerator. The working solutions were prepared by dilution of the stock solution with the phosphate buffer.

Stock solutions of caffeine and paracetamol were prepared freshly by dissolving a weighed amount in double distilled water and then stored in refrigerator. The working standard solutions of both caffeine and paracetamol were prepared by appropriate dilutions of the stock solutions in acetate buffer solution just before use. Similarly, the stock solution of uric acid was prepared with double distilled water. The aliquots were prepared from the stock solution by diluting with 0.1 M phosphate buffer solutions before commencing the voltammetric measurements. All extraction solvents for samples were used as received without further purification.

5.2. Apparatus and instrumentations

The voltammetric measurements of fenitrothion, endosulfan**,** uric acid and both caffeine and paracetamol were performed with a CHI760D electrochemical Workstation, CHI Instruments (Austin, Texas, USA) controlled by a personal computer. However, voltammetric measurements of phoxim and phenothrin were carried out on PalmSens Trace (Palm Instruments BV, Utrecht, Netherlands). Electrochemical impedance spectroscopic experiments were performed on a CHI604D Electrochemical Workstation (CH Instruments, Inc., Austin, Texas, USA). Three electrode cell systems were used to monitor the cyclic, square wave voltammetric and electrochemical impedance spectroscopic experiments. In addition, all pH measurements were determined by digital Jenway model 3345 ion meter. Ultrasonic cleaner YJ 5120-B (Shanghai, China) was used for dispersing MWCNTs.

In all the electrochemical measurements, platinum wire and Ag|AgCl (3 M KCl) electrode were used as counter and reference electrode, respectively. The working electrodes were GCE or MWCNTs/GCE for fenitrothion, GCE or MF/GCE for endosulfan, GCE or poly(AHNSA)/GCE for caffeine and paracetamol, GCE, MWCNTs/GCE, poly(AHNSA)/GCE or MWCNTs/poly(AHNSA)/GCE for uric acid, GCE, CoNPs/GCE, PPy/GCE or CoNPs/PPy/GCE for phoxim and GCE, GO/GCE, PPy/GCE or GO/PPy/GCE for phenothrin determinations.

UV–Vis spectra were recorded on a Nicolette Evolution 100 Spectrometer (Thermo-Electron Corporation, UK). FTIR spectra were recorded on a Perkin Elmer Spectrum 100-FTIR spectrometer (Waltham, USA).

The morphology and elemental compositions of PPy, CoNPs and CoNPs/PPy composite were examined using high resolution scanning electron microscopy (AURIGA, Field Emission Gun High resolution scanning electron microscope (FEG HRSEM, Zeiss), high resolution transmission electron microscopy (HRTEM, FEI Tecnai G2 F20 X-Twin 200 kV field-emission gun) and energy dispersive X-ray spectra were collected using EDX liquid nitrogen cooled lithium doped silicon detector. For HRSEM measurement, screen printed carbon electrodes were used for the electrodeposition of PPy, CoNPs and CoNPs/PPy composite. Moreover, in HRTEM measurements the samples were prepared by drop coating one drop of specimen solution onto a holey carbon coated copper grid. Then, it was dried under a Xenon lamp for about 10 min, where after the sample coated grids were analyzed under the microscope.

The Raman spectra were measured by Triax 320 Raman system (Jobin-Yvon, Inc., Longjumeau, France), equipped with 632.8 nm He/Ne laser line as excitation source (JDS Uniphase Corporation, Milpitas, CA) and liquid-nitrogen cooled Ge array detector (Jobin-Yvon, Inc.).

5.3. Preparation of modified electrodes

Before modification, glassy carbon electrode was carefully polished with different sizes (1.0, 0.3 and 0.05 μm) of alumina slurry in sequence until a mirror like surface was obtained and then it was washed with double distilled water. Finally, it was sonicated successively with ethanol and double distilled water in order to remove adsorbed particles, and then it was allowed to dry in air.

5.3.1. CoNPs/PPy/GCE

The synthesis of cobalt nanoparticles was performed according to the procedure proposed by Guo *et al*. and Phelane *et al*. Briefly, 0.5 M solution of $CoCl_2.6H_2O$ in ethanol was prepared. To this dark blue solution, a mixture of 1.0 M sodium borohydride and 0.2 M sodium hydroxide were added. The solution was allowed to stay for 24 h until the reaction is completed. Then after, the solution was centrifuged for 20 min and the precipitate was washed completely with double distilled water and ethanol. Finally, the precipitate dried in an oven for 24 h and ground with a

pestle and mortar [81, 169]. CoNPs/GCE was prepared by drop coating CoNPs dissolved in DMF on the surface of GCE.

A 0.25 M solution of pyrrole in 0.10 M $LiClO_4$ was electropolymerized on GCE by cycling in the potential range -1.1 to +0.7 V at a scan rate of 0.05 V s^{-1} for 15 cycles. Thenafter, CoNPs/PPy/GCE was prepared by drop coating 5 μL of CoNPs onto the PPy/GCE surface and dried in air prior to its use for analysis.

5.3.2. GO/PPy/GCE

GO was synthesized from graphite using the modified Hummer's method following a procedure similar to that reported by Hanifah *et al*. [170]. 3 g of $NaNO_3$ was dissolved in 140 mL of conc. H_2SO_4 in an ice bath. Next, 15 g of $KMnO_4$ and 3 g of graphite powder were added gradually into the above mixture. The temperature was maintained below 20 ^oC with vigorous stirring using a mechanical stirrer. The temperature of this mixture was then increased and maintained to 35 ^oC. The mixture was continuously stirred for 12 h at this temperature and the resulting solution was diluted with double distilled water under vigorous stirring. Consequently, 20 mL of H_2O_2 and 800 mL of double distilled water were added into the mixture. The color of the mixture was observed changing from brown to brilliant yellow. Then, the mixture was washed with HCl and water followed by repeated centrifugation and filtration until the pH of filtrate became neutral. Lastly, the final product was washed and dried in vacuum.

20 mg GO was dispersed in 10 mL of double distilled water (2 mg mL^{-1}) followed by ultrasonication for 30 min. The electrolyte was purged before voltammetric experiments for 10 min with highly purified N_2 inorder to eliminate the adsorbed oxygen. GO/GCE was prepared by drop coating GO solution on GCE. Whereas, GO/PPy/GCE composite was prepared by electrochemical polymerization of a mixture containing 30 μL of GO suspension and 10 μL of 0.25 M pyrrole in 0.1 M $LiClO_4$ using cyclic voltammetry by scanning the potential from -1.2 to +0.6 V at a scan rate of 0.05 V s^{-1} for 8 cycles.

5.3.3. MWCNTs/GCE

2 g of MWCNTs were allowed to be oxidized in a conc. HNO_3 and H_2SO_4 (1:3, v/v) at 90 ^oC for 8 h in order to remove impurities and to generate surface functional groups. Then after, the functionalized MWCNTs was allowed to cool to room temperature and the resulting slurry was decanted consecutively and finally washed throughly with double distilled water followed by filtration until the pH reached 7.0. Finally, the precipitate was dried at 90 ^oC in an oven for 10 h. A solution of functionalized MWCNTs was prepared by mixing 1 mg MWCNTs with 1 mL deionized water (1 mg mL^{-1}) followed by sonication in order to debundle and disperse the nanotubes [42]. 10 μL of MWCNTs solution was drop coated onto the surface of the polished glassy carbon electrode and was left to dry in sunlight until the solvent evaporated. Finally, the surface of the modified electrode was rinsed throughly with deionized water.

5.3.4. MF/GCE

Mercury film modified glassy carbon electrode (MF/GCE) was prepared by immersing the glassy carbon electrode in a solution of 10 mM $Hg(NO_3)_2.H_2O$ in 1.0 mM HNO_3/KNO_3 and electrodeposited at -1.0 V for 240 s. Once the mercury film was plated, the electrode was gently rinsed with doubly distilled water and was used in a freshly prepared endosulfan solution.

5.3.5. Poly(AHNSA)/GCE

The surface of the glassy carbon electrode was modified by scanning the electrode in 0.1 M HNO_3 solution containing 2 mM AHNSA monomer with a repetitive potential scan between -0.8 V and +2.0 V at a scan rate of 0.1 V s^{-1} for 15 cycles. Finally, the modified electrode was carefully washed with double distilled water and immersed in monomer free 0.5 M H_2SO_4 solution and the potential was scanned between -0.8 V and +0.8 V (at a scan rate of 0.1 V s^{-1}) until a stable voltammogram was obtained.

5.3.6. MWCNTs/poly(AHNSA)/GCE

First, poly(AHNSA)/GCE was prepared by electropolymerization of 4-amino-3-hydroxynaphthalene sulfonic acid solution by sweeping the potential between -0.8 V and +2.0 V in 0.1 M HNO_3 at a scan rate of 0.1 V s^{-1} for 15 cycles. Then, MWCNTs was drop coated on poly(AHNSA)/GCE to fabricate MWCNTs/poly(AHNSA)/GCE composite electrode.

5.4. Preparation of samples

5.4.1. Water samples

Water samples were collected from Kuils River, Cape Town, South Africa. The water samples were filtered using a Whatman No. 41 filter paper to remove particulate matter and were stored at 4 ^{o}C for one week in a refrigerator until analysis. To the water samples ethanol were added and the pH value of the water samples (2 mL) was adjusted with 5 mL of 0.1 M PBS of pH 6.0. The spiked sample solutions were prepared with the addition of various concentrations of standard phoxim solutions.

5.4.2. Fruit juice samples

Apple, grape and orange juices were purchased from Pick and Pay supermarket (Krush 100% Juice Blend) at Bellville suburb of Cape Town, South Africa. After centrifuging and filtering each juice sample, 5 mL clear solution was diluted with 10 mL of PBS pH 6.5. The samples were spiked with stock solution of phenothrin in PBS pH 6.5 for recovery test.

5.4.3. Soil and teff samples

Soil and teff samples used in this study were collected from different farm sites in Alamata Woreda, South Tigria Administer Zone, Tigria Regional State, Ethiopia. Before analysis, the soil samples were dried in a dish at room temperature for 5 days and then were ground in pestle and mortar in order to homogenize. Anhydrous sodium sulfate (200 mg) and dichloromethane–acetone mixture (2:1, v/v; 50 mL) were added to the soil samples. The mixture was sonicated for

5 min and was shacked vigorously by hand for 10 min. The mixture then centrifuged to obtain the supernatant layer followed by suction filtration with Buchner funnel. Finally, the solvent was evaporated to dryness using a rotatory evaporator. To the dry sample, 4 mL methanol was added and the solution was diluted with PBS pH 6.0 and the solution was analyzed using square wave voltammetry.

After homogenizing and powdering, 15 g of teff was extracted with of 50 mL of dichloromethane twice and it was transferred into a Buchner funnel and filtered under suction. To the extract, 50 mL water, 15 mL saturated sodium chloride and 50 mL dichloromethane were added. Then, the mixture was throughly shaked for 5 min in a separatory funnel. The combined extracts were filtered over 50 g of anhydrous sodium sulphate and the solvent was evaporated with a rotatory evaporator. Methanol (4 mL) was added to the residue and was further diluted with phosphate buffer for voltammetric analysis.

5.4.4. Onion and tomato samples

Samples were collected from a local market near to Koka Lake, Eastern Oromia Zone, Ethiopia. For endosulfan analysis, each sample was well washed with tap and double distilled water to remove dirt, and was chopped in to small pieces. 20 mL acetone was added to 10 g of each sample (onion and tomato) and was stirred for 5 min in order to homogenize. After the solutions were filtered, the filtrates were mixed with 50 mL NaCl (20%, w/v) and were subjected to extraction with 50 mL of ethylacetate:hexane (4:1, v/v). The organic extracted phase was then filtered on filter paper after the moisture was absorbed using 10 g of anhydrous sodium sulfate. The filtrate of each sample was then evaporated using a rotary evaporator at a temperature of less than 40 ^{o}C to dryness and the residues were dissolved with 6 mL acetonitrile/water (1:1, v/v). Before electrochemical analysis, both samples were diluted with Britton-Robinson buffer pH 5.0 (1:2, v/v).

5.4.5. Coca-cola, pepsi-cola and tea samples

Cola-beverages (coca-cola and pepsi-cola) were obtained from local supermarkets, Addis Ababa and were used by diluting with a factor of 1:10 (v/v) with acetate buffer solution (ABS) after sonical elimination of gas. Tea solutions were prepared by dissolving 15.0 g of tea (Ethiopian Black Lion Tea) in 250 mL of double distilled water followed by boiling for 1 h on a hot plate with stirring [170]. The residue was allowed to settle and was filtered through a filter paper and diluted with acetate buffer by a factor of 1:10 (v/v). The dilution process helps to reduce the matrix effects [171]. The standard addition method was used for the analysis of coca-cola, pepsi-cola and tea samples by spiking with aliquots of caffeine and paracetamol.

5.4.6. Urine samples

Human urine sample was collected from an adult and stored in refrigerator until analysis. The urine sample was diluted 100-fold with PBS (pH 7.0) without any further pretreatment. A certain volume of this solution was added into an electrochemical cell for an electrochemical measurement. To study the accuracy of the sensor, recovery experiments were carried out using addition of various concentrations of standard solution of uric acid in to the urine sample, and then analyzed by SWV.

6. RESULTS AND DISCUSSION

6.1. Synthesis, characterization and electrochemical application of cobalt nanoparticles-polypyrrole modified glassy carbon electrode for the determination of phoxim

6.1.1. Background

Organophosphate (OP) pesticides are the most extensively used pesticides across the world in agriculture. They have also contributed significant health and economic benefits to the society [172]. However, due to highly persistence and toxicity, even trace contamination of organophosphorus pesticides in the environment and food chain create a lot of pollution problems [173, 174]. The toxicities are caused by inhibiting the activity of acetylcholinesterase (an enzyme in the central nervous system), often leading to perturbation of the nerve conduction system and rapid paralysis of vital functions of living systems and finally death [175-177].

Phoxim (phenylgloxylonitrile-oxime-o,o-diethyl-phosphorothionate) is an organothiophosphate insecticide that is widely used to control a wide range of insect pests in fruits, vegetables and commercial crops [179]. Many analytical methods such as high performance liquid chromatography [180-182], liquid chromatography [183, 184] and spectrophotometry [185] have been reported in the literature for the determination phoxim residues. However, these methods require expensive equipments, large amounts of organic solvents and are time consuming. In recent years, electroanalytical sensors have attracted wide attention because of their compact nature, easy handling in field trials, low cost, higher sensitivity and selectivity [186]. Phoxim was determined electrochemically on the surface of a composite of gold nanoparticles and silk fibroin modified platinum electrode [175], graphene–modified glassy carbon electrode [187], graphene oxide–gold nanocomposite modified glassy carbon electrode [188], poly(3-methylthiophene)–nitrogen doped graphene modified glassy carbon electrode [189] and molecular imprinting graphene modified glassy carbon electrode [190].

Owing to small dimensional size, good conductivity and excellent catalytic activity of nanomaterials, composites of conducting polymers with metal nanoparticles can accelerate

electron transfer rate, enhance conductivity of electrodes and have good biocompatibility in electronics, sensors and catalysis application [39, 77]. Besides, the conducting polymers have been proven to be suitable host matrices for dispersing metallic particles. Based on the unique advantages of nanosize materials, a considerable amount of research has focused on developing synthetic methods for the fabrication of nanoparticles and nanocomposites of metals or metal oxides with electroactive noble polymers [80, 191-193].

In this work, CoNPs and CoNPs/PPy/GCE were prepared and characterized using FTIR, UV-Vis, HRSEM, HRTEM, EIS and CV and were also applied for the determination of phoxim in water sample.

6.1.2. Electropolymerization and characterization of electrode materials

The polymer film was obtained by electropolymerization of 0.025 M pyrrole in 0.1 M $LiClO_4$ on glassy carbon electrode by cycling in the potential range -1.1 to +0.7 V at a scan rate of 0.05 V s^{-1} for 15 cycles (Figure 6.1A). In the forward scan, an oxidation peak was observed around 0.1 V, which corresponds to the formation of pyrrole radical cations (PPy^{+}). In the reverse scan, a reduction peak appeared around -0.15 V due to the reduction of the pyrrole radical cations [194]. The increase in the intensity of the peak currents with increasing scanning cycles confirmed the formation of polypyrrole films. Therefore, the thickness of the polymer on the electrode could be controlled by the scan number. Furthermore, the electrochemical behavior of the modified electrode was studied in a monomer free supporting electrolyte and an oxidation peak and reduction peak appeared at 0.25 V and -0.32 V, respectively, indicating that the polypyrrole film was formed at the surface of the glassy carbon electrode (Figure 6.1B). Finally, CoNPs solution was drop coated on the surface of the polymer film in order to fabricate CoNPs/PPy/GCE.

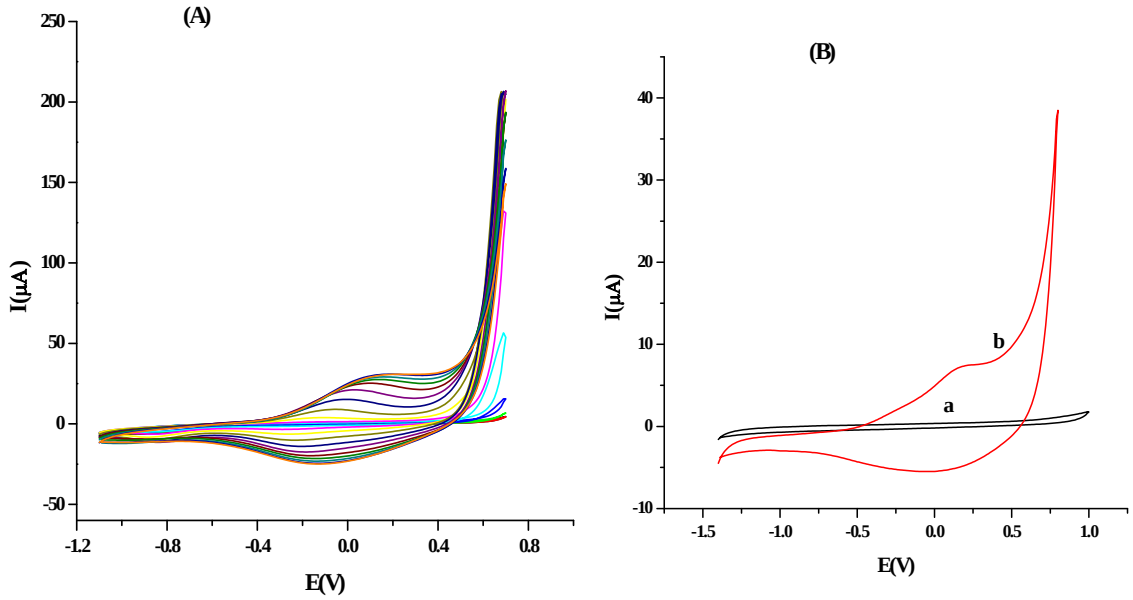

Figure 6.1. Cyclic voltammograms of (A) electropolymerization of 0.25 M pyrrole in 0.10 M $LiClO_4$ and (B) a monomer free 0.10 M $LiClO_4$ on GCE (a) and PPy/GCE (b).

6.1.3. Surface Characterization

The interactions between cobalt nanoparticles and polypyrrole were investigated using FTIR and UV-Vis spectroscopy. Figure 6.2 displays the FTIR spectra of PPy and CoNPs/PPy. For pure PPy, an absorption band at 3150 cm^{-1} attributed to the N-H stretching vibration, absorption peaks at 1500 cm^{-1} and 1400 cm^{-1} were due to C=C and C-N stretching of pyrrole ring, respectively. The broad band around 1210 cm^{-1} was caused by the C-N stretching and =C-H in plane deformation vibrations of the aromatic ring, while the two absorption peaks that appeared at 850 cm^{-1} and 620 cm^{-1} are due to C-H out-of-plane bending [195, 196]. The spectroscopic evidence confirms the formation of polypyrrole. The FTIR spectrum of CoNPs/PPy shows the characteristics peaks of PPy, with a shift of peak positions toward lower wave number (1400 cm^{-1} to 1390 cm^{-1} and 1200 cm^{-1} to 1108 cm^{-1}), indicating the dispersion of the electron density towards the nanoparticles [82, 197].

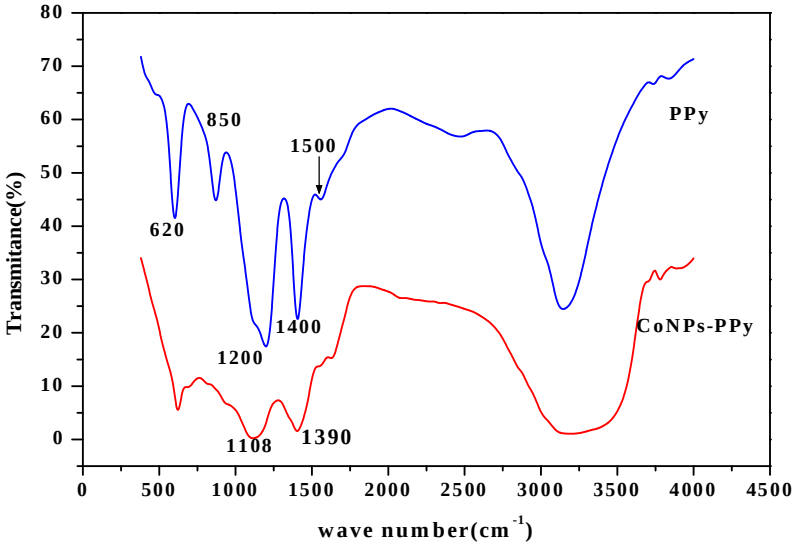

Figure 6.2. FTIR spectra of PPy and CoNPs/PPy.

Due to surface plasmon resonance (SPR), metallic nanoparticles manifest themselves in absorption spectra [198]. Figure 6.3 shows the UV-Vis spectral change of PPy, CoNPs and CoNPs/PPy composite. The CoNPs show adsorption bands at 250 nm and 310 nm and the spectrum obtained resembles with previous studies of the UV-Vis spectra of CoNPs [199, 200]. The spectral result indicates the formation of nanoparticles. Based on Mie's theory, Creighton and Eadon have reported the calculated SPR absorption of cobalt nanoparticles in the range of 250-450 nm [201]. Th PPy spectrum exhibited characteristic bands at around 265 nm, which is assigned to π-π^* transition of the pyrrole ring. However, the bands that appeared for both CoNPs and PPy were not observed in the CoNPs/PPy composite and a broad band observed around 410 nm, which indicate the composite was synthesized successfully.

From the spectral changes, a strong coordination bond was formed between cobalt and the negatively charged (deprotonated) pyrrolic nitrogen (Scheme 3), which is in agreement with the structure proposed by Shi *et al*. [202].

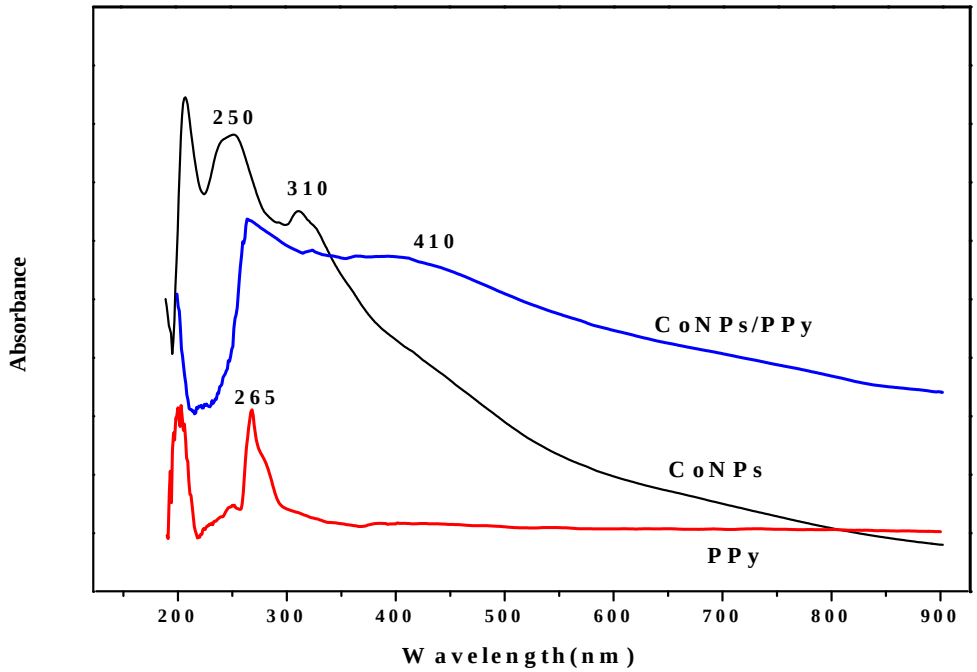

Figure 6.3. UV-Vis spectra of CoNPs, PPy and CoNPs/PPy.

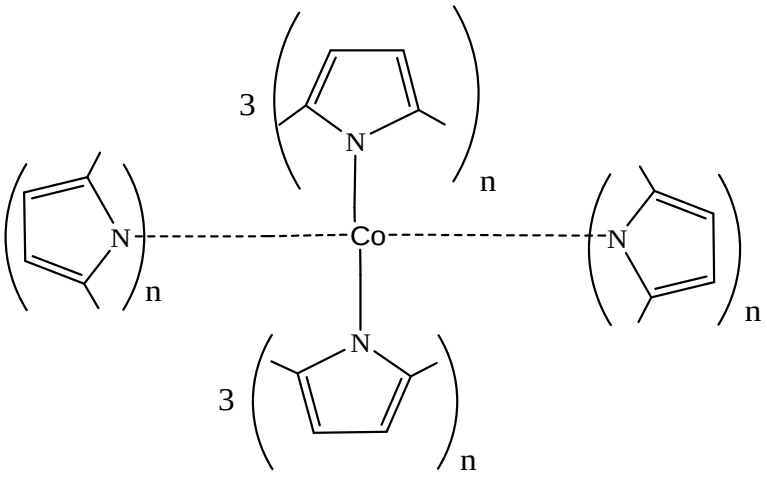

Scheme 3. Proposed active-site structure of CoNPs/PPy.

Besides, the surfaces of CoNPs, PPy and CoNPs/PPy were characterized using HRSEM and HRTEM analyses. HRSEM was employed to characterize the morphology of CoNPs, PPy and CoNPs/PPy deposited on the screen-printed carbon electrode. The HRSEM spectra are presented in Figure 6.4. The image of PPy shows non-uniform distribution of polypyrrole particles. In CoNPs, the shape of grain particle is spherical and distributed uniformly. However, the HRSEM image of CoNPs/PPy shows the size of nano-polymer composite was slightly larger than CoNPs [81].

Figure 6.5 shows the HRTEM images of PPy, CoNPs and CoNPs/PPy. HRTEM images of CoNPs and CoNPs-PPy composite showed agglomeration of particles which indicates the incomplete reaction. Besides, the large Van Der Waals forces and magnetic dipole interactions make it hard to get isolated Co nanocrystals [81].

The sizes of the particles in CoNPs/PPy were bigger than in CoNPs particles. As shown in the histogram, the mean diameter of CoNPs/PPy (8.5 nm) were slightly higher than CoNPs only (4.3 nm) (Figure 6.6). This size differences confirms the incorporation of CoNPs into the PPy in forming the composite. The increased particle sizes in the composite compared with the free CoNPs were due to the interaction of the nanoparticles with the polymer during the growth into larger crystals.

The chemical compositions of the CoNPs and CoNPs/PPy were analyzed using EDS. The EDS peaks of CoNPs showed the presence of Co, Cl, C and O (Figure 6.7). The chlorine atom observed is from the starting material $CoCl_2.6H_2O$, carbon and oxygen were from ethanol used to disperse powder samples for HRTEM analysis. CoNPs/PPy composite is composed of C, O and Co, which confirms that the composite is formed from cobalt nanoparticle and polypyrrole. The absorption peak of copper is attributed to the copper grid used for the characterization of nanoparticles [203].

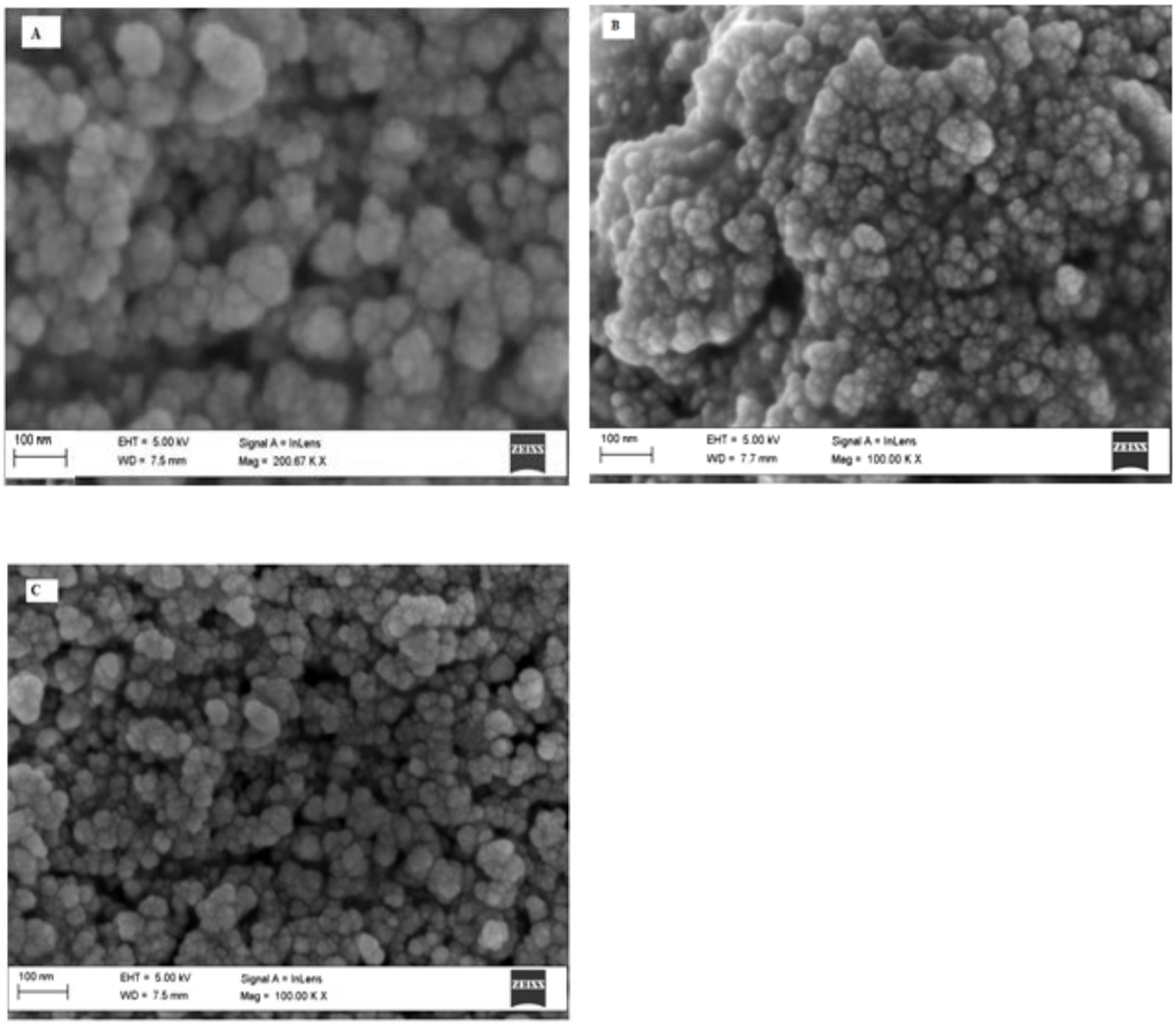

Figure 6.4. HRSEM images of PPy (A) CoNPs (B) and CoNPs/PPy (C).

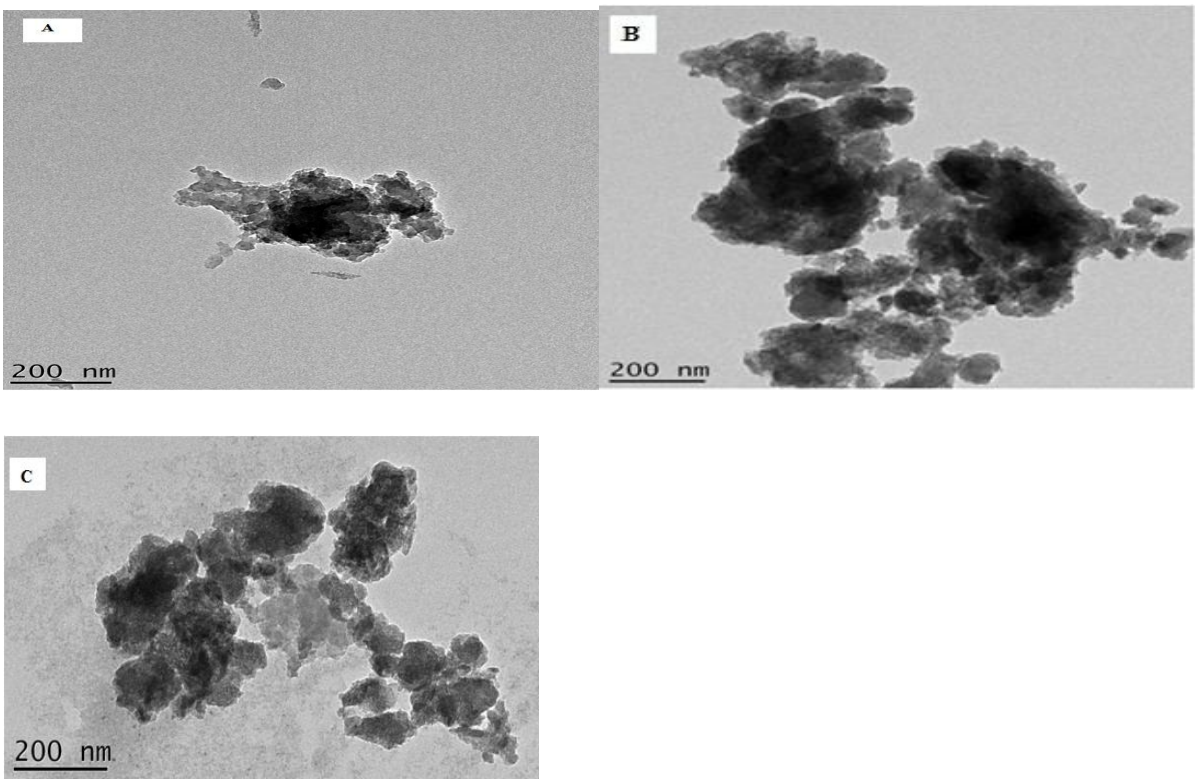

Figure 6.5. HRTEM images of PPy (A) CoNPs (B) and CoNPs/PPy (C).

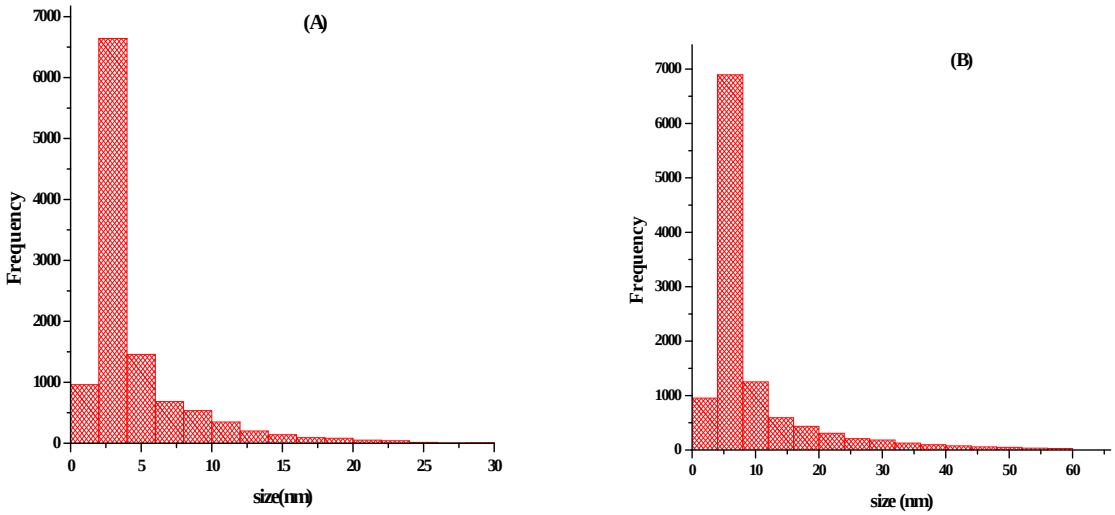

Figure 6.6. Size distribution of CoNPs (A) and CoNPs/PPy (B).

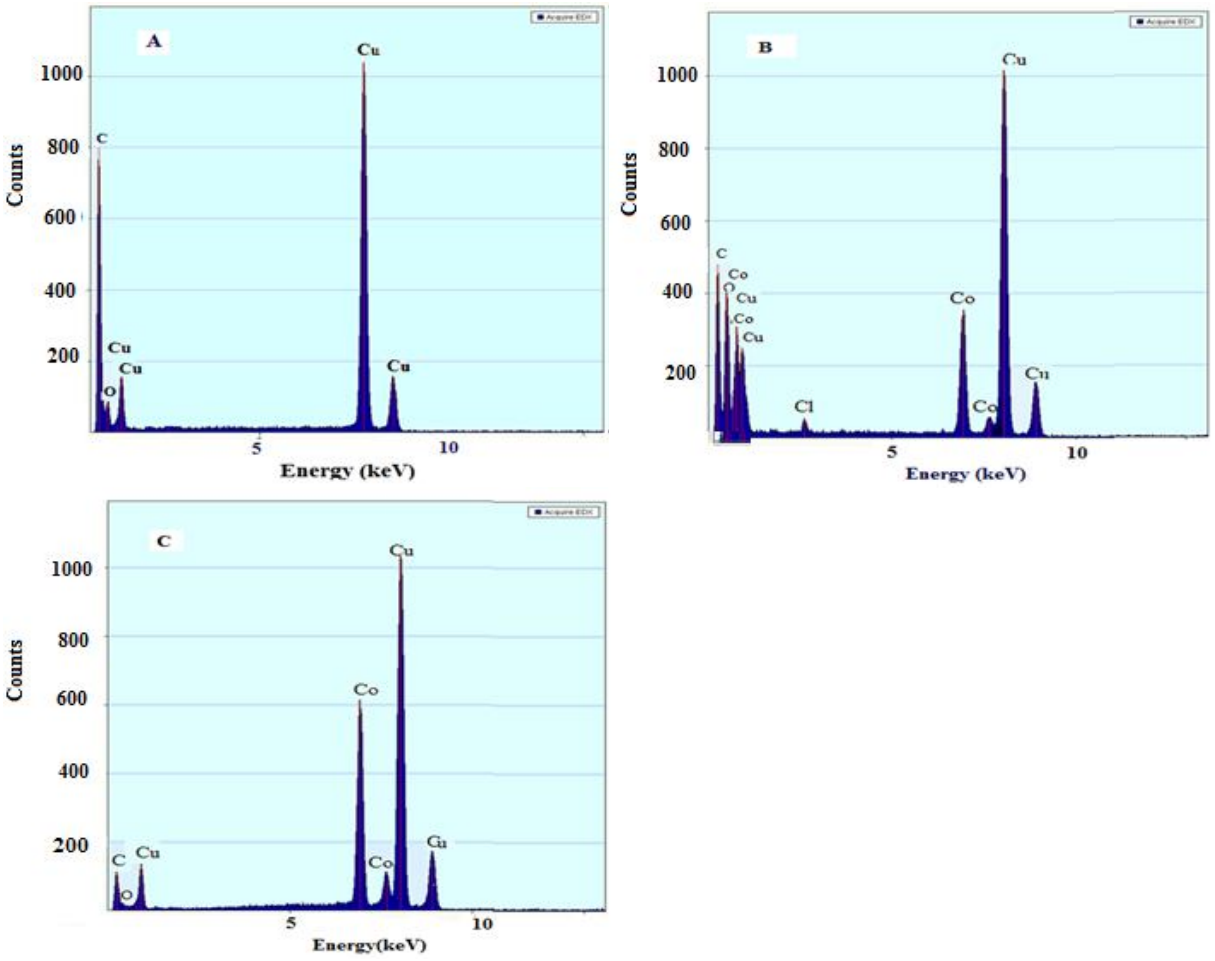

Figure 6.7. EDS images of PPy (A) CoNPs (B) and CoNPs/PPy (C).

6.1.4. Electrochemical characterization

After the electrode was prepared as shown in the schematic representation (Scheme 4), the electrochemical behavior of the electrodes was studied using cyclic voltammetry. The electroactive surface areas of the modified electrodes, PPy/GCE, CoNPs/GCE and CoNPs/PPy/GCE were determined in 1.0 mM $[Fe(CN)_6]^{3-/4-}$ in 0.1 M KCl solution at different scan rates. For a reversible process, based on the Randles-Sevcik equation (Eqn. 3) the electroactive surface areas were calculated from the slope of the plot of current *vs* the square root of scan rate. The result showed that the surface area of CoNPs/PPy/GCE was 2.6 and 2.1 times greater than the surface areas of PPy/GCE and CoNPs/GCE, respectively (Table 6.1). Significant

increased of the electroactive surface area of CoNPs/PPy/GCE can enhance the sensitivity of the electrode when used for electroanalysis.

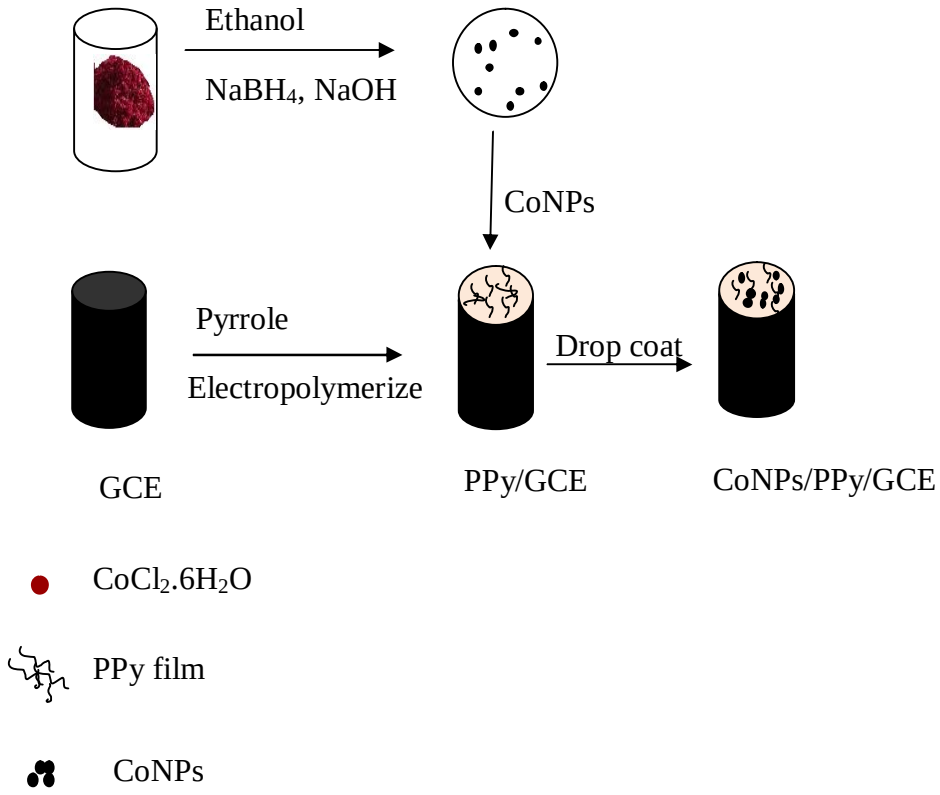

Scheme 4. Illustration of the preparation of CoNPs/PPy/GCE.

Table 6.1. Surface area of the modified electrodes.

Electrode	Surface Area (cm^2)
PPy/GCE	0.125
CoNPs/GCE	0.16
CoNPs/PPy/GCE	0.34

6.1.5. Electrochemical behavior of phoxim

The electrochemical behavior of phoxim was studied at the surfaces of GCE, PPy/GCE, CoNPs/GCE and CoNPs/PPy/GCE using cyclic volatmmetry. As shown in Figure 6.8, a well defined reduction peak was observed in the absence of any oxidation counterpart, indicating that phoxim is an electroactive and the cathodic peak is irreversible. Compared with the GCE, increased in the reduction peak current with shift of potential towards positive direction was observed at the surface of PPy/GCE, CoNPs/GCE and CoNPs/PPy/GCE. Furthermore, the decreased in overpotential and increased in the peak current were significant at the surface of CoNPs/PPy/GCE. These remarkable changes indicated that cobalt nanoparticles and polypyrrole have synergistic electrocatalytic effect for the electrochemical reduction of phoxim as a result of their high electroactive surface areas.

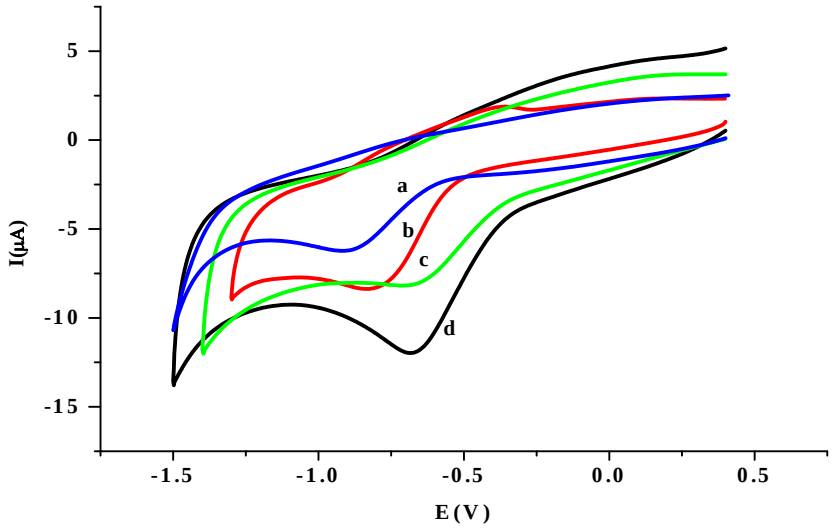

Figure 6.8. Cyclic voltammograms of 5 μM phoxim in 0.1 M PBS (pH 7) at GCE (a), PPy/GCE (b), CoNPs/GCE (c) and CoNPs/PPy/GCE (d).

Electrochemical impedance spectroscopy (EIS) was employed to study the interface properties of an electrode [144, 204]. Figure 6.9 shows the Nyquist plots for GCE (a), PPy/GCE (b), CoNPs/GCE (c) and CoNPs/PPy/GCE (d) in 20 μM phoxim solution. It is clearly seen that a

GCE exhibits a large semicircle at high frequency and nearly a straight line at low frequency regions.

Upon modifying the GCE with PPy (PPy/GCE), the diameter (R_{ct}) of Nyquist plot decreased, which is an indication of the increased in the surface roughness and enhanced electron transfer rate which occurred between the electrode and the phoxim. At CoNPs/GCE, the R_{ct} value decreased implying the deposition of highly conductive nanoparticles with high surface area that acted as electron transfer channels. Surprisingly, CoNPs/PPy/GCE, exhibited smallest electron transfer resistance as compared with the CoNPs/GCE and PPy/GCE. These results support the combined effect of increased surface area and good electrical conductivity of CoNPs/PPy/GCE. The significant change of R_{ct} as a result of modification of GCE indicated that both CoNPs and PPy films have been successfully attached to GCE surface. Thus, the EIS results strongly corroborated the results obtained from the CV study.

Furthermore, the effects of various concentrations of phoxim on the value of charge transfer resistance, R_{ct} were studied at the surface of CoNPs/PPy/GCE according to equation 19 [143, 152]. The Nyquist plot (Figure 6.10A) shows that with increasing phoxim concentration, the shape of the semicircle began to change and its diameter was gradually decreased. The reciprocal of charge transfer resistances were plotted against the phoxim concentration and the resulting plot is shown in Figure 6.10B. It was found that R_{ct} decreased with increasing phoxim concentration, which indicates that the rate of charge transfer was not hampered with the adsorption of various species on the surface of CoNPs/PPy/GCE.

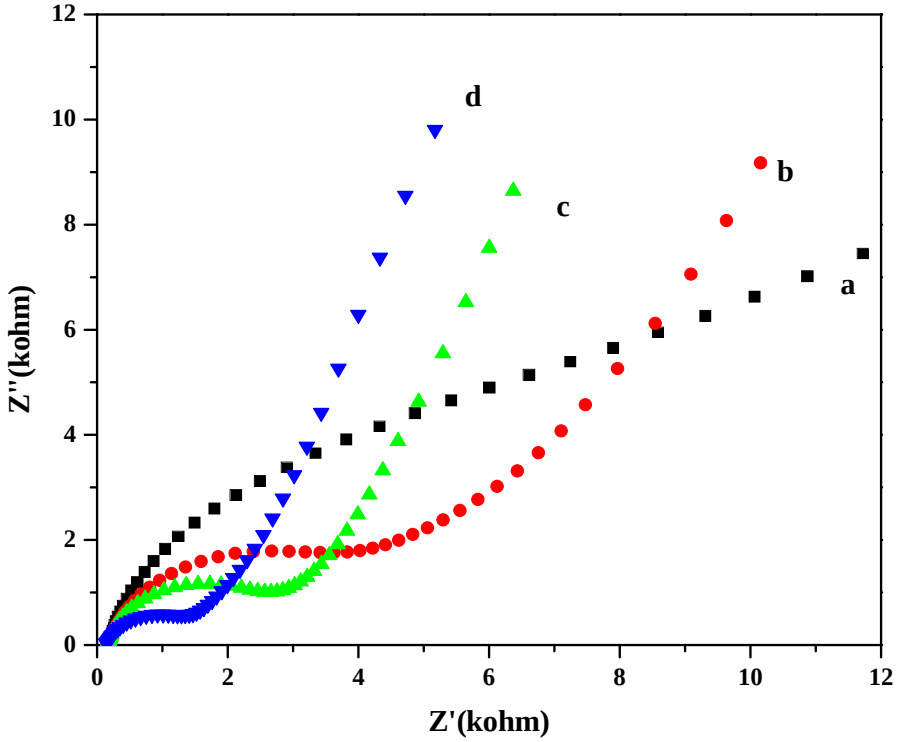

Figure 6.9. Nyquist plot of 20 μM phoxim in ethanol for the GCE (a), PPy/GCE (b), CoNPs/GCE (c) and CoNPs/PPy/GCE (d).

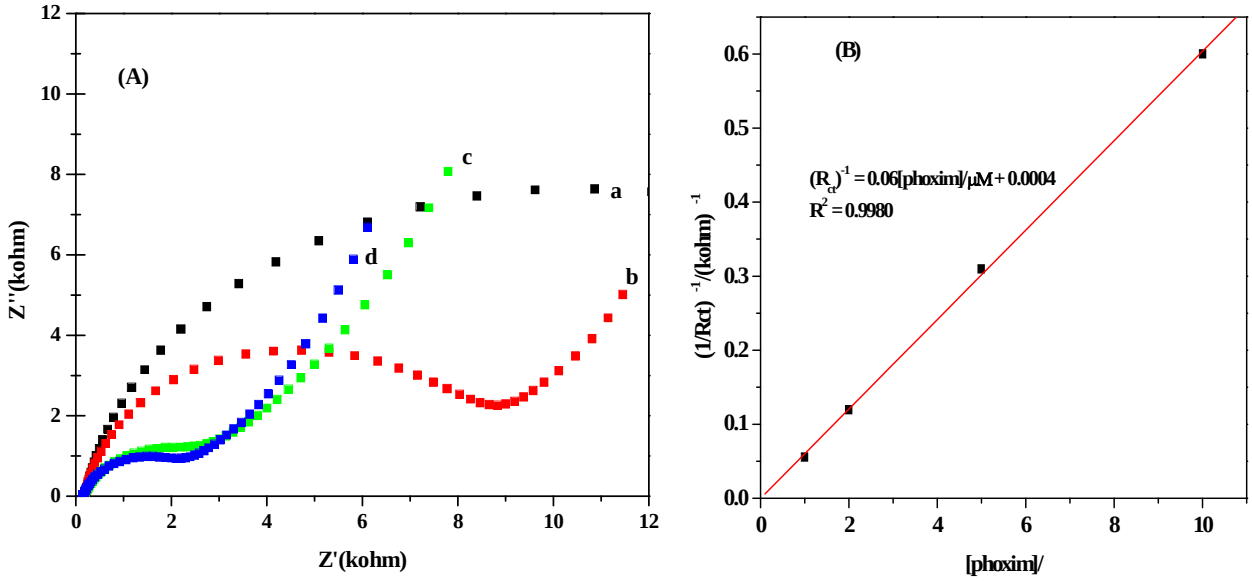

Figure 6.10. (A) Nyquist plots of CoNPs/PPy/GCE for various concentrations of phoxim in PBS pH 7 solution: 1.0 μM (a), 2 μM (b), 5 μM (c) and 10 μM (d) phoxim at CoNPs/PPy/GCE and (B) plot of $1/R_{ct}$ *vs* concentration of phoxim.

6.1.6. Effect of pH

The effect of solution pH on the reduction of phoxim at CoNPs/PPy/GCE was investigated in 0.1 M PBS. From Figure 6.11A, it can be observed that the peak current increased as the pH of the solution changes from pH 4 to 6 and decreased, then after. As a result, pH 6.0 was selected as the optimum value for subsequent studies. In addition, the peak potential shifted towards more negative values as the pH increased (Figure 6.11B) and are related linearly with a regression equation: $E_{pc}(V) = -0.054pH + -0.42$, $R^2 = 0.9995$. The slope 0.054 V/pH was close to the theoretical value given by the Nernst equation [205], suggesting that the reduction of phoxim involves the transfer of equal number of protons and electrons according to Scheme 5 [187].

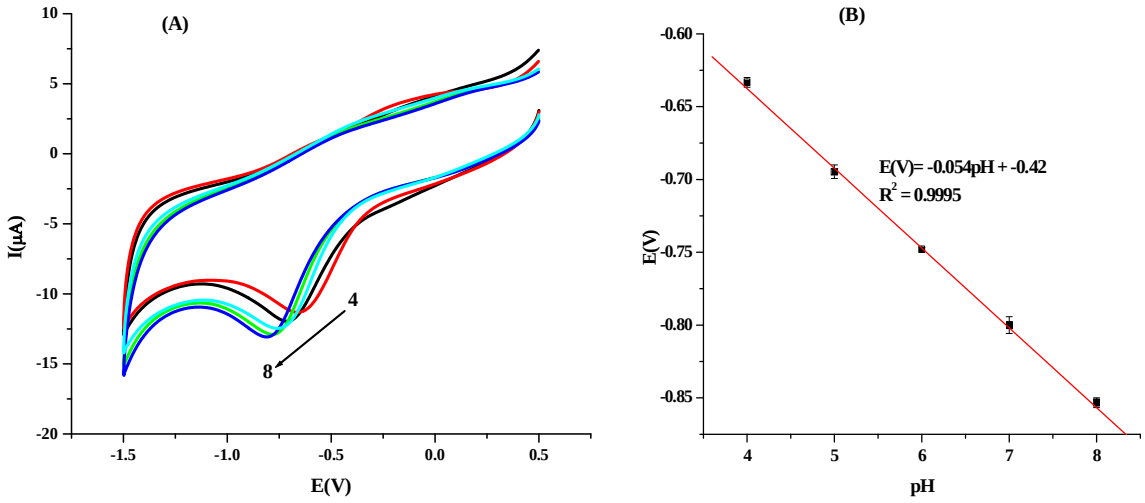

Figure 6.11. Effect of pH of PBS on the peak current for 5 μM phoxim at CoNPs/PPy/GCE (A) and plot of peak potential *vs* pH (B).

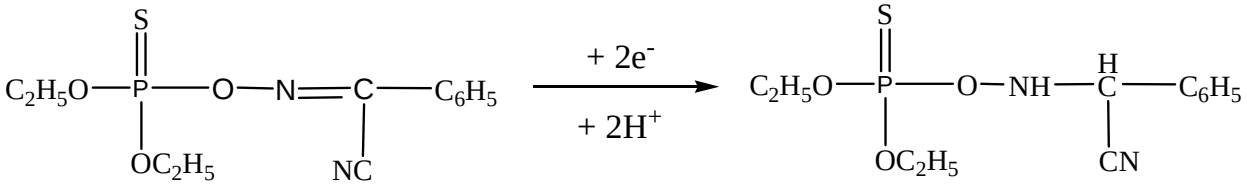

Scheme 5. Mechanism of phoxim reduction.

6.1.7. Effect of scan rate

The reaction kinetics of phoxim reduction was investigated by studying the effects of scan rate on the peak current and potential using cyclic voltammetry (Figure 6.12A). It can be seen that the reduction peak current increased linearly with an increase in the scan rate in the range 0.05 V s^{-1} –0.11 V s^{-1} (Figure 6.12B) with a regression equation: $I_{pc}(\mu A) = 126.1\nu + -1.53$, $R^2 = 0.9970$. This indicates that the reduction of phoxim on CoNPs/PPy/GCE is an adsorption-controlled process. Furthermore, the peak potential shifted to more negative values as the scan rate was

increased, this supports the fact that the electrontransfer is not diffusion-controlled only[206, 207].

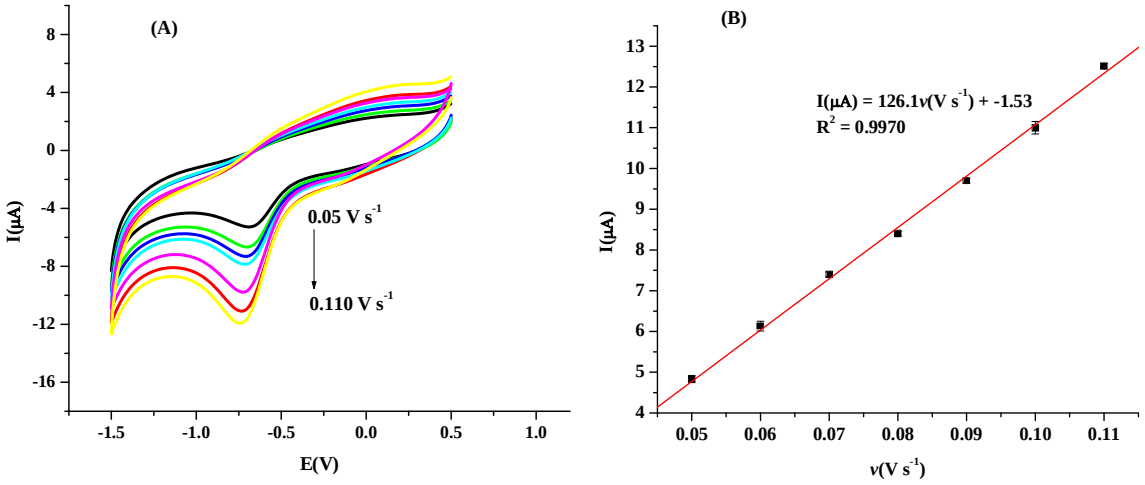

Figure 6.12. Cyclic voltammograms for 5.0 μM phoxim in 0.1 M PBS pH 6.0 at the CoNPs/PPy/GCE at various scan rates (A) and plot of the peak current *vs* scan rates (B).

6.1.8. Effects of accumulation potential and time

In an adsorption controlled process, both accumulation potential and time affect the amount of the adsorbed analyte on the surface of the electrode. The influence of accumulation potential was studied at various applied potentials (-0.2 V to -0.8 V) for a fixed period of time (40 s). The results indicated that the peak current increased from -0.2 V to -0.5 V and decreased when the potential was increased beyond -0.5 V (Figure 6.13A). Therefore, deposition potential of -0.5 V was taken as the optimum value. Similarly, the effect of accumulation time on the peak current for phoxim also studied in the range from 20 s to 70 s. Figure 6.13B shows that the peak current increased up to 50 s and then it gradually decreased due to the saturation of the electrode surface. Thus, 50 s was chosen as the optimal accumulation time for further analysis.

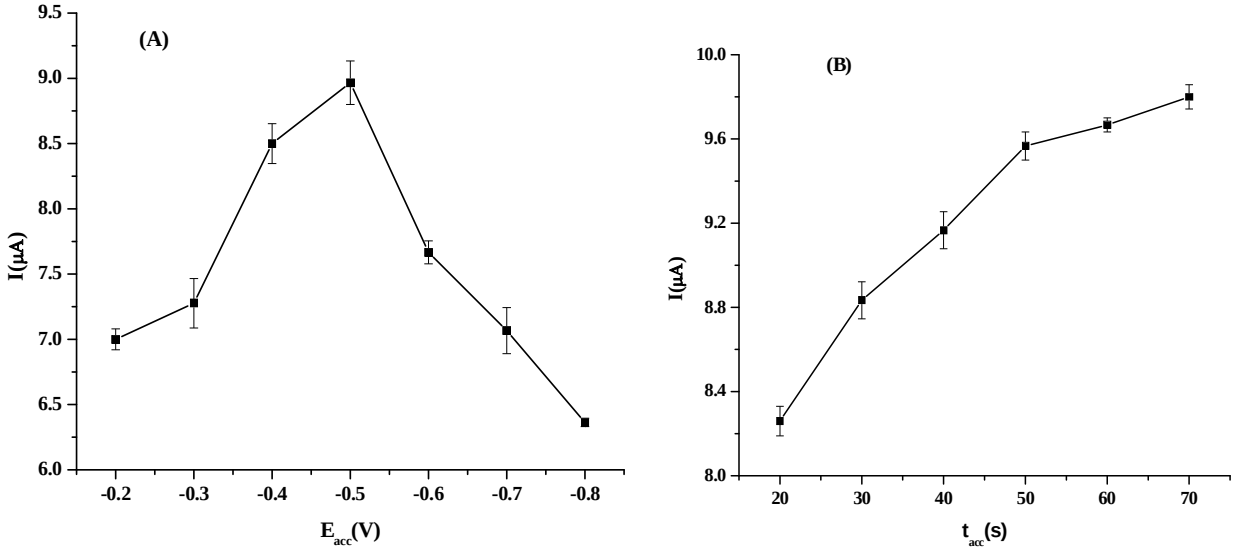

Figure 6.13. Effects of accumulation potential (A) and accumulation time (B) on the peak current of 2.5 μM phoxim in PBS solution (pH 6) at the surface of CoNPs/PPy/GCE.

6.1.9. Calibration curve

Under the optimal conditions, the relationship between peak current and the concentration of phoxim was examined using SWV. Figure 6.14 shows the SWV responses of the CoNPs/PPy/GCE for various concentrations of phoxim. The peak current increased upon increasing phoxim concentration and a linear response was obtained in the concentration range 0.025 μM to 12 μM with the linear equation: I(μM) = 2.1C(μM) + 5.9, R^2 =0.9984. The limit of detection of the sensor was calculated to be 0.0045 μM (S/N = 3).

The performance of this sensor was compared with other reported sensors. The linear range and detection limit of the prepared sensor are comparable with or even better than many of previously reported sensors (Table 6.2). This better performance can be ascribed to the faster electron transfer and high electrocatalytic performance of the sensor as a result of large surface area and good conductivity. Therefore, CoNPs/PPy/GCE could provide a good platform for the effective detection of phoxim.

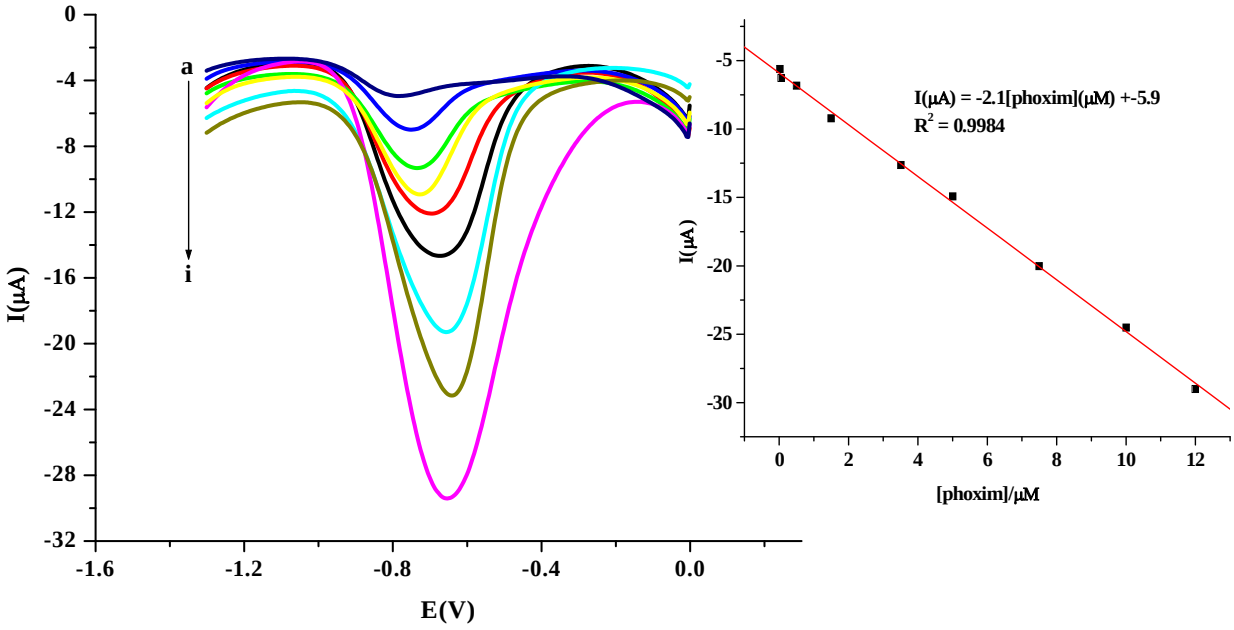

Figure 6.14. Square wave voltammograms for various concentrations of phoxim in PBS pH 6.0 at CoNPs/PPy/GCE electrode: (a) 0.025, (b) 0.05, (c) 0.5, (d) 1.5, (e) 3.5, (f) 5.0, (g) 7.5, (h) 10 and (i) 12 μM. Inset: The calibration plot of peak current with concentrations of phoxim at CoNPs/PPy/GCE.

Table 6.2. Comparison of different electrochemical sensors reported for the determination of phoxim.

Electrodes	Linear range (μM)	Detection limit (μM)	References
Gr/GCE	0.02-20	0.008	[187]
AuNPs/RGO/GCE	0.01-10	0.003	[188]
P3MT/NGE/GCE	0.02-0.2	0.0064	[189]
MIP/graphene/GCE	0.8-140	0.02	[190]
AchE/AuNPs/SF	0.005-0.2	0.002	[191]
AuNEES	59-12000	0.0048	[208]
CoNPs/PPy/GCE	0.025-12	0.0045	This work

6.1.10. Repeatability, reproducibility and stability

The repeatability of the CoNPs/PPy/GCE was evaluated with repeated current responses (n = 6) with the same modified electrode for 5 μM phoxim in PBS pH 6 solution and the relative standard deviation (RSD) of the peak current was calculated to be 4.1%. Similarly, the reproducibility of the CoNPs/PPy/GCE was examined by measuring the peak current of phoxim with three different electrodes prepared under the same conditions (n = 5). The relative standard deviation of the measurements for the three electrodes was 2.0%, which suggests that the precision and reproducibility of sensor were quite good.

The stability of the sensor was examined after storing it in a refrigerator at 4 ^{o}C for 5 days and the peak current was retained 91% of its initial value. This might be the absorption of reduction products which decreases the specific sites. This indicates that the modified electrode has good stability.

6.1.11. Interference study

To apply the method for analytical application, the effects of some common interfering substances such as inorganic ions (Fe^{3+}, Mg^{2+}, Zn^{2+} and Cl^{-}) and pesticides (dichlorvos and phenothrin) in the determination of phoxim were examined by SWV under the optimized conditions. The tolerance limit was defined as the maximum concentration of the interfering substance that caused an error less than 5% in the determination of phoxim [209].

The response of 10 μM phoxim was compared to the response obtained in the presence of these species at various concentrations. The results in Table 6.3 indicates that 1000-fold of Fe^{3+}, Mg^{2+}, Zn^{2+} and Cl^{-} did not interfere with the determination of phoxim. 10-fold of dichlorvos and phenothrin did not influence the current responses of phoxim. Change of ± 5% in the phoxim peak current in the presence of interferents proved the sensor had good selectivity.

Table 6.3. Influence of potential interferences on the voltammetric response of CoNPs/PPy/GCE to 10 μM phoxim.

Interfrences	Change in current response (%)	Signal change (%)
Fe^{3+}	101.5	+1.5
Mg^{2+}	97.3	-2.7
Zn^{2+}	95.3	-4.7
Cl^{-}	97.4	-2.6
Dichlorvos	95.3	-4.7
Phenothrin	95.6	-4.4

6.1.12. Application

Under the optimum conditions, CoNPs/PPy/GCE was applied for the determination of phoxim in river water sample. After the pH of the water sample was adjusted with 0.1 M PBS of pH 6.0, the water sample were analyzed first without addition of phoxim standard. As can be seen in Figure 6.15, no voltammeteric response which corresponds to phoxim was observed when the water samples were analysed. Subsequently, the water samples were spiked with various concentrations of phoxim (0.75, 2, 4 and 6 μM). The recovery of the water samples were ranged from 94.6 to 100.2% (Table 6.4), indicating that the sensor could be successfully applied for phoxim determination in real samples with good recovery.

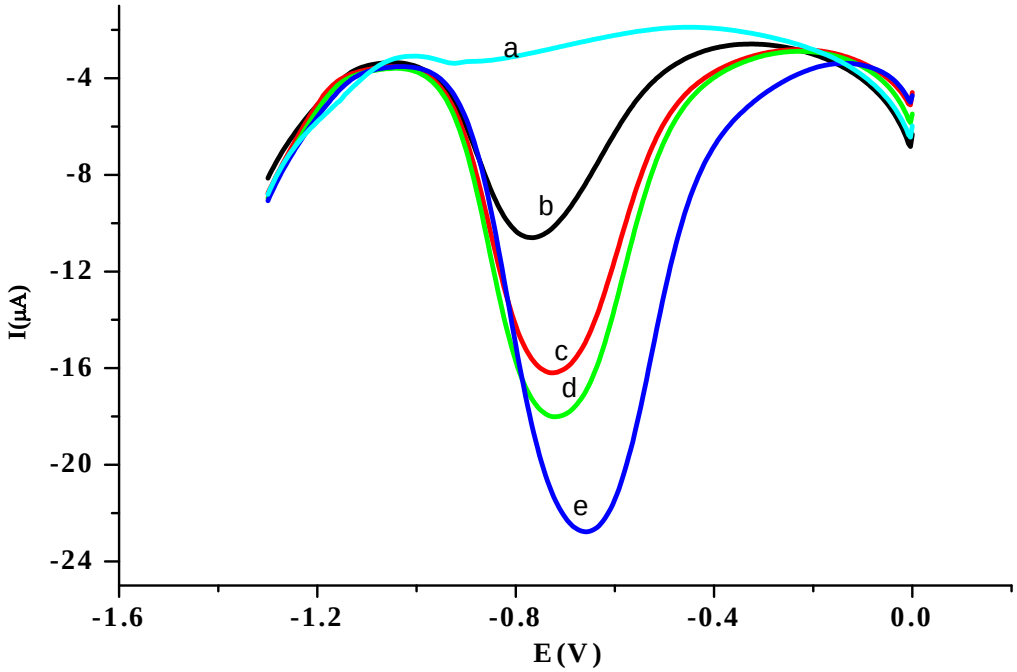

Figure 6.15. Square wave voltammograms of CoNPs/PPy/GCE for water samples spiked with different concentrations of standard phoxim (a = 0 μM, b = 0.75 μM, c = 2 μM, d = 4 μM and e = 6 μM).

Table 6.4. Recovery of phoxim in river water sample.

Sample	Added (μM)	Found [a] (μM)±sd	Recovery (%)
Water	0.75	0.71±0.013	94.6
	2.0	1.9±0.0.7	95.0
	4.0	3.85±0.20	96.3
	6.0	6.01±0.29	100.2

[a] triplicate measurements

6.2. Electrochemical determination of phenothrin in fruit juices at graphene oxide-polypyrrole modified glassy carbon electrode

6.2.1. Background

Pyrethroids are synthetic insecticides with structures based on the natural chemicals pyrethrins. They are broad spectrum, low resistant to pests and low mammalian toxicity, highly stable to light and temperature and are very lipophilic compounds. Due to these properties, they are widely used in pest control in agriculture, public health, horticulture and veterinary applications [210-217].

Phenothrin ($C_{23}H_{26}O_3$) belongs to the type I pyrethroids with chrysanthemate moiety non-cyanopyrethroid insecticide (Figure 6.16). It has been used extensively to control pests in agricultural crops such as vegetables, fruits, potatoes, cereals and household insects. Although phenothrin is thought to be of low toxicity to humans, the residues left after its use contaminate food, water, soil, etc. It can cause endocrine-disrupting diseases and depolarization to humans and paralyze the peripheral and central nervous system through interaction with sodium channels and eventually leading to death [218]. The general routes of phenothrin are through inhalation of household aerosol sprays, ingestion of food containing residual material, or dermal contact with pediculicides.

Owing to its toxicity, it is necessary to develop a rapid and effective method for the determination of phenothrin in the food samples. Analytical techniques such as gas chromatography [217, 219], gas chromatography with mass spectrometry [220], electrophoresis [221] and immunoassay methods [222] have been most widely used for the determination of phenothrin. Despite of their advantageous, most of them have limitation with respect to sensitivity, selectivity and simplicity, which make the detection time-consuming and requiring a tedious sample pretreatment [114, 223, 224]. Consequently, electrochemical methods have presented an alternative technique for the detection of pyrethroids. Thriveni *et al*. reported an electrochemical sensor based on a hanging mercury drop electrode for the determination of

phenothrin in agricultural formulations, vegetables, and storage bags of wheat and rice samples [225].

The combination of excellent properties of graphene oxide and polypyrrole, have brought synergetic effect that gave an improvement in the properties of each component. Thus, in this study, we report the use of graphene oxide-polypyrrole composite modified glassy carbon electrode for the determination of phenothrine in various fruit juices.

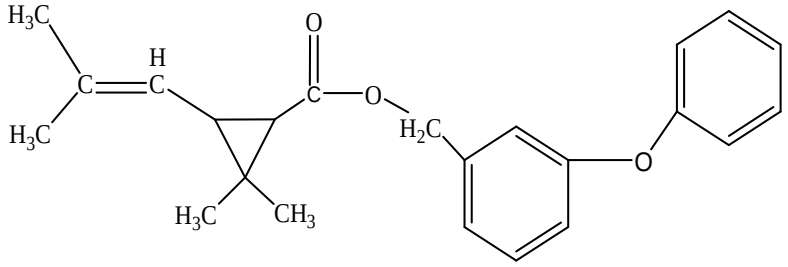

Figure 6.16. Structure of phenothrin.

6.2.2. Prepartion of GO/PPy/GCE

On electropolymerization of a solution of GO and pyrrole in 0.1 M $LiClO_4$ using CV in the potential range -1.2 to +0.7 V at a scan rate of 0.05 V s^{-1} for 8 cycles at a glassy carbon electrode, an oxidation peak current appeared in the forward direction due to pyrrole oxidation (Figure 6.17). In subsequent cycles the current appeared at potentials slightly shifted to the positive direction. In the reverse scan, a reduction of the pyrrole radical cation occurred and the peak current increased with increasing number of cycles. The overall preparation of this electrode is presented in Scheme 6.

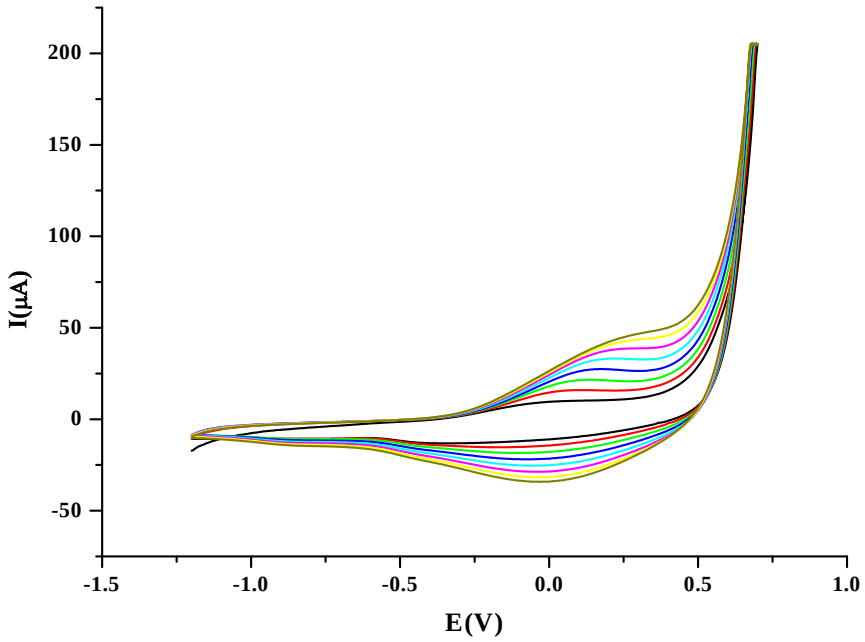

Figure 6.17. Cyclic voltammograms of electropolymerization of a solution of 0.25 M pyrrole in 0.10 M $LiClO_4$ and GO.

.

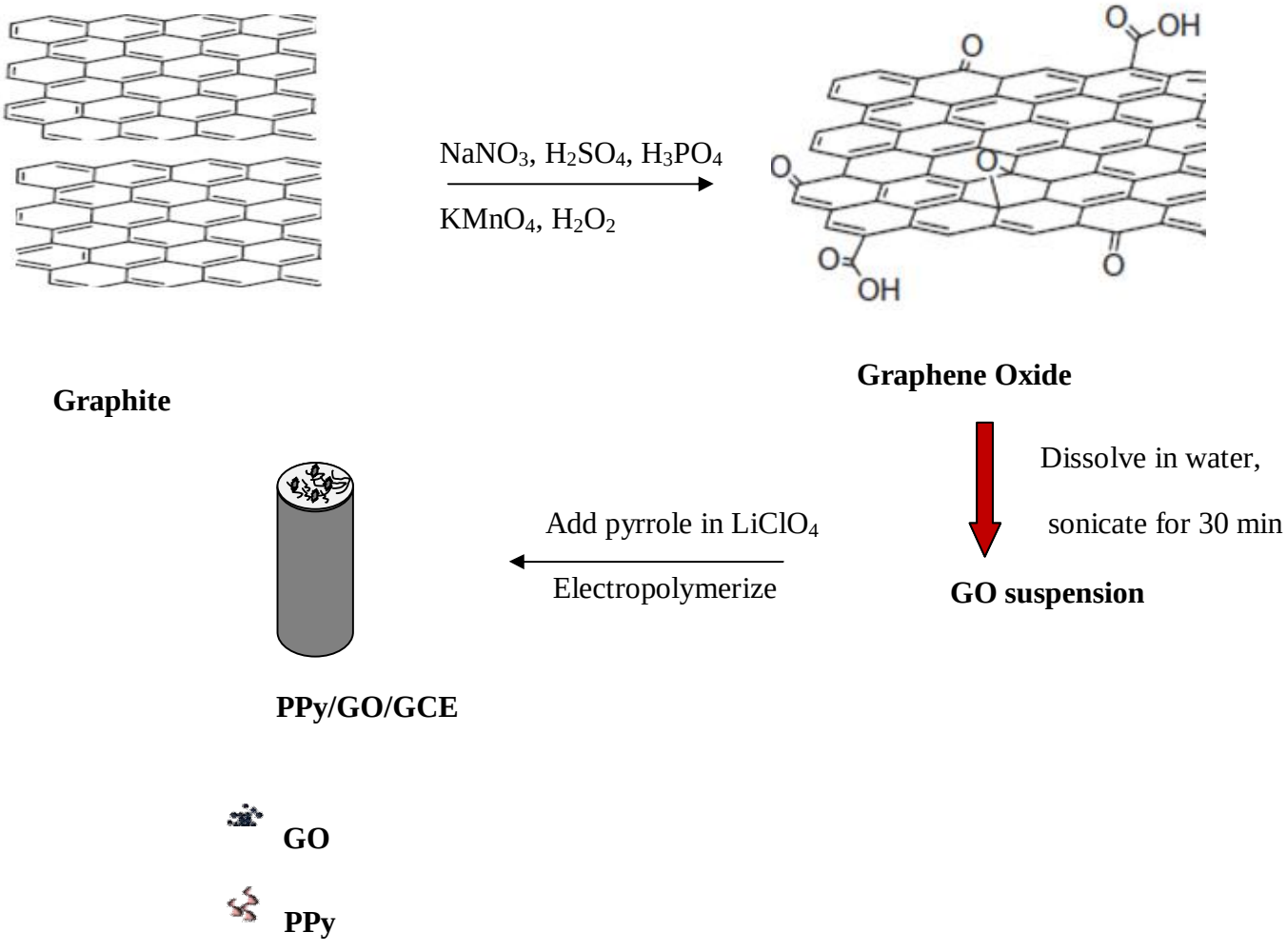

Scheme 6. Route for fabrication of GO/PPy/GCE**.**

6.2.3. Surface characterization

The surface morphology of the GO and GO/PPy composite was characterized using SEM. As shown in Figure 6.18A, GO shows a rough surface with many wrinkles, showing a three-dimensional (3D) morphological microstructure due to the presence of GO sheets. On careful looking a slight change in the morphology of GO/PPy can be observed, which confirms the formation of GO/PPy composite (Figure 6.18B).

FTIR spectra of GO, PPy and PPy/GO are shown in Figure 6.19. In GO, the broad peak at 3431 cm^{-1} corresponds to O-H stretching, which is responsible for good dispersibility in water [170]. The peaks at 2924 cm^{-1} and 2848 cm^{-1} are assigned to symmetric vibration and asymmetric stretching peaks of aromatic CH_2 group [100, 226, 227]. Peaks at 1640 cm^{-1} and 1740 cm^{-1} can be attributed to the aromatic C=C stretching and the carbonyl (C=O) stretching vibration, respectively [170]. The absorption peaks at 1539 cm^{-1} corresponds to the C=C stretching of the aromatic ring of GO [100]. Finally, the absorption peaks 1295 cm^{-1}, 1163 cm^{-1} and 1073 cm^{-1} correspond to C-OH of carbonyl, C-OH of alcohol and C-O of epoxy group, respectively [228]. For PPy, the absorption peaks at 3180 cm^{-1}, 1650 cm^{-1} and 1405 cm^{-1} correspond to N-H, C-N and C-C stretching vibration in the polypyrrole ring, respectively. In addition, the band at 1108 cm^{-1} is attributed to the C-H in plane vibration of pyrrole ring.

In the composite GO/PPy, the characteristic peaks of PPy at 1650 cm^{-1} and 1405 cm^{-1} have been shifted to 1717 cm^{-1} and 1454 cm^{-1}, respectively. This is most likely caused by the π–π interaction between the GO layers and aromatic polypyrrole rings. Furthermore, a broad peak with decreased in size exhibited at 3431 cm^{-1}, which are attributed to the hydrogen bonding between the GO layers and aromatic polypyrrole rings. The peak due to C=O of GO shifted towards lower wave number, which indicates that the electron density around the surface groups on the GO dispersed in polypyrrole polymer in forming the composite. However, the other characteristic peaks of GO can be found in the spectrum of PPy/GO composite with decreased in intensity. These results suggest that GO has been successfully incorporated into the PPy film [227-230].

Figure 6.20 shows the UV-Vis spectra of GO and GO/PPy. The spectrum of GO shows absorption band at 322 nm and 457 nm, corresponding to the π-π^* transition of the conjugated aromatic double bonds (C=C) and n-π^* transitions of the carbonyl groups, respectively [38]. After the polypyrrole electropolymerized in the presence of GO (GO/PPy), absorption peaks were observed at 260 nm and 322 nm, which are attributed to π-π^* transitions and n-π^* transitions, respectively. A shoulder-like appearance observed over the range 400 nm to 520 nm corresponds to the polaronic and bipolaronic transition (n-π^* transition) which are the feature of the oxidized state of PPy segments. The change in the intensity of the absorption band and

appearance of new band in GO/PPy indicates the electronic structure of GO was changed due to its interaction with PPy as a result of polymerization of pyrrole monomers. The energy of π-π* transitions of aromatic C=C bonds in GO has changed significantly by the addition of PPy, which is very likely caused by the π-π stacking between PPy and GO [95, 170, 202, 231, 232]. The UV-Vis results provide a good agreement with the FTIR results.

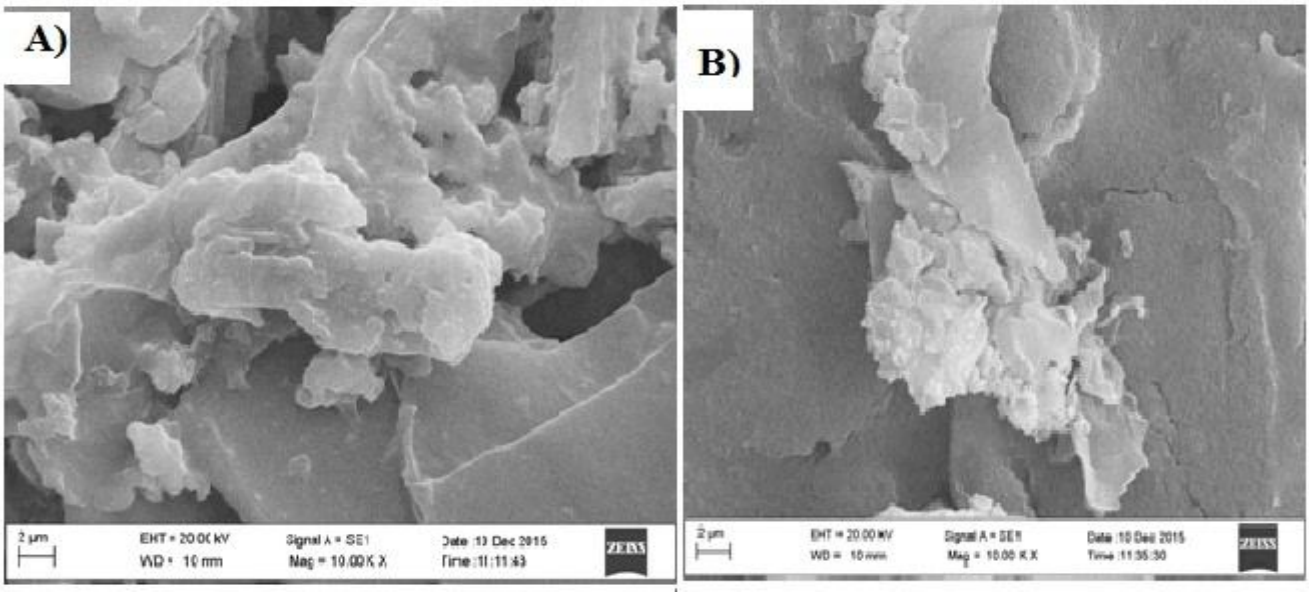

Figure 6.18. SEM images of the GO (A) and GO/PPy (B).

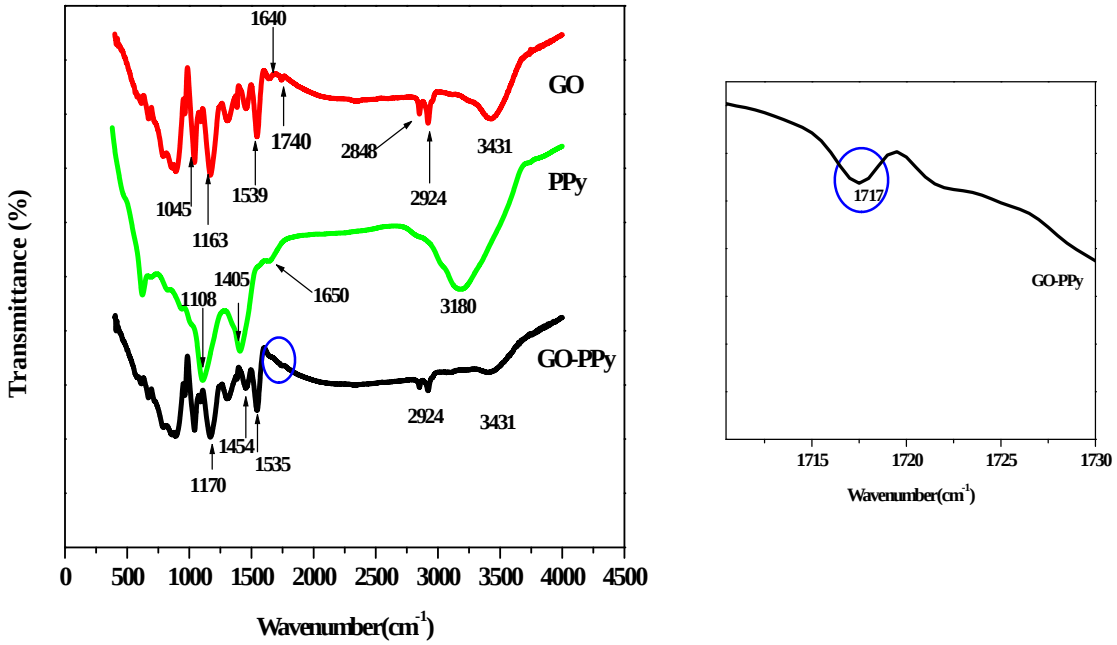

Figure 6.19. FTIR spectra of GO, PPy and GO/PPy.

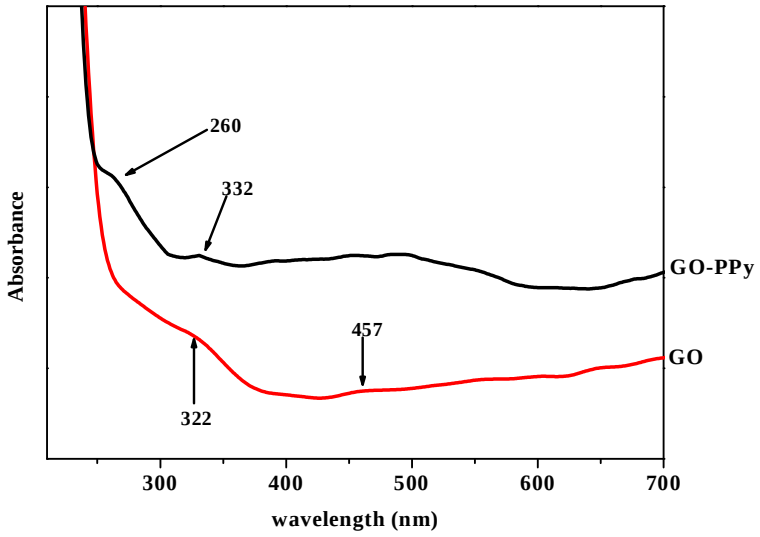

Figure 6.20. UV–Vis spectra of GO, PPy and GO/PPy.

The Raman spectrum of GO (Figure 6.21) shows two characteristic bands at 1335 cm^{-1} (D band) and 1608 cm^{-1} (G band). The D band corresponds to the structural imperfections created by the attachment of oxygenated groups (such as hydroxyl, epoxy, and carboxy) on the carbon basal plane, while the G band is related to the in-plane vibration of sp^2 carbon atoms in a 2D hexagonal lattice. The intensity ratio of the D-and G-bands (I_D/I_G) indicates the degree oxidation and the size of sp^2 ring clusters in a network of sp^3 and sp^2 bonded carbon.

In PPy, the band that appeared at 1585 cm^{-1} is attributed to the C=C backbone stretching of PPy and the band at 1373 cm^{-1} could be due to the ring-stretching mode of PPy. In addition, the bands in the range of 1080 cm^{-1} to 1240 cm^{-1} which are associated to the C–H in-plane deformation of the PPy and the band at 934 cm^{-1} is assigned to the ring deformation associated with dication (bipolaron) and radical cation (polaron) formation. As shown in the Raman spectrum of GO/PPy composite, there are two bands at 1595 cm^{-1} and 1375 cm^{-1} with decrease in intensity compared with the bands for GO, confirming decrease in the disorder due to the increase in size of the in-plane sp^2 domains in the presence of PPy. Furthermore, the intensity ratio of the D and G bands (I_D/I_G) decreased from 1.27 (GO) to 1.08 (GO/PPy), indicating a decrease in the defect sites [96, 97, 233-237].

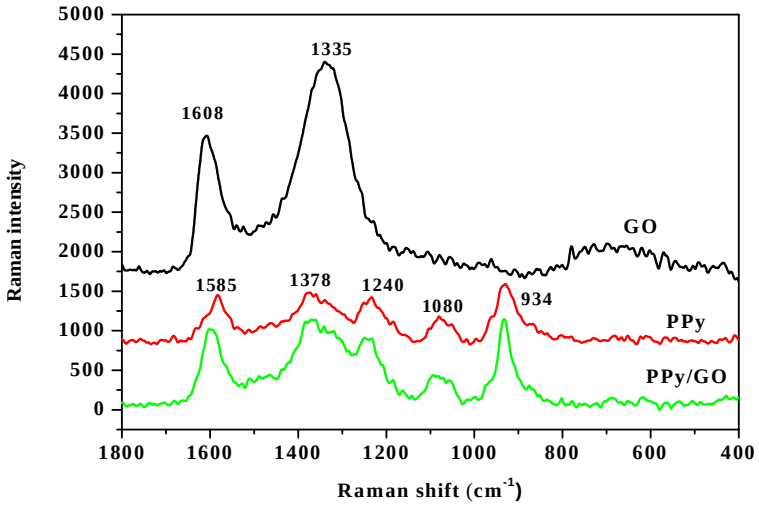

Figure 6.21. Raman spectra of GO, PPy and GO/PPy.

6.2.4. Electrochemical behaviors of phenothrin

To demonstrate the successful prepartaion of GO/PPy/GCE, electrochemical impedance spectroscopy was used to get information on the impedance changes of the electrode interface in the modification process. Electrochemical impedance spectra of phenothrin were analyzed in the frequency range of 1 Hz and $1x10^5$ Hz at GCE, GO/GCE, PPy/GCE and GO/PPy/GCE. From the Nyquist plots (Figure 6.22), R_{ct} values for different electrodes were found to increase in the order: GO/PPy/GCE < PPy/GCE < GO/GCE < GCE. GO/PPy/GCE shows the smallest semicircle at mid-high frequency regions because of its large surface area, high electrical conductivity. This can be accounted by the interaction of oxygen containing functional groups in GO through π-π interaction and H-bonding with polypyrrole, which well improving the contact rate of the composite and electrolyte.

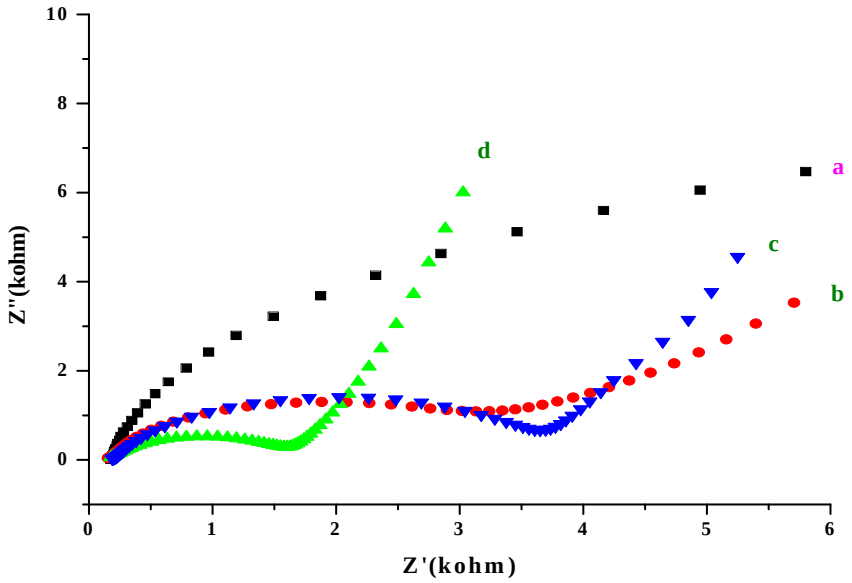

Figure 6.22. Nyquist plots of 0.1 mM phenothrin at GCE (a), PPy/GCE (b), GO/GCE (c) and GO/PPy/GCE (d).

The electrochemical behavior of phenothrin studied using cyclic voltammetry. Figure 6.23 shows typical cyclic voltammograms at GCE (a), GO/GCE (b), PPy/GCE (c) and GO/PPy/GCE (d) for 10 μM phenothrin in PBS (pH 7.0) at a scan rate of 0.1 V s^{-1}. In all the voltammograms, only a

reduction peak was observed without oxidation peak in the reverse direction, indicating the irreversibility of phenothrin reduction at the surface of these electrodes as reported in previous works [225]. The reduction peak of phenothrin at the surface of GCE is weak and broad due to slow transfer of electrons. However, at the modified electrodes the peak current responses are significantly enhanced. Moreover, at GO/PPy/GCE a remarkably sharp peak was observed at about 0.89 V, which showed 1.5-fold increase in current response compared to that at PPy/GCE (curve c), 1.7 fold to that at GO/GCE (curve b) and 3.2-fold at GCE (curve a). The results suggest that the GO/PPy film possess a more pronounced effect on the reduction of phenothrin than at GO or PPy modified electrodes. This can be attributed to the synergistic effect of fast electron transfer rate, large surface area, high electrical conductivity and increased active sites of GO/PPy/GCE. Furthermore, the electroactivity of phenothrin is more feasible due to π-π interactions between Go/PPy film and phenothrin which contribute to peak current enhancement.

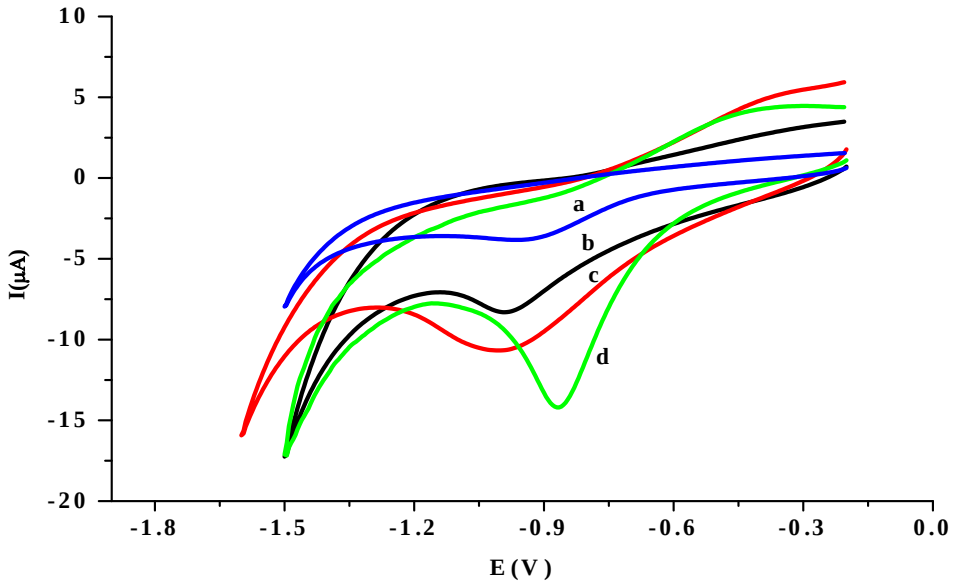

Figure 6.23. Cyclic voltammograms of 10 μM phenothrin in PBS (pH 7.0) at GCE (a), GO/GCE (b), PPy/GCE (c) and GO/PPy/GCE (d) at 0.1 V s^{-1}.

6.2.5. Effects of scan rate and pH

In order to obtain the optimum experimental conditions, parameters such as pH and scan rate that can affect the peak current and peak potential were studied for phenothrin solution at GO/PPy/GCE. The effect of the scan rate on the current response of phenothrin in PBS of pH 7.0 was studied using cyclic voltammetry (Figure 6.24A). With increased scan rate, the cathodic peak current also increased. A good linearity was observed between the peak current and scan rate in the range 0.05-0.12 V s^{-1} (Figure 6.24B), which shows that the reduction of phenothrin at GO/PPy/GCE is an adsorption controlled process. Their linear relationship is described with the regression equation: I(μA) = 150.4υ + 3.43, R^2 = 0.9973.

On the other hand, with increased in the scan rate, the potential shifted to more negative values, which confirms the irreversible behavior of phenothrin reduction. The linear relationship between the peak potential and the logarithm of the scan rate can be expressed using the regression equation: E_{pc}(V) = -0.13log*v* + -1.12, R^2 = 0.9960 (Figure 6.25). According to Laviron theory [238], the peak potential and scan rate can be related by:

$$E_{pc} = E^{o'} + 2.303\left(\frac{RT}{\alpha nF}\right)\log\left(\frac{RTk^{0}}{\alpha nF}\right) - 2.303\left(\frac{RT}{\alpha nF}\right)\log\ v \qquad (26)$$

where α is the transfer coefficient, k^o is the standard heterogeneous rate constant of the reaction, n is the number of electrons transferred, v the scan rate and $E^{o'}$ is the formal redox potential. Other symbols have their usual meanings. After substituting the values of T, R and F in the above equation, the value of αn was calculated to be 0.445. To determine the number of electrons transferred (n), the value of α is calculated using the equation:

$$\alpha = \frac{47.7}{E_p - E_{p/2}} mV \qquad (27)$$

From this, the value of α was found to be 0.23. Thus, the number of electrons transferred in the reduction of phenothrin was calculated to be 1.94 ≈ 2, which indicates two electrons are involved in the reduction of phenothrin as shown in the mechanism (Scheme 7) [225].

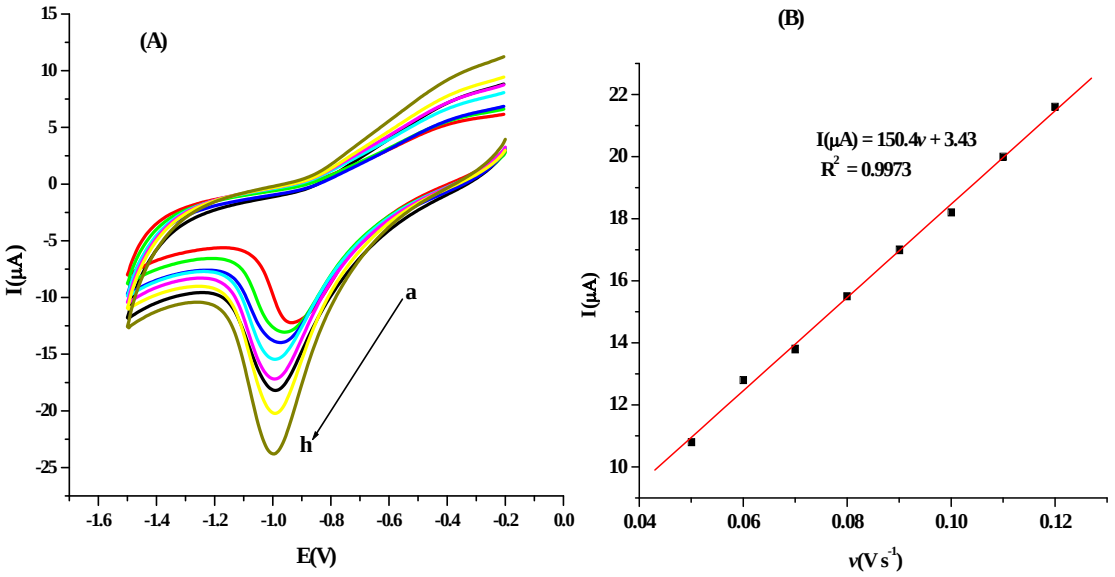

Figure 6.24. Cyclic voltammograms of 10 μM phenothrin in PBS of pH 7.0 at GO/PPy/GCE for various scan rates: (a) 0.05, (b) 0.06, (c) 0.07, (d) 0.08, (e) 0.09, (f) 0.1, (g) 0.11 and (h) 0.12 V s^{-1} (A) and plot of current *vs* scan rate (B).

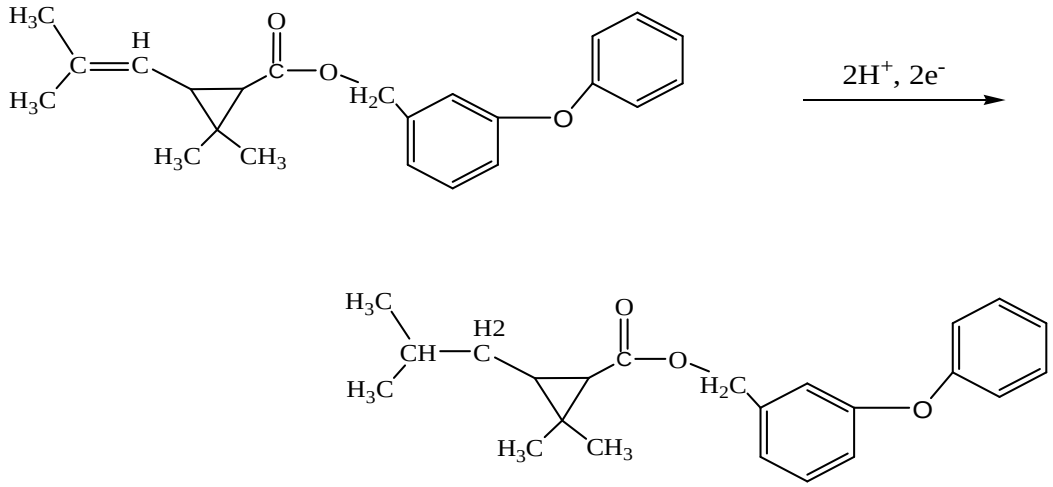

Scheme 7. Mechanism of phenothrin reduction.

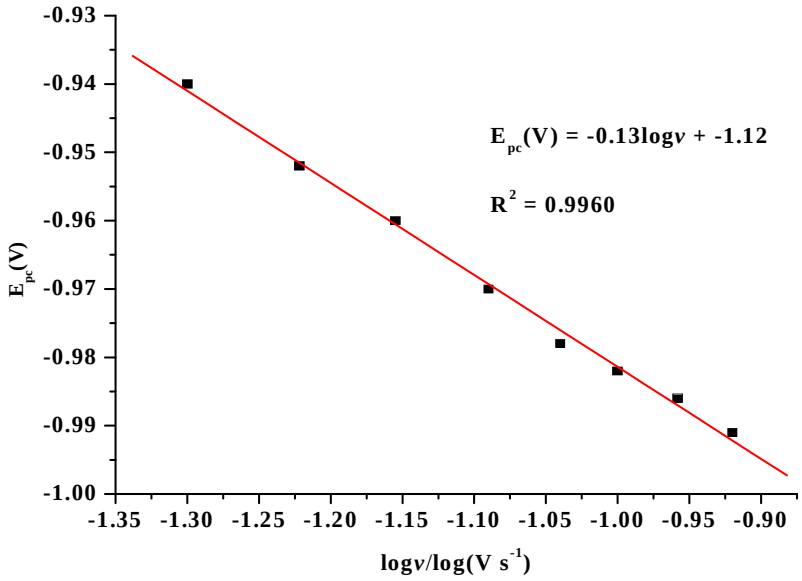

Figure 6.25. Plot of peak potential *vs* logarithm of scan rate for 10 μM phenothrin in PBS of pH 7.0 at GO/PPy/GCE.

The effect of pH on the electrochemical behavior of phenothrin was studied in the range 5.0 to 8.0 in PBS. It was found that the reduction peak current increased with increasing the pH values from 5.0 to 6.5 and then decreased when the pH exceeded 6.5 (Figure 6.26). Thus, pH 6.5 was selected as an optimum working pH for phenothrin determination.

In addition, with increased in pH, the reduction peak potential shifted toward more negative values. The shift in the values of reduction potential indicates the participation of protons in the electrode reaction. A plot of peak potential with pH values was found to be linear over the pH range of 5.0-8.0 with a regression equation of: $E_{pc}(V) = -0.061pH + -0.41$, $R^2 = 0.9950$. The slope -0.061 V/pH, which is close to the theoretical value of -0.059 V/pH, indicates that the same number of protons and electrons are involved in the reduction of phenothrin [225].

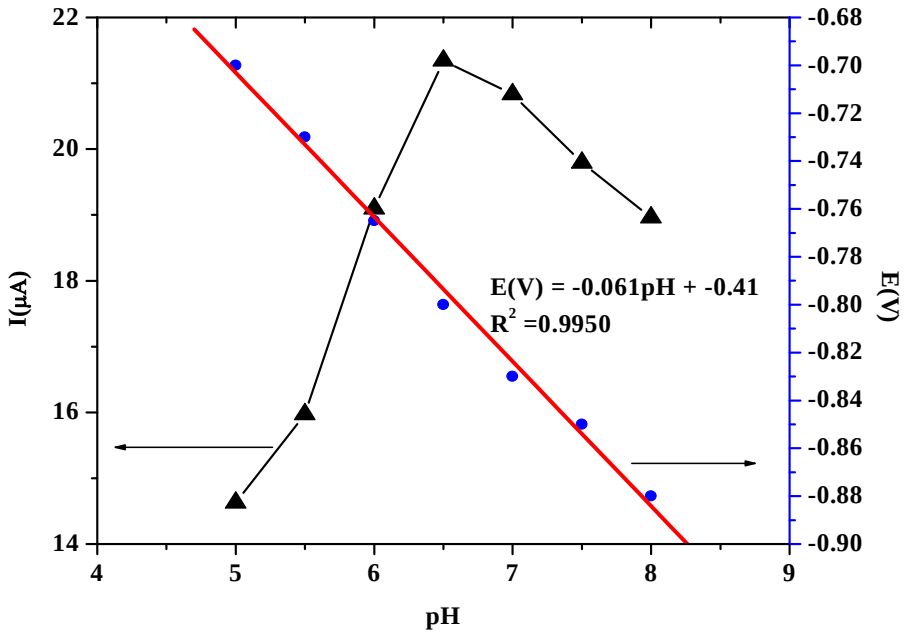

Figure 6.26. Plot of peak current and peak potential for 10 μM phenothrin at GO/PPy/GCE in PBS of varying pH.

6.2.6. Effects of accumulation potential and time

The sensitivity of the sensor is undoubtedly improved by varying accumulation parameters: potential and time. The effect of varying the accumulation potential on the reduction current of phenothrin was studied in the range -0.3 to -1.0 V at an accumulation time of 25 s using SWV. The current response increased up to -0.7 V and decreased after -0.7 V (Figure 6.27A). Therefore, the accumulation potential of -0.7 V was chosen as an optimum potential for further measurements.

The effect of accumulation time on the reduction peak current for 10 μM phenothrin was also investigated in the range 20–90 s by SWV, and the results are illustrated in Figure 6.27B. The peak current increased with increasing accumulation time in the range 20–60 s and then a current

plateau was observed as a result of surface saturation. Therefore, 60 s was chosen as the optimal accumulation time for the determination of phenothrin.

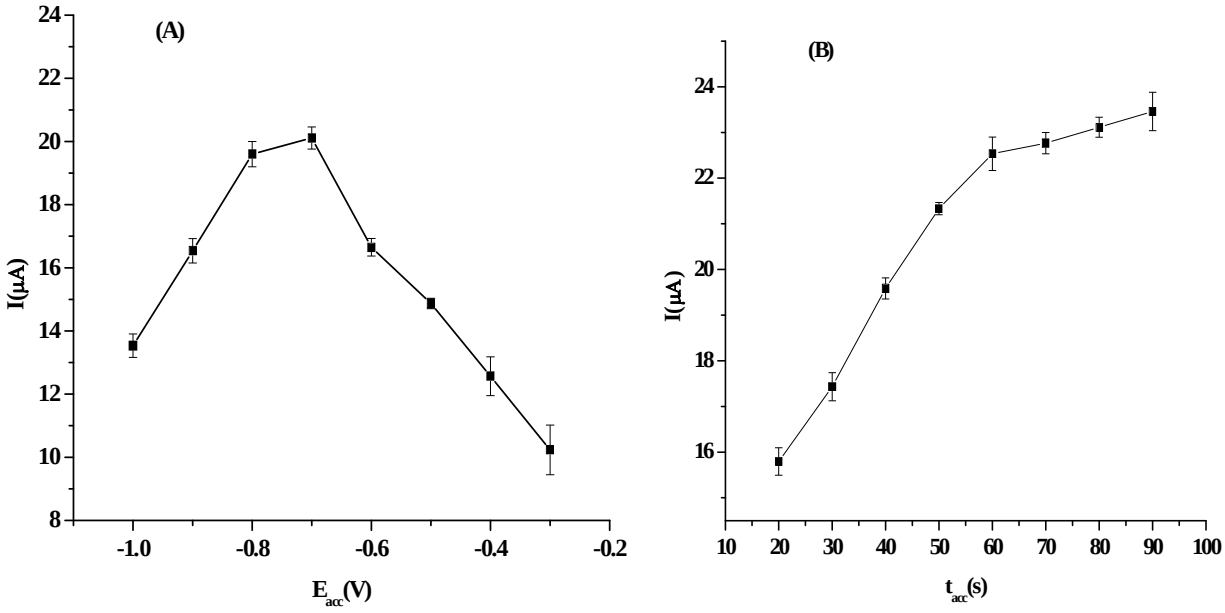

Figure 6.27. Effects of accumulation potential (A) and accumulation time (B) on the peak current of 10 μM phenothrin in PBS (pH 6.5).

6.2.7. Calibration curve

In order to validate the method for quantitative determination of phenothrin, the variation of the peak current with concentration of phenothrin in PBS (pH 6.5) was studied using SWV. As can be seen in Figure 6.28, the peak current increased linearly with phenothrin concentrations in the range 0.025 μM to 20 μM. The linear equation is: I(μA) = -1.21C(μM) + -5.86, R^2 = 0.9971. A detection limit of 0.0138 μM (S/N = 3) was obtained.

The performance of the GO/PPy/GCE was compared with the one reported based on hanging mercury drop electrode (HMDE). The result demonstrated that the detection limit of the sensor is better than the detection limit (0.019 μM) obtained at HMDE [225].

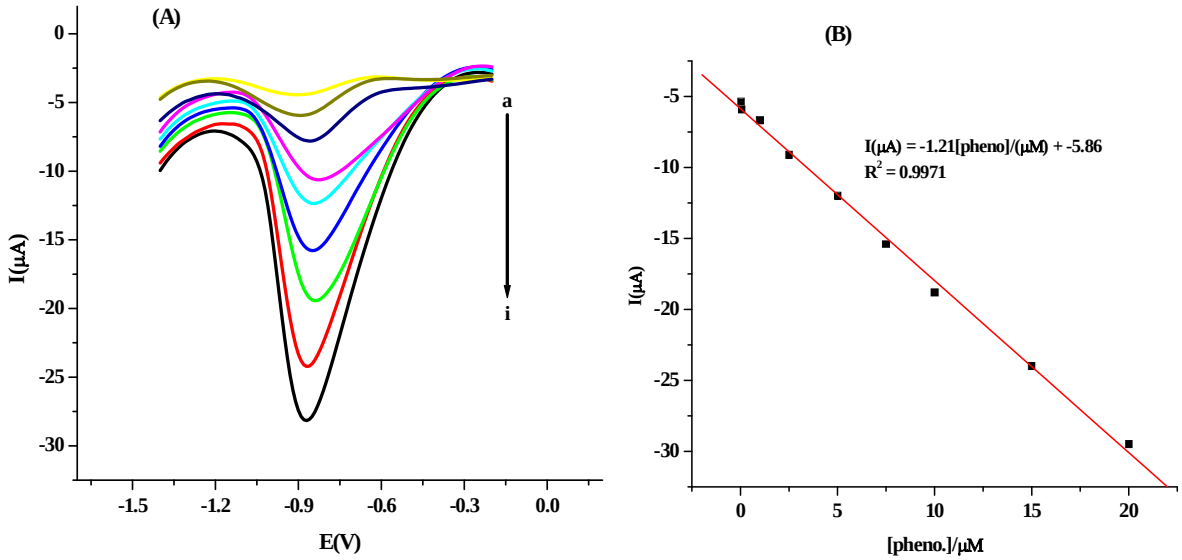

Figure 6.28. Square wave voltammograms of various concentrations of phenothrin (0.025, 0.05, 1.0, 2.5, 5.0, 7.5, 10, 15 and 20 μM in PBS pH 6.5) at GO/PPy/GCE (A) and the calibration plot of phenothrin at GO/PPy/GCE (B).

6.2.8. Repeatability, reproducibility and stability

The repeatability of the GO/PPy/GCE was studied using the same electrode for six consecutive determinations for 10 μM phenothrin and a relative standard deviation (RSD) of 4.28% was obtained. This indicates that the sensor has good repeatability. The reproducibility of GO/PPy/GCE electrodes was also evaluated with three different electrodes prepared in the same experimental procedure. The RSD was found to be 5.1%, demonstrating an excellent detecting reproducibility.

The stability of the sensor was also tested by keeping the electrode in 0.1 M PBS (pH 6.5) in a refrigerator at 5^{o}C. For 10 μM phenothrin solution, the current response of the electrode was found to decrease by 5.6% of its initial value after 7 days of storage. This indicates that the electrode has good stability.

6.2.9. Interference study

Selectivity of the sensor plays an important role in the determination of analyte in various samples. Investigation was made on species which may affect the signal for phenothrin in fruit samples. The interferents studied were ascorbic acid, citric acid, dichlorvos, phoxim and urea. The results indicated that the presence of 100–fold excess of ascorbic acid, citric acid and urea did not affect the determination of phenothrin (Table 6.5). Besides, a 10-fold concentration of the two pesticides (dichlorvos, phoxim) showed no interference effect. Thus, these results reveal that GO/PPy/GCE had a good selectivity for phenothrin.

Table 6.5. Influence of interfering substances on the voltammetric response for 10 μM phenothrin in PBS pH 6.5.

Interferences	Concentration ratio ([Interference]/[pheno.])	Signal change (%)
Ascorbic acid	100	-1.5
Citric acid	100	+3.4
Dichlorvos	10	+4.3
Phoxim	10	-5.7
Urea	100	+1.7

6.2.10. Application

To investigate the practical applicability of the developed method, the determination of phenothrin was carried out in commercial juice samples. The samples were prepared according to the procedure described in section 5.4.2. The voltammetric measurements were carried out in apple, grape and orange juices in PBS pH 6.5. The results did not show any electrochemical

response at the peak potential where phenothrin was reduced. This indicates that phenothrine was not available in all the juice samples.

Recovery experiments were performed by spiking the juice (apple, grape and orange) samples with three different concentrations of phenothrin. The results are summarized in Table 6.6. The recoveries of the spiked samples were in the range 90.0% to 105.0%. It proved that the sensor could be successfully applied for the detection of phenothrin in real samples.

Table 6.6. Recovery study of phenothrin in juice samples (n= 3).

Samples	Added (μM)	Found/μM (±sd)	Recovery (%)
Apple juice	2.5	2.45 (0.08)	98.0
	5.0	4.5 (0.25)	90.0
	10.0	10.3 (0.16)	103.0
Grape Juice	2.5	2.56 (0.23)	102.4
	5.0	4.83 (0.42)	96.6
	10.0	10.2 (0.52)	102.0
Orange Juice	2.5	2.46 (0.07)	98.4
	5.0	4.74 (0.3)	94.8
	10.0	10.5 (0.46)	105.0

6.3. Determination fenitrothion at multiwalled carbon nanotubes modified glassy carbon electrode

6.3.1. Background

Fenitrothion (o,o-dimethyl o-4-nitro-m-tolyl phosphorothionate) is a contact and non-persistent organophosphrous pesticide (Figure 6.29), which is used in agriculture, horticulture, forestry and public health against chewing and sucking insects on cereals, cotton, orchard fruits, rice, vegetables and forests [239-241].

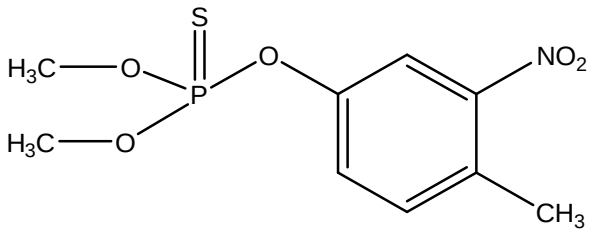

Figure 6.29. Structure of fenitrothion

With the introduction of OPs to the market in the 1970s and increasing concerns on health and their potential environmental impact, many analytical methods such as soxhlet extraction followed by gas chromatography [242], paper bio-chromatographic method [243], spectrophotometric [244], solid-phase extraction and solid-phase microextraction followed by gas chromatography and gas chromatography/mass spectroscopic methods [245-247] and high performance liquid chromatography [242, 248, 249] were developed to detect these compounds. However, these methods require complex separation and sample pretreatment processes, expensive equipments and toxic solvents, trained personnel and time consuming. Due to their high sensitivity, good stability and cost-effectiveness, electrochemical methods are more advantageous [250].

Glassy carbon electrodes (GCE) were used extensively in electrochemistry and often as the base for surface modified electrodes [251]. However, due to low sensitivity and reproducibility, slow electron transfer reaction, low stability over a wide range of solution composition and high

overpotential, GCE has limited electrochemical applications. Modification of the electrode surfaces helps to enhance the sensitivity and selectivity of electrochemical sensors and prevents surface fouling. Different materials were used for modification of these electrode surfaces, such as carbon nanotubes, metal oxides, conductive polymers, and inorganic catalysts [252-254].

Hanging mercury drop electrode [239, 255], static mercury drop electrode [256] and activated glassy carbon electrode [257] were commonly used for detecting fenitrothion. Recently, few modified electrodes have been reported for the electrochemical detection of fenitrothion, like polyaniline modified glassy carbon electrode [241], nano-TiO_2 modified glassy carbon electrode [258] and poly(AHNSA) modified glassy carbon electrode [106].

Due to their extraordinary properties, CNTs have been widely utilized in the electrochemical detection. However, the poor solubility and dispersity of CNTs in conventional solvents has restricted their use as an active layers processed by simple methods like spin coating. Acid-treatment as well as other modifications has been shown to assist in overcoming the disadvantage of poor dispersity of CNTs [124, 259-263]. In this study, the fabrication MWCNTs/GCE for the determination of fenitrothion is described. The application of the method for the determination of fenitrothion in real samples, soil and teff is also demonstrated.

6.3.2. Electrochemical characterization of MWCNTs/GCE

The electrochemical behaviors of MWCNTs/GCE were investigated using cyclic voltammetry using 0.1 mM potassium ferrocyanide in the presence of 0.1 M KCl. The electrochemical response of 0.1 mM $K_4[Fe(CN)_6]$ at MWCNTs/GCE exhibits a reversible reaction. Both the anodic and cathodic peak currents at the modified electrode show three-fold increase compared to the GCE. The enhancement of the peak current demonstrates the modification of GCE by MWCNTs.

Under the same experimental conditions, the surface active area of GCE and MWCNTs/GCE in $K_4[Fe(CN)_6]$ solution was estimated in the scan rate range 0.04 and 0.2 V s^{-1} using the Randles-Sevcik equation (eqn. 3). The slope of i_p *vs* $v^{1/2}$ was found to be 15.6×10^{-6} $A(V\ s^{-1})^{-1/2}$ and the

electrochemical active surface area of the MWCNTs/GCE was calculated to be 0.232 cm^2, which is about five times higher than the GCE (0·047 cm^2). The significant increase in the surface active area suggests that the GCE was modified and is useful for electrochemical sensing.

6.3.3. Electrochemical behavior of fenitrothion

The electrochemical behavior of fenitrothion at GCE and MWCNTs/GCE was examined in the potential range -0.9 V to 0.5 V at a scan rate of 0.1 V s^{-1}. Fenitrothion exhibits an oxidation peak at -0.083 V (O1) and two reduction peaks at -0.121 V (R1) and at -0.671 V (R1) and with remarkable peak increment at MWCNTs/GCE compared to the GCE (Figure 6.30). The increased currents as well as the potential shifts of the anodic peak to more negative and reduction peaks to more positive potentials demonstrates the catalytic behavior of MWCNTs/GCE towards fenitrothion. This behavior can be attributed to the presence of larger active surface area on MWCNTs to trap fenitrothion [73].

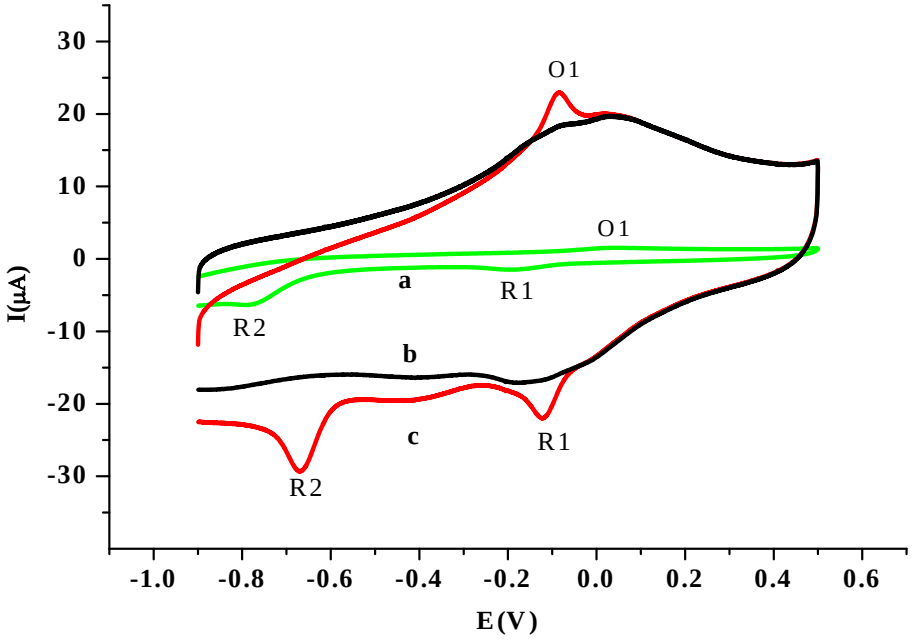

Figure 6.30. Cyclic voltammograms of 40 μM fenitrothion solution at GCE (a), 0.1 M PBS (pH 7.0) at MWCNTs/GCE (b) and 40 μM fenitrothion solution at MWCNTs/GCE (c). Scan rate: 0.1 V s^{-1}.

6.3.4. Effect of varying the amount of MWCNTs on fenitrothion determination

The quantity of MWCNTs needed to modify GCE was optimized in order to obtain a better electrochemical response. Figure 6.31 shows the effect of various volumes of MWCNTs coated on the surface of GCE towards the responses for fenitrothion. The reduction peak current increased as the volume of MWCNTs suspension was increased until it reached the maximum value of 10 μL. Then, the reduction peak current was nearly constant when the amount of MWCNTs exceeded 10 μL. Therefore, 10 μL of MWCNTs suspension was used to modify the surface of glassy carbon electrode in this study.

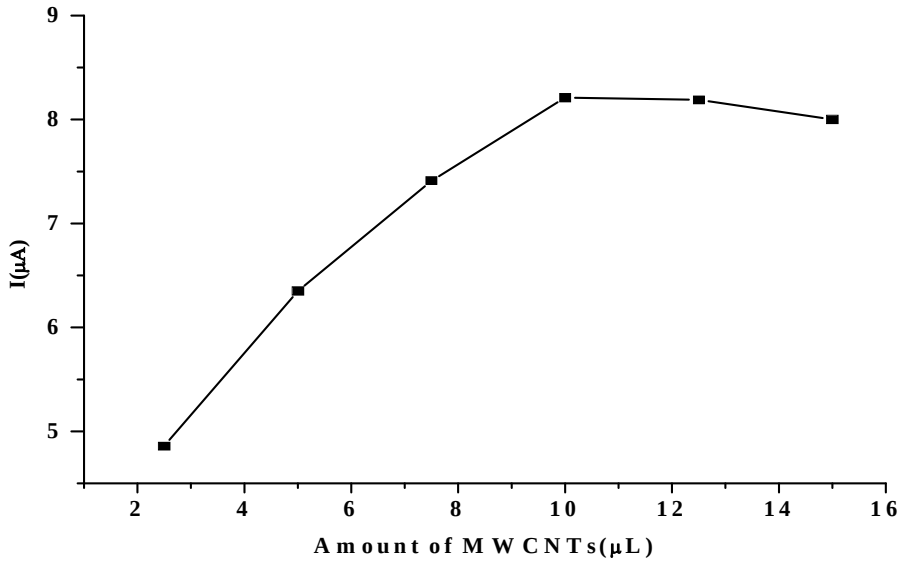

Figure 6.31. Effect of amount MWCNTs on the reduction peak current of 40 μM fenitrothion in 0.1 M PBS pH 7.0 at 0.1 V s^{-1}.

6.3.5. Effect of pH

The effect of solution pH on the reduction peak current and the peak potential of fenitrothion were investigated using cyclic voltammetry in PBS in the pH range 5–7.5. The peak current increased with the pH value until it attained the maximum value at pH 6.0 and then decreased with further increase in the pH value (Figure 6.32A). The reduction peak potential was also

affected by the solution pH and it shifted negatively with increasing pH values (Figure 6.32B). The peak potential showed a linear relationship with solution pH with a regression equation: $E_{pc}(V) = 0.040\ pH + -0.399$ ($R^2 = 0.9997$), indicating that the reduction of fenitrothion occurs by transfer of protons. Therefore, pH 6.0 was selected as the optimum pH.

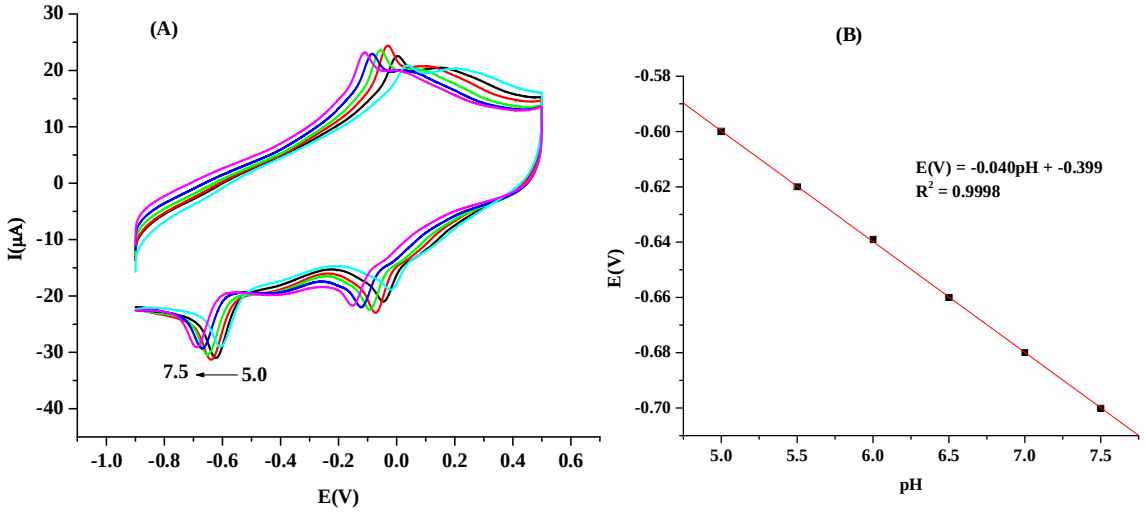

Figure 6.32. Cyclic voltammograms for 40 μM fenitrothion in 0.1 M PBS at various pH (A) and plots of peak current and peak potential *vs* pH for 40 μM fenitrothion at MWCNTs/GCE (B).

6.3.6. Effect of scan rate

The effect of scan rate on the reduction peak current of 40 μM fenitrothion at MWCNTs/GCE was studied within the range 0.04 V s^{-1} to 0.225 V s^{-1}. The reduction peak current increased linearly with increased the scan rate (Figure 6.33), with the linear equation: $I_{pc}(\mu A) = 0.118\nu + 15.91$, $R^2 = 0.9966$. This result indicates the electrochemical reaction of fenitrothion at MWCNTs/GCE exhibits an adsorption-controlled process. The reduction peak potential also shows dependence on the scan rate. The peak potential shifted to more negative values on increasing the scan rate, which further confirms the irreversibility of the reduction of fenitrothion at -0.671 V (R2).

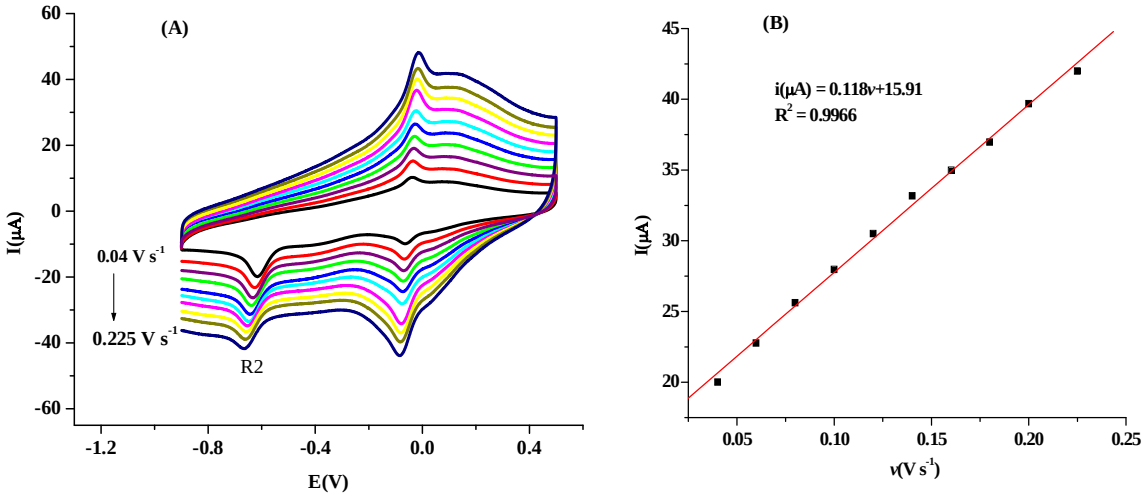

Figure 6.33. Cyclic voltammograms (A) for 40 μM fenitrothion in 0.1 M PBS (pH 6.0) at MWCNTs/GCE at various scan rates (0.04, 0.06, 0.08, 0.1, 0.12, 0.14, 0.16, 0.18, 0.2 and 0.225 V s^{-1}) and plot of reduction peak current *vs* scan rate (B).

6.3.7. Effects of accumulation potential and time

The effect of accumulation potential for the reduction current of 40 μM fenitrothion at MWCNTs/GCE was examined in the range -0.1 to -0.55 V at an accumulation time of 40 s. The results showed that the reduction peak current increased as the accumulation potential changed from -0.1 to -0.4 Vs and then the accumulation potential was further decreased (Figure 6.34A). Thus, an accumulation potential of -0.4 V was used in subsequent studies.

The effect of accumulation time on the reduction peak current for fenitrothion was also examined. The peak current increased as the accumulation time increased up to 80 s and then no significant change was observed after this time (Figure 6.34B), indicating that the accumulation of fenitrothion at MWCNTs/GCE nearly reached saturation at 80 s. Therefore, the optimum accumulation time selected for the measurement was 80 s.

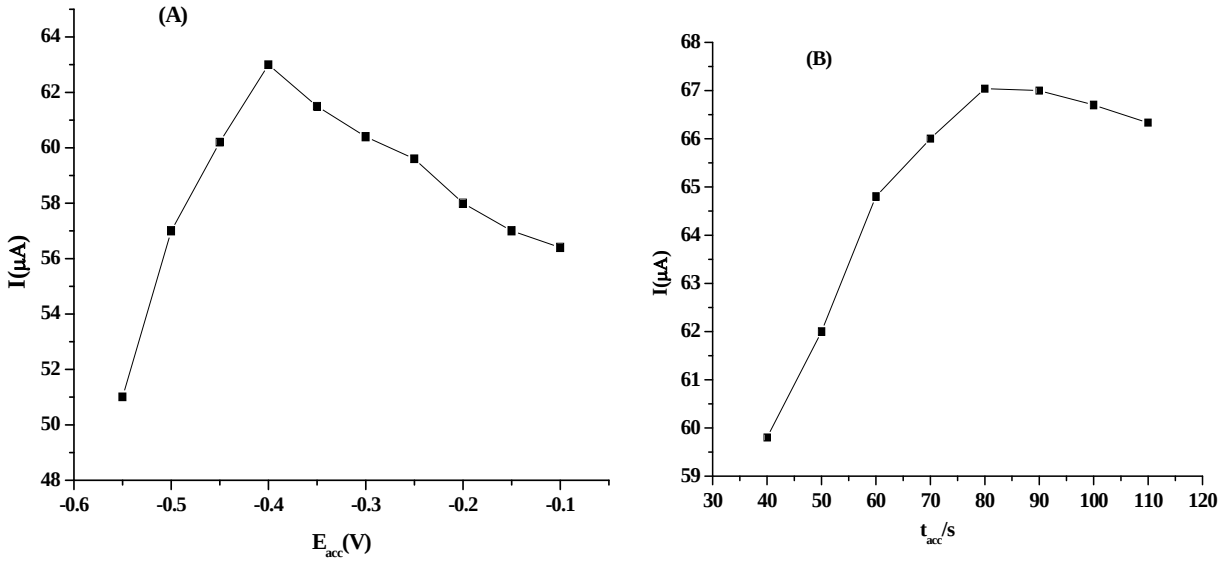

Figure 6.34. Effects of accumulation potential (A) and accumulation time (B) on the peak current for 40 μM fenitrothion in 0.1 M PBS of pH 6.0 at MWCNTs/GCE.

6.3.8. Effect of square wave parameters

The effect of step potential on the reduction current of fenitrothion was studied over the range 0.002 V–0.020 V by fixing the amplitude and frequency at 0.050 V and 15 Hz, respectively. The peak current increased significantly up to 0.01 V with the best shape for the peak. The influence of amplitude on the reduction current of 40 μM fenitrothion was also investigated in the range 0.020–0.110 V, the peak current was found to increase with increasing amplitude and reached maximum at 0.09 V and then decreased. Thus, 0.09 V was fixed as the working amplitude in the detection of fenitrothion. In addition, the influence of square wave frequency on the peak current was also evaluated at the optimized step potential and amplitude. The frequency was varied in the range between 5 and 30 Hz, the peak currents reached maximum at 20 Hz and gradually decreased thereafter. Hence, for further electrochemical investigation, a step potential of 0.01 V, amplitude of 0.09 V and 20 Hz frequency were selected as the optimal values.

6.3.9. Calibration curve

A calibration curve was constructed under the optimum conditions to demonstrate the relationship between the square wave voltammetry peak current and the concentration of fenitrothion. Figure 6.35 shows the peak current increases with increasing fenitrothion concentration in the range 0.01 µM–5.0 µM at the MWCNTs/GCE. The linear regression equation is: $I_p(\mu A) = -7.20C(\mu M) + -0.762$ and $R^2 = 0.9975$. The sensitivity of MWCNTs/GCE was 7.2 (µA/µM) and the detection limit was obtained as 0.0064 µM based on signal-to-noise ratio of 3.

The performances of the modified electrode were compared with those previously reported in the literatures and presented in Table 6.7. The results obtained in this work show a detection limit lower than or comparable with the results reported for other electrodes for the determination of fenitrothion.

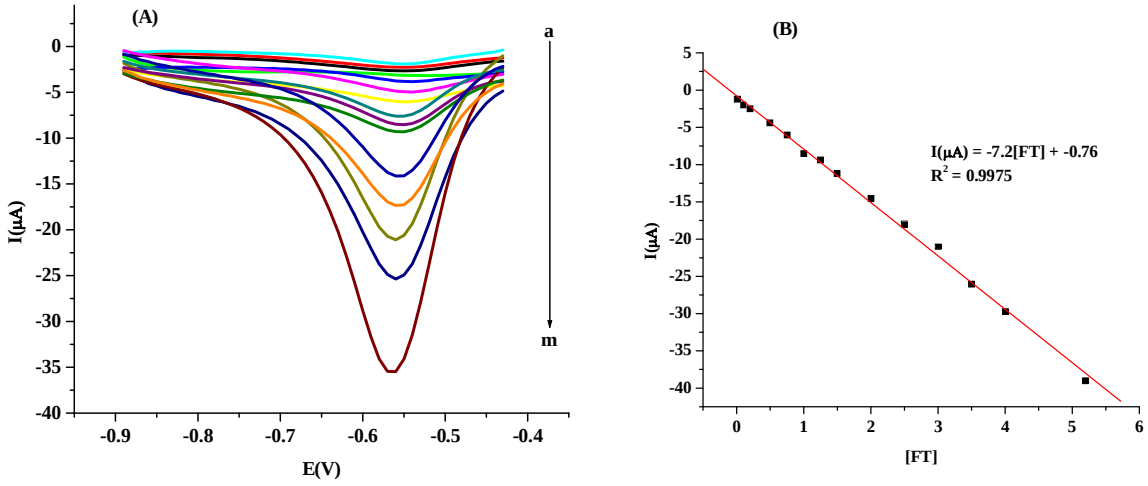

Figure 6.35. Square wave voltammograms of fenitrothion (a) 0.01 µM, (b) 0.2 µM, (c) 0.5 µM, (d) 0.75 µM, (e) 1.0 µM, (f) 1.25 µM, (g) 1.5 µM, (h) 2.0 µM, (i) 2.5 µM, (j) 3.0 µM, (k) 3.5 µM, (l) 4.0 µM and (m) 5.0 µM (A) and calibration plot of peak current *vs* concentrations of fenitrothion at MWCNTs/GCE (B).

Table 6.7. Comparison of analytical parameters for the reduction of fenitrothion at MWCNTs/GCE and other electrodes.

Electrode	Modifier	Linear Range (μM)	Detection limit (μM)	References
GCE	Poly(AHNSA)	0.001-6.6	0.0008	[106]
HMDE	-	0.093-0.89	0.0052	[239]
GCE	polyaniline	0.01-100	0.0072	[241
HMDE		0.01-1.0	0.00013	[242]
STMDE	-	0.01-6.2	0.01	[256]
GCE	activated	0.4-50	0.078	[257]
GCE	Nano-TiO_2	0.025-10	0.01	[258]
GCE	MWCNTs	0.01-5.0	0.0064	This work

6.3.10. Repeatability, reproducibilty and stability

The repeatability of the MWCNTs/GCE was evaluated with replicate measurements of the current for 40 μM fenitrothion solution under the optimized conditions and the relative standard deviation (RSD) was found to be 2.88% (n=10), indicating a good repeatability of the responses at the MWCNTs/GCE. The reproducibility of the sensor was also studied by measuring the current for 40 μM fenitrothion for three similarily prepared electrodes under the same experimental conditions, and the RSD of the responses of the modified electrodes was 4.5%, which demonstrates a good reproducibility.

Furthermore, the stability of the electrode was evaluated by measuring the current responses for 40 μM fenitrothion by keeping the electrodes in phosphate buffer solution (pH 6.0) over a period

of 10 days. The electrochemical responses indicated that the current responses decreased only by 7.2% compared to the initial response, which shows the long-term stability of MWCNTs/GCE.

6.3.11. Interference study

The effects of interfering substances on the determination of fenitrothion were investigated at the MWCNTs/GCE by adding various species to 2 μM fenitrothion in pH 6.0 PBS. The experimental results show that the voltammetric determination of fenitrothion was not affected in the presence of 1000-fold excess concentration of Na^+, Co^{2+}, ascorbic acid and phenol as presented in Table 6.8. Moreover, 100-fold increment in the concentrations of 4-aminophenol, 10-fold of nitrobenzene and 1:1 ratio of 4-nitrophenol had no influence on the current response of fenitrothion (signal change below 5%). NO_2-group containing interfrents exhibit a strong tendency to interfere with fenitrothion at higher concentrations. In general, the results reveal that MWCNTs/GCE electrode exhibited a good selectivity towards the determination of fenitrothion.

Table 6.8. Effect of interferents on detection of fenitrothion at MWCNTs/GCE.

Interferent	[interferent]/(μM)	Current response (%)[a]
Na^+	2000	99.2
Co^{2+}	2000	97.7
Ascorbic acid	2000	98.7
4-aminophenol	200	94.6
4-nitrophenol	2	95.3
Nitrobenzene	20	95.5
Phenol	2000	97.6

[a] average of tiplicate determinations

6.3.12. Application

The practical applicability of the MWCNTs/GCE was evaluated by applying it in the determination of fenitrothion in soil and teff samples collected from Alamata Woreda. The procedure for the fenitrothion analysis was followed as described in the procedured section (5.4.3). Voltammetric peaks corresponding to fenitrothion were not observed in analyzing the samples. Thus, in recovery tests, the standard addition approaches was adopted to estimate the reliability. Different amounts of fenitrothion were spiked into the soil and teff samples, and adjusted to a certain concentration. The results obtained are summarized in Table 6.9. The recoveries of soil samples were in the range 88% to 93.3% and for teff were in the range 86.7% to 91.4%. These results indicate that the sensor can effectively used for the determination of fenitrothion in soil and teff samples.

Table 6.9. Recovery study of fenitrothion in soil and teff samples (n = 3) at the MWCNTs/GCE.

Samples	Added (μM)	Found (μM)[a]	Recovery (±sd) (%)
Soil	2.5	2.2	88.0 (2.3)
	3.0	2.8	93.3(3.1)
	3.5	3.1	88.6(1.3)
Teff	2.0	1.8	90.0(1.8)
	3.0	2.6	86.7(2.5)
	3.5	3.2	91.4(1.5)

[a] average of tiplicate determinations

6.4. Voltammetric determination of endosulfan in vegetable samples using mercury film modified glassy carbon electrode

6.4.1. Background

Organochlorines pesticides (OCPs) are characterized by low polarity, low solubility in aqueous media and high affinity to accumulate in fatty tissues (lipophilicity). As a result, they are highly persistent and resistant to biodegradation and may lead to chronic toxicity in animals and humans when taken in to the body [264-267]. Since OCPs are more pollutant than other types of pesticides and most of them have been banned or restricted for some applications [268-270].

Endosulfan, (6,7,8,9,10,10-hexachloro-1,5,5a,6,9,9a-hexahydro-6,9-methano-2,4,3-benzodio xthiepine-3-oxide) is a broad spectrum insecticide, which is available as a mixture of two stereoisomers: alpha and beta in the ratio of 7:3 in a pure form. It is effective in killing insects on cereals, coffee berry, cotton, oil seeds and vegetables. It is harmful for both humans and animals and mainly affects the central nervous system, kidney, liver and testicules in animals, and the central nervous system and respiratory systems of humans [271, 272]. In addition, it persists in the soil and water from six to nine months. Therefore, it is necessary to develop a convenient, sensitive and reliable method for the determination of endosulfan in environmental samples.

In recent years, many research reports have presented the use of various analytical methods for the determination of endosulfan. Gas chromatography [273, 274], liquid chromatography [275], high-performance liquid chromatography [276], gas chromatography/mass spectrometry [277–285] and spectrophotometry [286–288] for the determination of endosulfan have been described. Compared with the above methods for endosulfan determination, electrochemical methods have attracted wide attention due to their convenience, higher sensitivity and selectivity and improved detection limits [264, 289].

So far, few studies have been reported in the literature for the electrochemical determination of endosulfan at the surface of various electrodes. Electrochemically endosulfan was determined using C18-modified carbon-paste electrode [271], glassy carbon electrode [290], 5,10,15,20-

tetraphenylporphyrinatoiron(III) chloride-modified glassy carbon electrodes [291], polypyrrole coated glassy carbon electrode [292] and sodium montmorillonite clay modified glassy carbon electrode [293]. Recently, Ribeiro *et al*. employed a hanging mercury drop electrode for detection of endosulfan in sugar cane, tomato and natural water samples [294].

In this study we report voltammetric methods based on mercury film modified glassy carbon electrode for the determination of endosulfan in vegetable samples.

6.4.2. Electrochemical behavior of endosulfan at MF/GCE

Figure 6.36 shows the cyclic voltammograms of 50 μM endosulfan at GCE and MF/GCE at scan rate of 0.1 V s^{-1} in the potential range -0.4 V to -1.5 V. The cyclic voltammetric curve at the GCE (curve a) shows no obvious electrochemical responses for endosulfan, indicating that either endosulfan exhibits a poor electrochemical response at the bare glassy carbon electrode or the reduction of endosulfan occurs beyond the potential window of glassy carbon electrode. Under identical conditions, a reduction peak current of about -18.5 μA at a peak potential of -1.25 V (curve b) with out any oxidation peak in the reverse scan was observed at the MF/GCE, indicating an irreversible behavior for the electrode reaction of endosulfan.

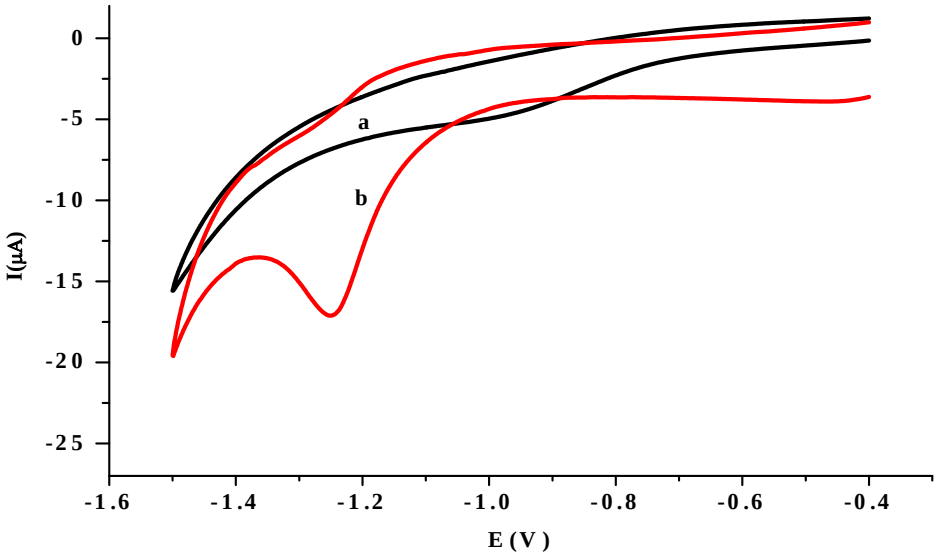

Figure 6.36. Cyclic voltammograms of 50 μM endosulfan at GCE (a) and MF/GCE (b) in BRB pH 7.0 at scan rate of 0.1 V s^{-1}.

6.4.3. Effect of pH

The effect of solution pH on the peak current and peak potential for the reduction of endosulfan at the surface of the modified electrode was investigated in Britton-Robinson buffer (BRB) using cyclic voltammetry at a scan rate 0.1 V s^{-1}. The reduction peak current increased with increasing solution pH up to 5.0, and then decreased gradually with increasing pH value (Figure 6.37A). Thus, pH 5.0 was taken as the optimum pH value for subsequent investigations.

Furthermore, the effect of pH on the reduction peak potential was also examined. It was found that the peak potential shifted to more negative values with increasing pH, showing that protons were taking part in the electrode reactions (Figure 6.37B). The peak potential and pH showed a linear relationship with a regression equation: $E_{pc}(V) = -0.027pH + -1.11$, $R^2 = 0.9956$. The slope -0.027 V/pH indicates that the number of electrons involved at the surface of MF/GCE were twice the number of protons. This is consistent with the mechanism (Scheme 8) reported by Ribeiro *et al.* [294].

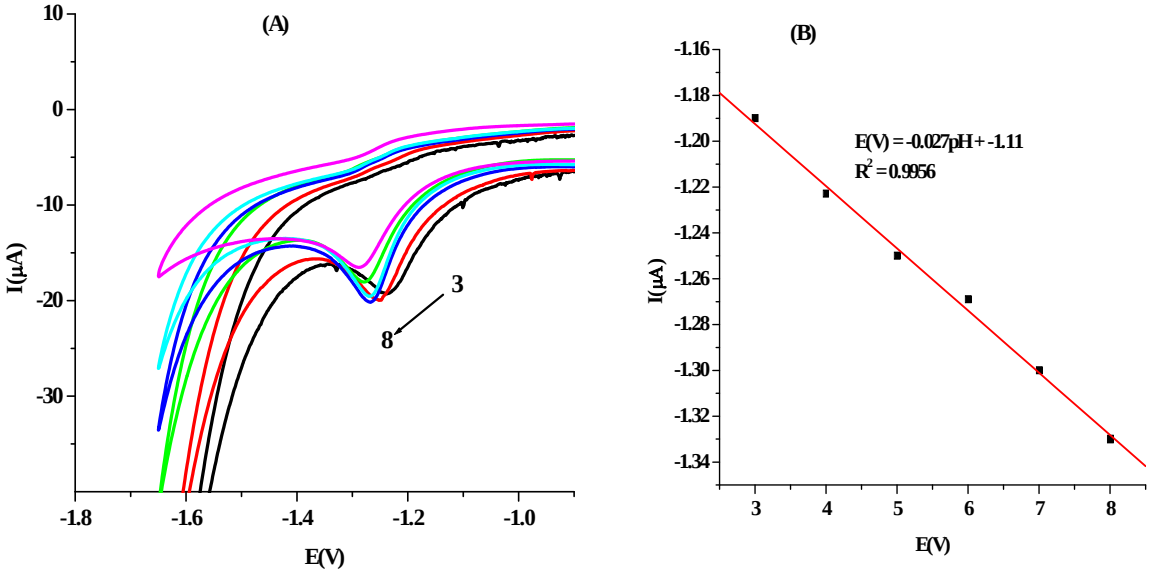

Figure 6.37. Cyclic voltammograms of 50 μM endosulfan at MF/GCE in various pH values of BRB (A) and plots of the peak current and potential *vs* pH of BRB (B).

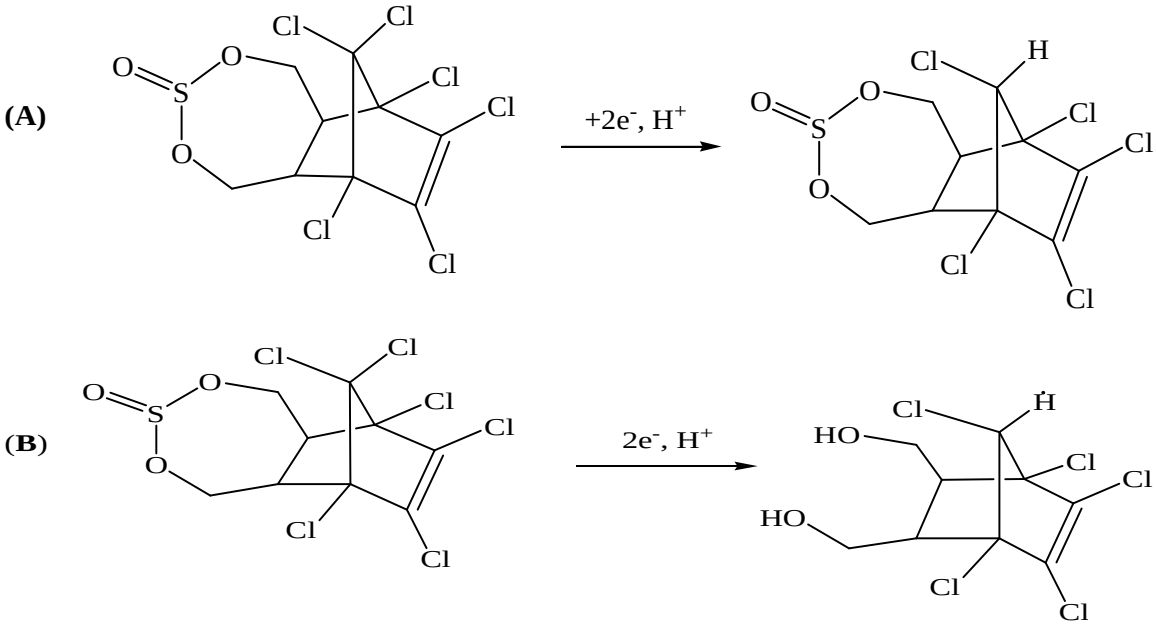

Scheme 8. Mechanism of endosulfan reduction in acidic (A) and basic solution (B).

6.4.4. Effect of scan rate

The effect of scan rate on the reduction current of endosulfan at MF/GCE was investigated in the potential scan range 0.05 V s^{-1} to 0.3 V s^{-1} using cyclic voltammetry. The peak current increased with increasing scan rate at MF/GCE (Figure 6.38). It is related linearly with the scan rate with a regression equation: I(μA) = 43.54*v* + 7.89, R^2 = 0.9976. This suggests that the reduction of endosulfan at MF/GCE is an adsorption-controlled process. Furthermore, the reduction peak potential also shifted to more negative values as the scan rate increased, which indicates that the reduction of endosulfan at MF/GCE is an irreversible process. According to Laviron's (eqn. 26), the linear relationship between the peak potential and logarithm of the scan rate is expressed with regression equation: E_{pc}(V) = -0.02log*v* + -1.31, R^2 = 0.9950. From the slope of Figure 6.39, the value of αn was calculated to be 2.95. Based on eqn. 27, the value of electron transfer coefficient (α) was calculated as about 1.35. So the electron transfer number (n) was found to be 2.1(≈ 2), suggesting that the electrocatalytic reduction of endosulfan at ME/GCE is a two-electron transfer mechanism (Scheme 8). As mentioned in section 6.4.3, the number of electrons involved in the reduction of endosulfan was twice the number of protons, therefore the electrochemical reduction of endosulfan at MF/GCE is a two electron and one-proton process.

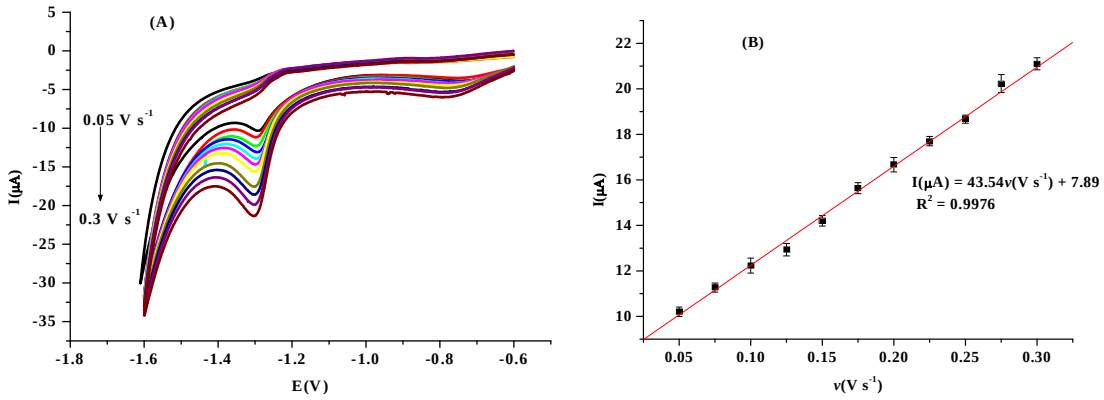

Figure 6.38. Cyclic voltammograms of 50 μM endosulfan in BRB solution (pH 5.0) at MF/GCE with increasing scan rates (0.05-0.3 V s^{-1}) (A) and plot of peak current *vs* scan rate (B).

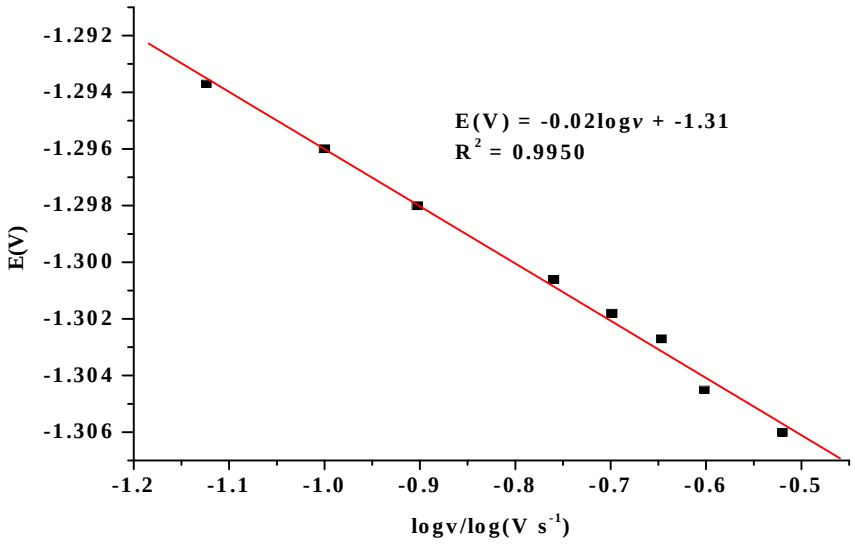

Figure 6.39. Plot of peak potential *vs* logarithm of scan rate for 50 μM endosulfan in BRB (pH 5.0) at MF/GCE.

6.4.5. Effects of accumulation potential and time

Accumulation parameters can influence the sensitivity and the intensity of peak current of endosulfan at MF/GCE. Initially, peak current of 10 μM endosulfan increased significantly with accumulation time up to 80 s. Then after, the peak currents increased slightly and then reached a plateau (Figure 6.40A). As a result, accumulation time of 80 s was chosen as the optimum accumulation time for further experiments. Figure 6.40B shows the effect of accumulation potential on the reduction peak current of endosulfan. As the accumulation potential changed from -0.5 V to -0.8 V, the reduction peak current increased. However, with further increase in the accumulation potential to more negative values, the reduction peak current decreased. Hence, -0.8 V was selected as the optimal accumulation potential for further experiments.

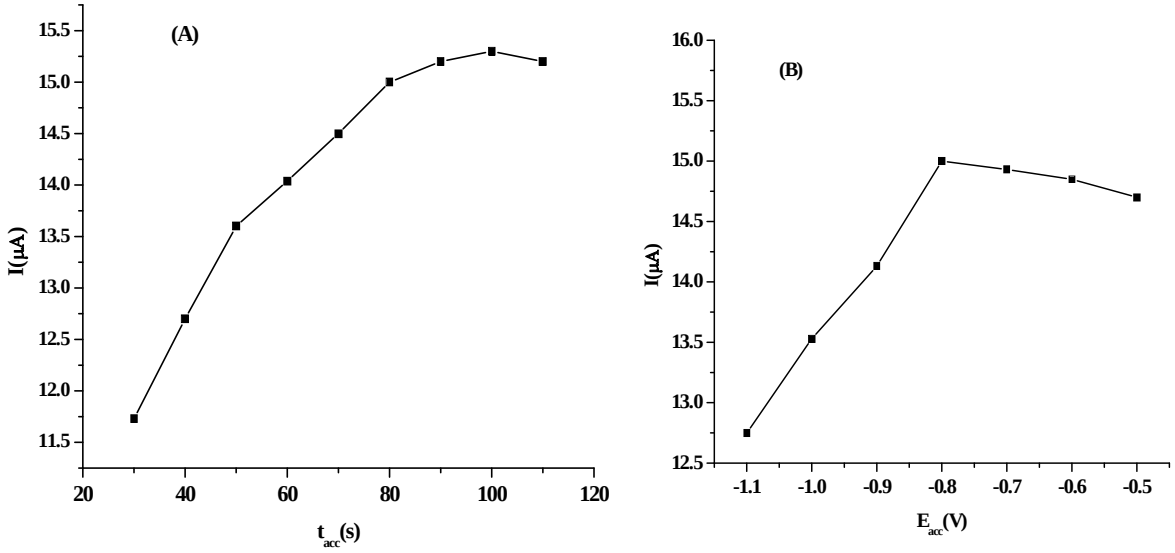

Figure 6.40. Effect of accumulation time (A) and accumulation potential (B) on the peak currents of endosulfan in BRB pH 5.0.

6.4.6. Calibration curve

Square wave voltammetry was used to investigate the variation of the peak current on the concentration of endosulfan. It was found that peak current increased linearly with endosulfan concentration over the range 0.05 μM–10 μM as shown in Figure 6.41 and the linear equation is: I(μA) = -1.35C(μM) + -2.63, R^2= 0.9953. The detection limit was found to be 0.0059 μM. In addition, the sensitivity of the MF/GCE was obtained from the slope of the calibration plot to be 1.35 μA/μM.

Moreover, the performance of the sensor was compared with some reported values. From Table 6.10, it can be seen that the detection limit of this method is lower than the octadecyl/carbon paste electrode [271], GCE [292] and hanging mercury drop electrode [293]. Meanwhile, the linear range is comparable with the mentioned sensors. This result suggests that the modified electrode can be a very promising electrochemical sensor for trace analysis of endosulfan.

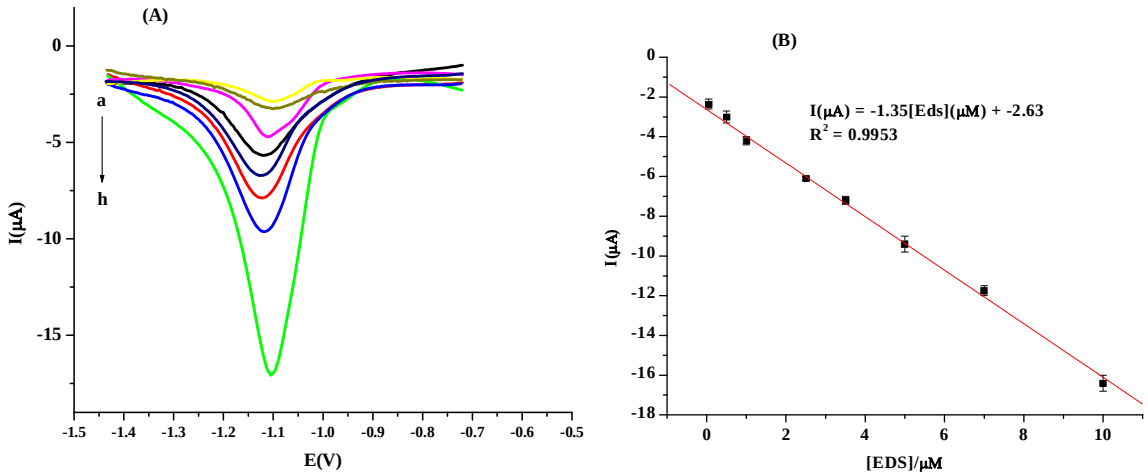

Figure 6.41. Square wave voltammograms of various concentration of endosulfan (from a to h): 0.05, 0.5, 1.0, 2.5, 3.5, 5.0, 7.0 and 10 μM in BRB pH 5.0 (A) and plot of the peak current *vs* concentration of endosulfan (B).

Table 6.10. Comparison of analytical performance for the reduction of endosulfan using different electrochemical sensors.

Electrode	Linear Range(μM)	Detection Limit(μM)	References
Octadecyl /Carbon Paste Electrode	NA	0.98	[271]
HMDE	0.154 –15.7	0.297	[294]
MF/GCE	0.05–10	0.0059	This work

6.4.7. Repeatability, reproducibility and stability

The repeatability of the modified electrode was estimated by five successive measurements of the current for 5 μM endosulfan in BRB solution at the optimized conditions using SWV. The RSD of the peak current was found to be 2.0%, which demonstrats an excellent repeatability of the method. Similarly, the reproducibility of the electrodes was determined by using three mercury films modified glassy carbon electrodes under the same working conditions and the RSD was 4.3 %. The results indicated that the MF/GCE showed good reproducibility for the detection of endosulfan.

Furthermore, the stability of the sensor was investigated after one week of storage in a refrigerator. The results showed that the sensor retained 93.2% of the initial response. This demonstrates the good stability of the film.

6.4.8. Interference study

Under the same experimental condition, the effect of interferences (Zn^{2+}, Cd^{2+}, Pb^{2} and fenitrothion) on the current response for 5 μM endosulfan was examined using square wave voltammetry. The current variation of endosulfan reduction due to these interferents was less than 5% of the current response in the absence of interference, indicating the excellent selectivity of the sensor (Table 6.11).

Table 6.11. Influence of potential interfering species on the current response of endosulfan.

Interfering agent	Concentration (μM)	Signal change (%)
Cd^{2+}	100	+1.3
Pb^{2+}	100	-4.7
Zn^{2+}	100	+2.7
Cl^{-}	100	-3.1
SO_4^{2-}	100	-1.8
Fenitrothion	100	-4.7

6.4.9. Application

The developed sensor was used to determine the quantity of endosulfan in onion and tomato samples which were collected from local market near Koka Lake. SWV results showed voltammetric responses at the reduction position of endosulfan in both onion and tomato samples. Besides, the peak current increased at about the same peak potential after the samples were spiked with known concentration of endosulfan standard solution (Figure 6.42). This indicates the presence of endosulfan in these vegetable samples. The recoveries of endosulfan were in the ranges 94.0%–101.2% and 90.2%–95.5%, for onion and tomato samples, respectively (Table 6.12), indicating that the developed method was reliable.

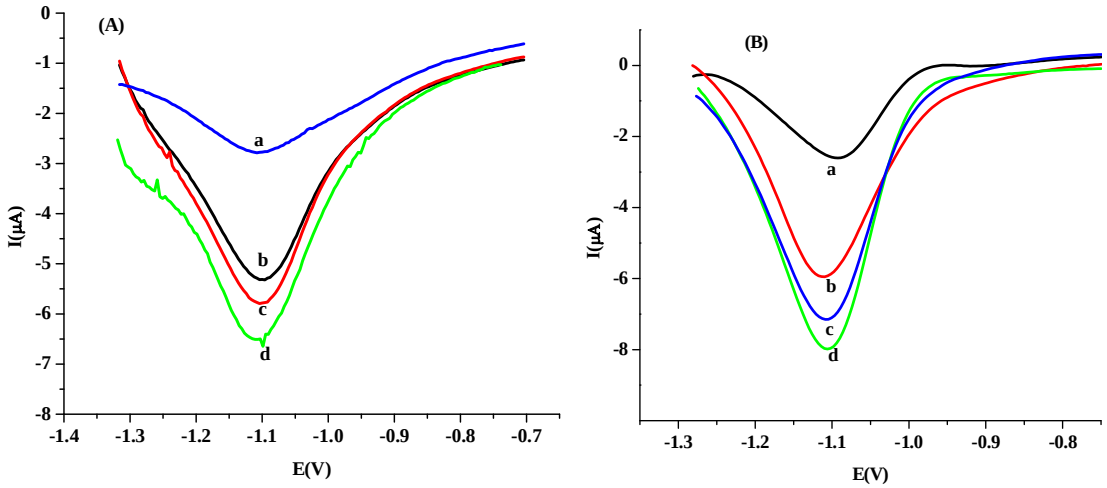

Figure 6.42. Square wave voltammograms of onion (A) and tomato (B) samples without (a) and spiked with 1.0 μM (b), 1.5 μM (c) and 2.5 μM (d) standard endosulfan in BRB pH 5.0 at MF/GCE.

Table 6.12. Recovery study of endosulfan in onion and tomato samples (n=3).

Sample	Added (μM)	Found(μM)	Recovery (%)
Onion	-	0.07	-
	1.0	1.01	94.0
	1.5	1.52	96.7
	2.5	2.45	101.2
Tomato	-	0.025	-
	1.0	0.98	95.5
	1.5	1.42	93.0
	2.5	2.28	90.2

6.5. Simultaneous determination of caffeine and paracetamol by square wave voltammetry at poly(4-amino-3-hydroxynaphthalene sulfonic acid) modified glassy carbon electrode

6.5.1. Background

Caffeine (1,3,7-trimethylxanthine) is a naturally occurring alkaloid belonging to N-methyl derivatives of xanthine, which is found in tea leaves, coffee beans, cola nuts, cocoa beans and other plants. It is used as a flavoring agent in a variety of beverages, including some soft and energy drinks. Caffeine is also a central nervous system stimulant. In moderate doses, it can increase alertness, reduce fine motor coordination, cause insomnia, headaches, nervousness and dizziness [170, 295-298]. However, intense use of caffeine over time can lead to irritability, mutation effects such as inhibition of DNA, anxiety and tremors, among other side effects [299, 300]. It can mobilize calcium from cells that leads to bone mass loss and is considered as a risk factor for cardiovascular diseases [301-303].

Paracetamol (N-acetyl-p-aminophenol, acetaminophen) is an effective and safe drug that is applied to reduce fever, relieve coughing, colds and pain including muscular aches, chronic pain, migraine headache, backache and toothache [304–309]. Recent researches suggest that paracetamol can help to protect hardening of arteries that cause cardiovascular disease. It also remains the analgesic choice for people with asthma [310]. In general, paracetamol does not exhibit any harmful side effects but overdosing. However, chronic use produces toxic metabolites accumulation that will cause kidney and liver damage [311–313]. Paracetamol is often used in the presence of other drugs like; aspirin, cetirizine, tramadol, caffeine and codeine [314, 315]. A combination of caffeine and paracetamol is used in migraine attack, child birth and avoiding postpartum hemorrhage [316]. The use of the mixture of paracetamol and caffeine as an analgesic and antipyretic is well established in pharmaceutical formulation [317]. Thus, a simple, fast, sensitive and accurate analytical method for the determination of caffeine and paracetamol in food, pharmaceutical products and biological samples is needed.

Different methods have been employed for the simultaneous determination of caffeine and paracetamol which include spectrophotometry [306, 317, 318–321] and high-performance liquid chromatography [296, 302, 322–326].

Using electrochemical methods, caffeine and paracetamol were determined simultaneously at the surface of glassy carbon electrode [327], cathodically pretreated boron doped diamond electrode [328], self-assembled monolayer of non-peripheral amine substituted copper(II) phthalocyanine modified with glassy carbon electrode [329], poly(taurine)/TiO_2-graphene nanocomposite modified glassy carbon electrode [330], Nafion/ruthenium oxide pyrochlore/GCE [331] and in situ surfactant-modified multi-walled carbon nanotube paste electrode [332].

6.5.2. Electrochemical properties of poly(AHNSA)/GCE

Poly(AHNSA) film formation at GCE was carried out by the electropolymerization of AHNSA monomers using cyclic voltammetry. Figure 6.43 depicts the electrochemical polymerization of AHNSA on a GCE in the potential range of -0.8 V and 2.0 V at a scan rate of 0.1 V s^{-1} for fifteen cycles in 0.1 M HNO_3 solution. In the first cycle, two oxidation peaks (ipa1 and ipa2) and one reduction peak (ipc) were observed at peak potentials of 0.054 V, 0.61 V and -0.11 V, respectively. With increase in the number of voltammetric scans, one oxidation peak (ipa3) was gradually observed at 0.38 V. As can be seen, all the anodic peak and cathodic peak currents are enhanced gradually with increasing in voltammetric scans, indicating the formation and growth of an electroactive layer on the GCE surface. The electrodeposition of the polymer on the GCE was examined using cyclic voltammety between -0.8 V and +0.8 V in 0.5 M H_2SO_4 solution without the monomer (inset Figure 6.43). Three couples of redox peaks (ipa1-ipc1, ipa2-ipc2 and ipa3-ipc3) were observed which further confirmed that glassy carbon electrode has already been modified. These results are consistent with the previous related work [104, 105].

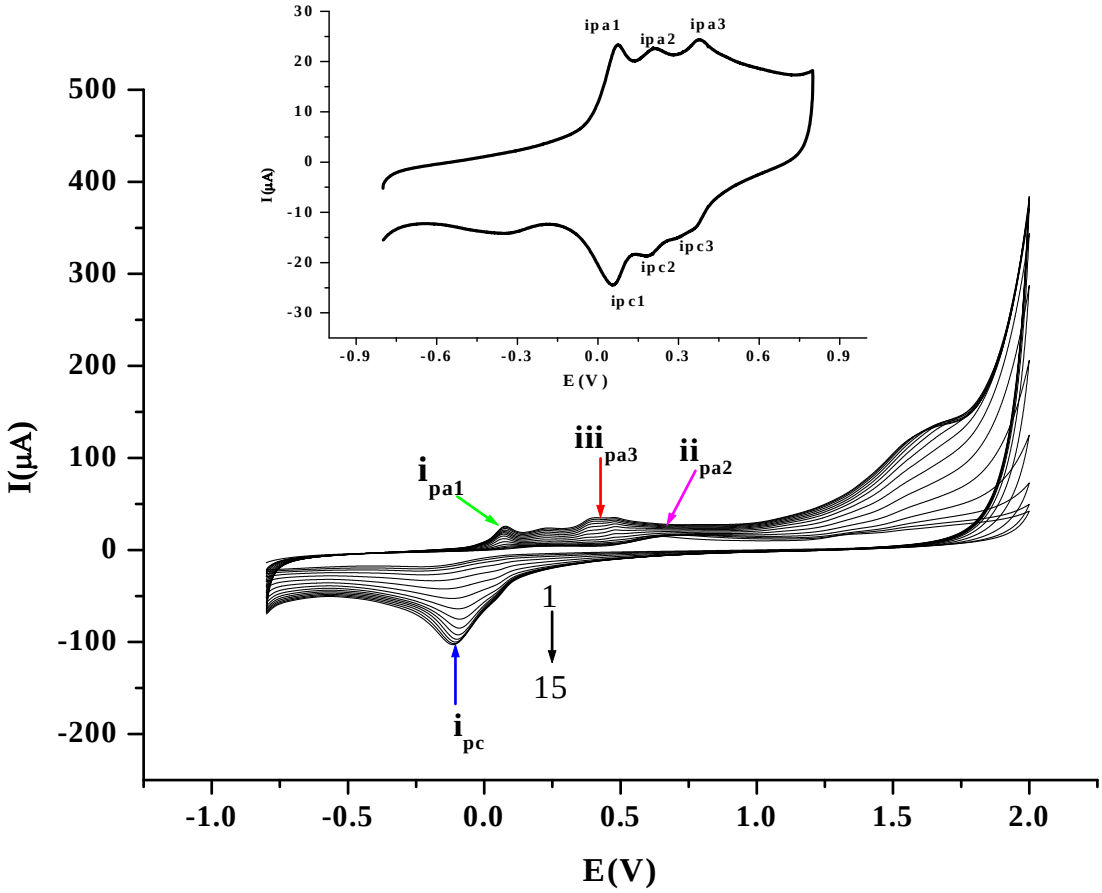

Figure 6.43. Cyclic voltammetric electropolymerization of $2x10^{-3}$ M AHNSA in 0.1 M HNO_3 at GCE. Inset: Cyclic voltammetry of poly(AHNSA)/GCE in a 0.1 M HNO_3 at 0.1 V s^{-1}.

6.5.3. Electrochemical behavior of caffeine and paracetamol

Figure 6.44 shows cyclic voltammograms of 1.0 mM caffiene in pH 5.0 ABS at a GCE and at poly(AHNSA)/GCE at a scan rate of 0.1 V s^{-1}. At the GCE, caffeine showed an electrochemically irreversible characteristic with an oxidation peak at 1.60 V (curve b). In comparison to the GCE, the poly(AHNSA)/GCE a much more enhanced current (curve c) was observed for caffeine oxidation with a shift for peak potential to 1.45 V, indicating the catalytic

activity of the modified electrode. The oxidation of caffeine at poly(AHNSA)/GCE is irreversible, as reported in the literature [170, 298, 301, 303, 333].

Paracetamol shows an irreversible wave with an oxidative peak at 0.563 V at GCE electrode (Figure 6.45 curve b), indicating a sluggish electron transfer kinetics at the GCE. However, a pair of well-defined redox peak currents at an anodic peak potential of 0.477 V and cathodic peak potential of 0.388 V with peak-to-peak separation of 0.089 V was observed at the surface of poly(AHNSA)/GCE (curve c). The remarkable oxidation potential shift, enhancement of the peak current (two fold) and appearance of a new peak in the cathodic direction provides clear evidence of the catalytic effect of poly(AHNSA)/GCE towards paracetamol.

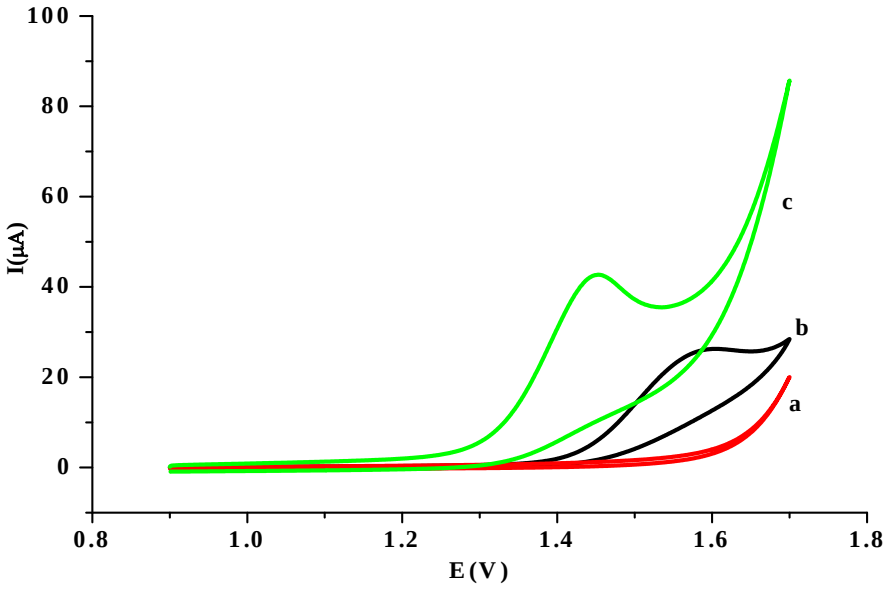

Figure 6.44. Cyclic voltammograms of poly(AHNSA/GCE without caffeine (a), 1.0 mM caffeine at GCE (b) and poly(AHNSA**)**/GCE (c) in 0.1 M ABS (pH 5.0), at scan rate of 0.1 V s^{-1}.

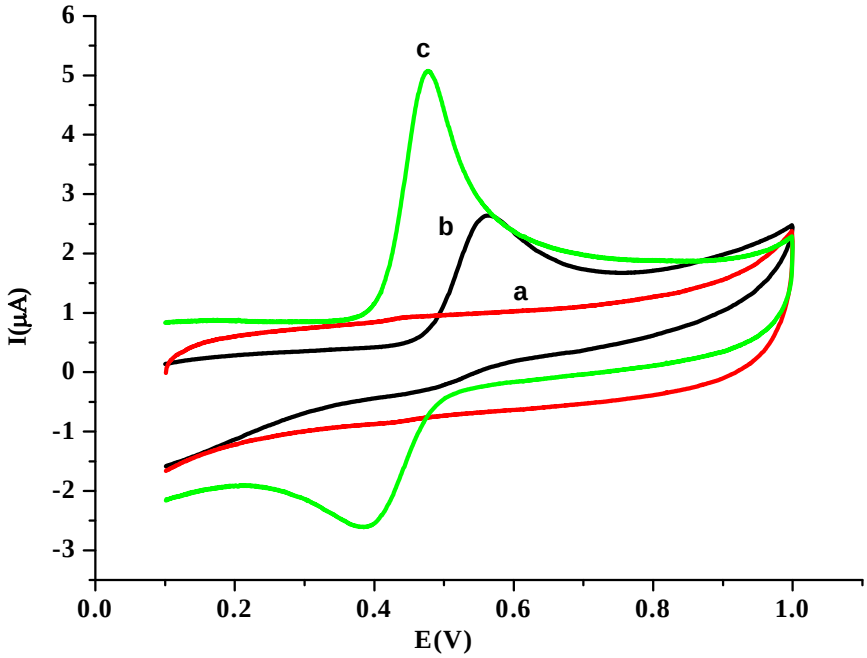

Figure 6.45. Cyclic voltammograms of 0.1 M ABS (pH 5.0) at poly(AHNSA)/GCE (a), 0.1 mM paracetamol in ABS of pH 5.0 at GCE (b) and at poly(AHNSA)/GCE (c), at a scan rate of 0.1 V s^{-1}.

6.5.4. Electrochemical behavior of caffeine and paracetamol mixture

The electrochemical performance of poly(AHNSA)/GCE was examined in ABS containing caffeine and paracetamol using cyclic voltammetry (Figure 6.46). Caffeine showed an oxidation peak at 1.53 V with a peak current of 35 μA at the GCE (curve b). However, at the poly(AHNSA)/GCE (curve c) the peak current for caffeine oxidation is enhanced (~53 μA) at a potential about 0.1 V less positive than at the GCE electrode. The oxidation peak of paracetamol appeared at +0.62 V without a reduction peak in the reverse scan at GCE (curve b). The hydrolysis of N-acetyl-p-quinoneimine (NAPQI) to p-benzoquinone is responsible for the disappearance of the cathodic wave in the cyclic voltammograms [307]. In contrast, at the poly(AHNSA)/GCE (curve c) a new peak appeared in the reverse direction around 0.458 V. In addition, the oxidation peak potential shifts to 0.525 V and the peak current is twice larger than

the current at the GCE. The increase in the oxidation peak currents and lowering of oxidation peak potentials of caffeine and paracetamol with improved reversibility for the latter are clear evidence of the catalytic effect of the modified electrode. The carbonyl group on caffeine and both carbonyl and hydroxyl groups of paracetamol form hydrogen bonds with both the hydroxyl and amino groups of poly(AHNSA) and thus, these bonds are responsible for increased adsorption tendency of both analytes on the surface of poly(AHNSA)/GCE.

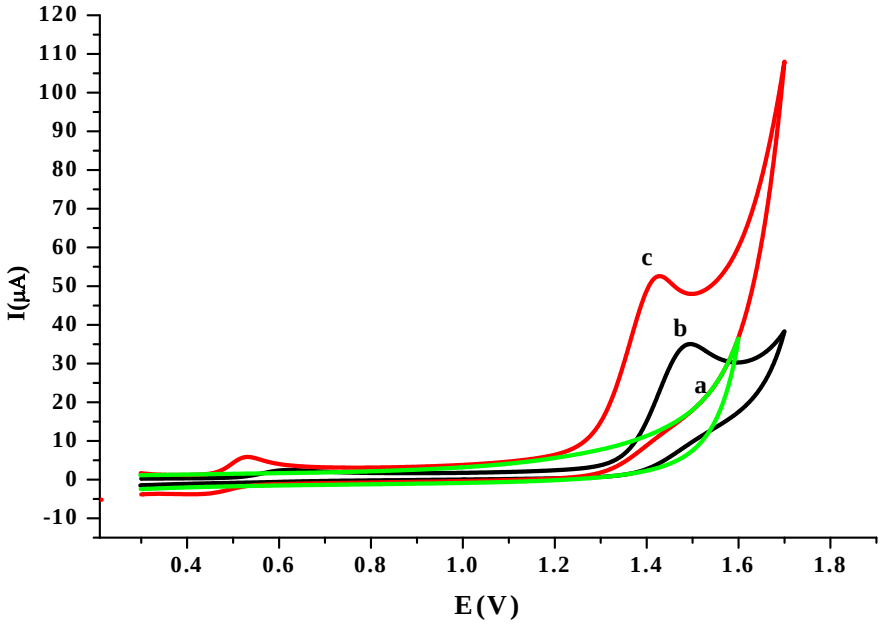

Figure 6.46. Cyclic voltammograms of 0.1 M ABS (pH 5.0) at poly(AHNSA)/GCE (a) 1.0 mM caffeine and 0.1 mM paracetamol at GCE (b) and (c) at poly(AHNSA)/GCE at a scan rate of 0.1 V s^{-1}.

6.5.5. Effect of pH

The pH of the supporting electrolyte is an important factor that affects the redox behavior of biomolecules, drugs and many electroactive compounds. The influence of the pH on the peak currents and potentials of caffeine were examined by cyclic voltammetry in the pH range 3.5 to 6.0 at 0.1 V s^{-1}. As depicted in Figure 6.47, the current increases from pH 3.5 to pH 4.5, and then decreases with an increase in pH.

The peak potential was also affected by a change in pH (Figure 6.48). The oxidation peak potential of caffeine shifted negatively with increasing pH values. A linear relationship was observed between the peak potential and pH with a regression equation of E(V) = -0.045pH + 1.67, R^2 = 0.9994. A slope of 0.045 V/pH suggests that the overall process involves transfer of equal number of protons and electrons (Scheme 9), which is in agreement with previous reports [170, 327, 334, 335].

Similarly, the effect of pH of the solution on the electrochemical behavior of paracetamol at scan rate of 0.1 V s^{-1} was studied using cyclic voltammetry. The peak current increased from pH 3.0 to 4.5 and then decreased at higher pH value (Figure 6.49). Moreover, as can be seen in Figure 6.50, both the anodic and cathodic peak potentials were shifted negatively when the solution pH was increased. The linear dependence of the peak potential on the pH is represented by the equations: E_{pa}(V) = -0.049pH + 0.673, R^2 = 0.9931 and E_{pc}(V) = -0.06pH + 0.679, R^2 = 0.9863. The slopes of -0.049 V/pH and -0.06 V/pH showed that equal number of electrons and protons ($2e^-$/2p) are involved (Scheme 10), which is in agreement with previous reports [305, 307, 309, 310]. The increase in peak current of caffeine and paracetamol at lower pH of acetate buffer solution were due to the interaction between the positive charge on caffeine (pKa = 10.4) and paracetamol (pKa = 9.7) and the negative charge of polymer-modified surface (pKa ≈ 4) [310, 335]. Therefore, pH 4.5 was chosen as the optimum pH value for further studies.

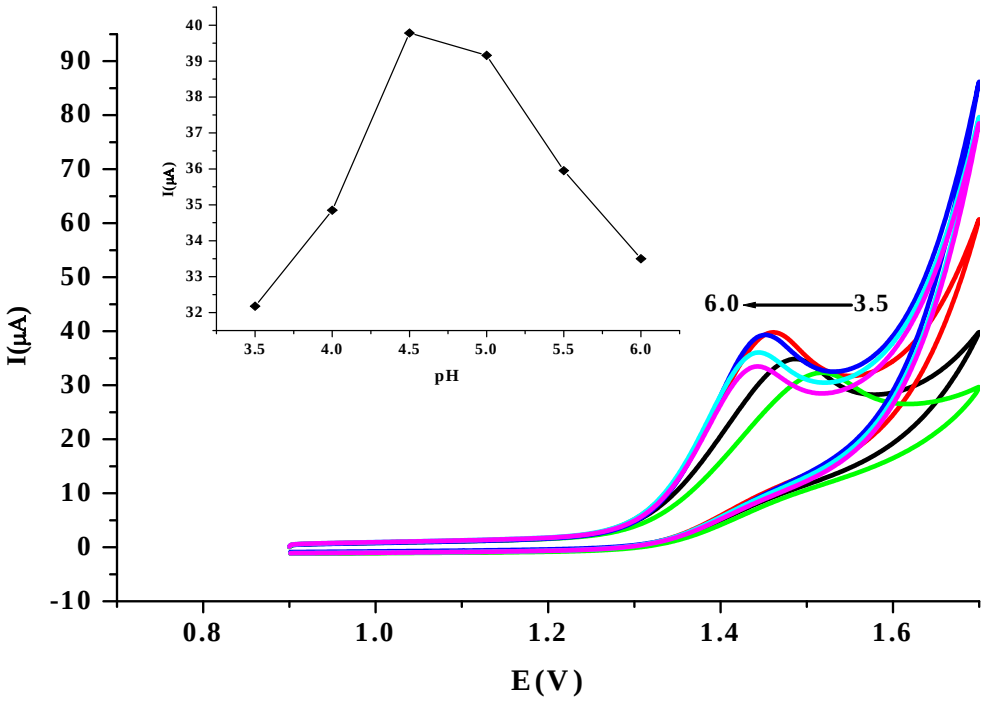

Figure 6.47. Cyclic voltammograms of 1.0 mM caffeine in ABS of various pH value at poly(AHNSA)/GCE. Inset: plot of peak currents *vs* pH at a scan rate of 0.1 V s^{-1}.

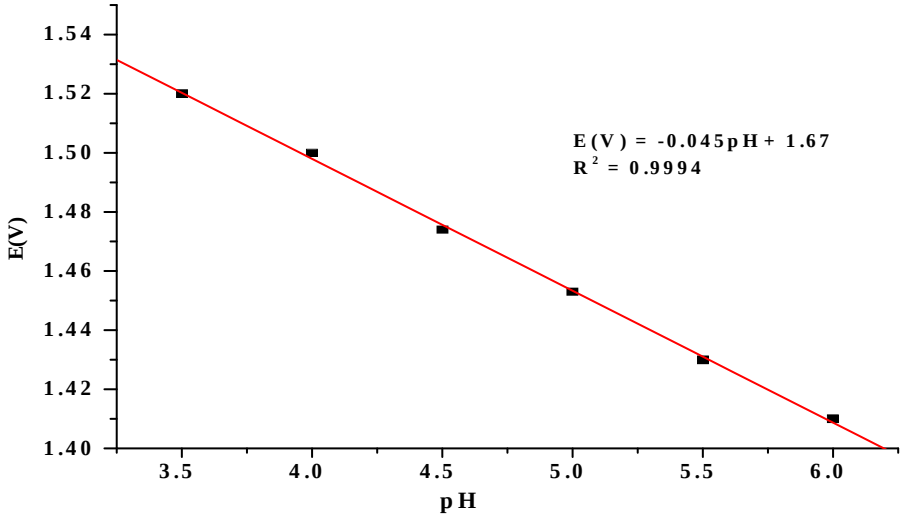

Figure 6.48. Plot of peak potential values for 1.0 mM caffeine as a function of pH at poly(AHNSA)/GCE.

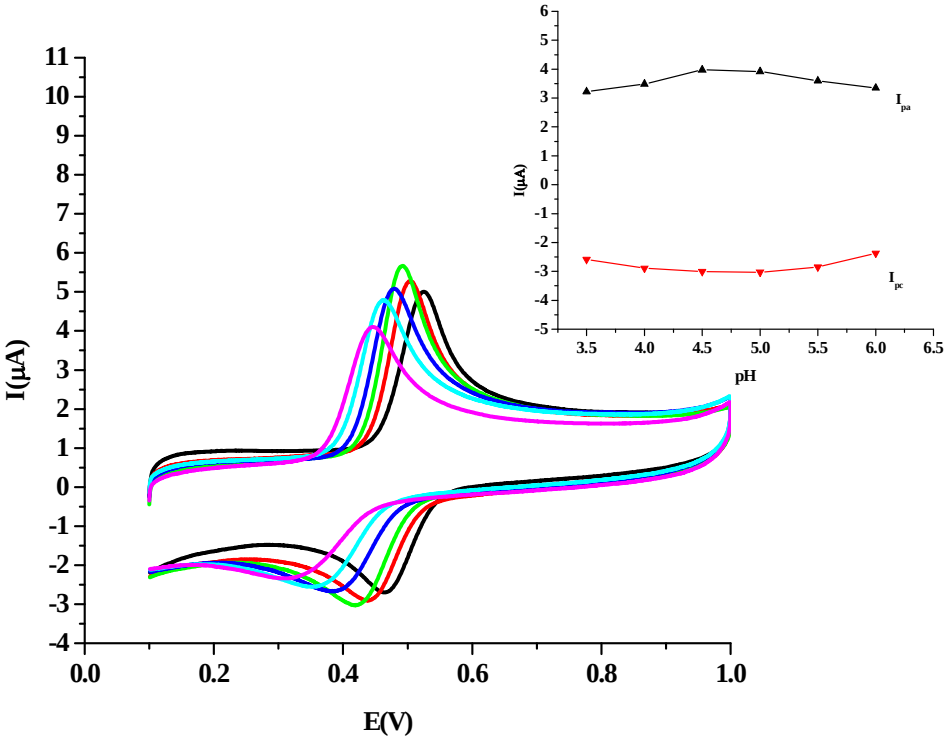

Figure 6.49. Cyclic voltammograms for 0.1 mM paracetamol in ABS of various pH value at poly(AHNSA)/GCE. Inset: plot of peak currents *vs* pH at a scan rate of 0.1 V s^{-1}.

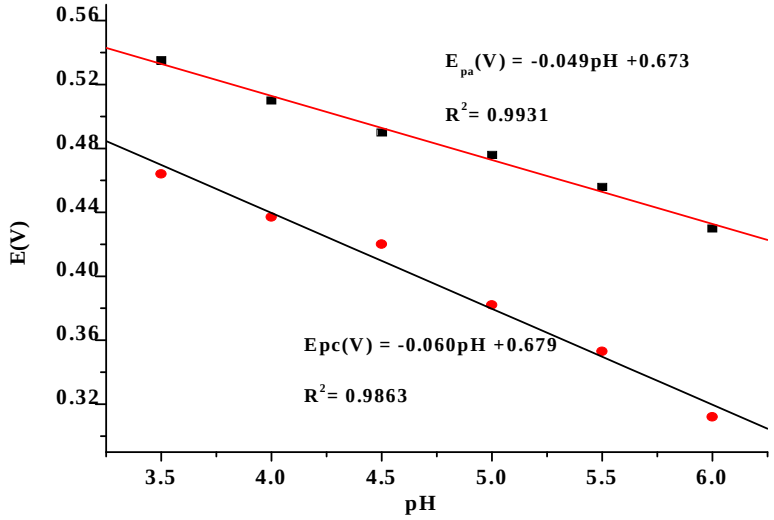

Figure 6.50. Plot of peak potentials for 0.1 mM paracetamol as a function of pH at poly(AHNSA)/GCE.

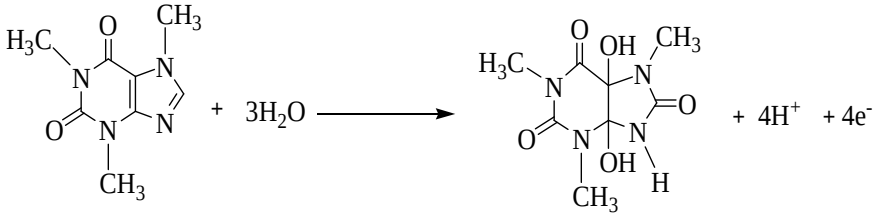

Scheme 9. Oxidation reaction of caffeine

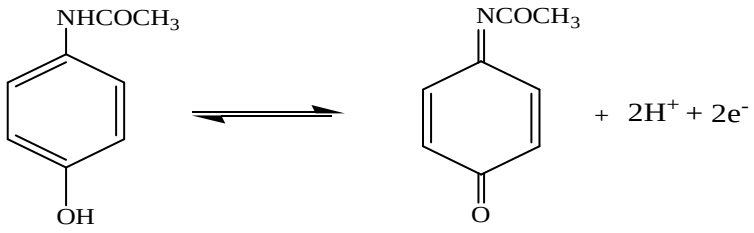

Paracetamol N-acetyl-p-quinoneimine

Scheme 10. Oxidation-reduction reaction of paracetamol

6.5.6. Effect of scan rate

The effect of scan rate on the peak current for these two species was investigated in ABS of pH 4.5 containing 1.0 mM caffeine and 0.1 mM paracetamol. As shown in Figure 6.51, the peak currents of both caffeine and paracetamol showed a linear relationship with the scan rate. This confirmed that the electrochemical behavior of caffeine and paracetamol at the surface of poly(AHNSA)/GCE is an adsorption–controlled processes. On the other hand, for both compounds the peak potentials are shifted to the positive direction with increase in the scan rate. This indicated that the oxidation of caffeine is irreversible and the redox reaction of paracetamol is quasi-reversible at poly(AHNSA)/GCE.

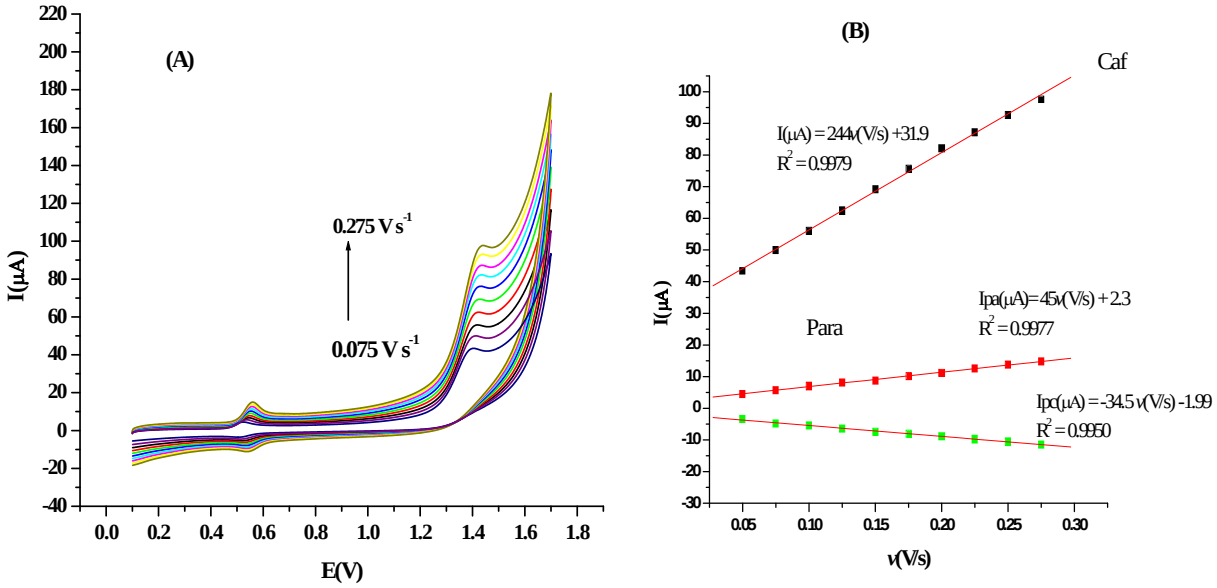

Figure 6.51. Cyclic voltammograms of 1.0 mM caffeine and 0.1 mM paracetamol in ABS pH 4.5 at the poly(AHNSA)/GCE at various scan rates (0.075, 0.10, 0.125, 0.150, 0.175, 0.20, 0.225, 0.250 and 0.275 V s^{-1}) (A) and plot of peak current *vs* scan rate of caffeine and paracetamol (B).

6.5.7. Optimization of square wave voltammetric parameters

The dependence of the peak current of caffeine and paracetamol on the square wave step potential, pulse amplitude and frequency were studied. The step potential was varied in the range 6–16 mV by fixing the frequency at 20 Hz and the amplitude at 30 mV. The peak height increases as the step potential was increased, exhibiting a maximum at 12 mV, after which it decreased accompanied by broadening of peak. Therefore, 12 mV was chosen as the optimum square wave step potential. The amplitude was also optimized in the range 40–100 mV by keeping the frequency and step potential at 20 Hz and 12 mV, respectively. The peak current increased up to 80 mV and then it decreased. Thus, 80 mV was employed in the subsequent measurements. Finally, by taking the optimum values of amplitude and step potential, the effect frequency on the current response was studied in the range 20–50 Hz. The peak current for caffeine and paracetamol increased up to 35 Hz, but after 35 Hz the peak current decreased. As a result, 35 Hz was selected as the optimal value for the subsequent measurements.

6.5.8. Determination of caffeine and paracetamol

Under the optimized conditions, square wave voltammograms (Figure 6.52) were recorded for different concentration of caffeine (5 μM–125 μM) in the presence of fixed concentrations of paracetamol (2 μM) in 0.1 M ABS (pH 4.5). The peak current for caffeine increased linearly with concentration and a regression equation: $I(\mu A) = 0.259C(\mu M) + 3.53$, $R^2 = 0.9988$, was obtained.

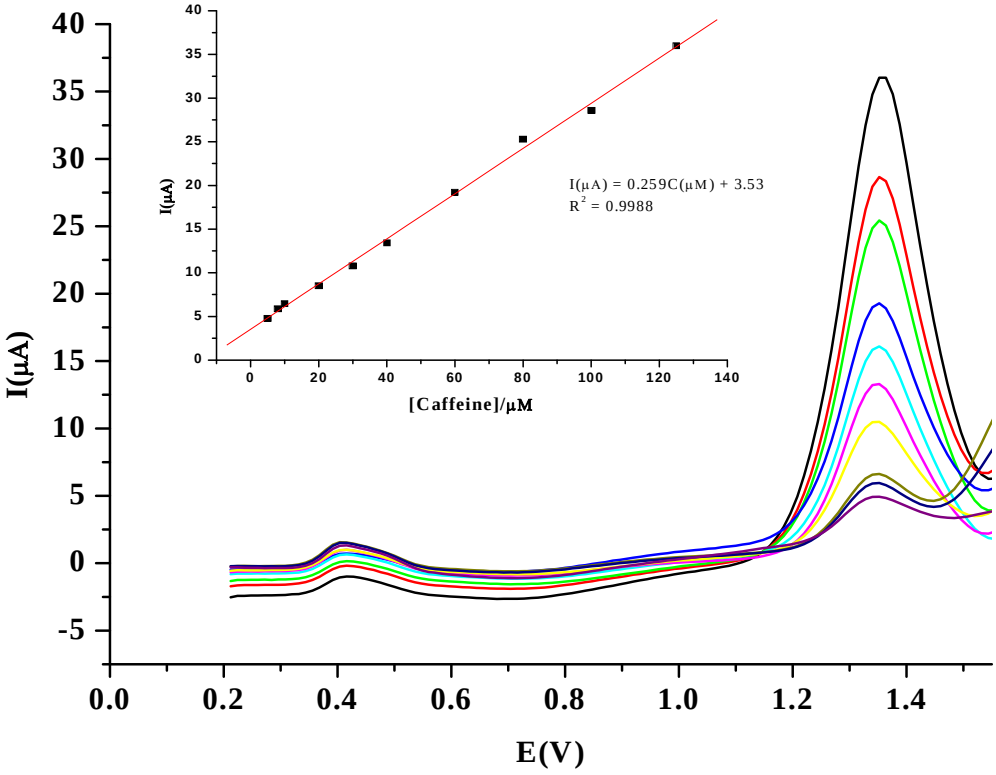

Figure 6.52. Square wave voltammograms of 5, 8, 10, 20, 30, 40, 60, 80, 100 and 125 μM of caffeine and 2 μM paracetamol at poly(AHNSA)/GCE. Inset: plot of peak current of caffeine *vs* concentration.

Similarly, Figure 6.53 shows the square wave voltammograms recorded for different concentration of paracetamol (3–60 μM) at fixed concentration of caffeine (10 μM). It can be seen that no significant changes were observed in the oxidation current of caffeine on addition of different concentration of paracetamol. This indicates that the addition of paracetamol does not affect the determination of caffeine. The peak current of paracetamol increased linearly with increase in paracetamol concentration with a regression equation: I(μA) = 1.66C(μM) + 3.83, R^2 = 0.9984. These results suggest that the poly(AHNSA)/GCE can effectively be utilized for the determination of caffeine in the presence of paracetamol and the *vice-versa*.

The simultaneous determination of caffeine and paracetamol was carried out using square wave voltammograms at the optimized conditions at the poly(AHNSA)/GCE by varying the concentrations of both caffeine and paracetamol. Figure 6.54 shows the SWV responses of poly(AHNSA)/GCE for caffeine and paracetamol when the concentrations of these species were increased at the same time. The peak currents for both caffeine and paracetamol increased linearly with concentrations in the range 10-125 μM. The linear regression equations are: $I_{caf}(\mu A) = 0.218C(\mu M) + 5.45$, $R^2 = 0.9989$ and $I_{para}(\mu A) = 0.332C(\mu M) + 3.26$, $R^2 = 0.9986$ for caffeine and paracetamol, respectively.

The detection limit was calculated by using the relationship 3s/b, where s is the standard deviation of the blank measured under the same conditions as for the standard sample analysis (n = 5) and b is the slope of the calibration curve. The detection limits of caffeine and paracetamol were estimated to be 0.79 μM and 0.45 μM, respectively.

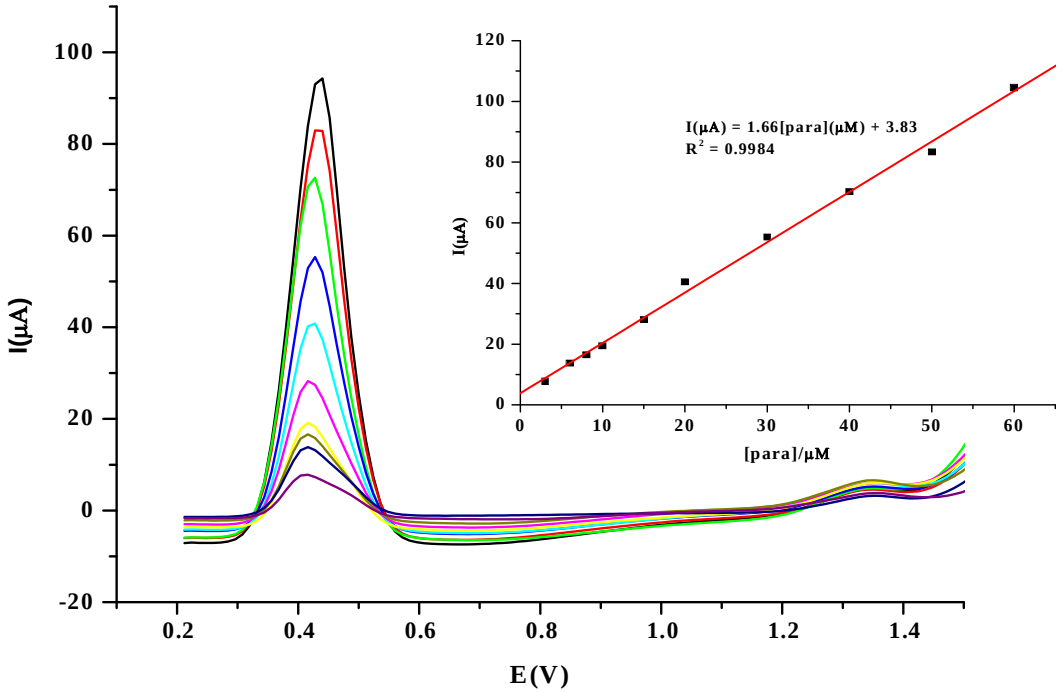

Figure 6.53. Square wave voltammograms of 3, 6, 8, 10, 15, 20, 30, 40, 50 and 60 µM of paracetamol and 10 µM caffeine in ABS (pH 4.5) at poly(AHNSA)/GCE. Inset: plot of current responses *vs* paracetamol concentration.

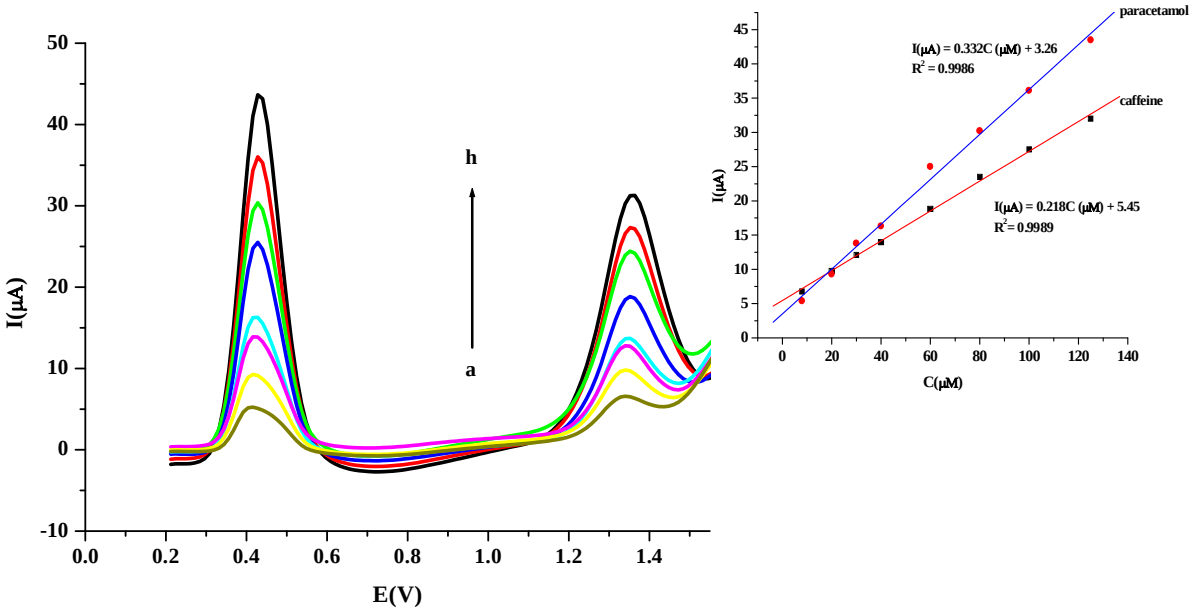

Figure 6.54. Square wave voltammograms for different concentrations (a = 10, b = 20, c = 30, d = 40, e = 60, f = 80, g = 100 and h = 125 μM) of caffeine and paracetamol at poly(AHNSA)/GCE. Inset: plot of current *vs* the concentration of caffeine and paracetamol.

6.5.9. Repeatability and stability of the modified electrode

Several measurements were taken to determine the repeatability of the electrochemical responses of poly(AHNSA)/GCE for 0.1 mM caffeine and 0.1 mM paracetamol in ABS (pH 4.5). The results of ten successive measurements showed RSD of 4.45% and 3.62% for caffeine and paracetamol, respectively, which indicates that the poly(AHNSA)/GCE has good repeatability. The long-term stability of the electrode was evaluated by measuring the response for 0.1 mM caffeine and 0.1 mM paracetamol by keeping the electrode in 0.1 M acetate buffer solution in a refrigerator for 15 days. The electrode retained about 95% and 97% of its original activity for caffeine and paracetamol, respectively, indicating the electrode was very stable.

6.5.10. Interference study

The selectivity of poly(AHNSA)/GCE for the determination of equimolar concentration (40 μM) of caffeine and paracetamol was investigated in the presence of different interfering substances such as ascorbic acid, citric acid, glucose, uric acid and Pb^{2+} with concetrtaions 40 and 400 μM by SWV at pH 4.5. The corresponding oxidation peak currents obtained in the presence of interfering substances were compared with those obtained in the absence of each interferents. The percent changes in the peak current response of these species were less than 5% (Table 6.13). Hence, it can be concluded that these species do not significantly interfere in the determination of caffeine and paracetamol, and the modified electrode had good selectivity for the determination of caffeine and paracetamol.

Table 6.13. Effect of interfrences in the analysis of 40 μM caffeine and 40 μM paracetamol under optimized conditions.

Interference	Conc./μM	Change in response (%)	
		Caffeine	Paracetamol
Ascorbic acid	40	2.1	2.2
	400	4.3	3.3
Citric acid	40	1.7	3.8
	400	0.5	7.0
Glucose	40	5.0	4.0
	400	3.9	2.7
Uric acid	40	4.2	2.8
	400	1.4	4.1
Pb^{2+}	40	2.2	4.3
	400	4.5	5.0

6.5.11. Application

The application of the developed method was examined in the determination of both caffeine and paracetamol in Coca-Cola, Pepsi-Cola and tea samples. The samples first were diluted with the supporting electrolyte and then spiked with known concentrations of standard caffeine and paracetamol. A peak for caffeine was observed exactly at the same potentials as that observed in the case of standard caffeine, which indicates the presence of caffeine in all the three samples. The values of caffeine in coca-cola, pepsi-cola and tea were found to be 111.5(±11.1) mg/L, 114.3(±5.50) mg/L and 13.1(±1.26) mg/g, respectively, which are in good agreement with values reported in the literature [299, 302, 336–339]. However, none of the samples analyzed contained paracetamol.

In addition, standard solutions of caffeine and paracetamol were added to the samples to test the applicability of the method in these matrices using recovery method. The results are summarized in Table 6.14. The recovery was acceptable, showing that the developed method could be effictively used for the simultaneous determination of caffeine and paracetamol in Cola and tea samples.

The analytical performance of the present modified electrode was compared with some other similar modified electrodes (Table 6.15). These data show that the detection limit is comparable and a relatively wider linear range, simple preparation of the electrode, remarkable sensitivity, stability and reproducibility were achieved in the present method.

Table 6.14. Recovery test for caffeine and paracetamol in coca-cola, pepsi-cola and tea samples (n=3).

Sample	Analyte	Added (μM)	Found (μM)	RSD (%)	Recovery (%)
		0	2.8	-	-
	Caffeine	10	11.7	3.8	89.0
Coca-cola		20	20.9	7.6	90.5
		0	-	-	-
	Paracetamol	5	4.7	6.5	94.0
		10	10.5	7.5	105.0
		0	3.0	-	-
	Caffeine	10	12.3	6.4	93.0
Pepsi-cola		20	21.7	6.6	93.5
		0	-	-	-
	Paracetamol	5	4.7	6.3	94.1
		10	10.6	8.7	106.0
		0	1.2	-	-
	Caffeine	20	17.4	10.8	81.0
Tea		30	30.5	8.8	97.7
		0	-	-	-
	Paracetamol	5	4.5	3.7	90.2
		20	9.7	2.9	97.9

Table 6.15. Comparison of the analytical performance of poly(AHNSA)/GCE for caffeine and paracetamol determination with previously reported work.

Electrode	Analyte	L. Range (μM)	LOD (μM)	Sample	Ref
Boron-doped diamond	Caffeine	0.78–35	0.096	Drugs	[327]
	Paracetamol	0.54–61	0.23		
Poly(taurine)/TiO_2-Gr/GCE	Caffeine	0.05–100	0.5	Serum	[330]
	Paracetamol	0.05–100	0.034		
Nafion/RuO_2/pyrochlore/GCE	Caffeine	10–250	1.2	Drugs	[331]
	Paracetamol	5–250	2.2		
Graphite-polyurethane/SPE	Caffeine	4–200	1.6	Drugs	[340]
	Paracetamol	1–40	0.84		
Boron-doped diamond	Caffeine	0.5–83	0.035	Drugs	[341]
	Paracetamol	0.5–83	0.49		
Poly(AHNSA)/GCE	Caffeine	10–125	0.79	Cola, Tea	This work
	Paracetamol	10–125	0.45		

6.6. An electrochemical sensor based on multiwalled carbon nanotubes coated poly(AHNSA) modified electrode for the determination of uric acid

6.6.1. Background

Uric acid (2,6,8-trihydroxypurine, UA) is the primary product of protein and purine metabolism in the human body. It is normally present in millimolar range in urine and in micromolar levels (0.13–0.46 mM) in serum [342-344]. It is excreted in urine. UA is a natural antioxidant, which can scavenge free radicals, superoxide, hydroxyl radical, and singlet oxygen. In addition, UA has the ability to bind iron and inhibit iron dependent ascorbate oxidation. Owing to these properties, UA prevents the destruction of human tissues and cells [345-347]. Humans have higher UA levels in serum when compared to other mammals due to the lack of uricase enzyme, which catalyses UA to more soluble end product (allantoin). Recently, due to improvement of dietary life as a result of economic development causes over nutrient of high protein for the people. Consequently, the level of uric acid is increasing in the blood serum. Over taking of alcoholic beverages, underexercise and a heavy stress can also influence the levels of uric acid [348-351]. Extreme level of UA in human body reflect purine metabolism disorders which may lead to several diseases, such as gout, hyperuricemia, pneumonia, obesity, diabetes, high cholesterol, high blood pressure, kidney disease and heart disease [347, 352]. Monitoring the levels of UA in body fluids can be used as an indicator in the diagnosis of many health problems [353]. Due to the high clinical and pharmaceutical significance, it is essential to develop new sensors with improved sensitivity for the determination of UA in real samples.

Various analytical techniques such as high performance liquid chromatography [354], high performance liquid chromatography-mass spectrometry [355], spectrophotometric method [356, 357] and chemiluminescence [348, 358] have been reported for the determination of UA. Over the last few decades, because of the electroactive nature of UA electroanalytical methods have gained considerable attention for the determination of UA [359].

Previous reports showed that UA has been determined electrochemically using various electrodes. Platinum nanosheets (PtNSs)/fullerene(C60)/glassy carbon electrode [360], graphene-

nickel hydroxide modified glassy carbon electrode [361], SnO_2/graphene nanocomposite modified glassy carbon electrode [362], poly(glyoxal-bis(2-hydroxyanil)) modified glassy carbon electrode [363], graphene oxide modified glassy carbon electrode [364], over-oxidized poly(3,4-ethylenedioxythiophene) nanofibers modified pencil graphite electrode (Ox-PEDOT-nf/PGE) [353], multiwalled carbon nanotubes modified glassy carbon electrode [365], polymerized Luminol Film modified glassy carbon electrode [366] and poly(chromotrope 2B) modified glassy carbon electrode [367] electrodes have been utilized for the detection of UA.

Eventhough, the electrocatalytic activity of conjugated polymers or CNTs individually showed good results, some properties such as mechanical stability, sensitivity for different techniques, and electrocatalysis for some compounds are poor [73, 116, 368, 369]. To overcome this difficulty, in recent years studies have been conducted in preparing composite electrodes which composed of both CNTs and conjugated polymers. The incorporation of CNTs in conjugated polymers resulted in the formation of new composite materials having the properties of each component with a synergistic effect such as high aspect ratio and high surface area, increasing the rate of electron transfer and high accessibility of the analyte to the surface of the electrode. As a consequence, they can enhance electrocatalytic properties, reduce the required overpotential, increase reaction rate, increase sensitivity and stability, and prevent surface fouling of the electrode. $\pi-\pi$ electronic and hydrophobic interactions between MWCNTs and polymers resulted in successful dispersion in forming homogeneity for electrochemical sensors [60, 73, 270, 347, 370].

In this study, a sensor based on MWCNTs/poly(AHNSA) modified glassy carbon electrode was prepared by electrodeposition of poly(AHNSA) on to GCE and then drop-coating with MWCNTs. The sensor was utilized for the investigation of the electrochemical investigation of uric acid and its determination in real samples.

6.6.2. Electrochemical behavior of uric acid

The electrochemical behavior of UA was studied using cyclic voltammetry at the surface of GCE and poly(AHNSA), MWCNTs and MWCNTs/poly(AHNSA) modified electrodes at a scan rate of 0.1 V s^{-1}. As can be seen in Figure 6.55, a broad oxidation peak without any peak in the reverse scan was observed at a potential of +0.595 V at the surface of the GCE. After modification with poly(AHNSA) and MWCNTs, the oxidation peak current was shifted to +0.354 V with a remarkably increment in its response. A very small reduction peak current appeared in the reverse scan near +0.281 V at these electrodes, which is due to the reduction of diimine to UA. Thus, UA shows a quasi-reversible electrochemical reaction at the surface of poly(AHNSA)/GCE (curve b) and MWCNTs/GCE (curve c).

The current response for UA at MWCNTs/poly(AHNSA)/GCE was higher than at poly(AHNSA)/GCE, MWCNTs/GCE and GCE. The current response obtained at the composite was found to be three-fold higher than observed at the GCE. The remarkable signal enhancement in electrochemical detection of UA at the composite modified electrode is due to the synergistic effect resulted from combining the individual characteristics, such as high electrical conductivity and large specific surface area. Therefore, due to high sensitivity MWCNTs/poly(AHNSA)/GCE was chosen as the sensing electrode for the determination of UA used in this study.

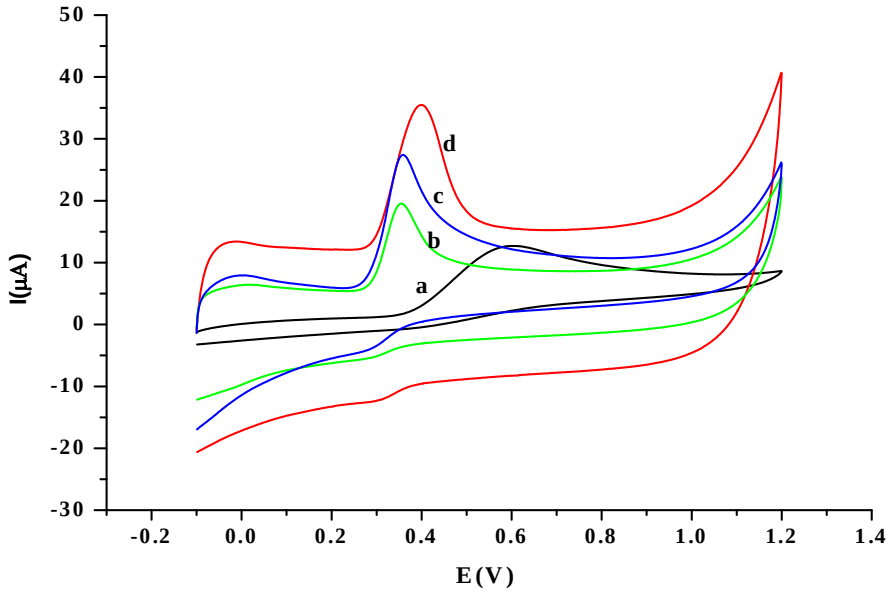

Figure 6.55. Cyclic voltammograms for 1.0 mM UA in 0.1 M PBS (pH 7.0) at GCE (a), Poly(AHNSA)/GCE (b), MWCNTs/GCE (c) and MWCNTs/Poly(AHNSA)/GCE (d) at scan rate of 0.1 V s^{-1}.

6.6.3. Effect of pH

The effect the pH of PBS on the electrochemical response for UA at MWCNTs/poly(AHNSA)/ GCE was studied over pH range 5.0−8.5 by cyclic voltammetry. As shown in Figure 6.56, the anodic peak current of UA at MWCNTs/poly(AHNSA)/GCE increased with increasing of pH until it attained the maximum at pH 7.0, and then decreased rapidly when the pH increased. Thus, pH 7.0 was chosen as the optimum value for subsequent experiments.

Furthermore, the effect of solution pH on the peak potential for UA at MWCNTs/poly(AHNSA)/GCE was studied. The potential shifted negatively with increasing pH, suggesting the involvement of protons in electrochemical process of UA (Figure 6.57). The relationship between the peak potential and the pH can be described as: E_{pa}(V) = -0.061pH + 0.840, R^2 = 0.9977. The slope 0.061 V/pH is close to the theoretical value 0.059 V/pH (at 25 ^{o}C)

given by the Nernstian equation [205], which indicates equal numbers of protons and electrons participatein the oxidation of UA as described in Scheme 11.

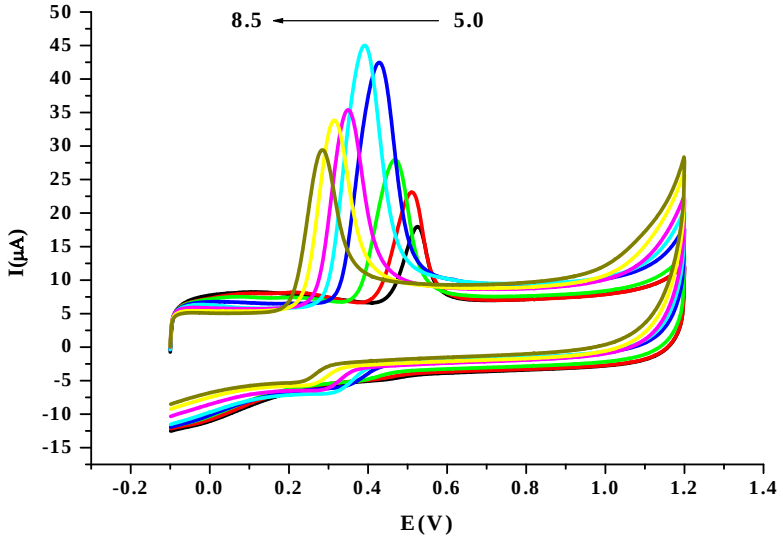

Figure 6.56. Cyclic voltammograms for 1.0 mM UA in 0.1 M PBS of various pH (pH 5.0-8.5) at MWCNTs/poly(AHNSA)/GCE at scan rate of 0.1 V s^{-1}.

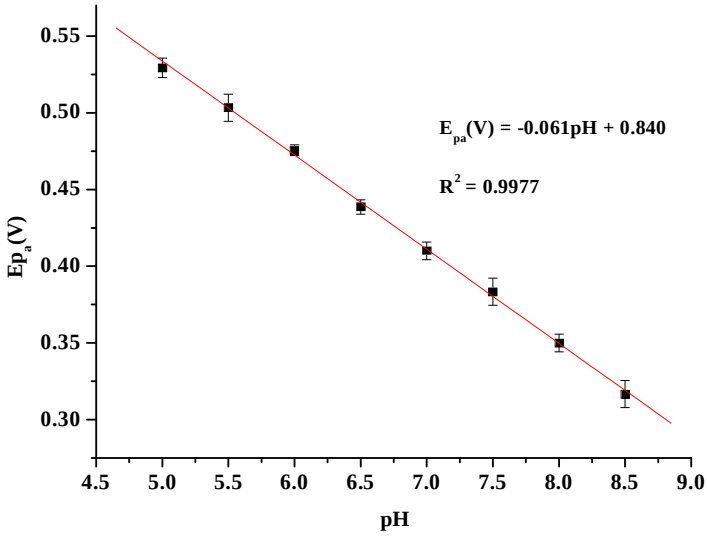

Figure 6.57. Effects of pH on the anodic peak potential for 1.0 mM UA in PBS at scan rate of 0.1 V s^{-1}.

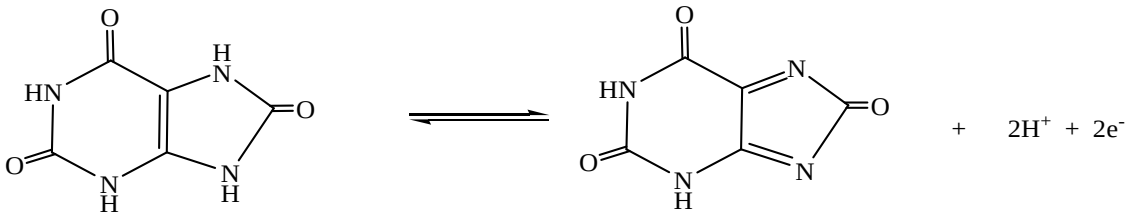

Scheme 11. Mechanism of UA oxidation

6.6.4. Effect of scan rate

The kinetics of the electrode reaction was investigated by studying the influence of scan rate on the anodic oxidation peak current of UA. Figure 6.58 shows the influence of scan rate on the oxidation peak current of UA at the MWCNTs/poly(AHNSA)/GCE. The oxidation peak current of UA in PBS (pH 7.0) increased with increase in scan rate over the range 0.050 to 0.25 V s^{-1}. The anodic peak currents showed a linear relationship with the scan rate and the linear regression equation obtained is: $I_{pa}(\mu A) = 251\nu(V/s) + 14.15$, $R^2 = 0.9982$. This indicating that the oxidation of UA at the MWCNTs/poly(AHNSA)/GCE is an adsorption-controlled process (in set of Figure 6.58). In addition, the oxidation peak potentials of UA shifted slightly in a positive direction with an increase in scan rate, demonstrating that the electrode reaction is quasi-reversible.

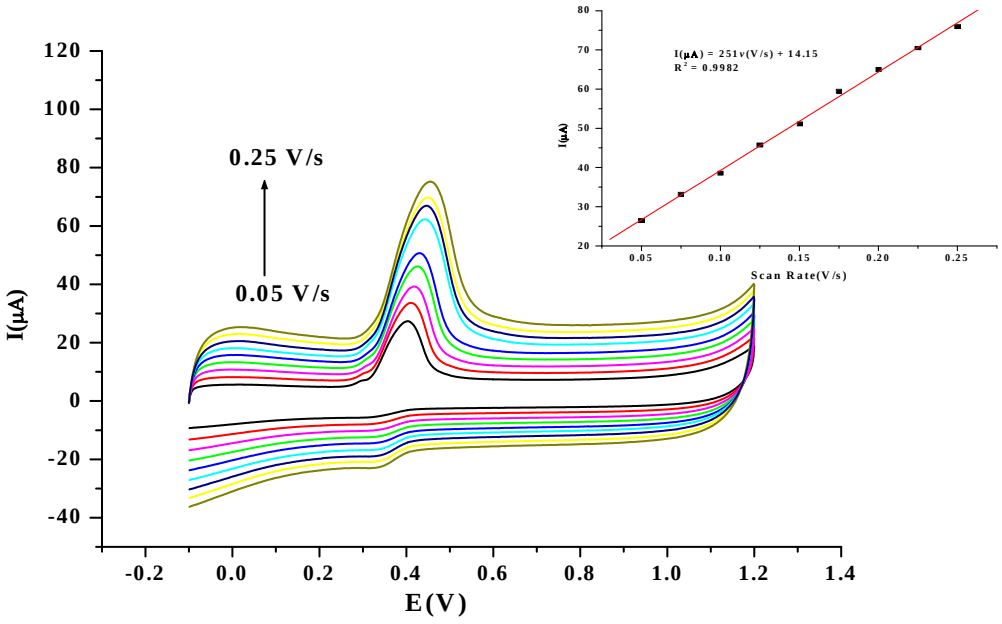

Figure 6.58. Cyclic voltammograms for 1.0 mM UA in PBS (pH 7.0) at various scan rates (0.05–0.25 V s^{-1}). Inset: plot of peak currents *vs* scan rates.

6.6.5. Accumulation potential and time

Since the electrochemical oxidation of UA at MWCNTs/poly(AHNSA)/GCE is an adsorption-controlled process, accumulation potential and time can influence on the magnitude of the peak current. The effect of accumulation potential on the oxidation peak current for 0.1 mM UA in PBS of pH 7.0 was studied using square wave voltammetry over the range 70 mV to 280 mV (Figure 6.59A). A maximum peak current was observed at 180 mV and then it decreased with increasing potential. Therefore, 180 mV deposition potential was selected as the accumulation potential for further measurements.

On the other hand, the effect of accumulation time on the oxidation peak current for 0.1 mM UA was also investigated, and the results are illustrated in Figure 6.59B. The peak current increased rapidly with increasing accumulation time in the range 30–60 s and remained almost unchanged

when the accumulation time was further increased due to surface saturation of the electrode. Consequently, accumulation time of 60 s was selected as the optimum accumulation time for further studies.

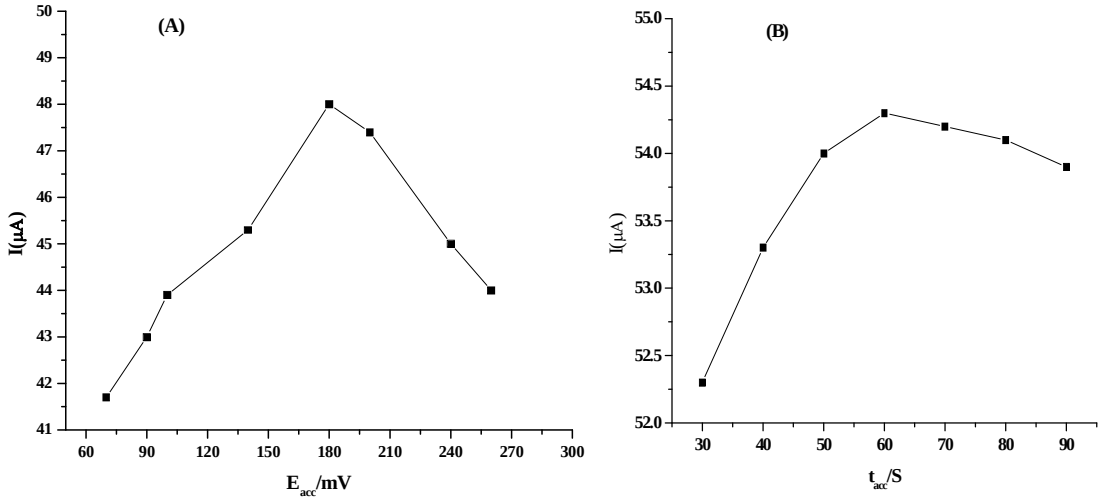

Figure 6.59. Effect of accumulation potential (A) and accumulation time (B) on the peak current for 0.1 mM UA.

6.6.6. Calibration curve

Under the optimum conditions, the oxidation peak currents for various concentrations of UA were recorded by SWV. A linear relationship between the oxidation peak current and the concentration of UA was obtained in the range 1.0 μM to 100 μM in PBS of pH 7.0 (Figure 6.60). The linear regression equation of the oxidation peak current versus concentration for this range is: $I_{pa}(\mu A) = 0.462C(\mu M) + 10.29$, $R^2 = 0.9972$. The detection limit calculated to be 0.046 μM based on the three times signal-to-noise ratio (3S/N).

The linear range and detection limit for UA at the MWCNTs/poly(AHNSA)/GCE were compared with those reported in the literature (Table 6.16). The sensor exhibited low detection

limits compared with reported values. Besides, the preparation of the modification was very simple and not time consuming.

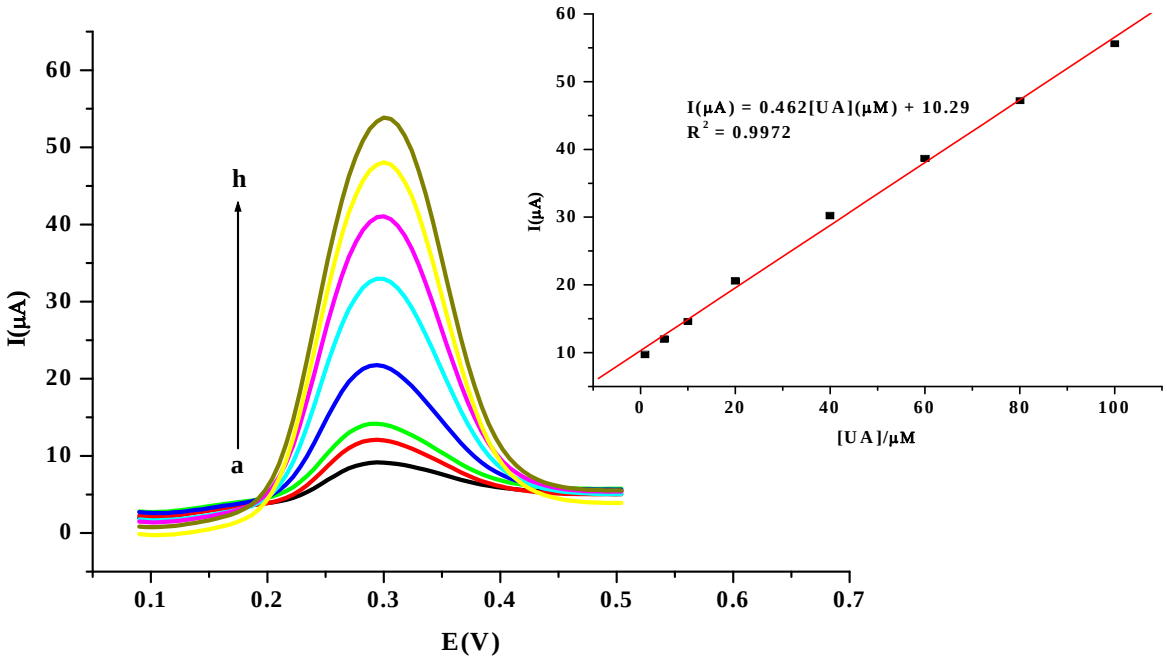

Figure 6.60. Square wave voltammograms responses for various concentrations of UA in PBS pH 7.0 (from a to h): 1.0, 5.0, 10, 20, 40, 60, 80 and 100 μM at MWCNTs/poly(AHNSA)/GCE. Inset: plot of peak current *vs* the concentration of UA.

Table 6.16. Comparison of the electrode with previously reported electrodes for the determination of UA.

Electrode	Method	L. Range (μM)	D. Limit (μM)	References
PtNSs/C60/GCE	DPV	9.5–1187	0.63	[360]
SnO_2/graphene/GCE	SWV	0.1–200	0.28	[362]
Poly(glyoxal-bis(2-hydroxyanil))/GCE	DPV	1.0–200	0.3	[363]
Reduced graphene oxide/GCE	DPV	0.5–60	0.5	[364]
Poly-(luminol)/GCE	DPV	0.3-100	2	[366]
NanoSnO_2/MWCNTs/Cpe(sim)	DPV	3–200	1.0	[371]
Poly(Aspartic Acid)AgNPs/GCE	LSV	5–100	0.3	[372]
Graphene/GCE	CV	2–120	0.6	[373]
Cetylpyridinium chloride /GCE	DPV	0.50–110	0.13	[374]
MWCNTs/poly(AHNSA)/GCE	SWV	1-100	0.046	This work

6.6.7. Repeatbility and stability

The repeatability of the modified electrode was investigated in ten successive measurement of the current response for $1x10^{-5}$ M UA under the same experimental conditions. The RSD of the response was found to be 2.3%, which suggests good repeatability of the measurement at the modified electrode. The stability of the sensor was also determined. The stability of the MWCNTs/poly(AHNSA)/GCE towards UA oxidation was also evaluated by measuring the response for $1x10^{-5}$ M UA in 0.1 M PBS (pH 7.0) by keeping the electrode in a buffer solution for a week. The current response decreases only 2.3%, suggesting that MWCNTs/poly(AHNSA)/GCE has a good stability.

6.6.8. Interference study

To assess the selectivity of the MWCNTs/poly(AHNSA)/GCE, the influence of possible interferents which may coexist with uric acid in real samples on the electrochemical determination of 20 μM uric acid was examined under the optimum conditions. The tolerance limit was defined as the maximum concentration of potentially interfering species, with a relative error of less than 5%. As shown in Table 6.17, a 100-fold excess concentrations of Co^{2+} and Cu^{2+}, and 50-fold concentrations of ascorbic acid, glucose and urea were shown no interference on the response current of UA (signal change below 5%), indicating that MWCNTs/poly(AHNSA)/GCE possessed excellent selectivity towards UA.

Table 6.17. Effects of interferences on the response of UA.

Interferent	Conc.(μM)	Signal change (%)
AA	1000	+4.3
Glucose	1000	+2.3
Urea	1000	+4.1
Co^{2+}	2000	+1.5
Cu^{2+}	2000	-3.1

6.6.9. Applications

The applicability of the MWCNTs/poly(AHNSA)/GCE sensor for the determination of UA was tested for urine samples collected from a normal person. After diluting the urine sample with PBS pH 7.0, an oxidation peak was appeared at 0.24 V. To confirm the oxidation peak was due to UA, the sample was spiked with known concentrations of standard UA. As can be seen in Figure 6.61, the standard solution of UA added to the urine sample caused an increase in the oxidation peak current, which confirmed that the peak observed for the urine sample was due to the oxidation of UA.

In addition, in order to evaluate the validity of the developed method for the determination of UA in urine samples, standard addition method was applied by spiking urine samples with different concentration of standard UA solutions. The percent recoveries were found in the range 92.0% to 102.9% (Table 6.18). These results indicate that MWCNTs/poly(AHNSA)/GCE has good reliability for detecting UA in human urine.

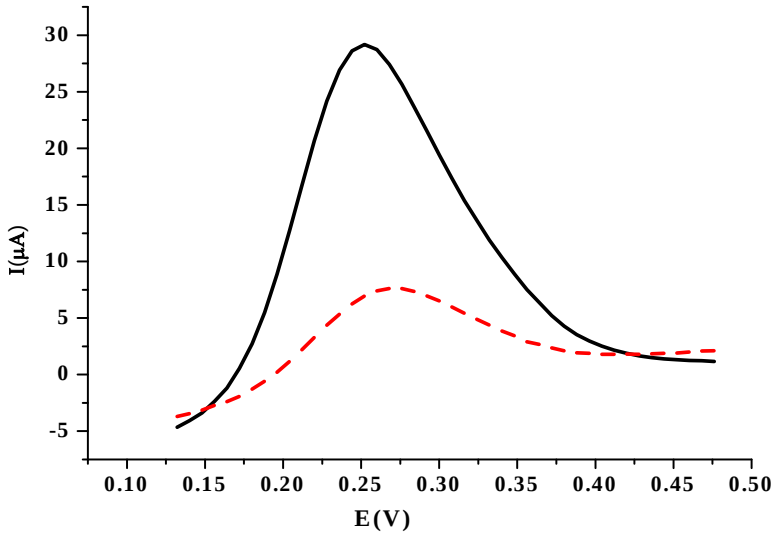

Figure 6.61. Square wave voltammograms of urine sample diluted with 0.1 M PBS (pH 7.0) (dash line) and after addition of 50 μM UA to the urine sample (solid line).

Table 6.18. Recovery study of UA in urine sample (n = 3)

Sample	Added (μM)	Found (μM)	Recovery (μM)
	-	6.12	-
Urine	15	21.57(±0.42)	102.9 (±2.81)
	25	31.71(±1.16)	102.4(±3.37)
	40	42.84(±0.74)	92.0(±1.73)

7. CONCLUSIONS

In this study, different types of electrochemical sensors were developed for the analysis of selected pesticides (phoxim, phenothrin, fenitrothion and endosulfan) and pharmaceuticals (caffeine, paracetamol and uric acid).

Cobalt nanoparticles (CoNPs) were synthesized and CoNPs/GCE was prepared by drop coating the nanoparticles on GCE. After preparing PPy/GCE using electropolymerization of pyrrole in $LiClO_4$ solution, the CoNPs/PPy/GCE composite electrode was fabricated by drop coating the CoNPs on the PPy/GCE. Different characterization techniques such as transmission electron microscopy, scanning electron microscopy, UV–vis spectroscopy, FTIR and energy dispersive spectroscopy (EDS) were used to study the morphological structure and surface analysis of the prepared sensors. Among all electrodes, CoNPs/PPy/GCE exhibited highest electroactive surface area and lowest electron transfer resistance towards phoxim. Besides, the composite electrode demonstrated excellent reproducibility, good stability and selectivity towards the possible interfering substances. All of these properties proved CoNPs/PPy/GCE a suitable electrochemical sensor for the electrochemical determination of phoxim in water samples by square wave voltammetry.

A new and sensitive electrochemical sensor for the determination of phenothrin is reported based on graphene oxide–polypyrrole modified glassy carbon electrode. Graphene oxide was successfully prepared from graphite and electropolymerized in a mixture containing pyrrole in $LiClO_4$ by cyclic voltammetry. The characterization of the composite film was performed by FTIR, UV-Vis, Raman spectroscopy, EIS, cyclic voltammetry and SEM. The characterization results confirmed that GO/PPy composite was synthesized successfully. Phenothrin showed an adsorption-controlled irreversible electron transfer reaction at GO/PPy/GCE. The electrode showed reproducible measurements, better selectivity and good recovery for the determination of phenothrin in fruit juice samples.

A sensor for fenitrothion was prepared by drop coating MWCNTs on to GCE. The MWCNTs/GCE exhibited an excellent electrocatalytic activity in lowering overpotential and a

significant enhancement of the peak current of fenitrothion as compared to the bare electrode, with a wider linear range, higher sensitivity and less than 5% reproducibility. The developed sensor was successfully applied for the determination of fenitrothion in soil and teff samples with a good recovery without the interference of coexisting species.

MF/GCE was prepared for the electroanalysis of endosulfan and it showed a better electrocatalytic activity towards the reduction of endosulfan. Compared with other electrodes available in the literature, low detection limit was obtained at MF/GCE. This low detection limit indicate that the electrochemical sensor is suitable for trace analysis. In addition, the method was also successfully applied for the detection of endosulfan in onion and tomato samples.

Caffeine and paracetamol were determined simultaneously at poly(4-amino-3-hydroxynaphthalene sulfonic acid) modified glassy carbon electrode. The electrode exhibited an enhancement in the peak current and shifts of the peak potential towards negative potential. Besides, the low detection limit, wider linear range, high selectivity and stability of the sensor, the simultaneous determination of caffeine and paracetamol was possible with this electrode. Moreover, the electrode was also utilized successfully for the analysis of caffeine and paracetamol in Coca-Cola, Pepsi-Cola and tea samples.

Multi-walled carbon nanotubes coated poly(4-amino-3-hydroxynaphthalene sulfonic acid) modified glassy carbon electrode was applied for the determination of uric acid.. The MWCNTs/poly(AHNSA)/GCE exhibited higher sensitivity to uric acid as compared to the MWCNTs/GCE, poly(AHNSA)/GCE and the GCE. This is due to the synergistic effect of larger surface area, higher accumulation efficiency of the MWCNTs film and the electrostatic interaction between the hydroxyl, sulphonic and amine groups of the polymer with the uric acid. The composite modified electrode also showed remarkable electrochemical advantages such as, high reproducibility and stability, wide linear range and low detection limit. Moreover, the sensor was employed for the analysis of UA in human urine.

8. REFERENCES

[1] G. Denuault, Ocean Sci., 5 (2009), 697–710.

[2] J. Koryta, W. Dvorak, L. Kavan, Principles of Electrochemistry, 2nd Ed., John Wiley & Sons, New York. 1987.

[3] A. Shrivastava, J. Sharma, V. Soni, Bull. Facu. Pharm., 51 (2013), 113–129.

[4] B. Uslu, S. A. Ozkan, Anal. Lett., 44 (2011), 2644–2702.

[5] A. S. Ahammad, J. J. Lee, M. A. Rahman, Sens., 9 (2009), 2289–2319.

[6] L. Krejcova, D. Hynek, V. Adam, J. Hubalek, R. Kizek, Int. J. Electrochem. Sci., 7 (2012), 10779–10801.

[7] Y. Wang, H. Xu, J. Zhang, G. Li, Sens., 8 (2008), 2043–2081.

[8] G. Mostafa, Open Electrochem. J., 2 (2010), 22–42.

[9] M. R. Plata, A. M. Contento, A. Rios, Sens., 10 (2010), 2511–2576.

[10] G. Hanrahan, D. G. Patil, J. Wang, J. Environ. Monit., 6 (2004), 657–664

[11] M. R. Ganjali, S. R. Siadat, H. Rashedi, M. Rezapour, P. Norouzi, Int. J. Electrochem. Sci., 6 (2011), 3684–3693.

[12] J. R. Stetter, W. R. Penrose, S. Yao, J. Electrochem. Soci., 150 (2003), 11–16.

[13] A. T. Law, S. B. Adeloju, Talanta, 114 (2013), 191–203.

[14] F. Akhgari, H. Fattahi, Y. M. Oskoei, .Sens. Actu. B, 221 (2015), 867–878.

[15] E. M. Garrido, C. D. Matos, J. L. Lima, A. M. O. Brett, Anal. Lett., 37 (2004) 1755–1791.

[16] A. Mulchandani, W. Chen, P. Mulchandani, J. Wang, K. R. Rogers, Biosen. Bioelectro., 16 (2001) 225–230.

[17] R. Ramachandran, V. Mani1, S. Chen, R. Saraswathi, B. Lou, Int. J. Electrochem. Sci., 8 (2013) 11680–11694.

[18] H. Ha, I. Kim, S. Hwang, R. S. Ruof, Electrochem. Solid State Lett., 14 (2011), 70–73.

[19] V. S. Bagotsky, Fundamentals of Electrochemistry, 2nd ed., Canada, John Wiley and Sons, 2006.

[20] P. Krzyczmonik, E. Socha, Chemik, 67 (2013), 801–810.

[21] K. Arshak, V. Velusamy, O. Korostynska, K. O. Stasiak, C. Adley, IEEE Sens. J., 9 (2009), 1942–1951.

[22] J. S. Hwang, T. H. Oh, S. H. Kim, S. S. Han, S. J. Lee, S. G. Lee, Y. J. Lee, S. S. Jang, J. Appl. polym. sci., 1 (2015), 1–6.

[23] J. Huang, Pure Appl. Chem., 78 (2006), 15–27.

[24] N. Gupta, S. Sharma, I. A. Mir, D. Kumar, J. Scien. Ind. Res., 65 (2006), 549–557.

[25] C. G. Zoski, Hand book of Electrochemistry, Amsterdam, Elsevier B. V, 2007.

[26] V. L. Finkenstadt, Appl. Microbiol. Biotechnol., 67 (2005) 735–745.

[27] F. Scholz, Electroanalytical Methods: Guide to Experiments and Applications, 2nd, Revised and extended ed., Springer-Verlag, Berlin, 2010.

[28] D. W. Hatchett, M. Josowicz, Amer. Chem. Soc., 1 (2008), 1–24.

[29] D. Cirmi, R. Aydın, F. Koleli, J. Electroanal. Chem., 736 (2015), 101–106

[30] S. Bilal, M. Sohail, A. A. Shah, J. Chem. Soc. Pak., 36 (2014), 976–982

[31] R. Ansari, Int. J. Chem. Tech. Res., 1 (2009), 1398–1402

[32] Y. Liu, K. Yang, Electrochim. Acta, 51 (2006), 5376–5382.

[33] J. Tabaciarova, M. Micusik, P. Fedorko, M. Omastova, Polymer Degra. Stab., 120 (2015), 392–401.

[34] J. V. Thombare, M. C. Rath, S. H. Han, V. J. Fulari, Mater. Phys. Mech., 16 (2013), 118–125.

[35] R. Ansari, J. Chem., 3 (2006), 186–201.

[36] D. Brezoi, J. Sci. Arts, 1 (2010), 53–58.

[37] S. Shahrokhian, M. Azimzadeh, P. Hosseini, RSC Adv., (2014), 1–33.

[38] S. Sadki, P. Schottland, N. Brodie, G. Sabouraud, Chem. Soc. Rev., 29 (2000), 283–293.

[39] T. Tsai, K. Lin, S. Chen, Int. J. Electrochem. Sci., 6 (2011), 2672–2687.

[40] P. Lepez, M. Guix, S. Alegret, A. Merkoci, Anal. Chem., (2005), 10–17.

[41] V. Sreeja, R. Sasikumar, M. Alagarsamy, P. Manisankar, Amer. J. Anal. Chem., 2 (2011) 814–819.

[42] E. N. Primo, F. A. Gutierrez, G. L. Luque, P. R. Dalmasso, A. Gasnier, Y. Jalit, M. Moreno, M. V. Bracamonte, M. E. Rubio, M. L. Pedano, M. C. Rodriguez, N. F. Ferreyra, M. D. Rubianes, S. Bollo, G. A. Rivas, Anal. Chim. Acta, 805 (2013), 19–35.

[43] M. E. G. Lyons, G. P. Keeley, Int. J. Electrochem. Sci., 3 (2008), 819–853.

[44] C. Guzman, G. Orozco, Y. Verde, S. Jimenez, L. A. Godinez, E. Juaristi, E. Bustos, Electrochim. Acta, 54 (2009), 1728–1732.

[45] A. B. Kaiser, Adv. Mater., 13 (2001), 927–941.

[46] A. Merkoc¸ M. Pumera, X. Llopis, B. Perez, M. Valle, S. Alegret, Trends Anal. Chem., 24 (2005), 826-838.

[47] R. C. Carvalho, C. G. Caridade, C. M. A. Brett, Anal. Bioanal. Chem., 398 (2010), 1675–1685.

[48] R. P. Raffaelle, B. J. Landi, J. D. Harris, S. G. Bailey, A. F. Hepp, Mater. Sci. Engin. B, 116 (2005), 233–243.

[49] O. Breuer, U. Sundararaj, Poly. Compos., 25 (2004), 630–641.

[50] Y. Wang, J. T. Yeow, J. Sens., 2009, 1–24.

[51] N. S. Lawrence, R. P. Deo, J. Wang, Electroanalysis, 17 (2005), 65–72.

[52] H. Chu, L. Wei, R. Cui, J. Wang, Y. Li, Coord. Chem. Reviews, 254 (2010), 1117–1134.

[53] R. C. Alkire, D. M. Kolb, J. Lipkowski, P. N. Ross, Advances in Electrochemical Science and Engineering, WILEY-VCH Verlag GmbH, Germany, 2009.

[54] F. Borondics, M. Bokor, P. Matus, K. Tompa, S. Pekker, Fullerenes, Nanotub. Carbon Nanostru., 13 (2005), 375–382.

[55] H. Kuzmany, A. Kukovecz, F. Simon, M. Holzweber, C. Kramberger, T. Pichler, Syn. Metals, 141 (2004), 113–122.

[56] J. Zhang, Z. Zhu, J. Zhu, K. Li, S. Hu, Int. J. Electrochem. Sci., 9 (2014), 1264–1272.

[57] Y. M. Gonzalez, J. C. Remigy, Mater. Lett., 65 (2011), 229–232.

[58] A. M. Hernandez, C. V. Santos, V. M. Castano, Current Nanosci., 6 (2010), 12–39.

[59] A. Merkoci, Microchim Acta, 152 (2006), 152, 157–174.

[60] S. Chen, S. Li, R. Thangamuthu, Electroanalysis, 21 (2009), 1505–1513.

[61] W. Badawy, K. Ismail, S. Medany, Int. J. Sci., 6 (2011), 4205–4217.

[62] H. Zare, N. Rajabzadeh, N. Nasirizadeh, M. Ardakani, J. Electroanal. Chem., 589 (2006), 60–69.

[63] G. Milczarek, A. Ciszewski, Electroanalysis, 15 (2003), 529–532.

[64] A. Malinauskas, J. Malinauskiene, A. Ramanavicius, Nanotechno., 16 (2005) 51–62.

[65] V. Ijeri, A. Srivastava, Fresenius J. Anal. Chem., 367 (2000), 373-377.

[66] C. Demirtas, S. Yilmaz, G. Saglikoglu, M. Sadikoglu, Int. J. Electrochem. Sci., 10 (2015) 1883–1892.

[67] A. A. Ciucu, J. Biosens. Bioelectron., 5 (2014), 2–10.

[68] J. Wang, Analytical Electrochemistry, 3rd edn., Wiely-VCH, New Jersy, 2006.

[69] J. Zen, A. S. Kumar, D. Tsai, Electroanalysis, 15 (2003), 1073–1087.

[70] A. Chira, B. Bucur, M. Radulescu, T. Galaon, G. Radu, Int. J. Electrochem. Sci., 9 (2014) 4493–4511.

[71] H. Bai, G. Shi, Sens., 7 (2007), 267–307.

[72] D. C. Tiwari, R. Jain, S. Sharma, J. Sci. Ind. Res., 66 (2007), 1011–1018.

[73] Y. Umasankar, A. P. Periasamy, S. Chen, Anal. Biochem., 411 (2011), 71–79.

[74] A. D. Arulraj, M. Vijayan, V. S. Vasantha, Anal. Chim. Acta, 899 (2015), 66–74.

[75] S. Yalcmkaya, C. Demirbilek, C. O. Dinc¸ Poly. Bull., 72 (2015), 2843–2855.

[76] B. I. Nandapure, S. B. Kondawar, M. Y. Salunkhe, A. I. Nandapure, Adv. Mater. Lett. 4 (2013), 134–140.

[77] N. F. Atta, A. Galal, E. E. Ads, Int. J. Electrochem. Sci., 9 (2014), 2113–2131.

[78] A. B. Moghaddam, M. R. Ganjali, A. Saboury, A. M. Movahedi, P. Norouzi, J. Appl. Electrochem., 38 (2008), 1233–1239.

[79] B. Muralidharan, G. Gopu, S. Laya, C. Vedhi, P. Manisankar, Mater. Sci., Appl., 2 (2011), 957–963.

[80] M. R. Mahmoudian,Y. Alias, W. J. Basirun, P. M. Woi, S. Baradaran, M. Sookhakian, Ceramics Int., 40 (2014), 9265–9272.

[81] L. Phelane, F. N. Muya, H. L. Richards, P. G. Baker, E. I. Iwuoha, Electrochim. Acta, 128 (2014), 326–335.

[82] K. Ghanbari, N. Hajheidari, J. Polymer Res., 22 (2015), 152–161.

[83] S. Ulubay, Z. Dursun, Talanta, 80 (2010), 1461–1466.

[84] I. Razavipanah, G. H. Rounaghi, M. H. Zavvar, Anal. Lett., 47 (2014), 117–133.

[85] L. Mikoliunaite, R. Kubiliute, A. Popov, J. Voronovic, S. Sakirzanovas, A. Ramanaviciene, A. Ramanavicius, Chemija, 25 (2014), 63–69.

[86] S. Singh, D. S. Jain, M. L. Singla, Anal. Methods, 5 (2013), 1024–1032.

[87] J. Li, H. Xie, Y. Li, J. Solid State Electrochem., 16 (2012), 795–802.

[88] M. Lin, RSC Adv., 5 (2015), 9848–9851.

[89] M. R. Mahmoudian, Y. Alias, W. J. Basirun, Mater. Chem. Phys., 141 (2013), 298–303.

[90] B. Paulchamy, G. Arthi, B. D. Lignesh, J. Nanomed. Nanotechnol., 6 (2015), 1–4.

[91] Z. Qiong, H. Y. Qiu, C. X. Gang, H. D. Hu, L. L. Jiang, Y. Ting, J. L. Li, Chinese Sci. Bull., 56 (2011), 331–339.

[92] H. Feng, B. Wang, L. Tan, N. Chen, N. Wang, B. Chen, J. Power Sour., 246 (2014), 621-628.

[93] D. Chen, H. Feng, J. Li, Chem. Rev., 112 (2012), 6027−6053.

[94] B. Wang, J. Qiu, H. Feng, E. Sakai, Electrochim. Acta, 151 (2015), 230–239.

[95] W. Lin, H. Chang, R. Wu, Sens. Actuat. B, 181 (2013), 326–331.

[96] P. A. Basnayaka, M. K. Ram, L. Stefanakos, A. Kumar, Graphene, 2 (2013), 81–87.

[97] Y. Liu, Y. Zhang, G. Ma, Z. Wang, K. Liu, H. Liu, Electrochim. Acta, 88 (2013), 519–525.

[98] H. Zhou, G. Han, Y. Xiao, Y. Chang, H. Zhai, J. Power Sour., 263 (2014), 259–267.

[99] W. Liu, Y. Fang, P. Xu, Y. Lin, X. Yin, G. Tang, M. He, ACS Appl. Mater. Interf., 6 (2014), 16249−16256.

[100] P. M. Nia, W. P. Meng, F. Lorestani, M. R. Mahmoudian, Y. Alias, Sens. Actu. B, 209 (2015), 100–108.

[101] K. Ho, A. Balamurugan, S. Chen, K. Lin, Int. J. Electrochem. Sci., 6 (2011), 4822–4828.

[102] A. Geto, M. Amare, M. Tessema, S. Admassie, Anal. Bioanal. Chem., 404 (2012), 525–530.

[103] A. Geto, M. Amare, M. Tessema, S. Admassie, Electroanalysis, 24 (2012), 659–665.

[104] M. Amare, W. Lakew, S. Admassie, Anal. Bioanal. Electrochem., 3 (2011), 365–378.

[105] M. Amare, S. Admassie, Bull. Chem. Soc. Ethiop., 26 (2012), 73–84.

[106] M. Amare, S. Abicho, S. Admassie, J AOAC Inter., 97 (2014), 580–585.

[107] G. C. Marjanovic, B. Marjanovic, I. Juranic, P. Holler, J. Stejskal, M. Trchova, Mater. Sci. Forum., 518 (2006), 405–410.

[108] J. B. Raoof, M. Baghayeri, R. Ojani, Anal. Bioanal. Electrochem., 6 (2014), 170–182.

[109] M. Afrasiabi, Z. R. Zad, S. Kianipour, A. Babaei, A. R. Taheri, J. Chem. Soc. Pak., 35 (2013), 1106–1112.

[110] A. Babaei, D. J. Garrett, A. J. Downard, Electroanalysis, 23 (2011), 417–423.

[111] A. R. Sikkander, C. Vedhi, P. Manisankar, Int. J. Indust. Chem. 3 (2012), 2–8.

[112] H. R. Zare, N. Nasirizadeh, J. Iran. Chem. Soc., 8 (2011), 55–66.

[113] P. S. Narayan, N. L. Teradal, S. S. Kalanur, J. Seetharamappa, Electroanalysis, 25 (2013), 2684–2690.

[114] J. Dong, X. Wang, F. Qiao, P. Liu, S. Ai, Sens. Actuat. B, 186 (2013), 774–780.

[115] K. A. Joshi, J. Tang, R. Haddon, J. Wang, Electroanalysis, 17 (2005), 54–58.

[116] Y. Umasankar, Y. Li, S. Chen, J. Electrochem. Soc., 157 (2010), 187–193.

[117] G. March, T. D. Nguyen, B. Piro, Biosens., 5 (2015), 241–275.

[118] V. Branzoi, F. Branzoi, A. Musina, L. Pilan, Rev. Roum. Chim., 56 (2011), 73–84.

[119] M. K. Sahoo, S. Sahoo, Adva. Appl. Sci. Res., 5 (2014), 66–74.

[120] H. J. Salavagione, A. D. Pascual, E. Lazaro, S. Vera, M. A. G. Fatou, J. Mater. Chem. A, 2 (2014), 14289–14328.

[121] K. Lin, P. Yeh, S. Chen, Int. J. Electrochem. Sci., 7 (2012), 12752–12763.

[122] P. A. Sundari, P. Manisankar, J. Braz. Chem. Soc., 22 (2011), 746–755.

[123] S. Ebrahim, R. E. Raey, A. Hefnawy, H. Ibrahim, M. Soliman, T. A. Fattah, Syn. Metals, 190 (2014), 13–19.

[124] P. Manisankar, P. L. Sundari, R. Sasikumar, D. J. Roy, Electroanalysis, 20 (2008), 2076–2083.

[125] C. M. A. Brett, V. A. Alves, D. A. Fungaro, Electroanalysis, 13 (2001), 212–218.

[126] J. Barek, A. G. Fogg, A. Muck, J. Zima, Critical Rev. Anal. Chem., 31 (2001), 291–309.

[127] L. C. Filho, V. B. Santos, B. C. Janegitz, T. B. Guerreiro, O. F. Filho, R. C. Faria, L. M. Junior, Electroanalysis, 22 (2010), 1260–1266.

[128] M. M. Ghoneim, A. M. Hassanein, N. A. Salahuddin, H. S. E. Desoky, M. N. Elfiky, J. Braz. Chem. Soc., 23 (2012), 1594–1605.

[129] B. Yosypchuk, M. Fojta, J. Barek, Electroanalysis, 22 (2010), 1967–1973.

[130] V. Arancibia, E. Nagles, C. Rojas, M. Gomez, Sens. Actu., B, 182 (2013), 368–373.

[131] T. Navratil, I. Svancara, K. Mrazova, K. Novakova, I. Sestakova, M. Heyrovsky, D. Pelclova, Electroanalysis, 6 (2011), 23–53.

[132] R. Gulaboski, C. M. Pereira, Handbook of Food Analysis Instruments, Electroanalytical Techniques and Instrumentation in Food Analysis, 26 (2008).

[133] O. A. Farghaly, R. A. Hameed, A. A. Nawwas, Int. J. Electrochem. Sci., 9 (2014), 3287–3318.

[134] F. G. Thomas, G. Henze, Introduction to Voltammetric Analysis Theory and practice, CSIRO Publishing, Australia, 2001.

[135] N. R. Stradiotto, H. Yamanaka, M. V. Zanoni, J. Braz. Chem. Soc., 14 (2003), 159–173.

[136] A. J. Bard, L. R. Faulkner, Electrochemical methods Fundamentals and Applications, 2nd edn., John Wiley & Sons, Inc., 2001.

[137] K. C. Leandro, J. D. Carvalho, L. F. Giovanelli1, J. C. Moreira, Braz. J. Pharm. Sci. 45 (2009), 331–337.

[138] U. Guth, W. Vonau, J. Zosel, Meas. Sci. Technol., 20 (2009), 1–14.

[139] C. M. A. Brett, Pure Appl. Chem., 73 (2001), 1969–1977.

[140] V. Mirceski, R. Gulaboski, M. Lovric, I. Bogeski, R. Kappl, Electroanalysis, 25 (2013), 1–11.

[141] V. Mirceski, S. K. Lovric, M. Lovric, Square-Wave Voltammetry Theory and Application, Springer-Verlag Berlin Heidelberg, 2007.

[142] E. Katz, I. Willner, Electroanalysis, 15 (2003), 913–947.

[143] M. Shamsipur, M. Asgari, M. F. Mousavi, R. Davarkhah, Electroanalysis, 24 (2012), 357–367.

[144] B. Rafiee, A. Fakhari, M. Ghaffarzadeh, Sens. Actu. B., 218 (2015), 271–279.

[145] Z. Zhang, Q. Jiang, Y. Liu, X. Sun, Y. Kong, H. Xi, Int. J. Electrochem. Sci., 10 (2015), 3478–3488.

[146] A. S. Hamdy, E. Shenawy, T. E. Bitar, Int. J. Electrochem. Sci., 1 (2006), 171–180.

[147] Q. Wang, J. Moser, M. Gratzel, J. Phys. Chem. B, 109 (2005), 14945–14953.

[148] C. M. A. Brett, A. M. O. Brett, Electrochemistry Principles, Methods, and Applications, Oxford University Press Inc., New York, 1994.

[149] N. Perez, Electrochemistry and Corrosion Science, Kluwer Academic Publishers New York, 2004.

[150] M. Shamsipur, Z. Karimi, M. A. Tabrizi, Mater. Sci. Engin. C, 56 (2015), 426–431.

[151] X. Huang, Y. Li, Y. Chen, L. Wang, Sens. Actu. B, 134 (2008), 780–786.

[152] M. Shamsipur, M. Asgari, M. Maragheh, A. M. Movahedi, Bioelectrochem., 83 (2012), 31–37.

[153] Y. Li, S. Chen, Int. J. Electrochem. Sci., 7 (2012), 2175–2187.

[154] V. Hodoroaba, S. Rades, W. E. Unger, Surf. Interface Anal., 1 (2014), 1–4.

[155] A. J. Schwoeble, D. L. Exline, Current Methods in Forensic Gunshot Residue Analysis, CRC Press, USA, 2000.

[156] E. Bettens, D. V. Dyck, A. J. Dekker, J. Sijbers, A. V. Bos, Ultramicros., 77 (1999), 37–48.

[157] K. Yehliu, R. V. Wal, A. L. Boehman, Combu. Flame, 158 (2011), 1837–1851.

[158] C. Kisielowski, Z. L. Weberb, E. R. Weber, Braz. Phys., 26 (1996), 83–94.

[159] M. Lentzen, Microsci. Microanal., 12 (2006), 191–205.

[160] P. Marcus, F. Mansfeld, CRC Press, USA, 2006.

[161] R. M. Amir, F. M. Anjum, M. Khan, M. R. Khan, I. Pasha, M. Nadeem, J. Food Sci. Technol. 50 (2013), 1018–1023.

[162] G. E. A. Swann, S. V. Patwardhan, Clim. Past, 7 (2011), 65–74.

[163] S. G. Kazarian, K. L. Chan, Biochim. Biophys. Acta, 1758 (2006), 858–867.

[164] B. Stuart, Infrared Spectroscopy: Fundamentals and Applications, John Wiley & Sons, Ltd, England, 2004.

[165] E. Smith, G. Dent, Modern Raman Spectroscopy –A Practical Approach, John Wiley & Sons Ltd, England, 2005.

[166] R. Desai, V. Mankad, S. K. Gupta, P. K. Jha, Nanosci. Nanotechno. Lett., 4 (2012), 30–34.

[167] M. M. Rodriguez, C. W. V. Neste, L. R. Senesac, S. M. Mahajan, T. Thundat, Sens. Actu. B 161 (2012), 961–966.

[168] F. W. Fifield, D. Kealey, Principles and Practice of Analytical Chemistry, 5th ed., Blackwell Science Ltd, Germany, 2000.

[169] F. Guo, H. Zheng, Z. Yang, Y. Qian, Mater. Let., 56 (2002), 906–909.

[170] M. F. Hanifah, J. Jaafar, M. Aziz, A. F. Ismail, M. A. Rahman, M. H. D. Othman, J. Techno., 74 (2015), 195–198.

[171] J. Svitkova, M. Machkova, P. S. Cinkova, L. Svorc, Acta Chimica Slovaca, 5 (2012), 42–46.

[172] T. F. Kang, F. Wang, L. P. Lu, Y. Zhang, T. S. Liu, Sens. Actu. B, 145 (2010), 104–109.

[173] X. Xue, Q. Wei, D. Wu, H. Li, Y. Zhang, R. Feng, B. Du, Electrochim. Acta, 116 (2014), 366–371.

[174] X. C. Fu, J. Zhang, Y. Y. Tao, J. Wu, C. G. Xie, L. T. Kong, Electrochim. Acta, 153 (2015), 12–18.

[175] H. Yin, S. Ai, J. Xu, W. Shi, L. Zhu, J. Electroanal. Chem., 637 (2009), 21–27.

[176] B. B. Narakathu, W. Guo, S. O. Obare, M. Z. Atashbar, Sens. Actu. B, 158 (2011), 69–74.

[177] Y. Zhang, H. Liu, Z. Yang, S. Ji, J. Wang, P. Pang, L. Feng, H. Wang, Z. Wu, W. Yang, Anal. Methods, 7 (2015), 6213–6219.

[178] Y. Wang, J. Jin, C. Yuan, F. Zhang, L. Ma, D. Qin, D. Shana, X. Lu, Analyst, 140 (2015), 560–566.

[179] G. Hamscher, B. Priess, H. Nau, Anal. Chim. Acta, 586 (2007), 330–335.

[180] Z. Lv, L. Gao, H. Gao, Z. Hou, B. Zhang, J. Food Sci., 74 (2009), 37–41.

[181] P. Liang, J. Xu, L. Guo, F. Song, J. Sep. Sci., 29 (2006), 366–370.

[182] L. Guo, P. Liang, T. Zhang, Y. Liu, S. Liu, Chromatogr., 61 (2005), 523–526.

[183] P. Liang, L. Guo, Y. Liu, S. Liu, T. Z. Zhang, Anal. Chim. Acta, 586 (2007), 330–335.

[184] J. H. Lee, S. Park, W. Y. Jeong, H. J. Park, H. G. Kim, S. J. Lee, J. H. Shim, S. T. Kim, A. E. Aty, M. H. Im, O. J. Choi, S. C. Shin, Anal. Chim. Acta, 674 (2010), 64–70.

[185] C. Gu, B. Xiang, J. Xu, Spectrochimica Acta Part A: Mole. Biomole. Spectro., 97 (2012), 594–599.

[186] M. Fouladgar, Sens. Actu. B, 230 (2016), 456–462.

[187] M. Chao, M. Chen, Food Anal. Methods, 7 (2014), 1729–1736.

[188] Y. Zheng, A. Wang, H. Lin, L. Fu, W. Cai, RSC Adv., 5 (2015), 15425–15430.

[189] L. Wu, W. Lei, Z. Han, Y. Zhang, M. Xia, Q. Hao, Sens. Actu. B, 206 (2015), 495–501.

[190] X. Tan, J. Wu, Q. Hu, X. Li, P. Li, H. Yu, X. Li, F. Lei, Anal. Methods, 7 (2015), 4786–4792.

[191] R. Ramachandra, V. Mani, S. M. Chen, G. G. Kumar, M. Govindasamy, Int. J. Electrochem. Sci., 10 (2015), 859–869.

[192] A. Balamurugana, K. C. Ho, S. M. Chen, T. Y. Huang, Colloids and Surfaces A: Physicochem. Engin. Aspects, 362 (2010), 1–7.

[193] A. Ejaz, M. S. Ahmed, S. Jeon, Sens. Actu. B, 221 (2015), 1256–1263.

[194] E. H. Hess, T. Waryo, O. A. Sadik, E. I. Iwuoha, P. G. Baker, Electrochim. Acta, 128 (2014), 439–447.

[195] C. Merlini, B. S. Rosa, D. Muller, L. G. Ecco, S. D. Ramo, G. M. Barra, Poly. Testing, 31 (2012), 971–977.

[196] N. Su, H. B. Li, S. J. Yuan, S. P. Yi, E .Q. Yin, Poly. Lett., 6 (2012), 697–705.

[197] M. Choudhary, R. U. Islam, M. J. Witcomb, K. Mallick, Dalton Trans., 43 (2014), 43, 6396–6405

[198] O. Yeshchenko, I. Dmitruk, A. Alexeenko, A. Dmytruk, V. Tinkov, Physica E 41, (2008), 60–65.

[199] J. Zhang, C. Q. Lan, Mater. Lett., 62 (2008), 1521–1524.

[200] Z. Kaminskiene, I. Prosysevas, J. Stonkute, A. Guobiene, Acta Phys. Polonica A, 123 (2013), 111–114.

[201] J. A. Creighton, D. G. Eadon, J. Chem. Soc., Faraday Trans., 87 (1991), 3881–3891.

[202] Z. Shi, H. Liu, K. Lee, E. Dy, J. Chlistunoff, M. Blair, P. Zelenay, J. Zhang, Z. S. Liu, J. Phys. Chem. C, 115 (2011), 16672–16680.

[203] K. Sethi, I. Roy, J. Colloid and Interface Sci., 456 (2015), 59–65.

[204] X. Zheng, D. Tian, S. Duanb, M. Wei, S. Liu, C. Zhou, Q. Li, G. Wu, Electrochim. Acta, 130 (2014), 187–193.

[205] F. Q. Schafer, G. R. Buettner, Free radical Bio. Med., 30 (2001), 1191–1212.

[206] M. H. Mashhadizadeh, E. Afshar, Electrochim. Acta, 87 (2013), 816–823.

[207] B. Zargar, H. Parham, A. Hatamie, Anal. Methods, 7(2015), 1026–1035.

[208] X. Lu, H. Bai, Q. Ruan, M. Yang, G. Yang, L. Tan, Y. Yang, Intern. J. Envi. Anal. Chem., 88 (2008), 813–824.

[209] J. I. Gowda, S. T. Nandibewoor, Electrochim. Acta, 116 (2014), 326–333.

[210] C. F. Ramos, D. Satinsky, P. Solich, Talanta, 129 (2014), 579–585.

[211] S. Mukdasai, C. Thomas, S. Srijaranai, Talanta, 120 (2014), 289–296.

[212] Y. Wang, Y. Sun, Y. Gao, B. Xu, Q. Wu, H. Zhang, D. Song, Talanta, 119 (2014), 268–275.

[213] T. Yamada, S. Ueda, K. Yoshioka, S. Kawamura, T. Seki, Y. Okuno, N. Mikami, Toxico., 186 (2003), 227–239.

[214] Y. Wang, P. Zhang, B. Yang, C. Liu, J. Shu, Chemosphere, 90 (2013), 848–855.

[215] C. Corcellas, E. Eljarrat, D. Barcelo, Envir. Int., 75 (2015), 110–116.

[216] A. Saillenfait, D. Ndiaye, J. Sabate, Int. J. Hyg. Enviro. Health, 218 (2015), 281–292.

[217] D. Wang, D. P. Weston, M. J. Lydy, Talanta, 78 (2009), 1345–1351.

[218] K. Nagy, G. Racza, T. Matsumotoa, R. Adanya, B. Adam, Mutat. Res., 770 (2014), 1–5.

[219] H. Yan, J. Du, X. Zhang, G. Yang, K. H. Row, Y. Lv, J. Sep. Sci., 33 (2010), 1829–1835

[220] I. S. Roman, M. L. Alonso, L. Bartolome, R. M. Alonso, Talanta, 100 (2012), 246–253

[221] J. H. Borges, S. F. Garcia, A. Cifuentes, M. R. Delgado, J. Sep. Sci. 27 (2004), 947–963.

[222] F. E. Turrillas, A. Pastor, M. Guardia, Anal. Chim. Acta, 560 (2006), 118–127.

[223] X. Wang, Y. Yang, J. Dong, F. Bei, S. Ai, Sens. Actu. B, 204 (2014), 119–124.

[224] W. Yazhen, Q. Hongxin, H. Siqian, X. Junhui, Sens. Actu. B, 147 (2010), 587–592.

[225] T. Thriveni, J. Kumar, J. Lee, N. Sreedhar, Food Anal. Methods, 2 (2009), 66–72.

[226] L. Shahriary, A. A. Athawale, Int. J. Renewable Ener. Environ. Engin., 2 (2014), 1–6.

[227] D. C. Tiwari, P. Atri, R. Sharma, Syn. Metals, 203 (2015), 228–234.

[228] S. Konwer, R. Boruah, S. K. Dolui, J. electronic mater., 40 (2011), 2248–2255.

[229] M. Deng, X. Yang, M. Silke, W. Qiu, M. Xu, G. Borghs, H. Chen, Sens. Actu. B, 158 (2011) 176–184.

[230] S. Sahoo, G. Karthikeyan, G. C. Nayak, C. K. Das, Syn. Metals, 161 (2011), 1713–1719.

[231] D. N. Huyen, N. T. Tung, T. D. Vinh, N. D. Thien, Sens. 12 (2012), 7965–7974.

[232] J. V. Thombare, S. K. Shinde, G. M. Lohar, U. M. Chougale, S. S. Dhasade, H. D. Dhaygude, B. P. Relekar, V. J. Fulari, J. Semicond. 35 (2014), 1-4

[233] G. Lalwani, A. M. Henslee, B. Farshid, L. Lin, F. K. Kasper, Y. Qin, A. G. Mikos, B. Sitharaman, Biomacromolecules, 14 (2013), 900−909.

[234] S. Bose, N. H. Kim, T. Kuila, K. Lau, J. H. Lee, Nanotechno., 22 (2011), 1–12.

[235] C. Zhao, K. Shu, C. Wang, S. Gambhir, G. G. Wallace, Electrochim. Acta, 172 (2015), 12–19.

[236] X. Zhang, D. C. Zhang, Y. Chen, X. Z. Sun, Y. W. Ma, Chin. Sci. Bull, 57 (2012), 3045–3050.

[237] C. Fu, G. Zhao, H. Zhang, S. Li, Int. J. Electrochem. Sci., 8 (2013), 6269–6280.

[238] E. Laviron, J. Electroanal. Chem., 101 (1979), 19–28.

[239] L. Z. Melgar, S. A. Machad, J. Braz. Chem. Soc., 16 (2005), 743–748.

[240] F. Ahmadi, B. Jafari, Electroanalysis, 23 (2011), 675–682.

[241] N. Y. Sreedhar, P. R. Prasad, C. N. Reddy, K. S. Prasad, J. Nanosci. Nanotechno., 1 (2011), 6–11.

[242] R. G. Diagne, G. D. Foster, S. U. Khan, J. Agric. Food Chem., 50 (2002), 3204–3207.

[243] D. Aparna, G. seethamma, K. M. Vijayalakshmi, N. V. Kumar, Am. Eur. Asian J. Agric. Environ. Sci., 7 (2010), 657–670.

[244] D. Na, N. Yongnian, K. Serge, Chin. J. Chem., 28 (2010), 404–410.

[245] D. Lambropoulou, T. Sakellarides, T. Albanis, Fresenius J. Anal. Chem., 368 (2000), 616–623.

[246] M. Khani, S. Imani, K. Larijani, Afr. J. Food Sci., 5 (2011), 499–502

[247] M. Gamon, C. Lleo, A. Ten, J. AOAC Int. 84 (2001), 1209–1216.

[248] Y. T. Gebreegzi, G. D. Foster, S. U. Khan, J. Agric. Food Chem. 48 (2000), 5165–5168.

[249] M. E. Sanchez, R. Mendez, X. Gomez, J. M. Villacorta, J. Liq. Chromatogr. Related Technol. 26 (2003), 483–497.

[250] G. Erdodu, J. Ana. Chem., 62 (2007), 466–469.

[251] H. Gu, A. Yu, H. Chen, Anal Lett., 34 (2001), 2361–2374.

[252] M. Mazloumardakani, E. Karami, H. Naeimi, B. Mirjalili, Turk J. Chem. 32 (2008), 571–584.

[253] H. Fili, A. Avan, S. Aydar, G. Cetintas, Int. J. Electrochem. Sci., 9 (2014), 148–160.

[254] J. B. Raoof, R. Ojani, M. Baghayeri, Turk J. Chem., 37 (2013), 36–50

[255] M. K. Pawlak, Polish J. Environ. Stud., 13 (2004), 411–414.

[256] C. L. Bourque, M. M. Duguay, Z. M. Gautreau, Int. J. Environ. Anal. Chem., 37 (1989), 187–197.

[257] W. Geremedhin, M. Amare, S. Admassie, Electrochim. Acta, 87 (2013), 749–755.

[258] C. Li, C. Wang, Y. Ma, S. Hu, Microchim. Acta, 148 (2004), 27–33.

[259] H. Yaghoubian, H. Karimimaleh, M. A. Khalilzadeh, F. Karimi, J. Serb. Chem. Soc., 74 (2009), 1443–1453.

[260] H. Zhang, K. Wu, Microchim. Acta, 149 (2005), 73–78.

[261] K. S. Ngai, W. T. Tan, Z. Zainal, R. M. Zawawi, M. Zidan, Int. J. Electrochem. Sci. 8 (2013), 10557–10567.

[262] H. Wang, M. Liu, X. Hu, M. Li, X. Xiong, Sens. 13 (2013), 16234–16244.

[263] X. Zhao, X. Fan, X. Chen, C. Chai, Q. Zhou, J. Polym. Sci., 44 (2006), 4656–4667.

[264] X. Jiang, D. Li, X. Xua, Y. Ying, Y. Li, Z. Ye, J. Wang, Biosen. Bioelectr., 23 (2008), 1577–1587.

[265] A. Ciucu, C. Negulescu, R. Baldwin, Biosens. Bioelectr., 18 (2003), 303–310.

[266] F. Kafilzadeh, A. Shiva, R. Malekpour, H. Azad, World J. Fish Marine Sci., 4 (2012), 150–154.

[267] C. Blasco, C. M. Lino, Y. Pico, A. Pena, G. Font, M. Silveira, J. Chromatogr. A, 1049 (2004), 155–160.

[268] N. Sharaf, S. Elserougy, A. Hussen, A. A. Arab, S. Ahmed, E. Hamid, Amer. Eur J. Agric. Envi. Sci., 4 (2008), 434–442.

[269] N. Priyantha, U. S. Weliwegamage, Ceylon J. Sc. Phys. Sci., 9 (2002), 95–101.

[270] K. Subramaniam, J. Solomon, Indian J. Clin. Biochem., 21 (2006), 169–172.

[271] H. E. Bakouri, J. P. Santander, L. C. Aguilera, A. Ouassini, I. N. Rodriguez, J. L. H. Cisneros, Chemosphere, 60 (2005), 1565–1571.

[272] M. C. L. Blanco, B. R. Rodriguez, B. C. Grande, J. S. Gandara, J. Chromatogr. A, 976 (2002), 293–299.

[273] S. Afful, E. Enimil, B. Blewu, G. A. Mantey, E. A. Ewusie, Res. J. Appl. Sci. Engin. Technol., 2 (2010), 592–595.

[274] C. M. Kin, T. G. Huat, Food Chem., 123 (2010), 760–764.

[275] S. N. Sinha, M. Odetokun, Amer. J. Anal. Chem., 2 (2011), 511–521.

[276] R. Paranthaman, A. Sudha, S. Kumaravel, Amer. J. Biochem. Biotechno., 8 (2012), 1–6.

[277] D. A. Lambropoulou, T. A. Albanis, Anal. Bioanal. Chem., 389 (2007), 1663–1683.

[278] C. Ravikumar, P. Srinivas, K. Seshaiah, J. Chem. Pharm. Res., 5 (2013), 361–366.

[279] F. J. Arrebola, J. M. Vidal, A. F. Gutierrez, J. Chromatogra. Sci., 39 (2001), 177–182.

[280] S. Chandra, A. N. Mahindrakar, L. P. Shinde, Middle-East J. Scient. Res., 5 (2012), 589–594.

[281] A. Therdteppitak, K. Yammeng, Sci. Asia, 29 (2003), 127–134.

[282] S. Shegefti, H. Sereshti, S. Samadi, Int. J. Environ. Res., 4 (2010), 237–246.

[283] J. M. Vidal, M. M. Frias, A. G. Frenich, F. O. Serrano, N. Olea, Rapid Commun. Mass Spectrom., 14 (2000), 939–946.

[284] S. Hossain, M. A. Chowdhury, M. M. Alam, N. Islam, M. H. Rashid, I. Jahan, Adv. Biochem. Biotechno., 1 (2015), 1–16.

[285] S. Chandra, A. N. Mahindrakar, L. P. Shinde, Int. J. Chem. Tech. Res., 6 (2014), 124–130.

[286] N. V. Venugopal, B. Sumalatha, S. Bonthula, Eurasian J. Anal. Chem., 8 (2013), 131–135.

[287] N. V. Venugopal, B. Sumalatha, S. Bano, J. Chem., 9 (2012), 857–862.

[288] K. Wani, M. K. Rai, R. Khatoon, Int. J. Sci. Res., 3 (2014), 202–205.

[289] N. Mai, X. Liu, W. Wei, S. Luo, W. Liu, Microchim Acta, 174 (2011), 89–95.

[290] N. Priyantha, S. Malavipathirana, Comparative Cevlon J. Sci.: Phys. Sci., 6 (1999), 38–46.

[291] H. G. Prabu, P. Manisankar, Analyst, 119 (1994), 1867–1873.

[292] P. Manisankar, S. Viswanathan, H. G. Prabu, Int. J. Environ. Anal. Chem., 82 (2010), 331–340.

[293] P. Manisankar, C. Vedhi, S. Viswanathan, H. Prabu, J. Environ. Sci. health, 39 (2004), 89–100.

[294] F. W. P. Ribeiro, T. F. Oliveira, F. F. Silva, G. F. Mendonca, P. H. Mello, H. Becker, P. L. Neto, A. Correia, V. N. Freire, Microchem. J., 110 (2013), 40–47.

[295] A. A. Aly, Food Sci. Quality Manag., 22 (2013), 28–34.

[296] D. Komes, D. Horzic, A. Belscak, K. Ganic, A. Baljak, Czech J. Food Sci., 27 (2009), 213–216.

[297] R. N. Goyal, S. Bishnoi, B. Agrawal, J. Electroanal. Chem., 655 (2011), 97–102.

[298] S. Guo, Q. Zhu, B. Yang, J. Wang, B. Ye, Food Chem., 129 (2011), 1311–1314.

[299] J. Zhang, L. Wang, W. Guo, X. Peng, M. Li, Z. Yuan, Int. J. Electrochem. Sci., 6 (2011), 997–1006.

[300] F. Zhao, F. Wang, W. Zhao, J. Zhou, Y. Liu, L. Zou, B. Ye, Microchim Acta, 174 (2011), 383–390.

[301] V. Nour, I. Trandafir, M. E. Ionica, St. Cerc. St. CICBIA, 11 (2010), 351–358.

[302] M. M. Ali, M. Eisa, M. I. Taha, B. Z. Abdalla, A. Elbashir, Pakistan J. Nutr., 11 (2012), 336–342.

[303] A. C. Torres, M. M. Barsan, C. M. A. Brett, Food Chem., 149 (2014), 215–220.

[304] M. K. A. Shwaiyat, Jordan J. Chem., 8 (2013), 79–89.

[305] S. Mehretie, S. Admassie, M. Tessema, T. Solomon, Anal. Bioanal. Electrochem., 3 (2011), 38-50.

[306] H. Tavallali, Y. Hamid, Asian J. Biochem. Pharm. Res., 1 (2011), 684–689.

[307] W. Y. Su, S. H. Cheng, Electroanalysis, 22 (2010), 707–714.

[308] L. Y. Shiroma, M. Santhiago, A. L. Gobbi, L. T. Kubota, Anal. Chim. Acta, 725 (2012), 44–50.

[309] V. Kumary, J. Divya, T. M. Nancy, K. Sreevalsan, Int. J. Electrochem. Sci., 8 (2013), 6610–6619.

[310] N. F. Atta, A. Galal, S. M. Azab, Int. J. Electrochem. Sci., 6 (2011), 5082–5096.

[311] X. Kang, J. Wang, H. Wu, J. Liu, I. A. Aksay, Y. Lin, Talanta, 81 (2010), 754–759.

[312] R. S. Babu, P. Prabhu, S. Anujaand, S. Narayanan, J. Chem. Pharm. Res., 4 (2012), 3592–3600.

[313] D. Sun, H. Zhang, Microchim Acta 158 (2007), 131–136.

[314] D. T. T. An, V. D. Hoang, Asian J. Res. Chem., 2 (2009), 143–147.

[315] S. Shahrokhian, R. S. Saberi, Int. J. Electrochem., (2011), 1–10.

[316] R. Chandra, K. D. Sharma, Int. J. Chromatogr. Sci., 3 (2013), 31–34.

[317] V. Vichare, P. Mujgond, V. Tambe, S. N. Dhole, Int. J. Pharm. Tech. Res., 2 (2010), 2512–2516.

[318] H. Wanyika, E. Gatebe, L. M. Gitu, E. K. Ngumba, C. W. Maritim, Afr. J. Food Sci., 4 (2010), 353–358.

[319] G. Alpdogan, K. Karabina, S. Sungur, Turkey J. Chem., 26 (2002), 295–302

[320] S. S. Chitlange, R. Soni, S. B. Wankhede, A. A Kulkarni, Asian J. Res. Chem., 2 (2009), 30–33.

[321] P. Y. Pawar, L. S. Zanje, S. S. Tambe, A. U. Nandgaonkar, P. V. Funde, A. A. Vyavhare, World J. Pharm. Pharmacol. Sci., 3 (2014), 744–750.

[322] M. R. Brunetto, L. Gutierrez, Y. Delgado, M. Gallignani, A. Zambrano, A. Gomez, G. Ramos, C. Romero, Food Chem., 100 (2007), 459–467.

[323] E. Dinc, F. Yurtsever, F. Onur, Turkish J. Pharmac. Sci., 1 (2004), 115‑138.

[324] B. Tsvetkova, B. Kostova, I. Pencheva, A. Zlatkov, D. Rachev, P. Peikov, Int. J. of Pharma. Sci., 4 (2012), 680–684.

[325] E. C. Demiralay, M. Gumustas, H. Canbay, Int. J. Compreh. Pharm., 6 (2011), 1–4.

[326] M. Idris, C. John, P. Ghosh, S. K. Shukla, T. R. Baggi, J. Anal. Sci. Tech., 4 (2013), 1–6.

[327] O. Lau, S. Luk, Y. Cheung, Analyst, 114 (1989), 1047–1051.

[328] A. P. Eisele, D. N. Clausen, C. R. T. Tarley, L. H. D. Antonia, E. R. Sartori, electroanalysis, 25 (2013), 1734–1741.

[329] A. J. Jeevagan, S. A. John, Electrochim. Acta, 77 (2012), 137–142.

[330] X. Q. Xiong, K. J. Huang, C. X. Xu, C. X. Jin, Q. G. Zhai, Chem. Ind. Eng., 19 (2013), 359−368.

[331] J. M. Zen, Y. S. Ting, Anal. Chim. Acta, 342 (1997), 175−180.

[332] B. J. Sanghavi, A. K. Srivastava, Electrochim. Acta, 55 (2010), 8638–8648.

[333] B. Brunetti, E. Desimoni, P. Casati, Electroanalysis, 19 (2007), 385–388.

[334] L. Svorc, P. Tomcik, J. Svitkova, M. Rievaj, D. Bustin, Food Chem., 135 (2012), 1198–1204.

[335] M. Amare, S. Admassie, Talanta, 93 (2012), 122–128.

[336] S. Yang, R. Yang, G. Li, L. Qua, J. Li, L. Yu, J. Electroanal. Chem., 639 (2010), 77–82.

[337] W. H. Khoo, M. Pumera, A. Bonanni, Anal. Chim. Acta, 804 (2013), 92–97.

[338] S. Khokhar, S. M. Magnusdottir, J. Agric. Food Chem., 50 (2002), 565–570.

[339] A. K. Ghosh, C. Ghosh, A. Gupta, J. Agric. Food Chem., 61 (2013), 3814−3820.

[340] T. R. Saciloto, P. Cervini, E. T. G. Cavalheiro, J. Braz. Chem. Soc., 24 (2013), 1461–1468.

[341] B. C. Lourencao, R. Medeiros, R. R. Filho, L. H. Mazo, O. F. Filho, Talanta, 78 (2009), 748–752.

[342] D. Wu, H. Lu, H. Xie, J. Wu, C. Wang, Q. Zhang, Sens. Actu. B, 221 (2015), 1433-1440

[343] D. Wu, Y. Li, Y. Zhang, P. Wang, Q. Wei, B. Du, Electrochim. Acta, 116 (2014), 244–249.

[344] P. V. Narayana, R. Madhusudana, P. Gopal, K. Reddaiah, P. Raghu, Res. J. Chem. Sci., 4 (2014), 37–43.

[345] L. Huang, S. Jiao, M. Li, Electrochim. Acta, 121 (2014), 233–239.

[346] Z. Sun, H. Fu, L. Deng, J. Wang, Anal. Chim. Acta, 761 (2013), 84–91.

[347] D. Lakshmi, M. J. Whitcombe, F. Davis, P. S. Sharma, B. Prasad, Electroanalysis, 23 (2011), 305–320.

[348] Y. Kim, J. H. Park, Y. Choi, Bull. Korean Chem. Soc., 25 (2004), 1177–1181.

[349] D. Oukila, L. Benhaddad, R. Aitout, L. Makhloufi, F. Pillier, B. Saidani, Sens. Actu. B, 204 (2014), 203–210.

[350] J. B. Claver, I. D. Ortega, M. C. V. Miron, L. F. C. Vallvey, Anal. Chim. Acta, 702 (2011), 254–261.

[351] J. Assob, M. Ngowe, D. Nsagha, A. Njunda, Y. Waidim, D. Lemuh, E. Weledji, J. Nutr. Food Sci. 4 (2014), 1–4.

[352] S. Lu, J. Luo, S. Ji, N. Li, H. Li, W. Li, Electrochim. Acta, 136 (2014), 130–137.

[353] A. Ozcan, S. Ilkbas, Electrochim. Acta, 133 (2014), 233–240.

[354] J. Perello, P. Sanchis, F. Grases, J. Chromatogr. B, 824 (2005), 175–180.

[355] V. Carrera, E. Sabater, E. Vilanova, M. A. Sogorb, J. Chromatogr. B, 847 (2007), 88–94.

[356] M. R. Shishehbore, A. Sheibani, M. Rezaie, Caspian J. Chem., 2 (2013), 65–73.

[357] A. Abbaspour, A. Khajehzadeh, A. Ghaffarinejad, Analyst, 134 (2009), 1692–1698.

[358] H. C. Hong, H. J. Huang, Anal. Chim. Acta., 499 (2003), 41–46.

[359] F. Ye, C. Feng, J. Jiang, S. Han, Electrochim. Acta, 182 (2015), 935–945

[360] X. Zhang, L. Ma, Y. Zhang, Electrochim. Acta, 177 (2015), 118–127.

[361] T. M. Nancy, V. A. Kumary, Electrochim. Acta, 133 (2014), 233–240.

[362] N. Lavanya, E. Fazio, F. Neri, A. Bonavita, S. G. Leonardi, G. Neri, C. Sekar, Sens. Actu. B, 221 (2015), 1412–1422.

[363] E. Ergun, S. Kart, D. K. Zeybek, B. Zeybek, Sens. Actu. B, 224 (2016), 55–64.

[364] L. Yang, D. Liu, J. Huang, T. You, Sens. Actu. B, 193 (2014), 166–172.

[365] P. Zhang, F. H. Wu, G. C. Zhao, X. W. Wei, Bioelectrochem., 67 (2005), 109–114.

[366] S. Kumar, H. Cheng, S. Chen, Electroanalysis, 21 (2009), 2281–2286.

[367] X. Li, M. Rahman, G. Xu, J. Lee, Electrochim. Acta, 173 (2015), 440–447.

[368] M. A. Kamyabi, M. A. Shafiee, J. Braz. Chem. Soc., 23 (2012), 593–601.

[369] Y. Umasankar, T. Huang, S. Chen, Anal. Biochem., 408 (2011), 297–303.

[370] D. Baskaran, J. W. Mays, M. S. Bratcher, Chem. Mater., 17 (2005), 3389–3397.

[371] D. Sun, Q. Zhao, F. Tan, X. Wang, J. Gao, Anal. Methods, 4 (2012), 3283–3289.

[372] J. Li, X. Zhang, Amer. J. Anal. Chem., 3 (2012), 195–203.

[373] M. Chao, X. Ma, X. Li, Int. J. Electrochem. Sci., 7 (2012), 2201–2213.

[374] A. P. Reis, C. R. Tarley, L. T. Kubota, J. Braz. Chem. Soc. 19 (2008), 1567–1573.